Stabilization of a high-resolution spectrograph and performance verification by measurements of the Rossiter-McLaughlin effect

Vanessa Fahrenschon

Munich 2022

Stabilization of a high-resolution spectrograph and performance verification by measurements of the Rossiter-McLaughlin effect

Vanessa Fahrenschon

Dissertation
an der Fakultät für Physik
der Ludwig–Maximilians–Universität
München

vorgelegt von
Vanessa Fahrenschon
aus Göppingen

München, den 05.01.2022

Erstgutachter: PD Dr. Roberto Saglia
Zweitgutachter: Prof. Dr. Thomas Preibisch
Tag der mündlichen Prüfung: 22.03.2022

Contents

List of Figures

List of Tables

Zusammenfassung

Die große Vielfalt von bekannten Exoplanetensystemen zeigt, dass eine Vielzahl von Effekten und Parametern die Planetenentstehung beeinflussen. Ziel dieser Arbeit war es, ein Messinstrument in Betrieb zu nehmen, das eine tiefergehende Charakterisierung von Planetensystemen erlaubt. Dazu wurde der Manfred-Hirt-Planeten-Spektrograf (MaHPS) mit Systemen zur Stabilisierung von Temperatur und Druck ausgestattet, die die notwendige Messgenauigkeit ermöglichen. Die Leistungsfähigkeit von MaHPS wurde anhand von Beobachtungen des Rossiter-McLaughlin-Effekts (RM-Effekt) nachgewiesen.

Diese Arbeit beginnt mit einem Überblick über die Parameter, die ein Exoplanetensystem beschreiben, und gibt eine Einführung in die Methoden, mit denen Exoplaneten entdeckt werden können. Anschließend wird der hochauflösende Spektrograf MaHPS vorgestellt, mit einem besonderen Augenmerk auf die Subsysteme für Kalibration, Temperatur- und Druckstabilisierung. Anhand von Messreihen mit Kalibrationslichtquellen wird die Temperatur- und Druckstabilität von MaHPS überprüft, mit dem Ergebnis, dass Radialgeschwindigkeitsmessungen mit einer Genauigkeit von wenigen m/s möglich sind.

Mit Hilfe des RM-Effekts kann der Winkel zwischen der Rotationsachse eines Sterns und dem Orbitnormalenvektor seines Planeten bestimmt werden. Der RM-Effekt bewirkt eine Anomalie der Radialgeschwindigkeitskurve während eines Transits des Planeten, wodurch der Orbitwinkel unter Berücksichtigung verschiedener Aspekte bestimmt werden kann. Die statistische Verteilung von bereits gemessenen Orbitwinkeln und deren Bedeutung für die existierenden Planetenentstehungsmodelle wird diskutiert.

Am Ende dieser Arbeit werden Beobachtungsdaten zum Nachweis des RM-Effektes für die drei Planetensysteme HD189733, HD149026 und HAT-P-2 präsentiert und interpretiert. Die Leistungsfähigkeit von MaHPS wird anhand von Vergleichen mit Messungen aus der Literatur bewertet, zudem werden Erfahrungen aus den Beobachtungen erläutert, um in Zukunft systematische Messfehler zu verringern.

In dieser Arbeit wurde dargelegt, dass MaHPS in der Lage ist, eine Messgenauigkeit von wenigen m/s bei Radialgeschindigkeitsmessungen zu erreichen. Darüber hinaus war es möglich, das Signal des RM-Effekts für die beobachteten Objekte mit einer Genauigkeit nachzuweisen, die vergleichbar ist mit der Genauigkeit anderer Spektrografen, die an Teleskopen der 2 m-Klasse betrieben werden. Dank dieser Erkenntnis wurde ein Beobachtungsprojekt initiiert, das Hinweise auf den RM-Effekt bei Objekten nachweisen soll, für die bisher keine Informationen über die Orbitorientierung bekannt sind, um eine Grundlage für detaillierte Beobachtungen mit präziseren Instrumenten zu schaffen.

Abstract

The vast variety of exoplanetary systems shows that multiple factors influence the formation of planets. This work aimed to take an instrument into operation that allows to thoroughly characterize planetary systems. To this end, the Manfred Hirt Planet Spectrograph (MaHPS) was equipped with systems for temperature and pressure stabilization to reach the required measurement precision. The performance of MaHPS was verified with observations of the Rossiter-McLaughlin (RM) effect.

This work gives an overview of the parameters that describe an exoplanetary system and provides an introduction to the methods used to detect exoplanets. The high-resolution spectrograph MaHPS is presented, including its subsystems for calibration, temperature and pressure stabilization. The thermal and pressure stability of MaHPS is demonstrated with measurement series of calibration sources, showing a radial velocity measurement precision on the order of a few m/s.

Furthermore, observations of the RM effect of the three planetary systems HD189733, HD149026, and HAT-P-2 are featured and interpreted. The overall performance of MaHPS is evaluated in direct comparison with measurements from the literature. In addition, experiences from the observation runs are summarized in order to reduce systematic measurement errors in the future.

This work shows that MaHPS is able to reach precisions of a few m/s for radial velocity measurements. Furthermore, the signal of the RM effect for all observed objects could be detected, with a performance comparable to that of other spectrographs operated at telescopes of the 2 m class. This finding forms the basis for future observation projects to detect hints of the RM effect for new objects, serving as starting point for observations with more precise instruments, in order to contribute to the understanding of planet formation mechanisms.

Chapter 1

Introduction

Is Earth a unique planet? This question has occupied humanity since ages. In the past decades, technological development and scientific progress have opened up the possibility to start finding answers to this question. Today, it is possible to use a variety of methods for the detection and characterization of planets outside of the Solar System, called exoplanets, which help to develop and improve our understanding of the formation and evolution mechanisms in planetary systems. Combining all the different measurements and theories, it is possible to find pieces to answer this age-old question.

In this work, a spectrograph is presented which is designed to detect exoplanets by radial velocity (RV) measurements, exploiting the Doppler effect. Special focus is laid on the technical requirements to obtain reliable results that are competitive with other state-of-the-art instruments. Moreover, observations of confirmed planetary systems have been made to verify the precision of the measurements.

In the following sections, an introduction to the scientific motivation and the fundamental physics relevant to this work is given. Chapter 2 features a general description of the *Manfred Hirt Planet Spectrograph* (MaHPS), while Chap. 3 contains a more detailed characterization of the subsystems this work made use of, as well as measurements thereof. The data reduction methods utilized for analyzing the measurements are described in Chap. 4 in detail. In Chap. 5 the astrophysical background of the scientific observations is presented and in Chap. 6 the observations of several planetary systems are discussed in detail. Finally, Chap. 7 gives a conclusion and future prospects.

1.1 Exoplanets

The term *exoplanet* or *extrasolar planet* is commonly used to refer to a planet that is not associated to the Solar System. Although this is no strict definition itself, it is based on the definition of the term *planet* by the International Astronomical Union (IAU):

> "A planet is a celestial body that (a) is in orbit around the Sun, (b) has sufficient mass for its self-gravity to overcome rigid body forces so that it assumes

a hydrostatic equilibrium (nearly round) shape, and (c) has cleared the neighbourhood around its orbit." Excerpt from *IAU Resolution B5* 2006, p. 1.

In the case of exoplanets, the orbit around the Sun in condition (a) is substituted by an orbit around a different star than the Sun, which can also be a multiple stellar system (e.g. a binary). This work only covers exoplanets in bound and cleared orbits around single stars, so that all three conditions of the adaption of the above definition of a planet will be fulfilled.

In the literature, the use of the term exoplanet is sometimes deviating from the given description. There are some cases of unbound objects that formed in an orbit around a star, like other exoplanets, and later got ejected from that orbit, e.g. by gravitational interactions with a third body. These so-called *rogue planets* or *free-floating planets* are occasionally also called exoplanets because of their shared formation history.

On the other hand, when talking about objects that are still under formation condition (c) is loosened, because *exoplanet* occasionally might as well refer to young objects that have formed around a young stellar system but still have significant amounts of gas, dust and rocks in their surroundings.

This work will not feature exoplanets around multiple stellar systems, so the assumption for all following considerations is that there is only one central star. Moreover, exoplanets may hereinafter also be referred to as *planets* due to the lack of a physical reason to distinguish between the two, e.g. when considering the geometry or the dynamics of the system.

1.1.1 Parameter definitions

Describing the geometrical and physical properties of an exoplanetary system involves a number of parameters. The notation presented here follows what is commonly used in literature. A compact overview of the used symbols is given in Tab. 1.1.

Kepler's first law states that the orbit of a planet describes an ellipse, which has the Sun at one of its focal points. This is also true for exoplanets on gravitationally bound orbits around other stars. However, a refinement has to be made: the central star (and also the Sun) does not sit precisely at the focal point. The focal point is in the barycenter, or center-of-mass, of the whole planetary system and the star orbits around it as a reflex motion of the planet's motion. Due to the large difference in mass between the star and the planet (or planets), for a significant fraction of systems the size of the orbit of the star is smaller than the stellar radius. Kepler's original law is therefore only an approximation, owing to the limited precision of orbit observations at those times.

The elliptical orbit

Let's consider a single planet orbiting a star on an elliptical orbit (Fig. 1.1) in two dimensions (2D). F_1 and F_2 are the two foci of the ellipse, with the convention that F_1 coincides

symbol	description	typical unit
a	length of semi-major axis	AU
b	length of semi-minor axis	AU
e	eccentricity	unitless
q	periastron distance	AU
ν	true anomaly	degree (°) or in units of 2π
P	orbital period	days
T_P	time of first periastron	Julian date (JD)
i	inclination of the orbit	degree (°)
Ω	longitude of the ascending node	degree (°)
ω	longitude of periastron	degree (°)
K	semi-amplitude of the radial velocity signal	m/s
M_P	planetary mass	M_{Jup} or M_{Earth}
R_P	planetary radius	R_{Jup} or R_{Earth}
ρ_P	mean planetary density	g/cm^3
M_S	host star mass	M_{Sun}
R_S	host star radius	R_{Sun}
T_{eff}	host star effective temperature	K
i_S	inclination of the stellar rotation axis	degree (°)

Table 1.1: List of important symbols used in this work to describe exoplanetary systems.

with the barycenter. The ellipse of the orbit is geometrically characterized by its **semi-major axis $\boldsymbol{a}$** and **semi-minor axis $\boldsymbol{b}$**. The deviation from the enclosing circle is given by the **eccentricity $\boldsymbol{e}$**, defined as

$$e = 1 - \frac{b^2}{a^2}. \tag{1.1}$$

Out of these three parameters, typically only a and e are used for describing a planet's orbit. The pericenter distance q, which is the smallest distance between the planet and the star and sometimes also called periastron, can be described as:

$$q = a(1 - e). \tag{1.2}$$

To parametrize the position of the planet on the orbit, the **true anomaly $\boldsymbol{\nu = \nu(t)}$** is used. It gives the angle between the direction of the pericenter and the actual position of the planet, measured at the focal point F_1. Because the analytical calculation of $\nu(t)$ for any given point in time t is not straightforward, it is often computed with help of the eccentric anomaly $E = E(t)$ and the mean anomaly $\mathcal{M}(t)$.

For the mean anomaly $\mathcal{M}(t)$, the (unphysical) assumption of a uniform motion without any change in the magnitude of the velocity of the planet on its orbit is made. This corresponds to the projected position of the planet on the auxiliary circle (illustrated in Fig. 1.1) and in the case of an orbit with $e = 0$, the mean anomaly and the true anomaly

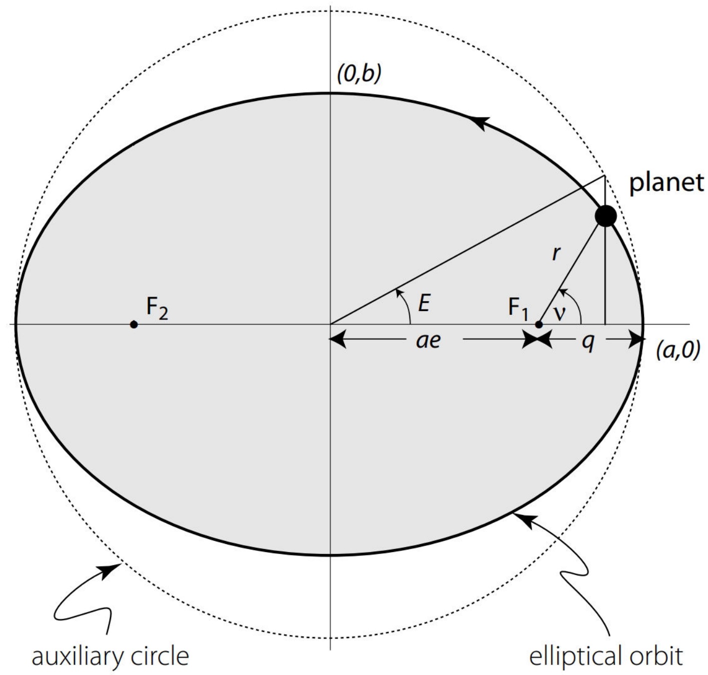

Figure 1.1: Schematic drawing of an elliptical orbit of a planet. The orbit is viewed face-on, perpendicular to the orbital plane. Adapted from Perryman (2018).

are identical: $\nu(t) = \mathcal{M}(t)$. The mean anomaly for any orbit can be written as

$$\mathcal{M}(t) = \frac{2\pi}{P}(t - T_P), \tag{1.3}$$

depending on the planet's **orbital period $\boldsymbol{P}$** and the **reference time $\boldsymbol{T_P}$** when the planet passed the point of periastron.

A word of caution is in place here regarding the reference time T_P. In the literature, one may also find the notation T_0 for the time of periastron passage. However, depending on the detection method used, T_0 in the literature can also refer to other times of reference during one orbit. Especially when the transit method is used, T_0 usually refers to the mid-time of the first detected transit, since most of the geometrical parameters are not known in that case and the periastron passage time cannot be determined. To clarify the explicit reference to the periastron, the notation T_P instead of T_0 is utilized in this work.

If the mean anomaly of a planet is known at time t, one can calculate the eccentric anomaly $E(t)$ for any given eccentricity e using *Kepler's equation* (Perryman 2018):

$$\mathcal{M}(t) = E(t) - e \sin E(t). \tag{1.4}$$

$E(t)$ gives the angle between the direction of the periastron and the projected position of the planet on the enclosing circle of the elliptical orbit, measured at the center of the circle

(Fig. 1.1). By using the relevant geometrical relations, the relation between the elliptical anomaly $E(t)$ and the desired true anomaly $\nu(t)$ is found to be

$$\cos\nu(t) = \frac{\cos E(t) - e}{1 - e\cos E(t)}. \tag{1.5}$$

With those definitions made, we can write the equation for the distance between the star and the planet as a function of time (see e.g. Ohta et al. 2005):

$$r_P = \frac{a(1-e^2)}{1 + e\cos\nu(t)}. \tag{1.6}$$

It can be immediately noted that for systems with $e = 0$, i.e. a perfectly circular orbit, $r_P = a$ is a constant.

The observed orbit

The case presented above corresponds to a system observed exactly face-on, with the orbit lying on the plane-of-sky (POS). The POS is the plane perpendicular to the line-of-sight (LOS) from the observer to the observed object, which contains the focus F_1 of the orbital ellipse, that by convention coincides with the barycenter.

In the general case of an orbit of an exoplanetary system observed under an arbitrary angle, three more parameters are needed to describe the 3-dimensional (3D) orbit (Fig. 1.2). Additionally to a, e, P and T_P, the angles i, Ω and ω need to be defined to account for the orientation of the real orbit relative to the POS.

The **inclination angle $\boldsymbol{i}$** is given as the angle between the POS and the plane of the orbit. By convention, i is measured in the direction away from the observer and restricted to values $0° \leq i \leq 90°$. This is due to degeneracies by symmetry and the fact that there is no physical difference between systems with positive or negative inclination angles.

The point on the POS in which the planet crosses the POS while moving away from the observer is called the ascending node, sometimes denoted with the symbol ☊. The **longitude of the ascending node $\boldsymbol{\Omega}$** gives the angle between the northern direction (or the direction of positive declinations[1] $+\delta$) on the POS and the direction of the ascending node, measured at the focus F_1 (Fig. 1.2). The convention is to measure Ω from north to east (or the direction of positive right ascensions[1] α) on the POS.

The last degree of freedom of the orbit orientation is constrained by the **argument of periastron $\boldsymbol{\omega}$**. It gives the angle between the ascending node direction and the periastron direction and is measured in the orbital plane at F_1 in the direction away from the observer. With these parameters, it is possible to completely describe an orbit of an exoplanet.

[1]Here, the common sky coordinate system of right ascension angle α and declination angle δ is used, both measured with respect to the equatorial plane of the sky.

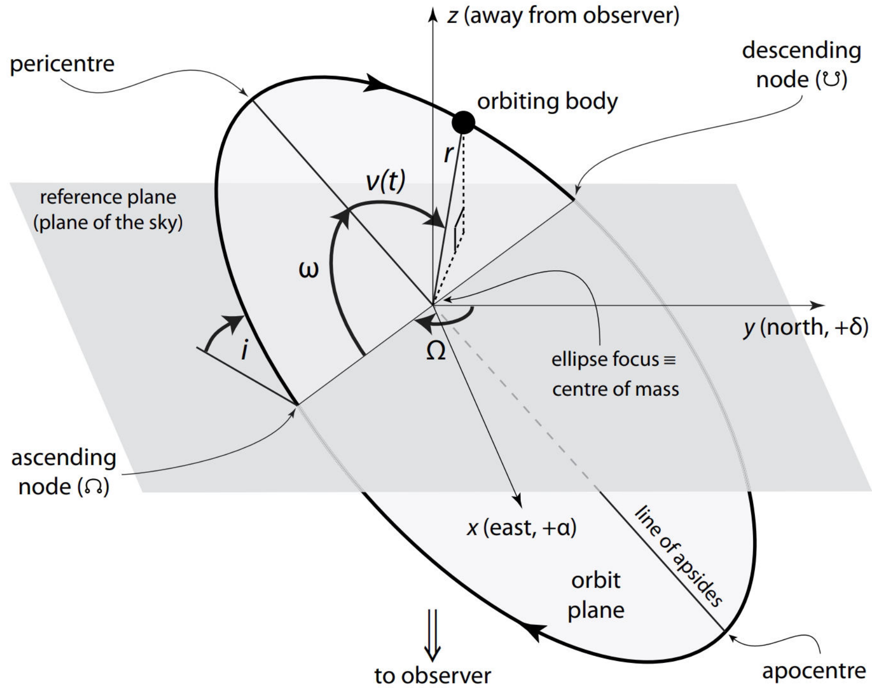

Figure 1.2: Schematic drawing of the observables of an elliptical orbit of a planet. The orbit is under an angle relative to the plane of sky and the line of sight of the observer. Adapted from Perryman (2018).

Physical parameters

Extending beyond the parameters introduced above, the characterization of exoplanets makes use of some more parameters. The most important one is the **mass of the planet M_P**. Of special interest is also the **planet radius R_P**, which in combination with the mass allows to calculate a **mean density ρ_P**. With that measure, it is possible to distinguish between planets that are mostly gaseous (like Jupiter), icy (like Neptune) or rocky (like Earth or Mars).

For planet formation models, it is important to know these parameters also in relation to those of the host star, specifically its **stellar mass M_S** and **radius R_S**. In context with possible detection biases, another relevant property of the star is the spectral type, where as a simplification often only the **stellar effective temperature T_{eff}** is given.

1.1.2 Detection methods

Exoplanets can be detected with a variety of methods, most of which are indirect measurements of the presence of a companion orbiting the host star. Each of the methods suffers from specific limitations, but also features unique advantages. In the following, an overview of the most common detection methods used today is given.

Radial velocity method

The first undisputed exoplanet discovery was achieved using the radial velocity (RV) method (Mayor and Queloz 1995). The RV method exploits the Doppler effect, which causes the spectral absorption lines of the star to shift periodically due to an orbital motion around the common barycenter with a companion. However, the Doppler effect is in first order, neglecting any relativistic terms, only sensitive to the projection of the motion onto the LOS (for more details see Sec. 1.2.1). This fact induces a systematic deficiency in detecting planets on orbits with small inclination angles i.

The orbital parameters that can be measured directly from RV observations include e, P, T_P, Ω and ω. The most important advantage of the RV method is its capability to give a lower limit for the mass of the planetary companion in the form of $M_P \sin(i)$, provided that the mass of the host star is known. The mass measurement is restricted to a lower limit because of a degeneracy with the inclination angle i due to the projection onto the LOS, as i cannot be obtained from RV measurements alone.

For the RV method, the amplitude of the effect scales with the mass ratio between the star and the planet M_P/M_S, making it hard to detect low-mass planets, especially around massive stars. There is also a dependency on the distance between both bodies, parametrized by a, since the star is moving more slowly if the planet is further away, owing to the correlation of period P and a in Kepler's third law. The combination of these statements leads to a major characteristic of the RV method: it is disproportionately sensitive to massive[2] planets on orbits close to their host stars.

Figure 1.3 illustrates the dependencies of the RV signal amplitude on the planet mass and distance for the four planets Jupiter, Saturn, Neptune and Earth in the Solar System. It can be immediately seen that the signal from a planet with the mass of the Earth is more than two orders of magnitude smaller than that of a planet with the mass of Jupiter. The currently prevalent instrument sensitivity allows to measure amplitudes around 1 to 10 m/s, which for a host star with the Sun's mass implies that planets less massive than Neptune cannot be detected (e.g. Hatzes 2016a). A new generation of instruments with sensitivities below 1 m/s is just going into operation to better probe the occurrence of low-mass planets similar to Earth (e.g. González Hernández et al. 2018; Pepe et al. 2021).

The bulk of planets discovered with the RV method are so-called *hot Jupiters*, with masses around $0.3 - 13 M_{Jup}$ (Jupiter masses) and orbit sizes of $0.01 - 0.2$ AU (astronomical units). Figure 1.4 shows all confirmed exoplanets that were discovered with the RV method, plotted by their orbital separation a and the planetary mass. The cluster of hot Jupiters is very evident (top left) and a second systematic effect can be seen: the cut-off towards smaller planet masses and larger separations, causing the sharp cut of available measurements on the lower right.

One of the current challenges of the RV method is to gain enough measurement precision to overcome the systematic hurdle when looking for these light-weight planets. Detecting a planet with a mass comparable to Earth ($\sim 0.003 M_J$) on an orbit of 1 AU requires extreme

[2] In this context, *massive* refers to the planet's mass in direct comparison with the mass of the host star.

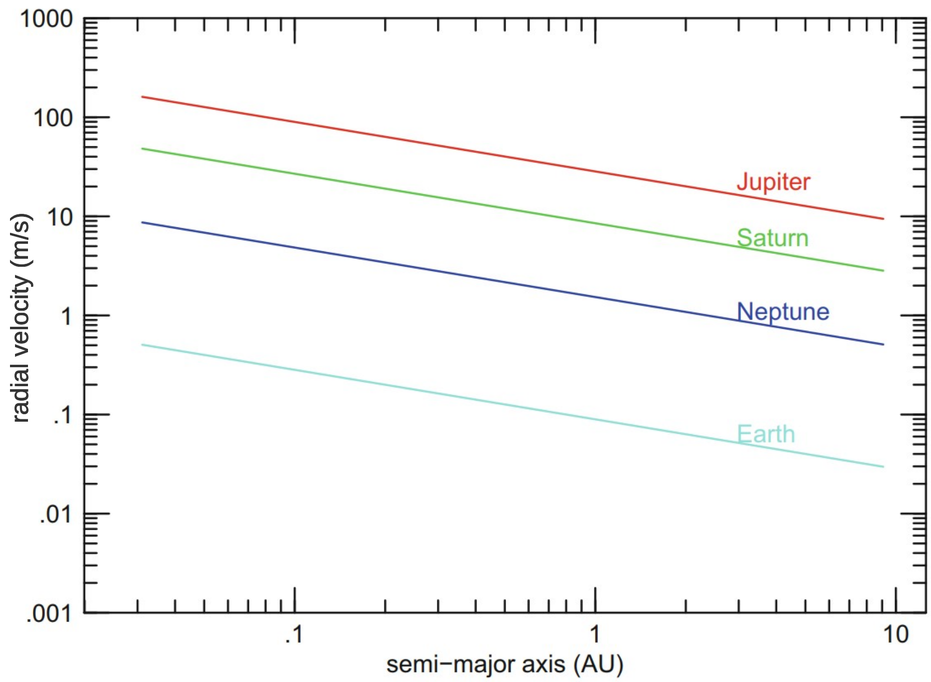

Figure 1.3: The expected RV signal amplitude for planets with masses corresponding to the Solar System planets Jupiter, Saturn, Neptune and Earth, as function of the separation from the Sun. Graphic adapted from Hatzes (2016a).

instrumental stability, as well as careful and precise treatment of intrinsic RV effects of the host star, that are of the same order of magnitude. Until now, only a few planets with Earth-like mass have been discovered with the RV method, which are all on very close-in orbits around small host stars.

The RV method is one of the most successful exoplanet detection methods to date, measured by the number of planets that were detected. Around 1500 planets are cataloged to have RV measurements (*NASA Exoplanet Archive* 2021), which corresponds to $\sim 25-30\%$ of all known exoplanets.

Transit method

The majority of the exoplanets known up to date has been discovered with the transit method. This method is based on the characteristic decrease in the measured brightness of a planet-hosting star, if the planet transits in front of the host star. But for such a transit to happen, the orbital inclination of the system is required to be close to 90° (edge-on).

The amplitude of the brightness drop during an exoplanet transit depends on the size ratio of the star and the planet, which permits to measure the radius of the exoplanet R_P if information about the stellar radius R_S is available from other sources. The beginning and end phases of the transit are called ingress and egress, respectively, and they allow to determine the parameters a, i, T_0, and P, the latter if multiple transits are observed

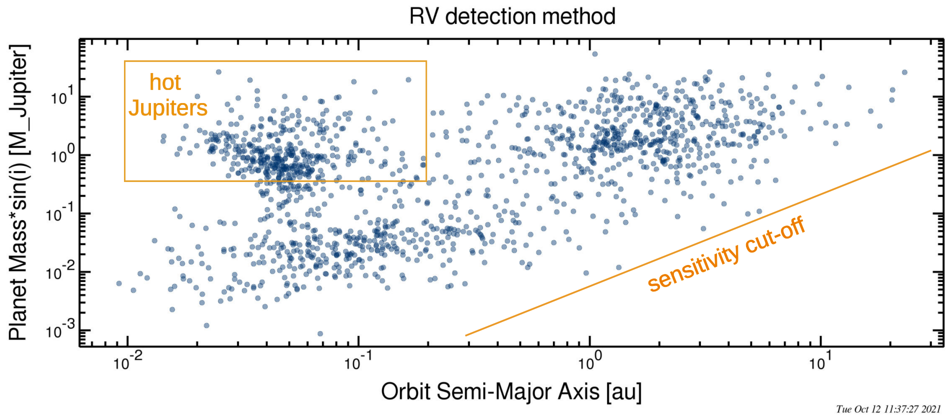

Figure 1.4: Exoplanets detected with the RV method, plotted by orbital separation and mass of the planet. The orange rectangle (top left) highlights the population of hot Jupiters, the orange line (bottom right) indicates where signal amplitude is too small for a detection. Error bars of the measurements are omitted for better visibility. Graphic compiled and adapted from the *NASA Exoplanet Archive* (2021).

(Santos et al. 2020). From transit measurements alone, it is for the vast majority of cases currently not possible to infer knowledge about the eccentricity e or the angles ω and Ω. Only for a few exceptional cases, the measurement precision and sampling rate is good enough to allow obtaining these parameters.

The systematic bias that is characteristic for the transit method builds on the probability to detect a transit in the first place, which is in approximation proportional to R_S/a (Santos et al. 2020). This relation can be understood intuitively, because on the one hand, the larger a star is the more geometries exist in which the planet is transiting, and on the other hand the further away this planet is, the less likely a passage is because of the smaller range of inclination angles that produce an alignment on the LOS. This means that, similarly to the RV method, there is a strong detection preference for close-in planets. As noted above, the signal strength depends on the size ratio of the star and the planet, which implies an advantage to observe bigger planets or transits in front of smaller stars.

Overall, the transit and RV method suffer from very similar restrictions, leaving a large portion of the planetary parameter space, especially towards earth-like planets, uncovered. This is demonstrated in Fig. 1.5, where the orbital separation a and the measured planet radius R_P are shown for all currently known transiting planets. Almost all planets are on orbits of < 1 AU, the majority is even inside of 0.1 AU. The bulk of hot Jupiters is clearly discernible in the upper left part of the plot and a second population is formed by a large number of planets with sizes of $\sim 1 - 5R_{Earth}$, which are commonly referred to as super-Earths and mini-Neptunes.[3]

[3]For reference, the radii of Neptune and Jupiter in units of Earth radii are $R_{Neptune} \approx 4R_{Earth}$ and $R_{Jupiter} \approx 11R_{Earth}$, respectively.

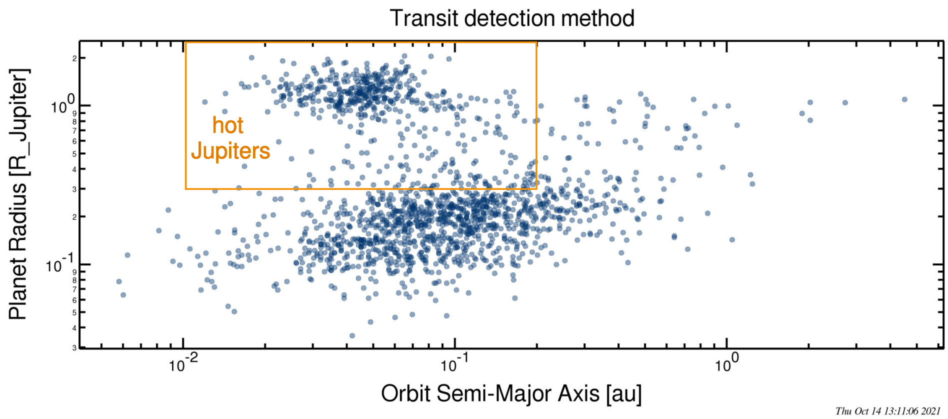

Figure 1.5: Exoplanets detected with the transit method, plotted by orbital separation and radius of the planet. The orange rectangle (top left) highlights the population of hot Jupiters. Error bars of the measurements are omitted for better visibility. Graphic compiled and adapted from the *NASA Exoplanet Archive* (2021).

The parameter set obtained from transit observations is complementary to the one from RV measurements, which makes the combination of the two very attractive whenever it is possible. Apart from the complete geometrical parameter set, one can get the density of the planet by combining mass and radius. This gives an insight into the composition of the planet, which is an important detail for planet evolution models.

Despite the unfavorable conditions for the detection of smaller planets, the advance in instrumentation has led to improved measurement precisions that allow to probe for planets that are roughly Earth sized. In these days, the most successful transit discovery machines are space-based all-sky photometrical surveys like TESS.[4] This instrument has been tailored specifically to detecting a large number of exoplanets by monitoring large fields of stars and providing very precise brightness measurements.

Since the observation of transits and even conducting blind surveys is cheap compared to the other methods, the transit method is currently the workhorse of exoplanet detection. Unfortunately, the transit effect is very prone to false positives, since several scenarios that do not involve planets can mimic a planet signal. In Fig. 1.6, several scenarios that can result in a photometric signal similar to that of an exoplanet are illustrated. Most false positive detections can be attributed to eclipsing binaries (EBs), binary star systems which show a partial or complete eclipse as the two stars orbit the common barycenter. The amount of light blocked during the eclipse varies as a function of the overlap between the two stellar disks and if the overlap is small, it is impossible to distinguish from photometry alone

[4]TESS is the Transiting Exoplanet Survey Satellite, a satellite telescope in operation since 2018. TESS performs a full-sky survey for photometric transit signals from exoplanets by observing a given sector of the sky continuously for 27 d and then proceeding to the next sector, until the plane of the sky is covered (e.g. Stassun et al. 2018).

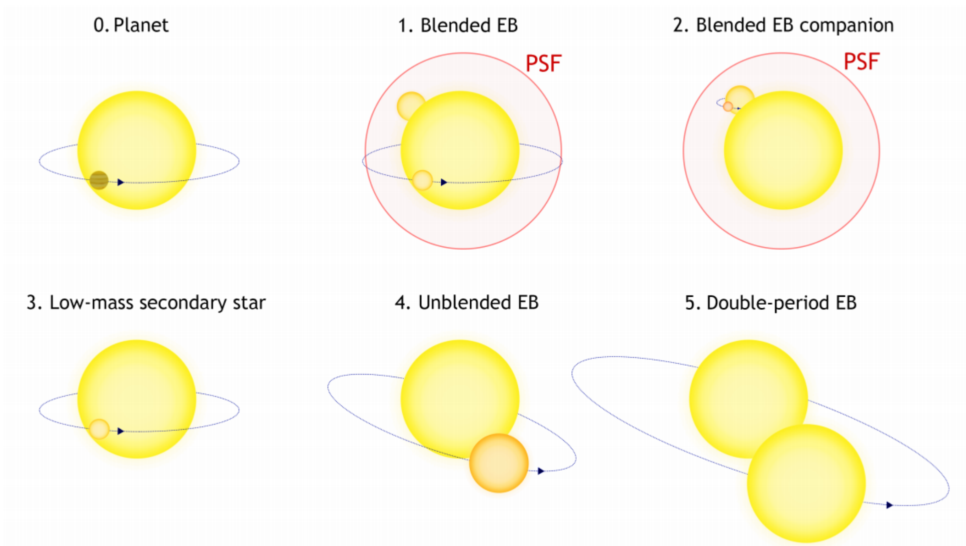

Figure 1.6: Scenarios for false positive detections with the transit method. 0: detection of a transiting planet; 1 and 2: unresolved binary stars, where either the more massive (1) or the less massive (2) star has a low-mass star as additional companion; 3: single star with a low-mass star as companion; 4 and 5: (partially) resolved eclipsing binary stars with a small overlap of the stellar disks, either with different stellar masses (4) or two stars of the same mass (5). Graphic taken from Obermeier (2016).

whether a star or a planet is the cause.

For this reason, follow-up observations for transiting planet candidates are essential and a significant amount of candidates is rejected. Nevertheless, surveys like TESS and Kepler are extremely successful, with a total of about 3300 transiting planets detected and confirmed so far, which makes up $\sim 3/4$ of the known exoplanets.

Astrometry

The term *astrometry* refers to measuring the positions and motions of stars on the POS. Detecting exoplanets with astrometry is based on the same effect as the RV method: the reflex motion of the star around the common barycenter with a companion. However, instead of measuring the motion component along the LOS, astrometry allows to measure the components in the other two spatial dimensions (Quirrenbach 2010).

The POS motion of a star without any companions has two causes: on the one hand the proper motion of the star in the gravitational field of its neighborhood and the galaxy, on the other hand the parallax motion due to the Earth's orbit around the Sun. If a companion is present, be it a second star or a planet, then the projected ellipse of the host star's motion around the barycenter is superimposed on the other two effects, resulting in a more complex pattern. Since the first two components can be modeled, e.g. by using reference stars, it is possible to obtain the companion-induced orbit. This allows to determine values for P, T_P, e, a, i, ω and Ω. In this particular case, a is not measured directly, but as θ in angular units

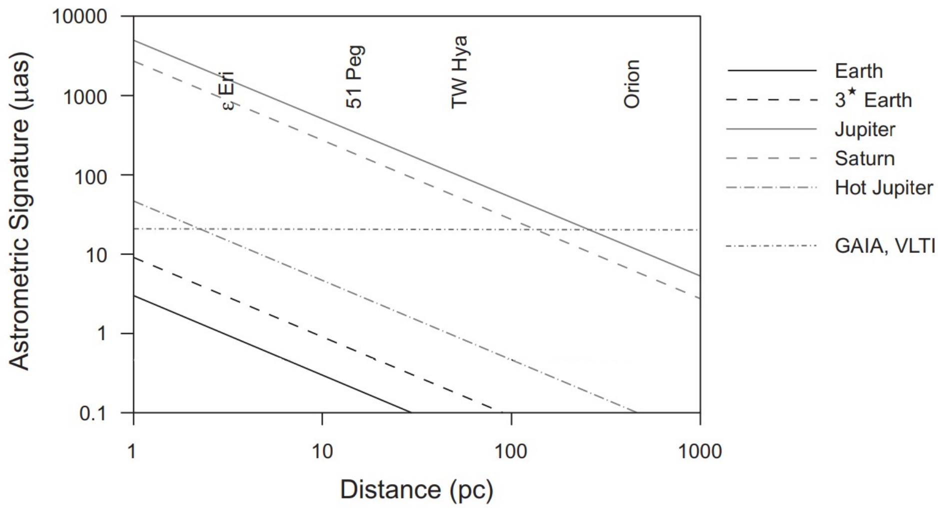

Figure 1.7: Amplitude of the astrometric signal for different given planet masses, depending on the distance of the system from the observer. The distances of several known objects are indicated. The dashed horizontal line gives the sensitivity limit of the state-of-the-art instruments GAIA and VLTI. Graphic adapted from Quirrenbach (2010).

(typically milliarcsec) and the distance d of the observer to the system, which is known from the parallax motion of the star, is required to convert to a in length units like AU.

The amplitude of the reflex motion of the star increases for larger semi-major axes a (or longer periods) and for larger planetary masses, but it decreases with the distance d of the system from the observer (Quirrenbach 2010). This implies a systematically better sensitivity for detecting high-mass planets with long periods and large orbit sizes, which is an important counterpart to the RV and transit methods. Furthermore, the astrometric measurements are independent of the spectral type and other characteristics of the host star, which is another important difference to the RV method that allows to probe for exoplanets around stars that are hot, massive, rapidly-rotating or in an early or late evolutionary state.

Figure 1.7 shows the expected signal for a selection of planets, depending on the distance of the host star from Earth. It can be clearly seen that the signal for a close-in Jupiter-like planet is about two orders of magnitude smaller than that of a Jupiter on a ~ 5 AU orbit like in the Solar System. The horizontal dashed-dotted lines give approximate sensitivity limits for two important instruments, illustrating that with the current state of technology, the astrometric detection of planets is limited to the direct solar neighborhood up to $10-100$ pc and Earth-like planets are not detectable.

The full strength of the astrometry method is unfolded when it is combined with RV observations. Most importantly, the measured 2D motion allows to determine i and thus can provide a real planetary mass for systems where a measurement of $m \sin i$ is available. While transit observations are a much easier way to determine i, they are restricted to values around $i \approx 90°$, which isn't the case for astrometry measurements. If a star has multiple planets, astrometry also allows to determine the inclination of their orbits relative to each other, which is an important insight used in the development of more accurate planet formation and evolution models.

Until now, astrometry has mainly been used to make follow-up observations of planets that have been detected with the RV method. Reaching the required precision of position measurements is challenging and the measurements are expensive in terms of observation time. Luckily, the development of increasingly precise astrometric instruments is also pushed forward by other fields than exoplanet science and there has been a lot of technological development in the past years, with the most remarkable instrument being the satellite GAIA. It performs an all-sky survey and reaches a typical measurement error of $0.05 - 0.1$ mas for an individual star (Makarov et al. 2021).

To date, a total of about 10 exoplanets have been characterized using astrometry (*NASA Exoplanet Archive* 2021), all of them using ground-based observatories. This small number is not surprising, considering the effort needed to obtain reliable measurements. However, the analysis of the large GAIA sample is still at its beginning and for the coming years, detections on the order of hundreds of exoplanets are expected (Quirrenbach 2010).

Direct imaging

As the name direct imaging (DI) already implies, this method aims to take images that resolve exoplanets from their host stars, but today is not limited to optical images anymore. In contrast to the other methods, DI can detect exoplanets already in a single observation, but then the orbital parameters remain unknown. The most important property of DI is its direct use of the photons reflected or emitted by the planet, which also allows to take a spectrum of the exoplanet's light.

If a time series of images is recorded, it is possible to obtain values for a, P, T_P, e, i, ω and Ω. However, these measurements are usually afflicted with large error bars, for although the basic idea of DI is very straightforward, the practical implementation is complicated by various challenges.

When trying to take a direct image of an exoplanet, two main obstacles have to be faced: first the small angular separation of the planet from its star, and second the difference in magnitude between the host star and the planet (e.g. Beuzit et al. 2019). The systematic detection biases for DI directly follow from this statement: it is much more sensitive towards exoplanets that are separated more widely from their host star, which also means that they have longer periods. Moreover, exoplanets that are either larger or are intrinsically hotter are also more likely to be detected, e.g. young planets that have not yet reached thermal equilibrium or massive gas giants that radiate in the IR wavelengths. Just like the astrometry method, DI is depending on the distance of the system from the observer, since the apparent (angular) planet-star distance decreases with increasing distance to the observer.

Figure 1.8 shows the exoplanets detected with direct imaging to date. Compared with Fig. 1.4, this illustrates the significantly larger orbital separations, most of them between $10 - 10^4$ AU, and the larger planet masses that do not reach masses smaller than $1 M_J$,

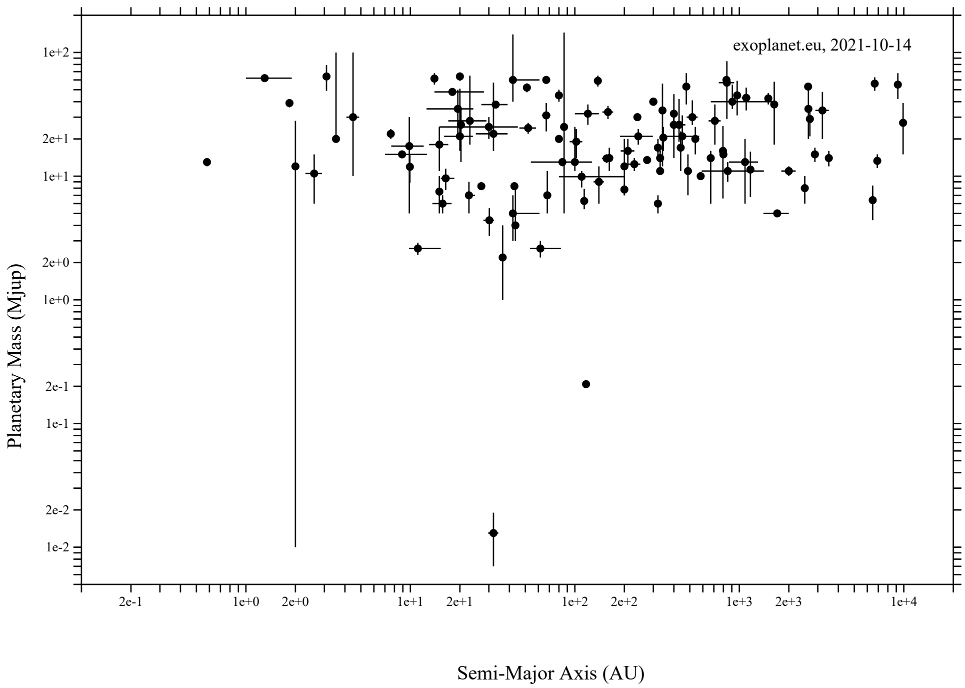

Figure 1.8: Exoplanets detected with direct imaging. The measured orbital separations and planetary masses are plotted. Graphic compiled from Roques (2021).

apart from very few exceptions. It should also be noted that a significant number of the exoplanets in this plot lie above the so-called brown dwarf limit of $13M_J$, in which case they commonly are not classified as planets anymore.

Due to the unique systematic limitations of the DI method, there are hardly any exoplanets currently known that can also be observed with the RV or transit method. However, even though the added value from observations with different techniques might not be available, DI brings its own outstanding benefits. As already mentioned, if the direct light of a planet can be recorded, it's also possible to get its spectrum. This spectrum cannot have a high resolution, owing to the small brightness of the planet, but it is enough to characterize broad bands of absorption lines, which are usually attributed to gaseous atmospheres. This means that the composition of the planet and its atmosphere can be studied, which is of incredible value for planet formation models.

Nowadays, there are both ground-based and space telescopes that are equipped for DI. When using ground-based telescopes, one has to compensate the atmospheric seeing so that the telescope can work near the diffraction limit in order to reach the required angular resolution. This can be done with a variety of active or adaptive optic systems, by exploiting optical interferometry and by observing preferably at longer wavelengths (near to mid-infrared). Examples are the instruments SPHERE (Beuzit et al. 2019) and GRAVITY (Gravity Collaboration et al. 2017), both operated at the Very Large Telescope. By using a space telescope, it is possible to make use of the diffraction limit without further complications, however the size of the primary mirrors of space telescopes and therefore the diffraction limit itself is considerably smaller.

The main challenge in the further development of DI is overcoming those restrictions, which is planned in different ways. On the one hand, new 30m-class telescopes like the E-ELT (European Extremely Large Telescope) are designed to have multistage adaptive optic systems with vastly improved performance, on the other hand space telescopes like the JWST (James Webb Space Telescope) are on the way to provide larger apertures without the need of compensating the atmosphere. Both instruments are believed to push the boundary of DI down to planets with several Earth masses on orbits < 1 AU around their host star.

Because of the technical challenges that are bound to direct imaging and the distance dependence, the number of detected planets so far is pretty modest, with around 140 registered in the Roques (2021) database. But considering the developments explained above, the expectation is that DI will gain significance in the next ten years.

Microlensing

The gravitational lensing effect, originally described in general relativity theory, is exploited when detecting planets with so-called microlensing. Whenever a mass, in this case a planet and its host star, traverse in front of a background star, the brightness of that background star is amplified in a very characteristic way and allows to detect the presence of exoplanets as a deviation from the usually symmetric brightness profile expected from an individual star (e.g. Santos et al. 2020).

Due to the physics behind the gravitational lensing effect, the main properties that can be measured are the distances to the star in the foreground (the lens) and the background (the source), along with the mass of the lens object. It is also possible to measure the separation of the planet from its host star, although the precision of that measurement depends on the position of the planet relative to the star in the POS. The usual orbital parameters of the planetary system can only be obtained if very special geometric conditions between the source, the lens and its companion are met, which are extremely unlikely.

One of the biggest advantages of this method is that the amplitude of the brightness magnification scales with the lens mass as $\sqrt{M_L}$. This makes microlensing unique in comparison with the other detection methods, because its sensitivity for smaller planets is comparatively higher. Furthermore, until today microlensing is the only way to detect rogue planets, meaning planets that are not bound to any host star anymore. However, microlensing has two fundamental drawbacks: first, the probability of a passage of a lens in front of a suited source is very low, which is why current microlensing measurements are exclusively directed towards the dense fields of the Milky Way or the Magellanic Clouds. Second, the observed transiting events are nonrecurring, so once a microlensing planet is found, there is little chance to study it again in the future and as much data as possible has to be collected during this one occasion.

Even though the systematic restrictions of microlensing are considerable, it has proven to be a valuable and productive detection method. Figure 1.9 gives a plot of the orbital

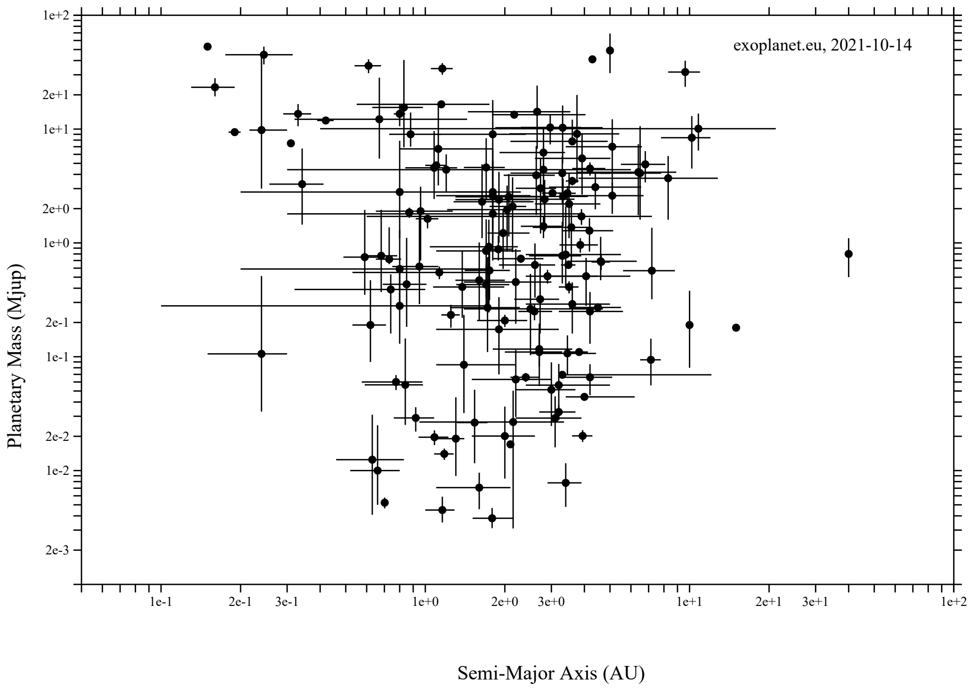

Figure 1.9: Exoplanets detected with microlensing. The measured orbital separations and planetary masses are plotted. Graphic compiled from Roques (2021).

separations and planetary masses of all microlensing planets. This makes clear how microlensing can add to the other methods, because basically all of the planets are within 10 AU from their star, and a significant number is even showing separations < 1 AU. All the planets have masses between 1 Earth mass and a few Jupiter masses, which allows to probe almost the complete mass spectrum that we find in the Solar System.

Since microlensing is based on single events of host stars that are commonly too faint to be observed with any (current) telescope, a direct combination with any of the other detection methods is not possible. In very exceptional cases, the host star could be resolved after it had separated sufficiently from the background source, but these objects are still too faint to successfully apply any other method with the current instrumentation. But at the same time, the photometric surveys searching for microlensing events have been able to detect a number of transiting planets as side products, since the methodology of staring at a particular stellar field for a given time interval and afterwards doing a photometrical analysis is very similar.

The technological limits of microlensing nowadays are dominated by the available field-of-view (FOV), the observation length and the photometric sensitivity that can be reached. To date, the available facilities have discovered about 150 planets (Roques 2021), and more will come as the surveys continue and technical upgrades are made.

1.2 Precise radial velocity measurements

Radial velocity measurements for exoplanets are commonly achieved by measuring the central wavelengths of a star's spectral lines as a function of time (e.g. Santos et al. 2020). In this section, the physical background will be outlined, followed by a presentation of the typical design of the used instruments.

1.2.1 Doppler effect

The direct measurement of the approaching or receding velocity of an object is possible because of the Doppler effect. As Christian Doppler noted in the middle of the 19th century, the wavelength of the waves emitted by an object changes, depending on its motion along the LOS to an observer (Doppler 1846).

The classical formulation of the Doppler equation gives the value of the observed wavelength λ_{obs} as function of the emitted wavelength λ_{em} and the radial velocity (e.g. Lovis and Fischer 2010):

$$\lambda_{obs} = \lambda_{em}(1 + \frac{1}{c}\ \vec{k} \cdot \vec{v}). \tag{1.7}$$

Here, $\vec{v}$ is the full velocity vector of the motion of the observed source, $\vec{k}$ is the unit LOS vector, pointing from the observer to the target, and c is the speed of light in vacuum. It is common convention that $v_{em} = \vec{k} \cdot \vec{v}$ is positive if the source is receding from the observer, which is in line with concepts like the cosmological redshift due to the expansion of the universe.

In the case of special relativity, the constancy of the speed of light c induces time dilation for any moving object. A direct consequence of time dilation is the change of frequencies (and thus wavelengths), which also has an effect on the measured Doppler shift (Einstein 1905):

$$\lambda_{obs} = \lambda_{em} \frac{1 + \frac{1}{c}\ \vec{k} \cdot \vec{v}}{\sqrt{1 - \frac{v^2}{c^2}}}, \tag{1.8}$$

where $v = |\vec{v}|$. In order to compute the correct absolute value for v, it is required to know the other two components of the velocity vector, which is usually not the case for RV measurements. However, since the velocities of the stars with exoplanets are small compared to the speed of light ($v \ll c$), the contribution of the term in the denominator can be neglected in most cases.

In principle, also general relativistic (GR) effects that arise from the curvature of spacetime due to gravitation should be taken into account when considering the Doppler effect. The treatment of all implications of GR is out of the scope of this work, but a thorough derivation of the necessary formulae is given by Lindegren and Dravins (2003). As a summary it can be said that, in the exoplanet context, as opposed to binary stars with much larger combined masses, almost all GR components have magnitudes of $\ll$1 m/s. The only significant factor is the gravitational redshift caused by the gravitational potential Φ between the source and the observer. The Doppler equation then reads (Lindegren and Dravins 2003)

$$\lambda_{obs} = \lambda_{em} \frac{1 + \frac{1}{c}\ \vec{k} \cdot \vec{v}}{1 - \frac{\Phi}{c^2} - \frac{v^2}{2c^2}}. \tag{1.9}$$

In approximation, the Newtonian gravitational potential $\Phi = \frac{GM}{r}$ at the source can be used to estimate the total contribution of the gravitational redshift. But since only relative variations of the RV are relevant for the detection of exoplanets and Φ is a basically constant term (at least at the <1 m/s scale), there is no restriction in the precision of the RV measurements if Φ remains unknown.

All in all, there is little need to treat relativistic effects when measuring signals of exoplanet hosting stars with the capability of today's instrumentation, although this might get more relevant in the future.

As a side note, it should be mentioned that any RV measurements made on Earth are superimposed with the RV signal of the orbital motion and rotation of the Earth. This has to be taken into account by doing a barycentric correction, using the exact location of the observer and precise models of the Solar System, before using the obtained RV values any further. However, since there are software packages like *barycorrpy* available to do that and no additional changes to them were made in this work, the reader is referred to the package documentation (Kanodia and Wright 2018) for a detailed explanation.

1.2.2 The radial velocity curve

Once a series of RV measurements has been obtained, a RV curve can be generated. The RV curve for the orbit of a planet can be calculated from the orbital equations given in Sec. 1.1.1, if the orbital parameters are known. Since only the motion of the host star can be measured, Eq. 1.6 needs to be modified with a scaling factor in order to compute the position of the star relative to the barycenter as a function of time:

$$r_S = \frac{M_P}{M_s + M_P} \frac{a(1-e^2)}{1 + e\cos\nu(t)}. \tag{1.10}$$

The radial velocity equation is then found by differentiating r_S with respect to t, which gives the velocity vector $\vec{v}$, and subsequently performing the projection onto the LOS in form of the dot product $\vec{k} \cdot \vec{v}$. Lovis and Fischer (2010) give an example of how the procedure described here looks in detail. The choice of the coordinate system in which $\vec{v}$ and $\vec{k}$ are expressed is arbitrary, since the result of the LOS projection gives the radial velocity v_R as a scalar independent of the coordinate system:

$$\begin{aligned} v_R &= \sqrt{\frac{G}{a\ (1-e^2)}}\ \frac{M_P \sin i}{\sqrt{M_S + M_P}}\ (\cos(\omega + \nu(t)) + e\ \cos\omega) \\ &= K \cdot (\cos(\omega + \nu(t)) + e\ \cos\omega). \end{aligned} \tag{1.11}$$

It should be noted that the mass difference between the star and the planet is typically several orders of magnitude. For this reason, the simplification $M_S + M_P \approx M_S$ can be made, allowing to solve the equation more easily for M_P.

The RV curve that results from Eq. 1.11 has a sinusoidal shape, which is distorted for $e \neq 0$, and its amplitude scales with the constant K. It is possible to re-write the expression for K with Kepler's third law so that it is a function of the orbital parameters that are directly obtainable with the RV method:

$$K = \left(\frac{2\pi G}{P}\right)^{\frac{1}{3}} \cdot \frac{M_P \sin i}{(M_S + M_P)^{\frac{2}{3}}} \cdot \frac{1}{\sqrt{1-e^2}}. \tag{1.12}$$

K is called the RV semi-amplitude, because its value gives half of the amplitude of the RV signal:

$$K = \frac{max(v_R) - min(v_R)}{2}. \tag{1.13}$$

In practice, the orbital parameters of an observed exoplanet are not known a priori. The usual procedure to extract the parameters combines several steps: First, a frequency analysis of the RV data is made, e.g. with a periodogram. If the number of data points is sufficient and therefore the sampling of the curve is good enough, the period of the planet shows up as a sharp peak. Once the value for P is found, Eq. 1.11 is fit to the RV data points to obtain e, ω, and K. The latter directly provides $M_P \sin i$ if knowledge about M_S is available.

In Fig. 1.10, the RV data and the best-fit curve are shown for the star 51 Pegasi. The planet is on an orbit without any significant eccentricity ($e = 0$ is assumed) and the signal has a semi-amplitude $K = (57.3 \pm 0.8)\,\mathrm{m/s}$ (Naef et al. 2004). For comparison, Fig. 1.11 shows the RV curve of HD108147, which hosts a planet with high eccentricity ($e \approx 0.5$) and a signal of $K = (36 \pm 1)\,\mathrm{m/s}$ (Pepe et al. 2002).

1.2.3 Spectroscopy of stars

The RV shift of a star is measured by taking a spectrum and determining the exact wavelengths of the absorption lines in said spectrum, which can be converted to a velocity with the Doppler equation. Since the RV signal of an exoplanet is small, the desired RV precision can only be reached if a large number of absorption lines is regarded simultaneously and the average of the individual shifts is computed. As straightforward as this concept is, as diverse are the complications that go along with it. There is a multitude of factors that influence the position, depth, width and shape of the spectral lines, causing shifts or uncertainties that in the RV data may look like, but are completely unrelated to the stellar motion that the observer wants to measure. The most important effects are compiled in this section in order to enable a good understanding of the errors that RV measurements are afflicted with.

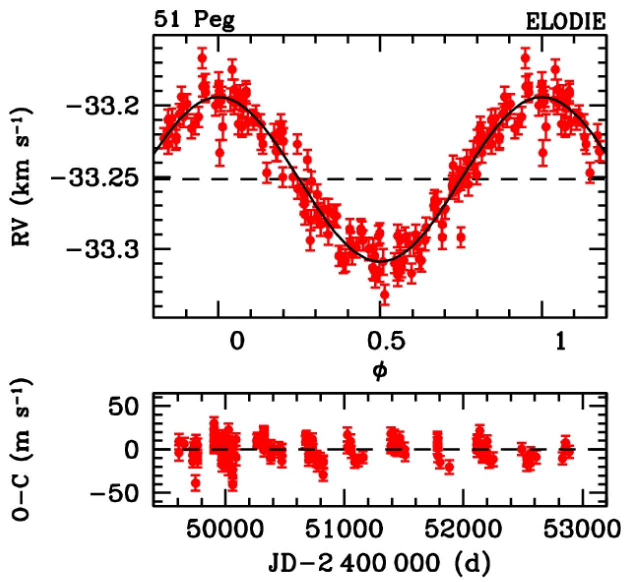

Figure 1.10: The RV curve of 51 Pegasi, as measured with the spectrograph *ELODIE*. Top: phase-folded plot of the data points (red symbols) and the best fit RV curve (black line); bottom: residuals after the subtraction of the orbit fit from the data, not phase-folded. Graphic taken from Naef et al. (2004).

Stellar temperature

Thermal broadening has a significant effect on the appearance of absorption lines in stars. The Maxwell-Boltzmann distribution relates the temperature of an ensemble of particles to a probability distribution of the velocities of the individual particles (Brownian motion). With higher temperature, the average velocity increases and the distribution broadens. Since the motions of the particles have random spatial distribution, there is always a fraction of particles moving along the LOS where the Doppler effect takes hold and traces this velocity distribution, thus causing a broadening of the spectral line which is stronger for higher temperatures. Stars with extremely high T_{eff} like O and B stars suffer from strong thermal broadening, washing out the absorption lines. As a consequence, only the few strongest lines are left, making these stars inferior for RV measurements compared to stars of cooler spectral types like F and G.

Rotation

All stars are rotating because of the conservation of angular momentum during their formation. The rotation of a star means that at any time one half of the stellar surface is approaching the observer while the other one half is receding, except for an exactly pole-on observation. This leads to Doppler shifts of the different stellar surface areas, causing a (constant and symmetrical) line broadening. The amount of broadening scales with the magnitude of the rotation velocity component along the LOS, which in turn depends on the inclination of the stellar rotation axis i_S relative to the LOS. The apparent rotation ve-

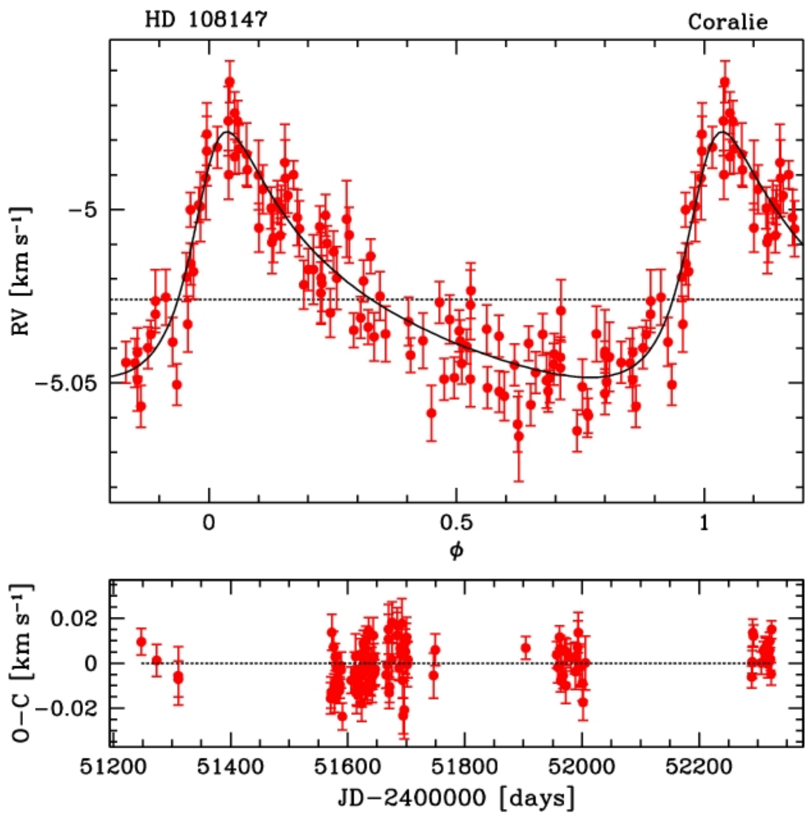

Figure 1.11: The RV curve of HD108147, as measured with the spectrograph *CORALIE*. Top: phase-folded plot of the data points (red symbols) and the best fit RV curve (black line); bottom: residuals after the subtraction of the orbit fit from the data, not phase-folded. Graphic taken from Pepe et al. (2002).

locity $v_{rot} \sin i_S$ can be measured from spectroscopic observations. Typical values for stars that are suited for high-precision RV measurements (e.g. main-sequence F and G stars) are of the order of ~1 to 30 km/s. If a star is rotating much more rapidly, the rotational broadening can become the dominating effect for the line width. Precise RV determinations are then basically impossible because the determination of the center of such broad lines involves larger intrinsic errors. Another big issue concerning rotation are star spots. They block part of the light that contributes to the rotationally broadened line profile and since the spots normally appear as an irregular pattern on the surface of the star, the line profile suffers from an asymmetry. As the star rotates, the spots come into and out of view, producing a periodic line shift of up to several m/s (Dumusque et al. 2012).

Convection

The presence of convection cells or granules on the stellar surface has several impacts on the absorption lines. If a star has a convective outer layer, this layer consists of a large number of convection cells that all have different temperatures. In general, the amount of radiation from the cells where hot material ascends is larger than that from the descending cells because of the transport of energy out of the star. This leads to an overall blueshift of the spectrum which has small variations of several m/s on the scale of minutes to hours. Furthermore, the line profile is a superposition of the individual profiles of all the convection cells. Since there is usually a large variety in the exact wavelength shift and intensity from single granules, often a line profile distortion is the consequence. The distortion can be measured by computing the line bisectors, where amplitudes of several 100 m/s are common, affecting the precision of the line center determination significantly.

Stellar oscillations

It is not unusual for the outer layers of stars to undergo periodic pulsations that are caused by density perturbations. Since this motion also occurs in the LOS direction, these oscillations cause a periodic shift of several m/s on timescales of minutes. In most cases, the exposure time of a spectroscopic observation is long enough to average over a few oscillation cycles, so the overall impact on the spectrum is only relevant for observations with high time resolution (Carrier et al. 2005).

Stellar activity

Most stars undergo activity cycles similar to the 11 year cycle known for the Sun. This variation of the magnetic activity influences the total number of star spots on the stellar surface significantly. Additionally to the impact already outlined in the context of rotation, star spots feature strong magnetic fields that also affect the absorption lines. The presence of electromagnetic fields gives rise to shifts in the atomic energy levels and thus the related absorption wavelengths. One example is the Zeeman effect, where a direct relation of the strength of the magnetic field to the amplitude of the shift is present. The observed line profile is a superposition of shifted and unshifted lines that is in consequence variable with the number and intensity of star spots. Overall, shifts of several 10 m/s are possible (Dumusque et al. 2011).

Proper motion

The biggest contributor to the absolute RV value that is measured is the proper motion of the observed star. The overall motion of the star in the gravitational potential of its large-scale surroundings has a RV component of typically 10 to 100 km/s. However, since this motion is mostly linear on timescales of decades, the effect can safely be approximated by a constant RV shift.

Companions

The presence of an unknown companion of the target star can be problematic for RV measurements, since the Doppler signal is independent of the nature of any companion.

Especially for companions which have periods a few times longer than typical RV observation campaigns the probability is high that they remain undetected. A second planet on a very far orbit with many years period is such an example. In that case, the RV shift contribution from this companion will appear in the (shorter-term) RV measurements of the first planet as a linear or quadratic perturbation. It is the standard procedure to include a free linear and quadratic term when fitting RV curves.

Instrumental effects

The instrument itself also changes the appearance of the spectral lines. The line width for unresolved lines is determined by the width of the slit or entrance aperture. A multitude of other significant effects exist, which are in large part highly specific and characteristic for each individual instrument. Since parts of the following chapters are devoted to describing a selection of instrumental effects, no further elaboration is made in this place.

1.2.4 High-resolution spectroscopy

Ever since the RV method has been used to successfully observe the first exoplanets, the field of spectroscopy with high spectral resolution has gained a lot of significance in the astronomical community. The aim of this section is to explain the structure of a basic spectrograph, give details about the relevant physical relations and the related technical challenges.

The basic spectrograph

The basic optical elements of a spectrograph are the entry aperture, a collimator, a dispersive element, a focusing system and a detector (Fig. 1.12). The characteristics and performance of the whole spectrograph are basically determined by two parts: the entrance aperture and the dispersive element.

The choice of entrance aperture is important, since it on the one hand determines the amount of light that is available in the spectrograph, and on the other hand influences the instrument-specific line width. Assuming a perfectly flat, monochromatic light source that illuminates a rectangular entrance slit, the intensity distribution that is detected in the image plane corresponds to the convolution of the image of the slit with the instrument function that incorporates the imaging functions of all optical elements. The result is called the instrumental profile (IP) and in the ideal case of perfect optical elements is described by a sinc function. The instrumental line width is then given by the full width at half maximum (FWHM) of the central peak.

For very precise measurements of the centers of spectral lines, the instrumental FWHM should be as small as possible. However, there are two reasons why the slit width cannot be arbitrarily narrow: the diffraction limit and the intensity of the light passing through the slit. The latter can be easily understood by considering that the amount of light after the slit is proportional to the slit area and therefore the signal is decreased when the slit is

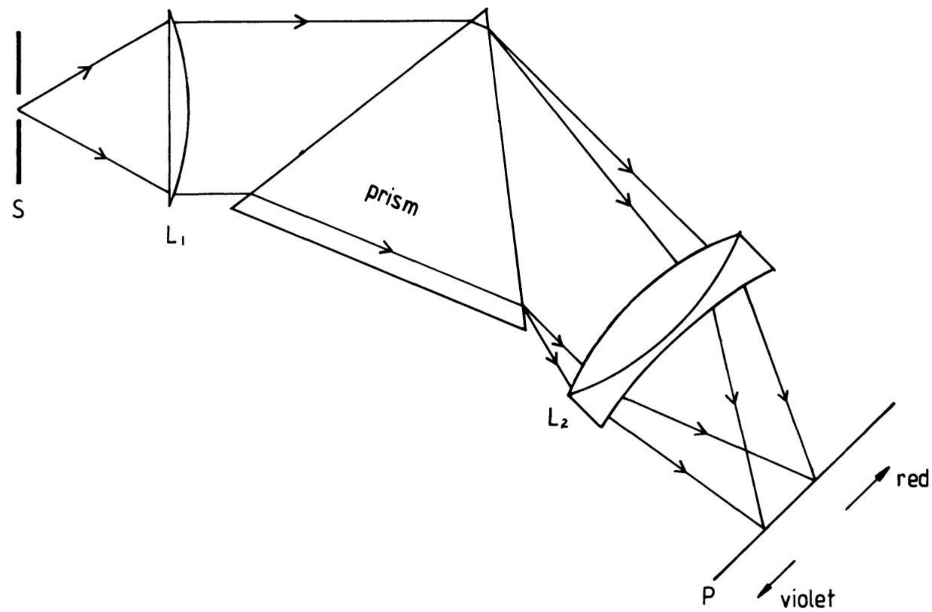

Figure 1.12: Schematic drawing of the setup of a basic prism spectrograph. The light enters the spectrograph through the entry slit S, passes the collimating lens L_1, gets dispersed by the prism and focused onto the image plane P (detector) by the camera lens system L_2. Graphic taken from Thorne (1988).

narrowed. The diffraction limit is reached when the slit width is small enough so that the dispersion effects of the slit become significant. In total, the slit width has to be chosen for a specific instrument as a trade-off between these factors and needs to be carefully balanced.

The heart of the spectrograph is the dispersive element, in the example of Fig. 1.12 a prism. It disperses the incoming light because of the fact that the refractive index of the prism material is a function of wavelength. Prisms feature many advantages, e.g. easy manufacturing and a high throughput, but their dispersive power is limited. Other dispersive elements that are frequently used are gratings and grisms (a combination of a grating and a prism). Both exploit the wavelength dependence of the constructive interference condition as the cause for the dispersion.

The grating equation

A grating can be imagined as an assembly of many small slits with the same width next to each other. In practice, gratings come in two types: transmission and reflective gratings. As the name implies, transmission gratings act like actual slits where the light enters from one side and leaves at the other, while reflective gratings consist of a regular pattern of facets that reflect the light. However, the principle for both types is the same and will be illustrated here for a transmission grating.

Figure 1.13 (a) shows a simple transmission grating, which is often realized by scratching

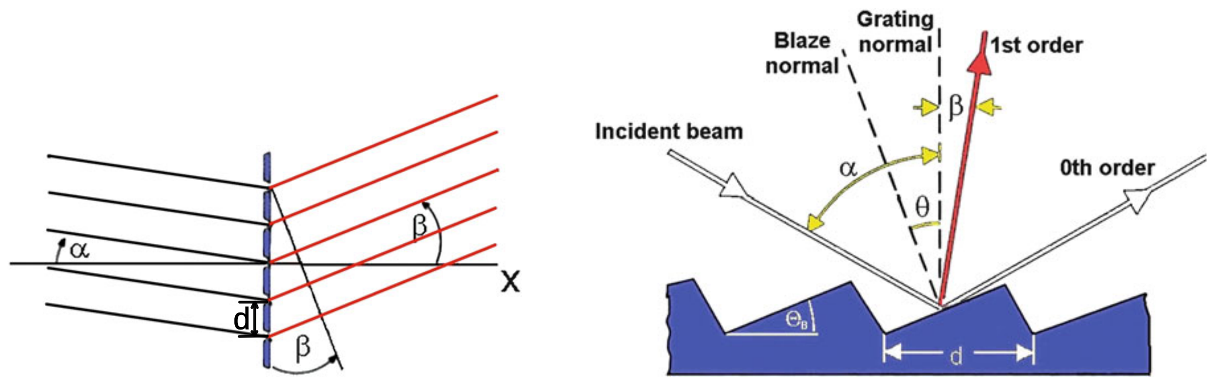

(a) Transmission grating. (b) Blazed grating.

Figure 1.13: Schematic of a simple transmission grating (a) as example for the working principle of a grating. The incoming beam at angle α gets diffracted at the slits. The outgoing angle β depends on the separation of the slits d and the wavelength of the light λ. Schematic of a blazed grating (b) with blaze angle θ, for which the light is mainly reflected into the first instead of the zeroth order. Graphics taken and adapted from Eversberg and Vollmann (2015).

or etching small grooves into a glass plate. A parallel beam of light falls onto the grating under the angle α, which is measured relative to the grating surface normal X. Each slit or groove then acts as a source for an elementary wave according to Huygens' principle. These waves will interfere constructively or destructively and form the outgoing beam under the deflection angle β. It is essential to understand that this deflection angle is purely caused by interference and is not related to the refraction or reflection at or in an optical material.

Constructive interference happens whenever the difference of the optical path length between two waves with wavelength λ is equal to any integer multiple of λ. Taking this condition and combining it with geometrical considerations about the possible path length differences yields the grating equation (e.g. Eversberg and Vollmann 2015):

$$m \cdot \lambda = d\,(\sin\alpha + \sin\beta)\,. \tag{1.14}$$

Here, m can be any integer value and is called the (spectral) order, while d is the separation of two adjacent slits. Equation 1.14 immediately shows that if the incident angle α is fixed, β changes for different wavelengths, giving rise to the desired spectral dispersion of the light. Only in the special case of the zeroth order ($m = 0$) the wavelength dependence vanishes and a white-light image of the entrance aperture is delivered.

Transmission gratings have a large drawback, namely the optical transmission efficiency. This can be problematic for applications where a large spectral spread of only few incoming photons is needed, as is the case for the RV method. Reflective gratings offer the possibility to drastically reduce the light loss and therefore are predominantly used in state-of-the-art planet spectrographs.

For a flat geometry of the grating as shown in Fig. 1.13 (a), the main part of the

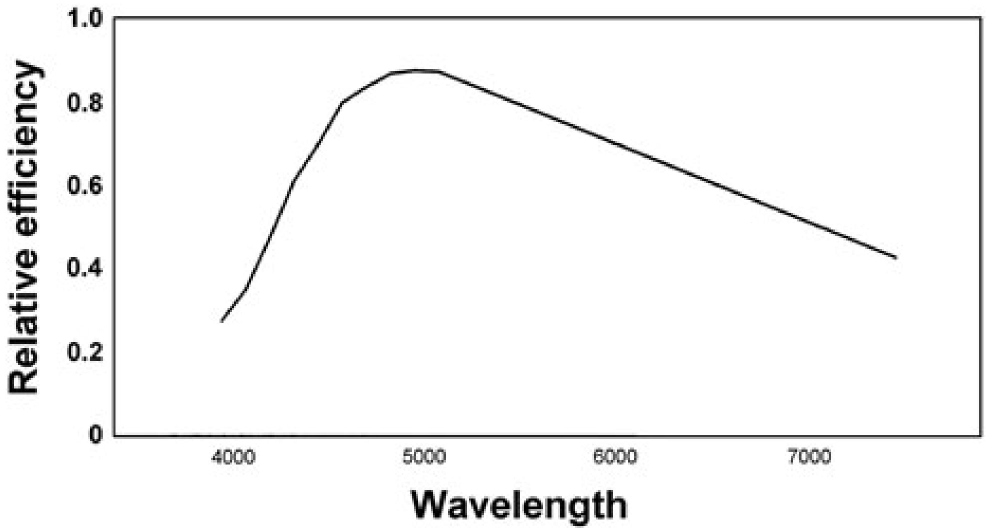

Figure 1.14: Typical efficiency curve for a blazed grating, depending on the wavelength. The grating has a blaze wavelength of $\lambda_B \approx 5500\,\text{Å}$. Graphic taken from Eversberg and Vollmann (2015).

light is diffracted into the zeroth order and the intensity decreases for all following orders. For spectral analysis, this is not desirable, because the zeroth order does not contain any wavelength information. By arranging the grooves under a so-called blaze angle θ, the peak intensity can be moved into a different order (Fig. 1.13, b).

The blazing of the grating facets means that the surface of each facet is tilted by θ relative to the grating surface (or the normal on the facet is tilted to the grating normal). As a consequence, the light is mainly diffracted into a higher order (corresponding to the specular reflection direction) while the positions of the single orders, given by Eq. 1.14, remain the same.

It has to be noted that the maximum achievable intensity in a given order $m \neq 0$ is wavelength dependent (Fig. 1.14), since the grating equation 1.14 can only be fulfilled perfectly for a given combination of α and β for a single wavelength λ_B. This so-called blaze wavelength is a basic characteristic of any blazed grating and has to be chosen according to the intended aim of the measurements with the grating.

A further consequence from the use of a grating is the blaze function. Although carrying the same name, the blaze function is not related to the blaze angle or blaze wavelength. As in any diffraction of light on a multi-slit setup, the resulting diffraction pattern is the interference pattern of the slits convoluted with the intensity distribution of the diffraction at a single slit. The latter one in spectroscopy is called the blaze function and takes the form of a sinc function with the width depending on the width d of the slit or facet. For smaller d, the sinc function gets broader, so gratings that are more finely grooved suffer less from this overall intensity envelope than gratings with broad grooves.

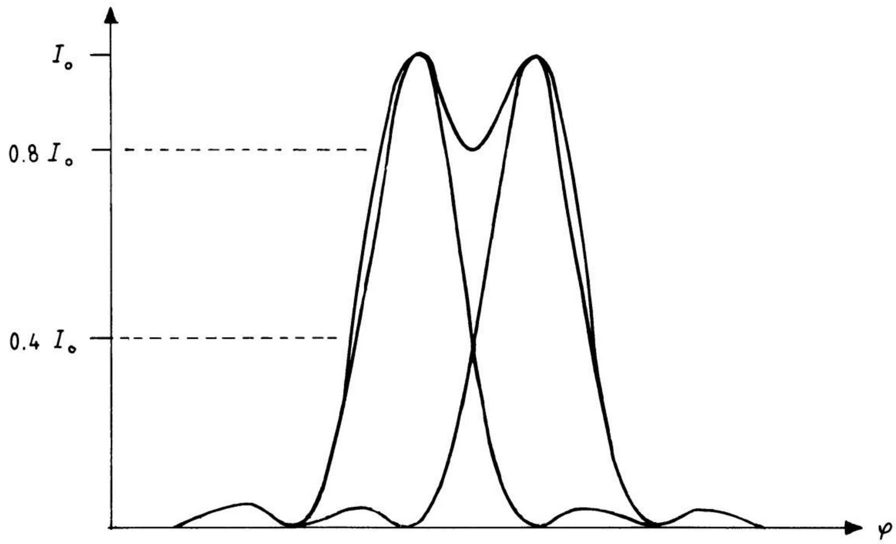

Figure 1.15: Illustration of the Rayleigh criterion for the case of two just resolved spectral lines with equal intensity I_0. The peak of one line coincides with the first minimum of the other line. In the added light profile, the intensity dip between the lines falls to 0.8 I_0. Graphic taken from Thorne (1988).

Spectral resolving power

The main characteristic of a spectrograph is its spectral resolving power R. It gives a quantitative measure for the smallest difference $\delta\lambda$ of two wavelengths λ and $\lambda + \delta\lambda$ that can be resolved in the spectrum.

Suppose that light from two monochromatic sources with equal intensity I_0 enters the spectrograph. After the diffraction at the grating, each of the sources will produce a line with a sinc function intensity distribution. Following the Rayleigh criterion, the two lines are regarded as just resolved if the intensity peak of one line coincides with the first minimum of the second line (Fig. 1.15). For sinc function line profiles, it can be shown that the added intensity profile has a minimum between the two peaks with an intensity of 0.8 I_0 (Thorne 1988). This quantitative condition is usually utilized for real spectrographs, since they never produce perfect sinc function profiles due to optical abberations and imperfections.

The resolving power R of a spectrograph is defined as (Thorne 1988):

$$R = \frac{\lambda}{\delta\lambda}. \tag{1.15}$$

The characteristic R value of a specific grating is determined by its angular resolution $d\beta/d\lambda$ and the width of the diffracted beam D. By substituting these two contributors with different formulations, as done by Thorne (1988) and Eversberg and Vollmann (2015), a simple equation for R can be reached:

$$R = D\frac{d\beta}{d\lambda} = m \cdot N, \tag{1.16}$$

where N is the total number of lines that are illuminated by the incoming beam. In other words, a higher resolving power can be achieved in two ways: either by increasing the total number of lines by using a broader beam or finer grooves, or by going to higher orders. In that context, the preference for blazed gratings in exoplanet RV measurements becomes clear immediately, since the beam and groove size cannot be optimized arbitrarily.

For the spectrographs in operation today, the resolving power is often only given as a rough number, because the ability to resolve two adjacent lines depends strongly on their relative intensities. Here, an identical peak intensity was assumed, which is a case that nearly never occurs for natural absorption lines in stars. So although R can be computed easily from the grating properties, the values achieved in reality are smaller and less precise.

Due to the multitude of applications of spectroscopy in observational astronomy, typical values for R can range from a few tens or hundreds to several 10^5 for state-of-the-art spectrographs. In the literature, there is a distinction between different resolving power domains as listed in Tab. 1.2. This should be understood as ballpark figures, as the use of one term or another may vary depending on the scientific context.

	typical R values
low resolution	< 1000
medium resolution	$\sim 1000 - 50000$
high resolution	$\sim 50000 - 100000$
ultra-high resolution	~ 200000 and more

Table 1.2: Common names for spectroscopy domains and the values of the resolving power that are typically associated to them.

1.2.5 Echelle spectrographs

In the RV search for exoplanets, high resolution spectrographs with $R \sim 50000 - 100000$ are mainly employed, with ongoing technical development towards even higher resolutions, e.g. ESPRESSO with $R \sim 200000$ (González Hernández et al. 2018). This is achieved by utilizing high physical order numbers in the range $m \sim 50 - 200$ (Hatzes 2016a; Eversberg and Vollmann 2015). An echelle grating is a special form of a blazed grating, optimized for such high orders by featuring large blaze angles of typically $\theta \approx 65°$ (Hatzes 2016a), corresponding to a diffraction of the light on the short side of the grating facets.

According to Eq. 1.14, the diffraction angle β for a given incident angle α stays the same if the width of the grooves d and the order m that is observed are varied such that $m/d = constant$. This implies that the resulting spectrum in a single order is identical, either when using gratings with a fine grooving and looking at small orders, or when the grating has a larger groove distance and higher orders are utilized (Hatzes 2016a). For

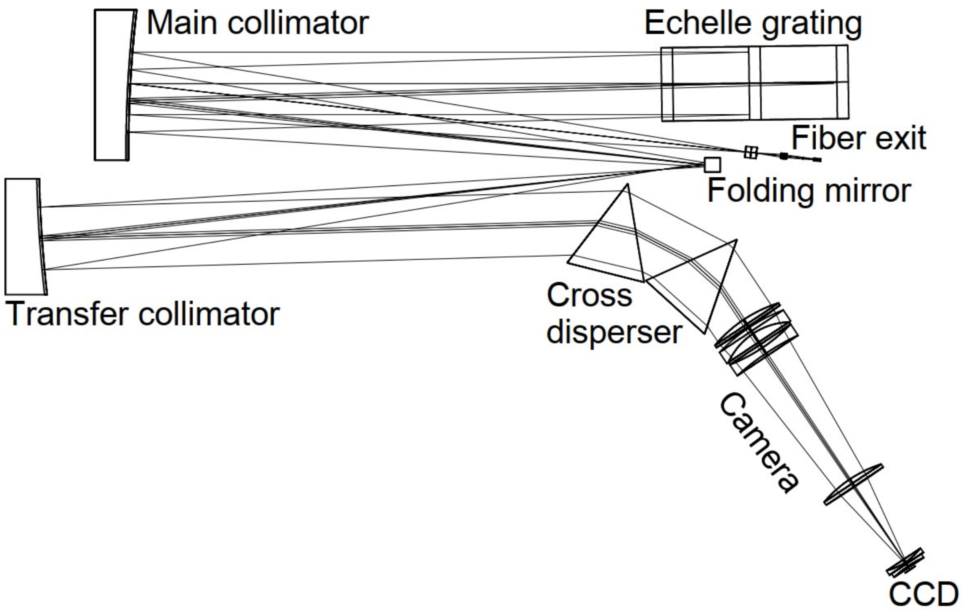

Figure 1.16: Optical design of the HERMES spectrograph as an example for a quasi-Littrow design. The fiber exit is the entrance aperture and after diffraction at the grating, the light follows the same path back and hits the folding mirror due to a small displacement angle. A cross-disperser in the optical path removes the overlap of the spectral orders by shifting them perpendicular to the main dispersion direction of the grating. Graphic taken from de Cuyper et al. (2007).

echelle gratings, the high order numbers allow to use gratings with comparably broad grooves, ensuring a better manufacturing quality, especially concerning the precision of θ.

In many echelle spectrographs, the grating is used in a so-called quasi-Littrow configuration. The grating is aligned to the optical axis of the spectrograph in such a way that the incident and outgoing angle (α and β, respectively) are identical. In the perfect Littrow configuration, the diffracted beam would be directly reflected onto the entrance slit, so in practice a small deviation angle has to be used in order to project the spectrum to a position where it can be used further (Fig. 1.16).

A side effect of choosing high physical orders is that the spatial (or angular) distance between the orders decreases with increasing m. The consequence is a strong overlap with numerous adjacent orders. However, this problem can be solved by introducing a cross-disperser in the optical path of the dispersed light (Fig. 1.16).

This cross-disperser has a small resolving power and displaces the beam in the direction perpendicular to the dispersion direction of the grating (Fig. 1.17). Typically prisms or low resolution gratings are used as cross-dispersers. In this way, the orders are separated and the typical image of the orders stacked over each other is formed on the detector.

In order to obtain 1D spectra for each order that can be used for further analysis, each strip corresponding to an order has to be extracted from the 2D image and collapsed. Fig-

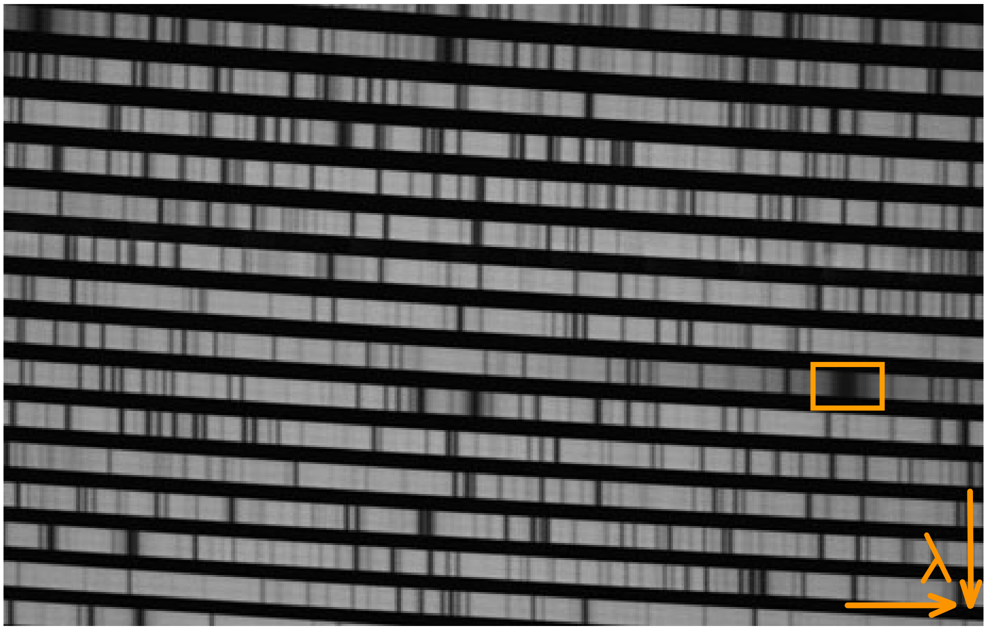

Figure 1.17: The spectrum of the Sun taken with a cross-dispersed echelle spectrograph. Each horizontal band corresponds to a physical order. The stacking of the spectral orders in the vertical direction is caused by the cross-disperser. The orange box (right) highlights the strong H_β absorption line. Graphic taken and adapted from Hatzes (2016a).

ure 1.18 shows an example for the resulting 1D spectrum for one order of a cross-dispersed echelle spectrograph. The continuum exhibits an intensity variation, which corresponds to the blaze function due to the width of the individual grating facets. The spectrum in Fig. 1.18 is rich in narrow absorption lines, making it very suitable for high precision RV determination.

Wavelength calibration methods

The most critical step when measuring a RV from a spectrum is the wavelength calibration. Since the wavelength shift of the observed stellar spectrum is the desired observable, a separate wavelength reference has to be used in order to make the mapping of each detector pixel to a specific wavelength. Different methods exist, which all share the same basic principle: using a source with sharp emission or absorption features that have precisely known wavelengths. Due to the overall importance of the wavelength calibration, the most frequently used methods are presented here.

When the wavelength calibration is made with a spectrograph, possible sources of instrumental errors have to be taken into consideration and how to best mitigate them. Any negligence at this point severely impacts the values and errors of the RV measurements, in the worst case resulting in the detection of a false signal.

The ideal wavelength calibration is achieved when the light from the calibration source follows the exact same path as the stellar light does, at the exact same time. Under this

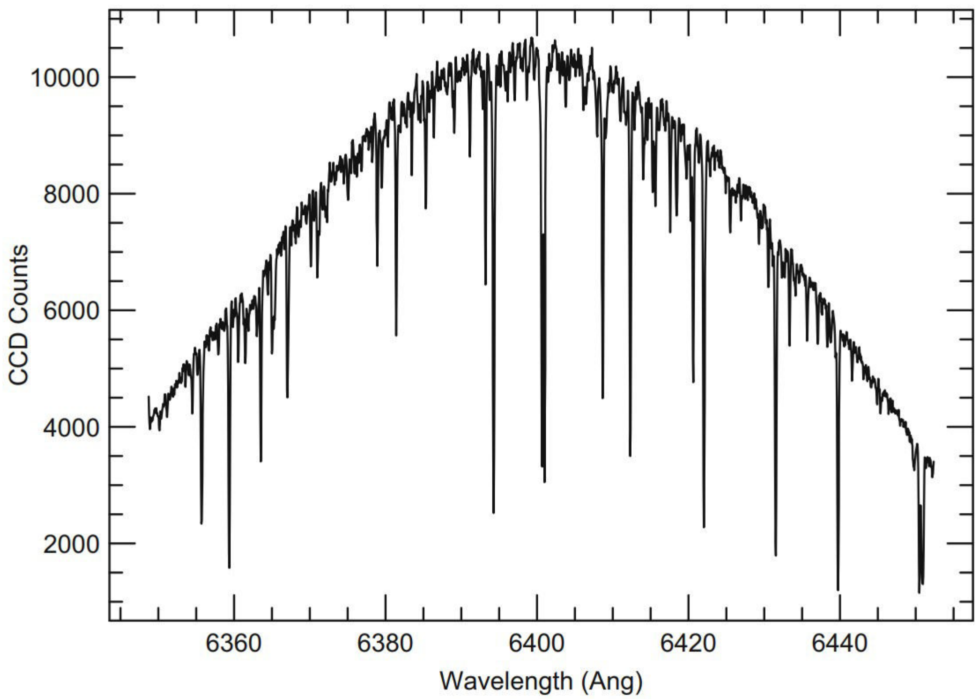

Figure 1.18: A 1D spectrum extracted from a typical stellar spectrum taken with a cross-dispersed echelle spectrograph. A number of narrow (metallic) absorption lines is present in this spectrum. The overall intensity distribution of the continuum is due to the blaze function. Graphic taken from Hatzes (2016a).

condition, all instrumental wavelength shifts are imprinted on the calibration source in the same way as on the stellar spectrum and therefore can be perfectly calibrated out. Atmospheric absorption or emission lines[5] can provide such a reference. Since they are imprinted on the spectrum before the telescope is reached, a good calibration of effects along the optical path can be ensured. These so-called telluric lines bring along a great advantage: no technical or financial effort has to be made in order to use them. However, there are also several drawbacks: on the one hand, only very specific wavelength regions are covered by the telluric lines and an interpolation has to be made for regions without tellurics. On the other hand, the observed spectrum is a superposition of the stellar and telluric lines, which means that in regions with a high density of tellurics, the stellar spectrum might not be usable for scientific analyses.

Figure 1.19 shows a typical spectrum of telluric absorption lines from an observation of 59 Cygni. This B-type star with $T_{eff} \approx 25\,000\,\mathrm{K}$ (Chauville et al. 2001) is a fast rotator with $V_{rot} \approx 325\,\mathrm{km/s}$ (Abt et al. 2002) and therefore has a spectrum very close to a black body without prominent features. This allows to take a nearly isolated spectrum of the telluric lines.

[5]Further on in this work, atmospheric emission lines are neglected, as they are intrinsically faint and no emission lines were detected in spectra obtained with MaHPS.

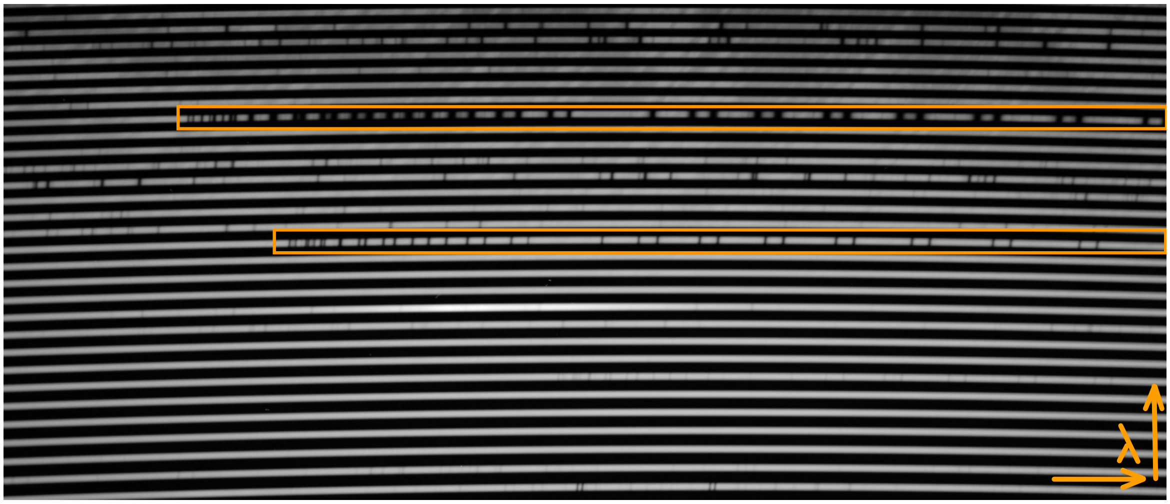

Figure 1.19: Telluric absorption lines in the emission spectrum of 59 Cyg. The stellar spectrum is basically free from lines due to the fast rotation and high T_{eff} of 59 Cyg. The strong and regular absorption lines in the upper third and the center (orange boxes) are the O_2 A and B bands, respectively. The bright region in the center is a stellar H_α emission feature. Spectrum recorded with MaHPS as part of this work.

In the visible wavelength band, as shown in Fig. 1.19, the telluric lines originate from the vibrational and rotational states of O_2 and H_2O molecules in the atmosphere (Caccin et al. 1985). While the O_2 lines form regular patterns in two bands (upper third and center) with mostly saturated lines, the H_2O absorption lines are distributed over a wider wavelength range and have a more irregular spacing, as well as very different line strengths. The bright feature in the center of Fig. 1.19 is caused by H_α emission processes in the star and is not related to the telluric spectrum.

Especially the H_2O lines suffer from strong variations in intensity and line position due to weather conditions and atmospheric processes, which limits the precision of wavelength calibrations to a few 100 m/s (Campbell and Walker 1979). For precision RV work on the 1 m/s level this is not enough, but especially in some IR bands, where there is a lack of alternative calibration sources, tellurics are frequently used.

Artificial calibration sources have to be used in order to reach better calibration precisions. A derivative of the telluric line method is the absorption cell method: a glass cell is filled with a gas and then inserted into the light path of the telescope. When the stellar light passes through the gas, the absorption lines of the gas are superimposed on the observed spectrum, analogously to the tellurics. In the gas cell, the possible variation of line intensity and position can be controlled by using a fixed temperature and pressure. Furthermore, it is possible to choose an appropriate gas that is suited best for the wavelength range and resolution of the particular spectrograph in question.

The first gas employed in an absorption cell was hydrogen fluoride (HF), that enabled to reach precisions on the ∼15 m/s scale for the first time (Campbell and Walker 1979). Nowadays, cells filled with molecular iodine (I_2) are more popular, on the one hand because

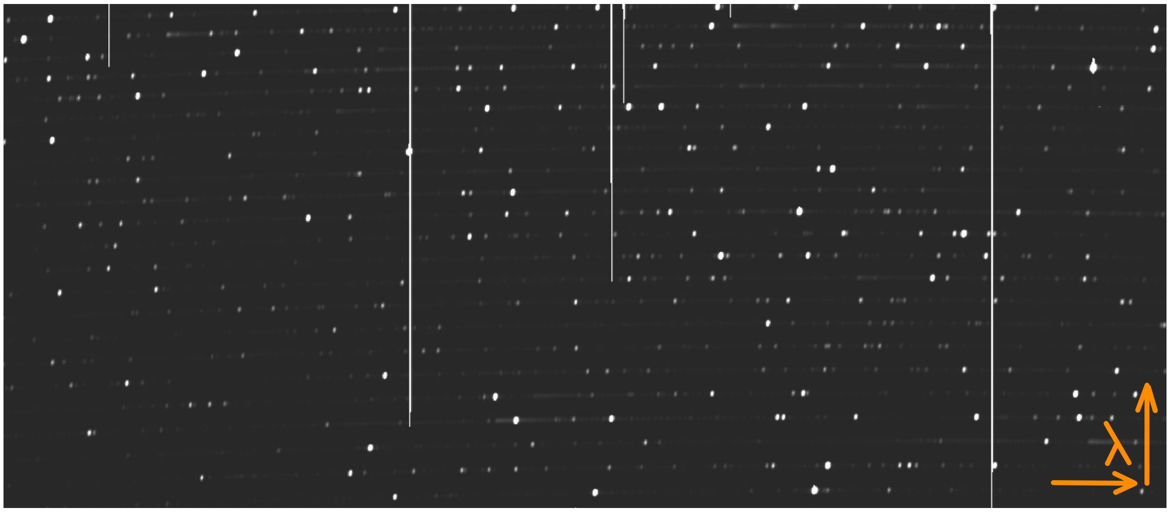

Figure 1.20: The emission line spectrum of a ThAr lamp that is used for wavelength calibration. The intensity and spacing of the lines is irregular. The white vertical columns are caused by heavily saturated emission lines that are not in this picture. Spectrum recorded with MaHPS as part of this work.

of the strong toxicity of HF, on the other due to the larger number of absorption lines available from I_2. The precision limit of iodine cell calibration is ~3 to 5 m/s (Butler et al. 1996; Cochran and Hatzes 1993), allowing to detect a large range of exoplanets. The big drawback of the gas cell method is the computationally intense disentangling of the absorption spectra of the star and the gas. However, the manufacturing of the gas cells and their maintenance is comparably cheap and straightforward.

A different calibration option are emission line lamps such as hollow cathode lamps (HCLs). The atoms of the buffer gas and the cathode material form characteristic emission lines when a high voltage is applied. Since such emission lines are typically very sharp and their position can be measured accurately, e.g. with a Fourier transform spectrometer, they make a good wavelength reference. For spectroscopy in the visible and near-IR ranges, often HCLs made from $Th + Ar$ or $U + Ne$ (cathode material + buffer gas) are chosen.

A spectrum of a *ThAr* lamp is shown in Fig. 1.20. A large number of lines with different intensities is spread irregularly over many echelle orders. The white vertical stripes are caused by charge spill-over from extremely bright lines that saturate on the CCD detector and lie outside of the shown image. This illustrates how large the difference in line intensity between the individual lines can be.

The RV precision that can be achieved with HCLs is limited by each lamp's properties to a level of ~1 to 10 m/s (Lovis and Pepe 2007). A big issue are the aging effects that HCLs undergo because of the sputtering of the cathode material. This can result in changes of the intensities of individual lines on the timescale of several years, where in the extreme case some lines may vanish and others can appear. Another critical factor is the purity of the elements used to manufacture HCLs. Each contamination has a direct effect on the

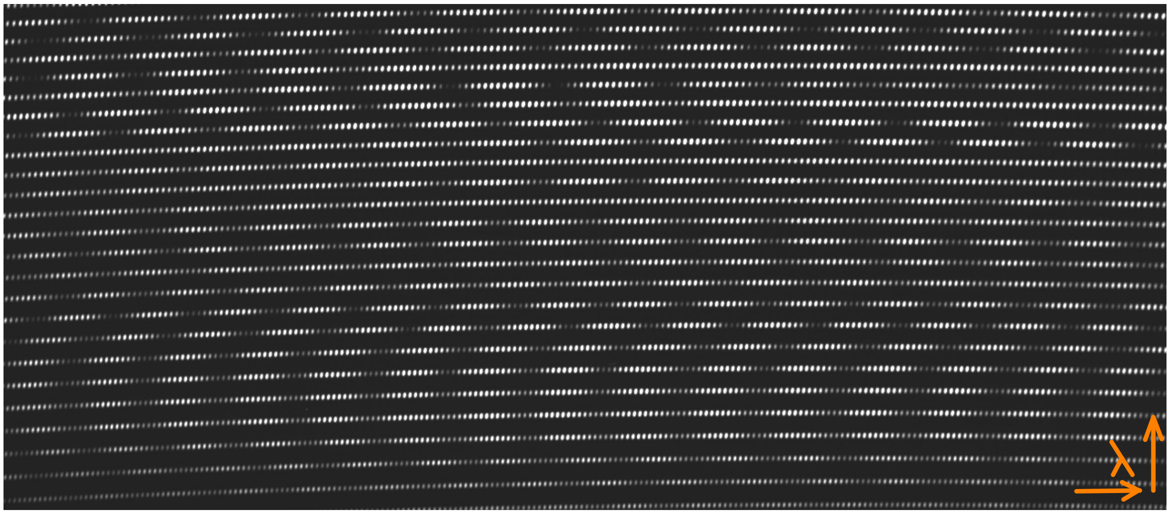

Figure 1.21: The emission line spectrum of a laser frequency comb that is used for wavelength calibration. The intensity and spacing of the lines is very regular. The wave-like intensity variations are due to an envelope function produced by the LFC itself. Spectrum recorded with MaHPS as part of this work.

spectrum and therefore it is basically impossible to get two lamps with exactly the same spectrum, even from the same production batch. This has the consequence that, whenever a new HCL is employed, a manual identification of all lines has to be made to ensure the correct line detection of the calibration algorithm. Nevertheless, HCLs are still comparably cheap, easy to handle and very reliable, which makes them attractive.

The third class of calibration sources are equidistant line emitters like Fabry-Perot etalons (FPEs) and laser frequency combs (LFCs). In contrast to the other methods, FPEs and LFCs provide a large number of lines with regular spacing and similar intensity, as shown in Fig. 1.21 for a LFC. The overlaying wave-like structure originates from a spectral envelope function which is intrinsic to the LFC, but may vary with time.

The heart of FPEs are so-called cavities, typically made from two reflective plates that are placed at a small defined distance to each other. When light is coupled in, it gets reflected numerous times with a small amount escaping on the other side each time. In this way, an optical path length difference is created, resulting in constructive and destructive interference. Depending on the effective width of the cavity d_{cav}, each interference order m is associated with a specific wavelength λ_m by the constructive interference condition $m\lambda_m = 2d_{cav}$ (Bauer et al. 2015). The result is a spectrum of almost equally bright peaks at defined wavelengths.

Although FPEs give the user control over the distance and intensity of the lines, the determination of the absolute wavelength of each peak is afflicted with a rather large error bar (Bauer et al. 2015). Another drawback is the technical effort needed to operate a FPE, because a precise positioning mechanism and thermal stabilization of the cavity is required. Still, if these hurdles are overcome, FPEs are reliable and their spectral coverage can be tailored to the spectrograph. The typical calibration precision of FPEs is on the order of 8 m/s or smaller (Ge 2008), already enabling exoplanet detections.

Laser frequency combs (LFCs, also called astro-frequency combs or AFCs) use a pulsed femtosecond laser as basis, which in the frequency domain corresponds to peaks (ideally delta functions) at a periodic interval, called the repetition frequency f_{rep}. In general, the envelope function of the pulses does not have the same phase as the pulse carrier function, resulting in a small frequency offset f_0 of the frequency peaks relative to $f = 0\,\mathrm{Hz}$ (Wilken et al. 2012). By locking the laser to an atomic clock, the exact values of f_{rep} and f_0 can be controlled at an extremely high precision level, resulting in the knowledge of the frequency (or wavelength) of each individual peak.

Because the Fourier transformed repetition frequency of the LFC's source laser originally lies in the radio frequency range and the atomic clock operates in a similar frequency band, a conversion to frequencies that correspond to optical or near-IR wavelengths has to be made. This concerns on the one hand f_{rep}, which by default is far too small to be resolved by a typical echelle spectrograph. The problem is countered by using FPEs as filters, leaving only a small number of peaks with larger overall separation. On the other hand, the range of the emission needs to be extended, which is usually done by utilizing a photonic crystal fiber (PCF), that exploits highly non-linear effects (Wilken et al. 2012). In this way, a spectrum of regular peaks with precisely known wavelength positions is generated (Fig. 1.21).

The intrinsic line position precision of LFCs is on the 1 cm/s scale (Milaković et al. 2020), easily enabling wavelength calibrations on the level of $\sim$0.1 m/s (Wilken et al. 2012) and thus providing a suitable method for the detection of small exoplanets. Unfortunately, the cost and effort required to manufacture a LFC are enormous and there is no wavelength coverage for the blue part of the optical spectrum so far. Additionally, today's LFCs do not reach operation reliabilities that are comparable to HCLs or FPEs, raising the need for regular maintenance by specialized personnel. Nevertheless, LFCs are an important calibration technique for the future of exoplanet science thanks to their unmatched intrinsic precision.

In contrast to the gas absorption methods, the spectrum of the emission sources cannot be directly combined with the stellar spectrum. The two possibilities that can be used are either sequential or simultaneous calibration.

The concept of sequential calibration is simple: before or after an observation is made, a calibration spectrum is taken. The wavelength solution of the calibration exposure is then applied to the stellar spectra. The necessary assumption for this is that any instrumental drifts are smaller than the uncertainty of the wavelength calibration itself. In the few m/s precision regime, that assumption usually doesn't hold, so refinements have to be made. Bracketing calibration exposures before *and* after an observation and interpolating the wavelength solution for the time in between brings an improvement. The best precision for sequential calibration is obtained by alternating between a calibration and a science exposure, however at the cost of valuable observation time.

Simultaneous calibration allows to use the full observation time on the stellar target. The light from the calibration source is fed into the spectrograph on a path that is slightly

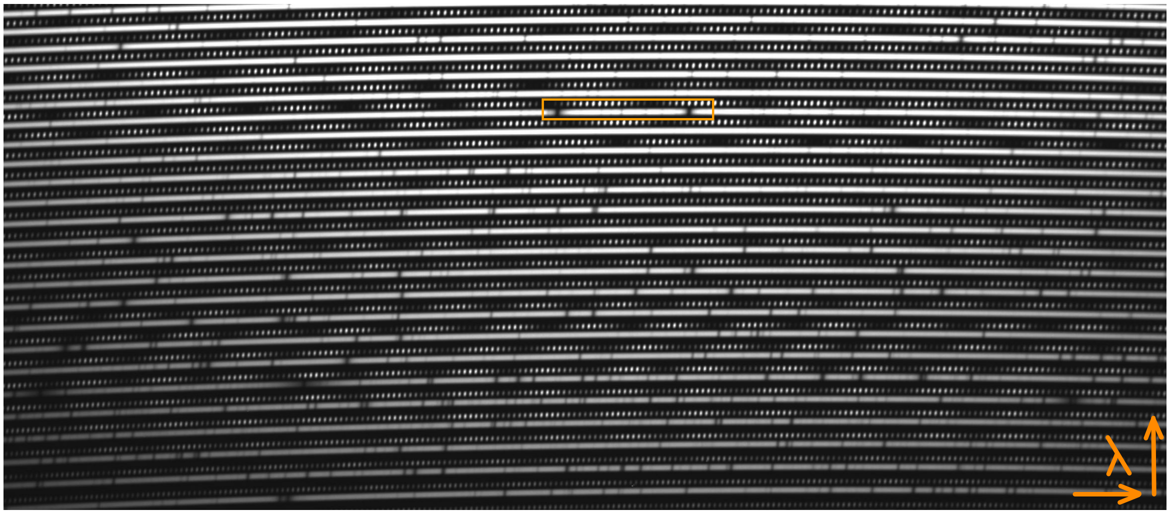

Figure 1.22: The simultaneous recording of a stellar spectrum and a LFC spectrum for a simultaneous wavelength calibration. The orange box highlights the NaD doublet. Spectrum recorded with MaHPS as part of this work.

offset from the stellar light path, so that two separate spectra are formed on the detector (Fig. 1.22). For fiber-fed spectrographs, this is achieved by putting a second fiber for the calibration light right next to the fiber with the stellar light at the spectrograph entrance. In this way, the calibration light does not exactly follow the same path as the science light, but both can be recorded simultaneously. A cross-reference when both light paths are illuminated with the same calibration source can prove that there are no differential shifts at a significant level due to the optical path offset. State-of-the-art results that can be reached with simultaneous calibration with a LFC or FPE are just below the 1 m/s level, as e.g. shown by Udry et al. (2019), with the first instruments already pushing towards the 0.1 m/s regime (Pepe et al. 2021).

Chapter 2

The Manfred Hirt Planet Spectrograph (MaHPS)

The University Observatory Munich (USM) operates a 2.1 m Fraunhofer telescope at the Wendelstein Observatory (WST), situated at 1838 m above sea level in the Bavarian Alps. The telescope is equipped with three different instruments:

- Wendelstein Wide-Field Imager (WWFI): a wide field-of-view imaging camera for visible bands (Kosyra et al. 2014),
- Three Channel Imager (3KK): an imager for simultaneous exposures in three different filters, with one near-infrared and two visible channels (Lang-Bardl et al. 2016),
- Manfred Hirt Planet Spectrograph (MaHPS): a LFC-calibrated high-resolution spectrograph for the optical band.

While the WWFI and 3KK are mounted directly to the telescope, the Manfred Hirt Planet Spectrograph (MaHPS) is located in the basement of the observatory and connected to the telescope by optical multi-mode fibers. This has several advantages: protection from stray light, decoupling of mechanical influences from the telescope and the dome, and protection from the radiation of a nearby broadcast antenna.

2.1 Scientific goals

The main science case of MaHPS is the detection and characterization of exoplanets with RV measurements on the few m/s precision level.

A special focus lies on follow-up observations of planetary candidates from the TESS satellite mission, which carries out a photometrical all-sky survey for transit signals of exoplanets. One contribution MaHPS can make to the TESS planetary candidates is the determination of the planet mass M_P through the RV curve. In the case of so-called single transiting planets, where only one transit was registered so far during the TESS survey, it is possible to estimate the period of the planet from the observed transit data, while RV observations provide a way of confirming the actual value. Furthermore, with the transit method the signal of a binary star in some cases cannot be distinguished from a planet signal, whereas spectroscopic follow-up observations allow to identify the nature of the companion.

For already confirmed planets, observations for further characterization can be made. One such application is the Rossiter-McLaughlin (RM) effect, which allows to obtain information about the orientation of the inclination angle of the planet's orbit i relative to the inclination of the star i_S. RV observations of the RM effect were part of this work, a detailed treatment of which is given in Chap. 6, whereas Chap. 5 features an explanation of the effect itself.

Aside from exoplanet observations, other science projects are carried out with MaHPS. These include the refinement of stellar parameters, e.g. measurements of the surface gravity $\log(g)$ for nearby stars within 10 pc distance, and the investigation of processes in hot stars, e.g. atmospheric winds.

The following sections provide a detailed description of MaHPS and its auxiliary systems, which are necessary for achieving the goals stated here.

2.2 Instrument description

The instrument description of MaHPS was already published in parts in Fahrenschon et al. (2020). Therefore, the graphics presented here are carried over from the publication. However, Fahrenschon et al. (2020) only provide a compact overview of the instrument hardware, while this work gives a much more detailed description and documentation. Additionally, since the date of the publication, changes to the instrument have been made, which are also presented here.

MaHPS is made up of two large subsystems: on the one hand the Fiber Optical Cassegrain Echelle Spectrograph (FOCES) and on the other hand a laser frequency comb (LFC) that is used for calibration. Despite the clear distinction of MaHPS and FOCES, for historical reasons the name FOCES can be found in some places of this work where instead MaHPS would be the technically correct denotation.

The LFC in use for MaHPS was manufactured by Menlo Systems. It covers a wavelength range of roughly 500 to 680 nm and produces spectral lines with a separation of $f_{rep} = 25\,\text{GHz}$. For further information regarding the LFC, the reader is referred to Kellermann (2021), since this work will focus on FOCES and the subsystems dedicated to its regular operation and environmental stabilization.

Table 2.1 contains the most important characteristics of the fiber-fed spectrograph FOCES, which operates in the optical range. FOCES was designed and manufactured in the 1990s at the USM in collaboration with several other institutes (Pfeiffer et al. 1992) and operated at the 2.2 m telescope of the Calar Alto Observatory in Spain from 1995 to 2009 (Grupp et al. 2010).

[6] The conversion of pixel interval to wavelength or RV interval was done using the central wavelength of the H_α absorption line (656.28 nm) as reference.

	FOCES
resolving power	$\sim 65\,000$
spectrograph design	white pupil (quasi-Littrow)
grating constant	$31.6\,\frac{1}{\mathrm{mm}}$
grating blaze angle	63.5°
wavelength calibration	*ThAr* lamp (sequential)
	LFC (sequential and simultaneous)
FOCES spectral range	389 to 885 nm
LFC spectral range	500 to 680 nm
pixel size	13.5 µm
RV interval[6] per pixel	∼2.1 km/s

Table 2.1: The basic specifications of FOCES.

After the transport back to the USM labs, a period of stability tests and optics upgrades followed. In order for FOCES to remain competitive in the rapidly progressing field of high-resolution spectroscopy and enable the science projects described in Sec. 2.1, the 1 m/s regime was defined as new instrumental precision goal. Simulations of the effect of temperature and pressure changes on the spectrograph's stability were carried out in this context, with the goal of formulating new requirements for the environmental stabilization (Grupp et al. 2009). Since the simulations can only approximate the real instrument's behavior, the working requirements (Tab. 2.2) were conservatively chosen to be about an order of magnitude stricter than the simulation results to compensate for any modelling imperfections.

RV accuracy (object+calibration simultaneous)	$\leq$1 m/s
Spectrograph stability	$<$0.001 pixel (avg.)
Temperature stability	$<$0.01 K
Pressure stability	$<$0.1 hPa

Table 2.2: Requirements for the environmental stability of MaHPS.

The process of upgrading and testing the optical, mechanical and electronic components of FOCES in the lab to match the stability requirements is described in detail by (Grupp et al. 2010, 2011; Brucalassi et al. 2012, 2013, 2016). After that phase, in 2016 FOCES was finally transferred to its current site of operation at the Wendelstein Observatory.

2.2.1 Spectrograph optics

The optical layout of FOCES is shown in Fig. 2.1. A so-called white pupil design is used, for which the light first is dispersed by the echelle grating (top left) in quasi-Littrow configuration (see Sec. 1.2.5) and after that refocused to an overlapping image of all orders

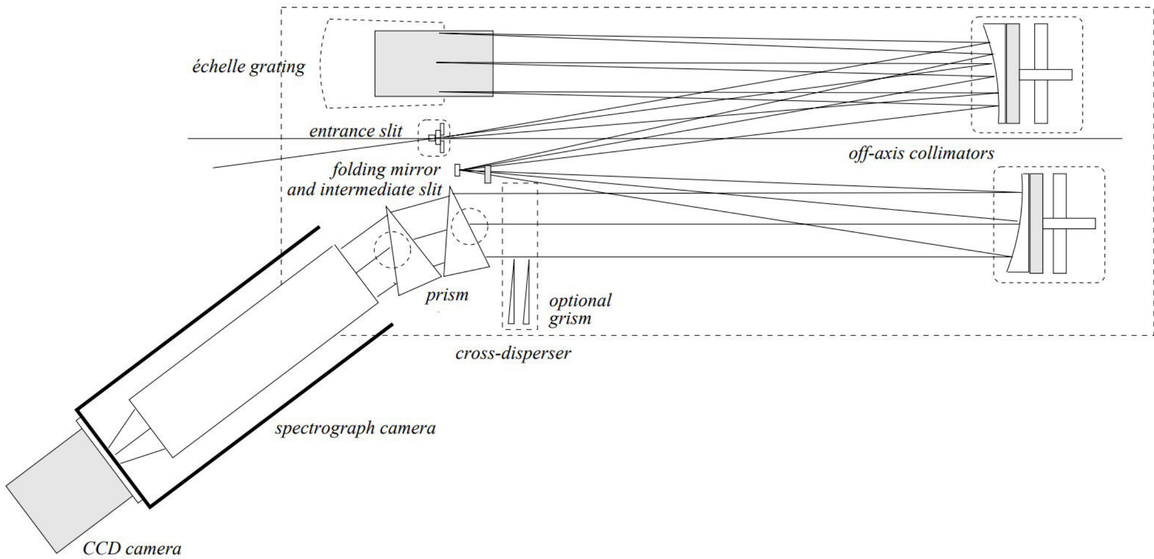

Figure 2.1: The optical layout of the FOCES spectrograph. Graphic taken from Pfeiffer et al. (1998).

(the "white light" image) at the intermediate slit (center left). The beam is collimated and refocused by two off-axis collimators (right). Next to the folding mirror (center left), an intermediate slit is placed in order to block any existing stray light. Two prisms act as cross-dispersers, which couple the light into the camera optics where the beam is focused onto the CCD detector (bottom left).

The original design also featured an optional grism (Fig. 2.1, left), which could be inserted into the optical path at request. The consequence was an approximately doubled cross-dispersion (Pfeiffer et al. 1998), leading to a larger distance between the single echelle orders on the detector at a smaller overall wavelength coverage. This allowed to use a second fiber for obtaining a simultaneous reference spectrum of the sky (Pfeiffer et al. 1998). The grism was removed during the optical upgrade process of FOCES because the entrance aperture was completely redesigned to provide simultaneous spectra from two fibers at full spectral coverage by using only the two cross-dispersing prisms.

The entrance aperture, a four-fiber-slit, connects the spectrograph to the telescope and the calibration light sources (see also Sec. 2.2.2). The installation of the four-fiber-slit was part of the upgrade of FOCES prior to scientific operation at the WST. A detailed description of the design, manufacturing and testing of the four-fiber-slit is given by Kellermann et al. (2015, 2016, 2019).

Figure 2.2 schematically shows the setup of FOCES, the calibration unit and the telescope with the optical fibers. For scientific operation of the spectrograph, two multi-mode fibers with 100 µm core diameter are available, one for the light from the telescope (*fiber A*), the other for light from the calibration unit (*fiber B*). An independent fiber can bring calibration light to the telescope, so it can be recorded in FOCES through fiber A. Thus, a cross-calibration of fiber A and B is possible. Two mono-mode fibers are also part of the

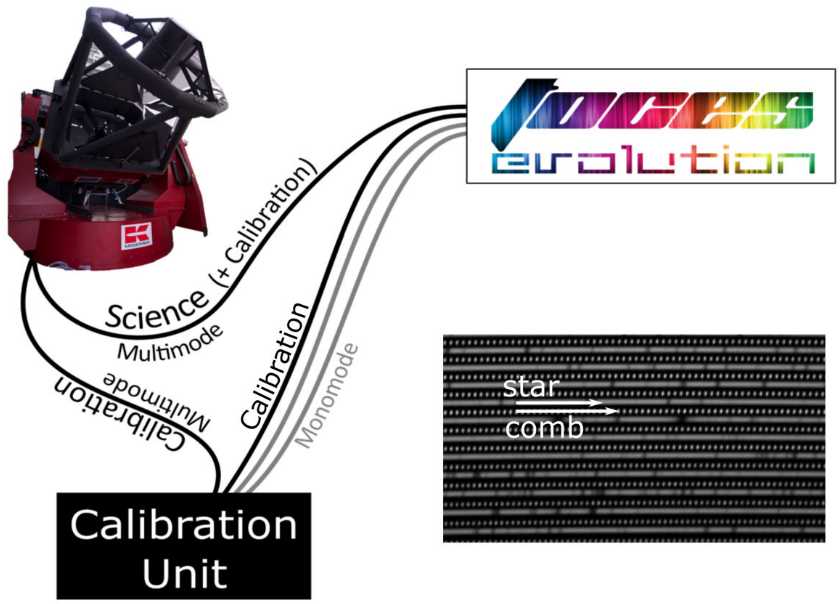

Figure 2.2: The fiber connections of FOCES (top right) with the telescope (top left) and the calibration unit (bottom left). Inset: extract of a simultaneous exposure of light from a star and the LFC. Graphic taken from Kellermann et al. (2020).

four-fiber-slit, however those are only for testing purposes and ordinarily not connected to any light source. A slit mask in front of the fiber ends defines the entrance slit of the spectrograph.

The multi-mode fibers installed in the four-fiber-slit provide a relatively efficient transport of light, but produce a characteristic speckle pattern at the fiber exit. This pattern is highly unstable and changes when the bending or stretching of the fiber changes even slightly, e.g. during operation of the telescope, leading to a possible shift of the centroid of the speckle image and consequently a possible false RV signal. Therefore, mode scrambling is required, which is realized with a fiber shaker that continuously moves the fibers during exposures. In this way, the speckle pattern produced by the fiber constantly changes and gets smoothed out in each exposure.

In Fig. 2.3 (a), the echelle grating of FOCES is shown. The grating is mounted upside down, fixed between two massive arms with the grooved side facing towards the optical bench. Micrometer screws are installed for precise alignment of the grating. On the left of Fig. 2.3 (a), the folding mirror and the shutter can be seen, the latter of which is mounted directly onto the entrance slit unit.

The cross-dispersing prisms can be seen in Fig. 2.3 (b). The prism mounts were originally constructed such that the prisms can be rotated, so different wavelength regions could be imaged on the detector when the enhanced cross-dispersion mode with the optional grism was used. Since the goal of the upgrade phase in the lab was to improve the intrinsic stability of the spectrograph, all adjustable parts had to be either removed or, if not

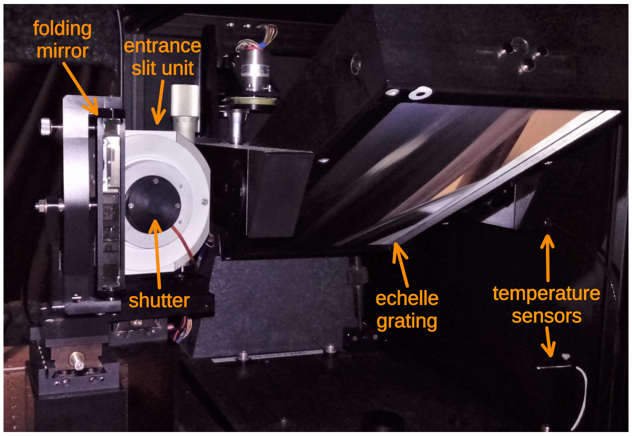

(a) The echelle grating and entrance slit unit.

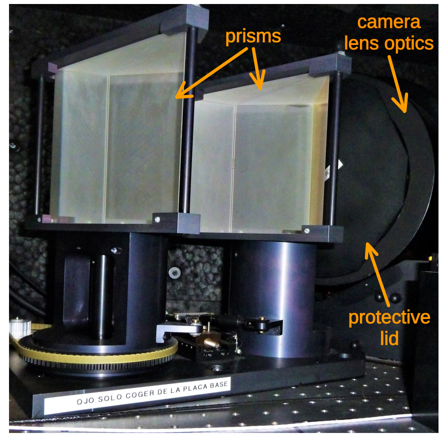

(b) The cross-dispersing prisms and camera optics.

Figure 2.3: The optical elements of FOCES.

possible, disabled. In this context, the motor for the prism rotation was uninstalled and all cables removed, leaving only the remainders seen in Fig. 2.3 (b). On the right behind the two prisms, the entrance of the camera optics tube is depicted, which in this picture is covered by a black lid in order to protect the camera while working on the optics.

As detector, an Andor iKon-L is used with 2048x2048 pixels, which has a square shape and an edge length of 13.5 µm. The camera was also part of the optical upgrade and was chosen due to its ability to cool the CCD chip to $-100\,^{\circ}\mathrm{C}$ by using a five-stage Peltier element that is run through by a liquid coolant at room temperature. The use of a fan or of liquid nitrogen for cooling had to be avoided, because both can cause vibrations of the detector mount, which would influence the precision of the RV measurements. As operating temperature for the camera detector, $-80\,^{\circ}\mathrm{C}$ were chosen, so as to keep a safety margin for the control loop in case adjustments to environmental disturbances are needed. For the highest possible electronic and mechanical stability of the detector, the camera is continuously operated in the cooled state with a coolant temperature of 16 °C. Any deviations from this state are reduced to an absolute minimum, e.g. if maintenance is unavoidable.

2.2.2 Calibration unit

The calibration unit (CU) of FOCES (Fig. 2.4, bottom) is located in the spectrograph room and acts as distribution point for the light from the different calibration sources. As shown in Fig. 2.4, a *ThAr* HCL and a halogen lamp as flat lamp are mounted directly onto the CU, while the light from the LFC is coupled in via a fiber and an integration sphere. A *UNe* lamp is equipped as backup HCL, but not in use.

Figure 2.5 shows the two optical tables of the LFC, which contain the essential optical elements for the production of the comb spectrum. The FPEs that are used for filtering

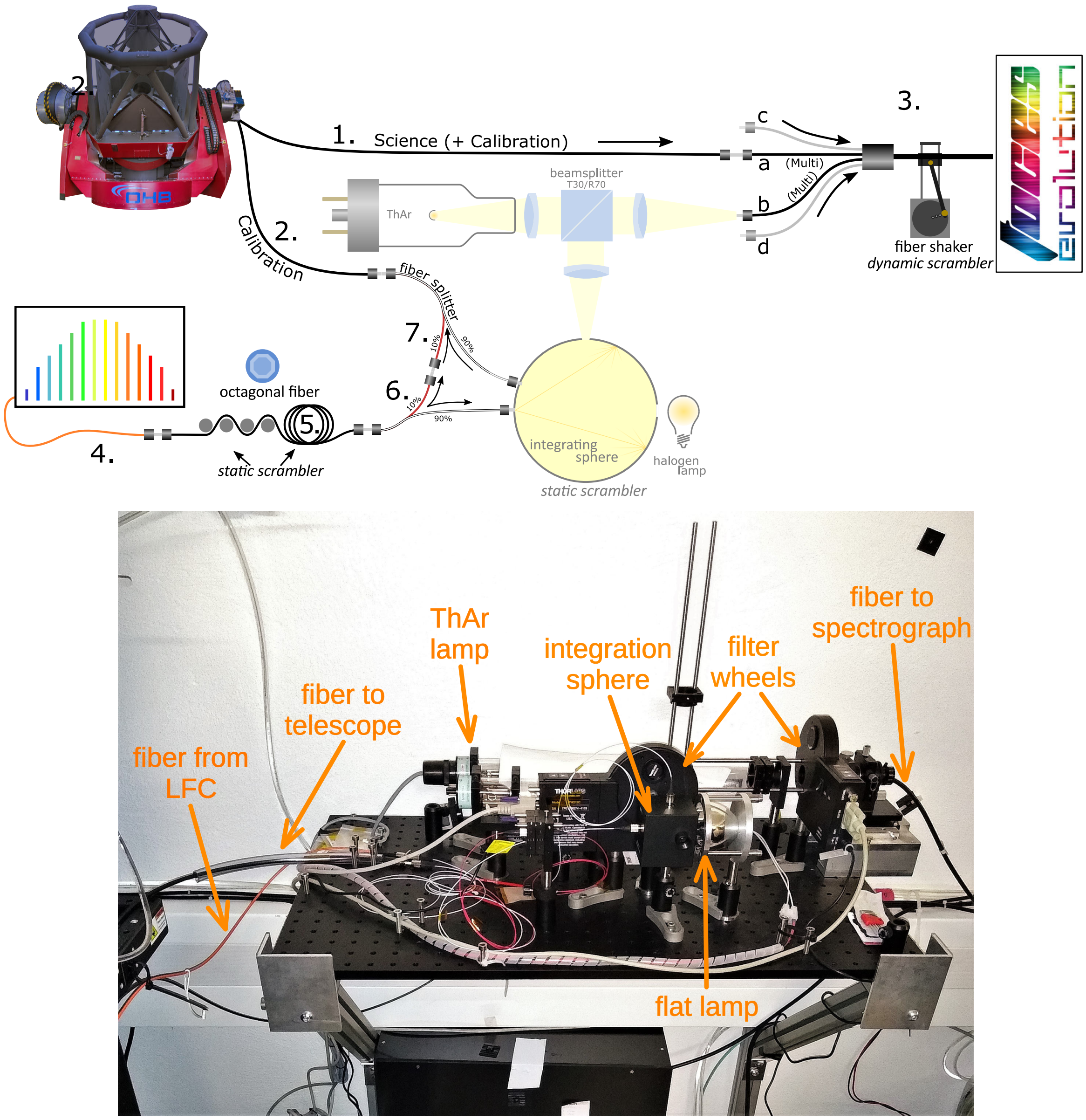

Figure 2.4: Top: The fiber connections of FOCES (top right) with the telescope (top left), the calibration unit (center), and the LFC (bottom left). In the center, the setup of the CU is shown schematically, including the *ThAr* HCL, a beam splitter, an integration sphere and the flat (halogen) lamp. Graphic kindly provided by Hanna Kellermann.
Bottom: Photo of the calibration unit.

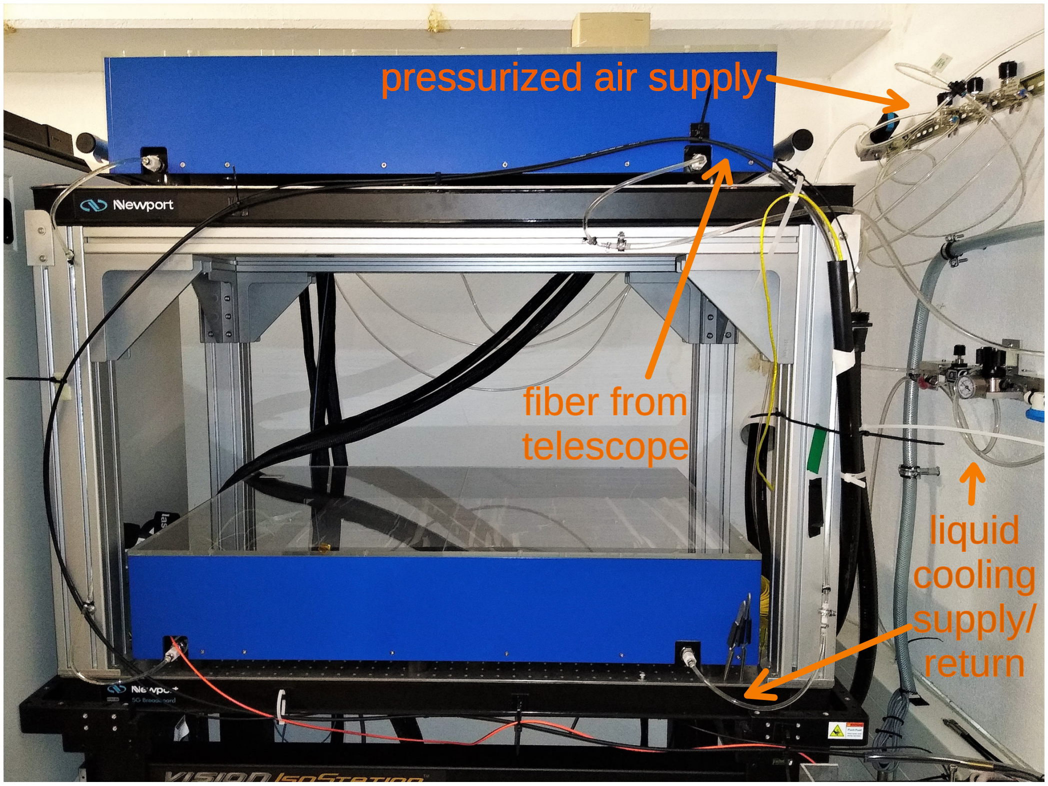

Figure 2.5: The optical tables of the laser frequency comb.

the peaks of the LFC need to be controlled in their length very precisely, on a level where thermal expansion plays a significant role. A flow of liquid coolant through the baseplates of the benches provides improved temperature stability for these parts. Furthermore, the FPEs are constantly flooded with dried and filtered air in order to avoid degradation of the reflective surfaces.

With the setup of fibers as shown in Fig. 2.2 and 2.4 (top), both sequential and simultaneous calibration modes are available. A fixed daily calibration routine before the start of the night ensures that all necessary calibration exposures for the two modes are made. This routine consists of bias exposures, flat exposures and exposures of the wavelength references. Dark exposures, which are also usually required for CCD detectors, are omitted because of the very low dark current of the used CCD chip, which is on the level of 0.5 $e^{-}/(h \cdot pixel)$ (*iKon-L Series - datasheet* 2020) and thus can be safely neglected.

The flat exposures are necessary for tracing the exact position of the individual orders on the detector chip as well as for the correction of pixel-to-pixel sensitivity variations and are made by illuminating either fiber A or fiber B with the flat lamp. Since the overall efficiency of the spectrograph is notably smaller for the blue than for the red wavelengths, three different exposure times are used in order to create a mosaic of regions with optimal signal level.

For wavelength calibration, *ThAr* exposures in fiber B are combined with LFC expo-

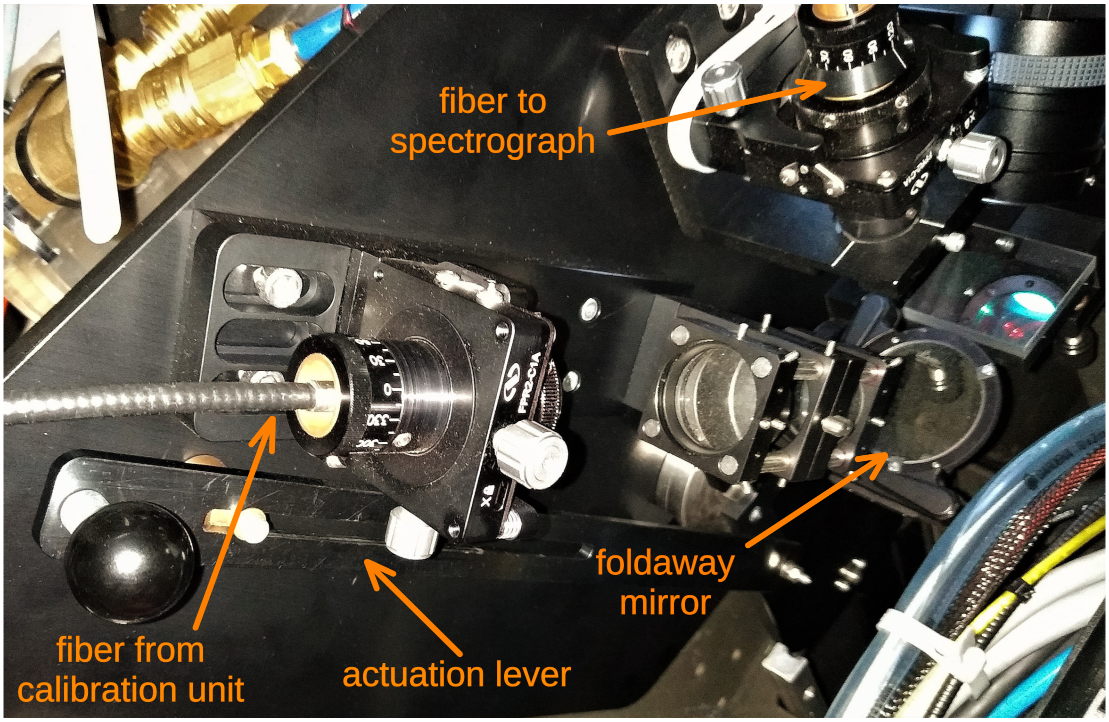

Figure 2.6: The optics in the telescope that are used to couple the calibration light into the science fiber entrance.

sures in fiber A, B, or both simultaneously. The LFC exposures of the single fibers are needed to provide an accurate correction of the background stray light which is characteristic for each fiber, varies slowly, and can systematically influence the LFC line shapes if not corrected. The simultaneous LFC exposure gives the direct cross-calibration of the two fibers in terms of wavelength solution and a direct comparison of the two optical paths.

The overall sequence of the calibration exposures is optimized such that the interaction with the observer on site is kept at the smallest level possible.

Sequential calibration

As stated in Sec. 1.2.5, the calibration light for sequential calibration has to follow the path of the science light in order to avoid systematic errors. A dedicated fiber is connecting the CU to the telescope (*calibration fiber*, Fig. 2.4, 2.) to inject the light from the CU into the FOCES science fiber. The entrance of the calibration fiber at the CU is equipped with a fiber splitter, which in this direction is acting as a combiner. One end is mounted to the integration sphere (Fig. 2.4, center) and the other to a fiber directly from the LFC, so that light from both the flat lamp and the LFC can be coupled into it. The optical path of the *ThAr* lamp is independent from the integration sphere and therefore sequential calibration with the *ThAr* lamp is not available.

Figure 2.6 shows the optics necessary for the sequential calibration, which are mounted in the telescope. The exit of the calibration fiber (left) is re-imaged onto the entrance of the science fiber (top right) by a foldaway mirror (right). Since the foldaway mirror is blocking the light path from the telescope, it has to be retracted during observations. Thus, it is not possible to couple light from a star and a calibration source into the science fiber (fiber A) at the same time.

The foldaway mirror mount sits on a platform that can be rotated by an actuation lever (Fig. 2.6, bottom left). This concept permits to move the mirror while it keeps its alignment relative to the science fiber entrance, as long as the platform returns to the same position. In order to reposition the mirror correctly, v-shaped grooves are cut into the platform side. A spring-loaded ball snaps into the groove at the desired position and locks the mirror and platform in place. In the original design of the foldaway mechanism, a spring-loaded pin was used instead of the ball. However, this configuration suffered from bad repositioning precision, because the pin was able to tilt inside the grooves.

To date, the foldaway mirror actuation lever has to be operated manually, which creates several disadvantages. First, during the regular calibration routine before the start of the night, actions from the observer are required to enable the illumination of fiber A, which is problematic during short winter days, when the calibration time overlaps with the observer's resting time. Furthermore, the reproducibility is still somewhat prone to human factors in the operation of the lever, e.g. depending on the experience level of the user. It has been tested that the position of the mirror after actuation by a single person is sufficiently consistent, but slight offsets between different operators cannot be fully excluded.

Simultaneous calibration

The few m/s precision goal of MaHPS can only be reached with simultaneous calibration. The redesign of the FOCES entrance aperture as four-fiber-slit was the key to provide simultaneous calibration information over the complete wavelength range of the spectrograph. As shown in Fig. 2.4 (top), fiber B directly delivers the light from the CU to the spectrograph, in parallel to the light from the telescope in fiber A. Both fibers are slightly offset in the cross-dispersion direction, resulting in two adjacent spectra on the detector for each physical echelle order (for an example, see Fig. 1.22). In order to obtain reliable calibration results despite the different light paths of fiber A and B, the cross-calibration of both fibers is essential.

When using the simultaneous calibration in scientific observations, some brightness adjustment for the wavelength reference source, the LFC in this case, has to be made due to the magnitude range of the observed objects. The LFC signal, which is much brighter than the star, needs to be dimmed such that the signal level between both light sources is balanced. To this end, the CU is equipped with two filter wheels which contain a selection of neutral density filters with different transmission.

While it is in principle possible to make simultaneous exposures of a star and the *ThAr* lamp, in practice only the simultaneous calibration with the LFC is used. This is due to the saturated lines in the *ThAr* spectrum, which also contaminate the stellar spectrum

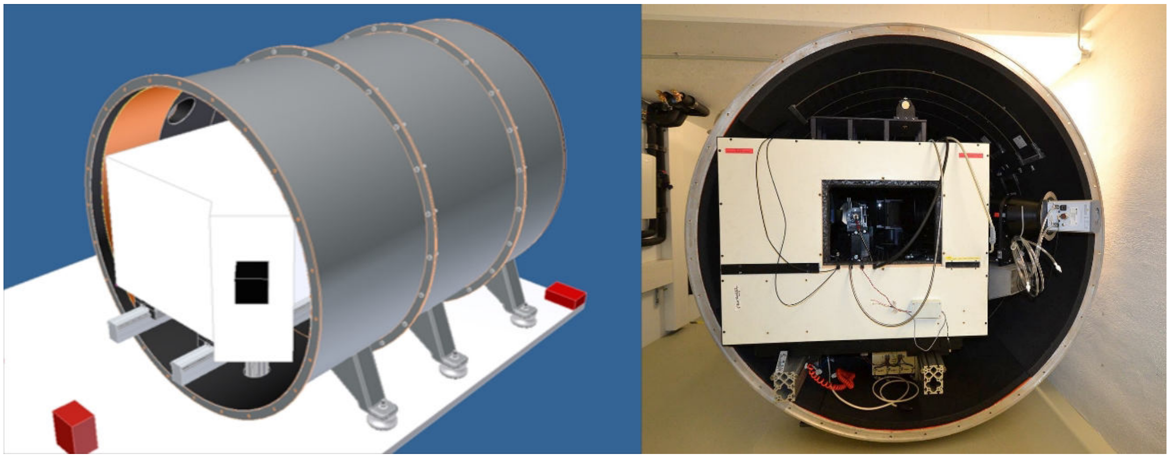

Figure 2.7: The FOCES tank and box for environmental stabilization. The box is mounted on rails so the optical table can be drawn out. Left: the position of the CCD camera (black cube) and a heating mat (orange) is indicated. Right: the service hatch of the wooden box is open (center) and a heating mat is visible on top edge of the tank. Graphic taken from Fahrenschon et al. (2020), photo provided by Hanna Kellermann.

and make the reduction much more time-consuming.

2.2.3 Temperature control system

For high-resolution spectrographs like MaHPS that do not employ a gas cell, a precision of the order of 1 m/s can only be achieved by environmentally stabilizing the spectrograph optics and mechanics. This is on the one hand due to the refractive index of the air, which is a function of the temperature and pressure. On the other hand, thermal expansion causes the mounts and mechanical structures to move and drift. Therefore, some kind of control of this behavior is needed.

To this end, FOCES is surrounded by an enclosure to decouple it from external influences and fitted with control systems for the temperature and pressure. An obvious way to eliminate any influences from the air would be to operate the spectrograph in vacuum. However, for FOCES this is not an option, since it was never designed for vacuum conditions and therefore the optical and mechanical parts are not suited. The alternative approach followed here for providing environmental control is to maintain defined temperature and pressure levels slightly above ambient inside the enclosure, as has been done already for other spectrographs, e.g. PEPSI (Strassmeier et al. 2008).

Figure 2.7 shows FOCES in its enclosures. The optical bench is contained inside a wooden box (white), which in turn is located inside an aluminum tank. The box is mounted on a rail system inside the tank in order to slide out the box and optical bench to allow for easier access. The tank has been designed to just fit the wooden box to keep the volume of air for which temperature and pressure control is needed as small as possible while still having enough volume for the mixing processes to happen efficiently. In total, the tank has a diameter and length of 1.75 m and 3.20 m, respectively. The FOCES tank is placed inside a dedicated spectrograph room, where it takes up about 1/3 of the available space. The room, tank and box are all part of the temperature control concept with three thermally stabilized layers or shells.

The complete temperature control system with all three layers is depicted in Fig. 2.8. The first shell is the spectrograph room, the second is the aluminum tank and the third, innermost layer is the wooden FOCES box.

Inside the spectrograph room, the temperature is controlled by a commercial air conditioning unit (AC; Fig. 2.8, bottom right). The LFC (right) is depicted as one of the significant sources of heat loss from electronics, which cannot be neglected due to the small size of the room. An optional heat load enhancer helps to keep the room temperature in the operating range of the AC.

The FOCES tank and box make up the second and third shell, respectively. Both layers are insulated and the temperature inside is controlled with heating mats by a PID controller (Fig. 2.8, gray). A second identical controller (light gray) is not connected to the heating mats but fitted with a set of additional sensors to provide a temperature readout independent of the control unit.

Furthermore, two low-resolution thermometers with a direct Ethernet connection for fast readout are installed (Fig. 2.8, dark gray). Their sensors are placed inside the FOCES tank and on the ceiling of the FOCES room.

Shell structure

In order for FOCES to reach the temperature stability level of <0.01 K as stated in Tab. 2.2, the optical elements are contained inside a three-layer shell structure. In each shell, the temperature stability is aimed to be about an order of magnitude better than in the surrounding shell. To this end, the FOCES tank and box are both fitted with layers of insulation material as well as heating elements.

The structure of the insulation and heating material is shown schematically in Fig. 2.9 for the tank and the box. The tank insulation (left) is composed of a layer of 30 mm black Armaflex® foam, on top of which 14 heating mats are distributed. The heating mats are glued to the Armaflex® surface and additionally attached with drywall dowels. The insulation of the box (right) consists of 30 mm insulation foam with a 1 mm sheet of aluminum on top to reduce the radiation of heat from inside the box into the tank. In total 11 heating mats are glued onto the aluminum sheets, topped by a 1.5 mm layer of neoprene to avoid direct irradiation of the optical elements and facilitate an even distribution of the temperature.

Heat shield

Inside the FOCES box, there are some places with only a small distance (<10 cm) between the heating mats and the optical elements or mounts. Despite the layer of neoprene on top of the heating mats, this proved to be a problem especially for the grating mount. The

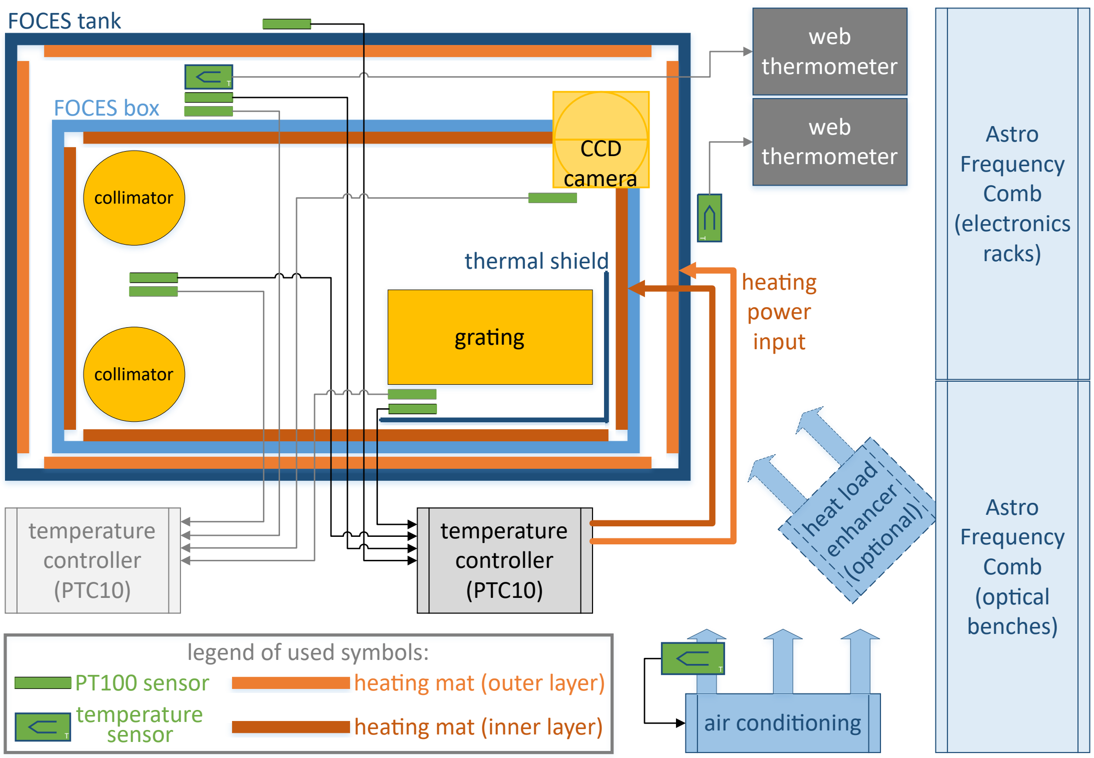

Figure 2.8: The FOCES temperature control system with all three shells.
First shell: FOCES room (total), with air conditioning (blue, bottom), heat load enhancer (blue, dashed) and LFC (light blue), representing the heat load from all electronics; second and third shell: FOCES tank (dark blue) and box (light blue), with heating mats (light and dark orange), PTC10 temperature controllers (gray) and PT100 temperature sensors (green).
Some optical elements are shown for orientation (yellow). Independent fast-readout low-resolution temperature sensors are installed in the room and the tank (green/dark gray). Graphic taken from Fahrenschon et al. (2020).

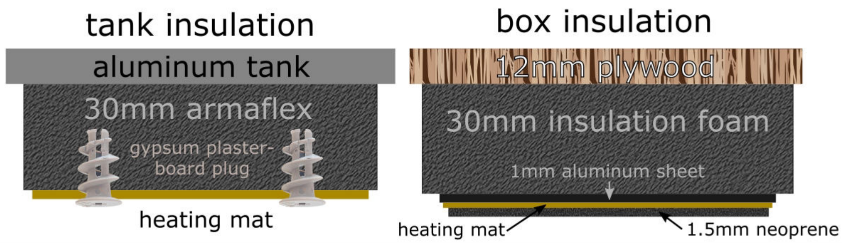

Figure 2.9: The individual insulation layers of the FOCES tank (left) and box (right). Graphic taken from Fahrenschon et al. (2020).

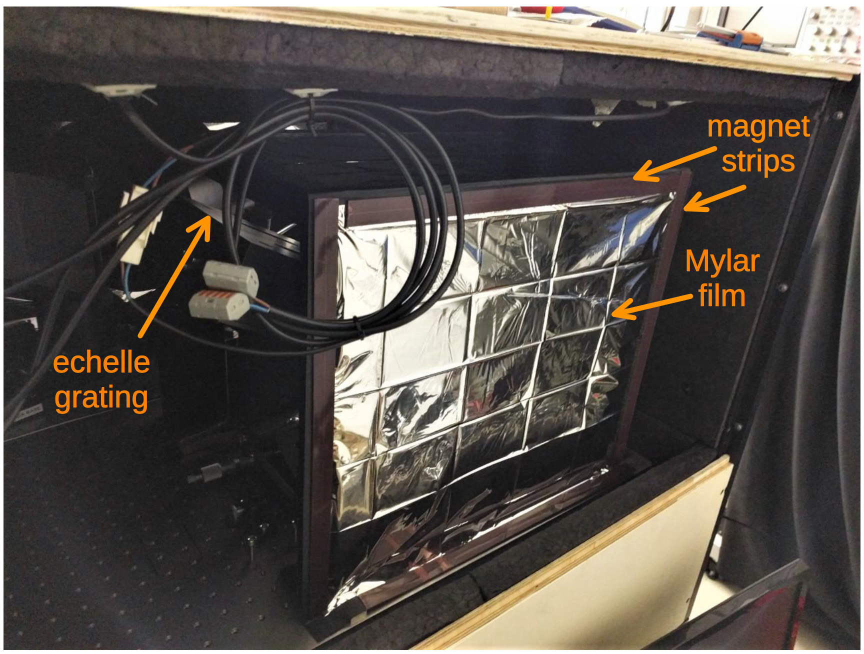

Figure 2.10: Heat shield installed at the grating.

whole structure is prone for direct coupling to the behavior of the heating mats because of the micrometer screws for the adjustment of the grating angle and position, which extend from the mount structure and immediately pick up the heat radiation. Since the grating is an essential part which defines the position of the spectral lines on the detector, it has to be made sure that the thermal expansion influence is as small as possible.

To decrease the influence of direct heating, the grating and its mount are surrounded by a heat shield on the three sides where heating mats are located (Fig. 2.10). The remaining sides were left open to not obstruct the heat transport through the air. The heat shield consists of a frame of aluminum profiles covered by an aluminum foil with a black matte coating. The foil is topped by several layers of reflective Mylar film (polyethylene terephthalate sheet with thin reflective aluminum coating) with air trapped between the individual sheets for a better insulation effect. Magnets keep the insulation foils in place while providing the possibility to quickly disassemble and remount the foils for maintenance.

Figure 2.11: The two PTC10 temperature controllers. Top: unit controlling the power input of the heating mats, indicated by the activated red LED at the bottom right corner of the operation panel; bottom: unit for independent sensor readout.

Since the heat shield does not offer a perfect protection from the heating mats' irradiation, the remaining systematic effects need to be calibrated out by simultaneous calibration. As the light paths from both fibers are subject to the potential grating movements at the same time, this is a valid assumption to make. Additionally, in Chap. 3 verification measurements of the cross-calibration of both fibers are presented.

Temperature controllers

The temperature control concept inside the FOCES tank and the box consists of only three basic components, as shown in Fig. 2.8: a temperature controller (gray) powers the heating mats (orange) and PT100 sensors (green) at selected positions deliver temperature measurements as feedback for the control loop. It has to be noted that no cooling device is installed, instead the temperature adjustment to lower temperatures is realized passively by heat loss to the surroundings. Furthermore, it is assumed that the heat generated by the heating mats is proportional to the amount of power supplied to them.

As temperature controller, a *PTC10* controller (*Stanford Research Systems*, Fig. 2.11) is used. A second, identical *PTC10* controller unit is installed for two main reasons: First to be quickly available as backup unit, and second to provide temperature sensor readings independent of the temperature control loop.

The installation of the two controllers is realized in a way that only one unit is connected to the heating mats and actively controlling the temperature, while the second unit is only monitoring its sensors. A few steps are enough to exchange the heating mats and sensors of one unit with the sensors of the other. In this way, long down-times of the instrument in case of damage to one of the units are prevented. It is even possible to completely remove one unit for repairs without impeding the instrument operation.

The *PTC10* provides a temperature stability of up to 0.002 K (*PTC10 - Programmable Temperature Controller - manual* 2019) for the chosen configuration, which utilizes a closed control loop with a PID (proportional, integral and derivative) algorithm. The principle of a PID control loop is the following: If one has a defined *setpoint* (SP), which is the desired value for the temperature T_{SP} (or more generally the process variable), and a measurement of the true value of the temperature $T(t_m)$ at a given time t_m, the required input for the control loop, so that the temperature reaches T_{SP} in the next time step t_{m+1}, can be calculated. This calculation consists of three contributions: the proportional, the integral and the derivative part.

The proportional part is obtained by calculating the difference between the SP temperature T_{SP} and the measured value $T(t_m)$, which gives the error $E(t_m)$:

$$E(t_m) = T_{SP} - T(t_m). \tag{2.1}$$

Then, the required amount of power to the heating mats P_P is given by multiplying the error with the *proportionality factor* C_P, which is a constant:

$$P_P = C_P \cdot E(t_m). \tag{2.2}$$

It becomes evident that the input P_P goes to zero as the measured temperature approaches the SP. However, since T_{SP} is above the ambient temperature, a certain amount of power is needed to maintain the elevated temperature. This information is provided by the integral part, which takes into account the power that was needed in the previous time step t_{m-1}.

Instead of computing a real integral, an approximation is made to obtain the integral input power P_I. This approximation takes the following form:

$$P_I = C_I \cdot E(t_m) + P_I(t_{m-1}). \tag{2.3}$$

The current error is multiplied with the *integral factor* C_I and added to the last applied integral input power $P_I(t_{m-1})$. This way, a constant delivery of power is made when T_{SP} is reached.

The combination of the proportional and integral control already provides a good control stability if the response of the system is fast. However, in systems where the response time is long, this leads to overshooting of the SP, since the measurement of the effect of a certain action arrives only several – or in extreme cases many – time steps later. One solution would be to increase the length of the time step, but this has a severe disadvantage: the reaction to external changes, e.g. of the ambient temperature, becomes equally slow, worsening the stability further if the time scale of external changes is smaller than the chosen time step.

A better way to deal with slowly reacting systems is to make use of the derivative part of the control loop. Similar to the integral part, instead of an actual derivative, an empirical approximation is made: The derivative component makes use of the temperature measurement of the last two timesteps $T(t_m)$ and $T(t_{m-1})$ to determine the current temperature change rate, which is then multiplied with the *derivative factor* C_D to obtain the input power P_D:

$$P_D = C_D \cdot (T(t_{m-1}) - T(t_m)) \,. \tag{2.4}$$

This way, the input power contribution of the derivative part is positive if the measured temperatures are falling and negative if temperatures are falling, resulting in a damping behavior and providing better stability of the temperature control.

The total power applied to the heating mats P_{tot} is given by the sum of the three contributions from Eq. 2.2, 2.3 and 2.4:

$$P_{tot} = P_P + P_I + P_D. \tag{2.5}$$

The exact values of the factors C_P, C_I and C_D are determined by the physical and electronic properties of the system, e.g. the total power of the heating mats, the total volume of air to be heated or the total thermal load of the system, and always have to be determined empirically. It should be noticed that, although C_P, C_I and C_D are constant for a given system, they can change when parts of the system are changed. This can be the case also if the changes are not made to the heating system directly, but to other parts that contribute indirectly, e.g. over the heat load of the system. If that is the case, the three values need to be redetermined.

Finding the correct PID values is a challenge of its own. If they are not chosen well, the behavior of the control loop can take undesired forms, with the response to external changes being too slow or too harsh, in the worst case resulting in overshoots and oscillations. To make finding the correct values easier, a number of PID-loop tuning strategies exist, a discussion of which is out of the scope of this work but details can be found in the related literature (e.g. Bansal et al. 2012; George and Ganesan 2020).

The temperature controllers used for FOCES offer a function for automatically finding the best PID values. Two different approaches are available: *relay tuning* and *step response tuning* (*PTC10 - Programmable Temperature Controller - manual* 2019). In both cases, first the typical noise value for the used sensor is measured, in order to avoid confusing any random sensor noise with a real signal and thus getting a wrong set of PID values. The relay tuner then starts to create artificial oscillations of the temperature by switching between two heating power states (the amplitude is defined by the user) each time the measured temperature falls under or rises over the starting temperature. After two full oscillation cycles, the PID values are calculated from the period and amplitude of the oscillations. In contrast, the step response tuner only changes the output power amount once, for a length specified by the user, and during that time the amplitude and slope of the temperature change are measured, which then serve as base for the PID value calculation.

While the step response tuning requires a lower noise level to produce a good result, the relay tuning needs to make use of a wider range of the heater input power. Both options have been tested for tuning the temperature control in the FOCES tank and box, with the step response tuner delivering values that result in a more stable temperature control. Additionally, the step response tuning overall takes less time and is more sparing to the optical elements, which suffer from increased degradation at temperatures >25 °C. For more details on the automated tuning process, as well as the recommended tuning strategy for manual tuning of the PTC10, the reader is referred to the extensive and descriptive manual (*PTC10 - Programmable Temperature Controller - manual* 2019).

The PTC10 controllers are connected via Ethernet to the observatory IT infrastructure and can be operated remotely.

Other temperature control hardware

The sensors used as input for the PTC10 controllers are class AA PT100 sensors. PT100 sensors consist of a platinum wire, which exhibits a characteristic variation of the resistance as a function of the temperature it is exposed to. The sensor denomination contains the nominal resistance of the sensor at the reference temperature of 0 °C: 100 Ω. Class AA sensors feature excellent long-term stability and provide an intrinsic measurement accuracy of at least $(0.1\,^{\circ}\mathrm{C} + 0.0017 \cdot T)$, where T is the measured temperature given in °C.

The resistance of the PT100 sensor is measured by connecting a cable to each side of the wire. The cables also make a contribution to the measured resistance, which cannot be neglected. If the contribution is constant, then a simple offset factor, which can be determined experimentally, is enough to correct the measured temperature. However, when the used cables have a considerable length and when additionally measuring very small temperature changes on the <0.1 K level, the contribution from the cables to the measured resistance is typically not constant. The cables can pick up even small electric fields from their surroundings, resulting in a false measurement signal. A strategy to mitigate this issue is the use of so-called *four-wire sensing*. Two additional cables are installed in parallel to the cables connected to the platinum probe, but without any contact to the probe. This gives an independent measurement of the signal caused by the wires themselves and allows to correct the actual temperature measurement.

The locations of the sensors inside the FOCES tank and box (Fig. 2.8) were chosen to provide a good impression of the overall temperature while still keeping some attention on the most important optical elements. Table 2.3 gives an overview of the sensor locations and the corresponding sensor labels.

The FOCES box as innermost shell with the strictest temperature stability requirements is fitted with a total of five sensors. The two collimator sensors 3A-1 and 3A-2 are located closely together between the collimating mirrors. They are mounted with different orientations: 3A-1 is arranged parallel to the optical bench, while 3A-2 is pointing upwards, perpendicular to the optical bench surface. Sensor 3B-1 is placed inside one of the arms of the grating mount and has direct contact to the mount material, whereas 3B-2 sits in the air beneath the grating, just behind the heat shield (see Fig. 2.3). The fifth sensor in the box, 3D-2, is placed inside one of the tapped holes of the optical bench, next to the entrance of the camera lens system to monitor whether the optical bench shows any signs of direct thermal coupling to the outer shells.

sensor label	shell	location	redundancy
3A-1	box	between collimating mirrors	with 3A-2
3B-1	box	inside grating mount arm	with 3B-2
3C-1	tank	on top of FOCES box	with 3C-2 and WUT-tank
3D-1	room	behind the FOCES tank	with WUT-room
3A-2	box	between collimating mirrors	with 3A-1
3B-2	box	next to heat shield under grating	with 3B-1
3C-2	tank	on top of FOCES box	with 3C-1 and WUT-tank
3D-2	box	optical bench at the camera optics	no
WUT-tank	tank	on top of FOCES box	with 3C-1 and 3C-2
WUT-room	room	ceiling of FOCES room	with 3D-1

Table 2.3: The locations of the FOCES temperature sensors.

Three more sensors are available for temperature measurements in the FOCES tank. The sensors are all located on top of the wooden box and similarly to the collimator sensors in the box, sensors 3C-1 and 3C-2 also have a horizontal and vertical orientation in their mounts. The WUT-tank sensor is a *Wiesemann & Theis 57713* web-thermo-hygrobarometer, which has a temperature resolution of only 0.1 K, but can be read out directly over an Ethernet connection and independently from the PTC10 controllers. Additionally to the temperature measurements, the WUT-tank sensor gives simultaneous readings of the pressure and the relative humidity. Monitoring the humidity in the tank is essential, because the spectrograph optics tend to degrade faster if humidity is too high, while on the other hand in case of a very low humidity, problems with the glues used in the tank might occur.

The outermost shell, the spectrograph room, is equipped with two sensors that monitor the room temperature. Different locations have been chosen to check whether the temperature distribution is homogeneous or distinct temperature zones exist. Sensor WUT-room has a very exposed position, hanging from the ceiling of the spectrograph room, while 3D-1 was placed at a more secluded spot behind the FOCES tank. Because 3D-1 does not have a mount which decouples it from the temperature of the FOCES tank hull, it was enclosed in a plastic tube. In principle, the air conditioning units add two more temperature sensors, but since those are closed commercial systems, it is not possible to access their data.

Most of the sensors were installed in a way that redundancy with a second sensor placed nearby or at least in the same shell is given. On the one hand, this was done to prevent having to access the tank interior in the case of failure of one sensor. On the other hand, the readings of the sensors used for the control loop feedback by design show optimized values and the other, independent sensors are essential for a more realistic picture. It has to be noted that there is no possibility to combine the information from several sensors for the input of the control loops, but only one sensor can be used at a time.

The heating mats in the tank work with a supply of alternating current at a voltage of 230 V. The total heat output of the 14 mats amounts to 1150 W, smaller amounts are generated by pulse-width modulation (PWM). In contrast to that, heating mats with a direct current (DC) supply at only 50 V are deployed in the FOCES box. The heating power of the DC mats is controlled by directly modifying the supply voltage and a maximum power of 50 W from the 11 mats combined is available.

Since the sensors and the *PTC10* electronics are very sensitive to disturbances from the electric supply power, the controllers are not connected to the power grid directly. Instead, a *polyMIT 1700e* medical grade isolating transformer is installed in between (Fig. 2.17 b). The isolating transformer transmits the common 230 V line voltage with a ratio of 1 : 1 between two identical coils and thus generates the benefit of having a physical separation of the two circuits, while at the same time damping any rapid changes or short peaks in the supply voltage because of a large inertia.

Air conditioning

The outer shell of the FOCES temperature control is formed by the FOCES room, which is equipped with commercial air conditioning (AC) systems. Throughout the year, the surroundings of the spectrograph room experience large temperature differences of the order of 50 K. The room is partly built into the solid rock of the mountain, which by itself provides a naturally stabilized temperature, but the ceiling and one wall are directly exposed to the outside with little insulation material. As both are facing south, especially in summer the direct irradiation from the sun can be very intense and thus the temperature stability of the mountain rock is effectively negated.

Besides providing the first temperature stabilization level, the operation of ACs brings other benefits, like the reduction of the humidity level in the room. A lower overall humidity helps to protect the electronics because it results in a lower dewpoint, preventing condensation on cool surfaces.

Two different AC units are installed in the FOCES room: AC version 1 (AC V1) and AC version 2 (AC V2), both depicted in Fig. 2.12. AC V1 (Fig. 2.12 a) is a *GEA Flex-GeKo* unit, model number GF22.UWE3.L00C2, with a maximum cooling capacity of 1750 W (*Gebläsekonvektoren Flex-Geko: Technische Daten* 2018). The heat removal from the room is realized by a connection to the facility water supply of the observatory, which carries a glycol coolant with a constant temperature of ~8 °C. Additionally, AC V1 has an integrated heater with an output power of 2540 W, to provide temperature stabilization both in summer and in winter conditions.

With AC V1, the typical peak-to-valley variation of the room of one cooling and heating cycle amounts to 1.0 K to 1.5 K over a typical time of 30 to 45 min. During a 24 h window, temperature differences of 2.0 K can occur. These numbers are to be understood as ballpark estimates, the measurements depend on several factors like the precise location of the measurement in the room and the outside weather conditions.

To achieve a reliable stability between two exposures of the spectrograph, the duration of the cooling and heating cycles is relevant. Systematic effects might cause the equipment, optics and fibers in the room to show drifts and variations depending on the temperature, which could result in shifts on the detector. In order to average such effects out, it is desired

(a) Air conditioning version 1: GEA Flex-GeKo.

(b) Air conditioning version 2: Panasonic TKEA.

Figure 2.12: The air conditioning units in the FOCES room.

to fit the largest part of one cycle into the exposure time, which is typically around 30 min. The cycle length of AC V1 was modified to fulfill this condition by placing its temperature sensor closely to the air outlet. A larger distance to the sensor would lengthen the cycle time of AC V1, since the installation position of AC V1 relative to the FOCES tank in combination with the position of AC V1's air intake and outlet results in a limited airflow in the room and consequently a slow temperature mixing.

The need for installing a second AC unit arose because the cooling capacity of AC V1 was not sufficient to get rid of the heat dissipated by the electronic devices in the room, especially in summer when additional heat was introduced from the outside. Another big disadvantage of AC V1 is the absence of a dial to set the desired room temperature, instead only a color-coded dial is installed to choose a constant power level in arbitrary units.

Figure 2.12 (b) shows AC V2, a *Panasonic CS-Z50TKEA* with a nominal cooling capacity of 5000 W (*KIT-Z50-TKEA - technical data* 2021). The unit is connected to an external heat exchanger, located outdoors at a protected position between two observatory buildings, to dissipate the heat collected in the room. A heating function with a nominal heating capacity of 5800 W is also included. In contrast to AC V1, AC V2 is fitted with a temperature dial and the air outlet is not fixed in its position. The outlet can be set to swing mode, where the outlet angle is varied periodically, or a fixed angle within the available range can be chosen. This allows to achieve a more efficient distribution of the air.

In order to avoid disturbances between the two control loops of the ACs, the units are not in operation simultaneously. Instead, AC V2 is used with priority and AC V1 only takes over in exceptional cases like a failure or necessary maintenance downtime of AC V2.

The fact that the temperature regulation given by the AC in the room is only imprecise is acceptable, since the room is only the first temperature-stabilized shell. The typical amplitude of a single control cycle, consisting of one cooling and heating phase, is on the order of 0.4 K to 0.8 K at a typical length of 15 to 25 min. The 24 h stability is on the level of 0.8 K to 1.5 K, mainly depending on the outside weather conditions. Measurements of the AC performance and a discussion of the stability results are given in Chap. 3 in more detail.

Heat load enhancer

Due to the large variance of the outside conditions over the year, the heat load in the room undergoes a large variation. For the commercial AC units, which are specified and optimized for working in a defined range of heat loads, this spread is too wide to be fully covered. Especially in winter, when a lot of heat is drained to the outside because of low surrounding temperatures, the integrated heaters of the ACs are not sufficient to keep the room temperature at the desired level of $\sim 19 - 20$°C.

Besides providing a basic stability for the temperature control loops in the FOCES tank and box, a limited room temperature variation is also essential for the LFC. The filtering FPEs of the LFC are stabilized thermally and direct motors to adjust the distance of the plates are installed only for fine-tuning purposes. The overall range of the motors is small, traded for better positioning accuracy, but this implies that if the ambient temperature changes by a too large amount, the motors reach their limits and the motor range has to be manually adjusted to the new temperature. To avoid such complications, a long-term stability of the room temperature of $<$2 K is desirable.

For improvement of the room temperature stability, two heat load enhancers (HLEs) are available in the FOCES room (Fig. 2.8, dashed lines), which generate a constant amount of heat. It is necessary that the delivered heating power is constant, because then interference with the AC control loop is avoided. The HLEs can be turned on during cold weather periods, when the AC reaches its lower limit of temperature regulation, and switched off in warm weather conditions. The two different units, HLE1 and HLE2 (Fig. 2.13), feature different choices for the power that is dissipated to cover a large variety of outside weather conditions.

As HLE1, a *Honeywell* fan heater, model CZ-2104E (Fig. 2.13 a), with 2500 W heating power is employed. A fan option is available, which is useful for a better distribution of the heat in the FOCES room. The power output of HLE1 is only adjustable when periodic switching of the heating element is used, which doesn't fulfill the requirement of constant heat delivery. Thus, HLE1 can only be operated with the full power of 2500 W. An additional fan to further accelerate the mixing in the room is also available.

Due to its high output power, HLE1 is suited for operation in very cold winter conditions

(a) HLE1: Honeywell fan heater. (b) HLE2: control cabinet heaters.

Figure 2.13: The two generations of heat load enhancers (HLE) for the FOCES room.

with outside temperatures of around −20 °C to −5 °C. However, during a significant part of the year, transition conditions prevail with typical temperatures in the range −5 °C to 15 °C. In these times, a constant operation of HLE1 would lead to exceeding the cooling capacity of the AC. In order to provide a constant heating source with less overall power and several power adjustment steps, HLE2 was constructed.

HLE2 – its unofficial name is *heat organ* – consists of four individual heating elements that are mounted on a top-hat rail. The heating elements (*Pfannenberg PFH 200* and *PFH 300*) are off-the-shelf products which were originally intended for use in electric cabinets. They feature a fixed output of heating power, along with an integrated fan, and are running continuously as long as they are connected to the power supply. In the current configuration, heaters with different power levels are installed: two with an output of 200 W (*PFH 200*) and two with 300 W (*PFH 300*).

The employed heating elements are PTC heaters, which stands for *positive temperature coefficient*. This refers to the resistivity of the heater and means that its electrical resistance is small when the material is cold, but increases as the temperature rises. The consequence is a large current through the heater immediately after turning it on, which rapidly decreases as temperature builds up. Eventually, the heater reaches an equilibrium level that is defined by the material's composition and the power supplied to it. Due to this very specific behavior, the simultaneous turning-on of several heaters should be avoided to not overstress the observatory's power grid.

Each heating element is connected to a socket of a surge protected *Allnet ALL4076* power bar, which offers the possibility to switch each individual socket on or off. The power bar can be connected to the internet, so besides the manual switching by pressing the buttons on the bar, it is also possible to switch the sockets remotely. An additional 6 A slow-blow fuse is installed in the supply cable of the power bar to provide an independent safety measure.

The mounting structure of HLE2 consists of several 20 mm × 20 mm aluminum profiles as stand, between which a metal plate is fixed to form the main body. A top-hat rail is screwed to the metal plate, onto which the heating elements are clipped. Since the air outlets of the heating elements are oriented upwards and in continuous operation their surface can heat up considerably, a roof-like structure was added. A plate of POM generates a secure distance to the heating outlets and a perforated metal plate covers the top while still allowing the air to permeate. This protects the heating elements from any loose items which could fall onto the outlets and are a potential fire hazard.

The modular design of HLE2 facilitates the addition, removal or exchange of individual heating elements. This could be relevant in the future, if it turns out that the 1000 W total power is not sufficient or that it is desirable to have different combination possibilities of the single units. In total, six heating elements can be installed on the top-hat rail, with only four being mounted to date.

2.2.4 Pressure control system

Since the refractive index of air depends not only on the temperature, but also on the pressure, a pressure control system is required for FOCES to reach the desired stability. To this end, the FOCES tank was designed to act as closed volume that holds a certain overpressure.

The basic principle of the pressure control is the following: Pressurized and treated air is introduced into the tank, causing the pressure level to rise. As the tank is not completely airtight, a certain amount of air leaks out of it, at a rate depending on the pressure difference between the tank and the surroundings. By choosing an appropriate supply rate, it is possible to reach an equilibrium state of the pressure in the tank.

In order to keep the pressure level in the tank constant instead of just creating an offset to the ambient pressure, variations of the ambient pressure need to be compensated by adjusting the air inflow. A PID controller actuating a valve for the incoming air is employed for that. Figure 2.14 shows the complete setup used for the pressure control, starting from the supply line of pressurized air from the compressor (top left, gray).

Air filters

Since the pressurized air is generated by a compressor, it potentially can be contaminated with oil droplets and small particles originating from the compressor. Therefore, the air is filtered to avoid damage to and reduce degradation of the subsequent installations.

A filter bench (Fig. 2.15 a) consisting of four filters takes care of the air treatment, where the first filter, an active carbon filter, extracts any remainders of oil or water from the air. Following are three particle filters with a filtering grain size of 5 µm, 1 µm and

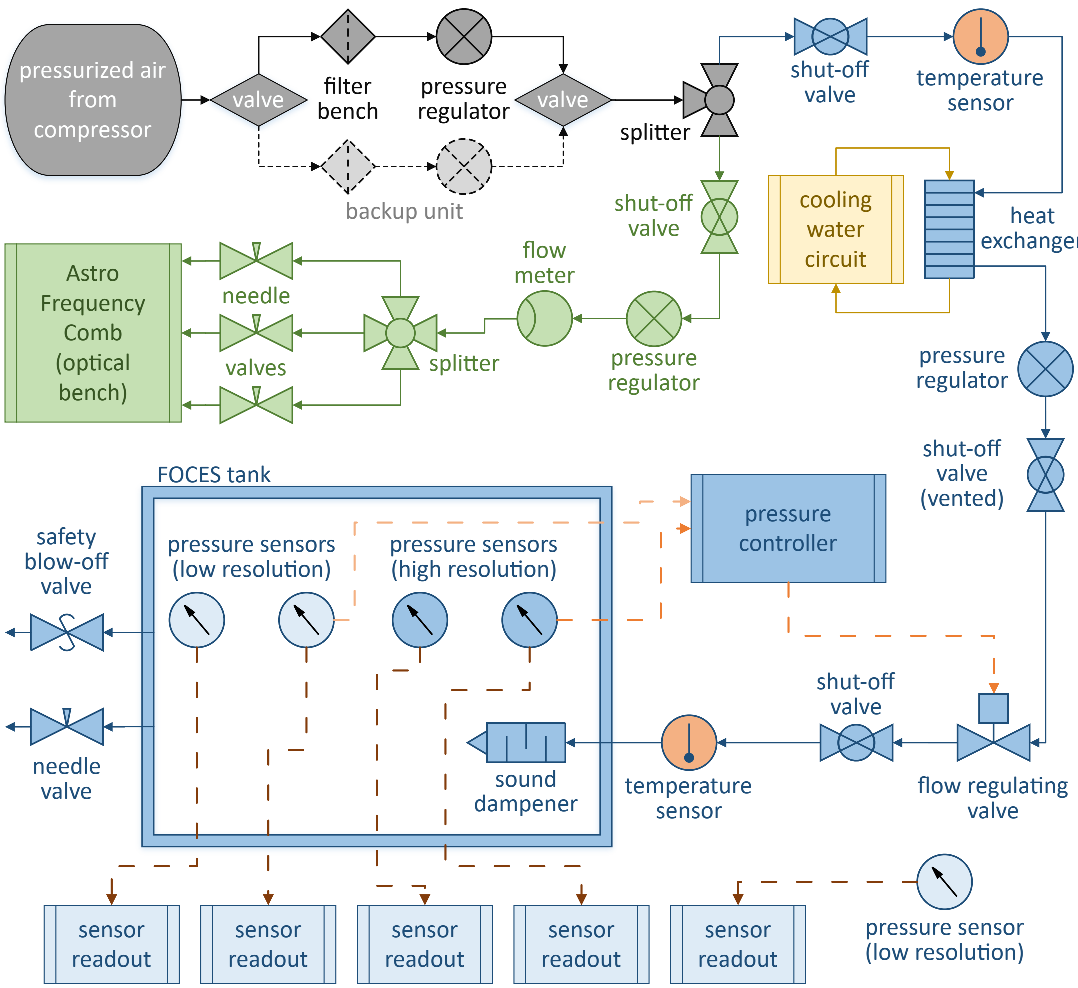

Figure 2.14: Schematic of the FOCES pressure control system. Gray: general path, preparation of the air; blue: FOCES tank path, further treatment and regulation for injection into the FOCES tank; green: LFC path, regulation for injection into the LFC. Graphic taken from Fahrenschon et al. (2020).

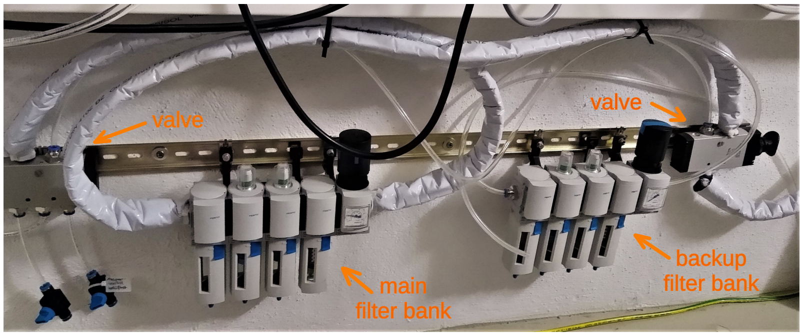

(a) Filter benches with pressure regulator.

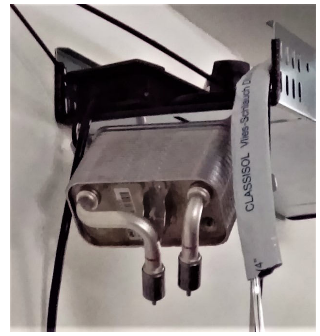

(b) Heat exchanger.

Figure 2.15: Filter benches and heat exchanger for treatment of the pressurized air before entering the FOCES tank.

0.01 µm, respectively. The filters are immediately followed by a pressure regulator, which limits the overall consumption of air. As the compressor at the observatory also supplies other equipment, e.g. the pneumatic brakes of the telescope, the maximum amount of air used by FOCES needs to be limited so all systems at the observatory can be operated simultaneously.

Over the course of time, the filters get clogged up with the restrained particles and the filtering material has to be exchanged. To nevertheless provide a continuous operation of the pressure control, backup units of the filter bench and pressure regulator are installed (Fig. 2.14, gray) and two valves allow to seamlessly switch between the two arms.

Branch structure

After the air treatment and regulation the air flow is split into two branches. One branch is supplying the LFC (Fig. 2.14, green), while the other one is used for the FOCES tank pressure regulation (Fig. 2.14, blue). Immediately after the splitter, both branches are fitted with a shut-off valve, so an independent operation is possible.

The LFC branch provides the Fabry-Perot cavities with dry air to decelerate the degradation process of the optics. A pressure regulator (Fig. 2.14, center) allows to further reduce the pressure on the supply line and a flow meter gives a measure of the amount of air that is consumed by flushing the LFC cavities, which is typically on the order of 2.5 l/min. The air is then distributed by a three-way splitter to the three compartments that contain the FPEs (Fig. 2.14, left). Needle valves allow to adjust the flow to each compartment individually. The LFC branch installations are depicted in Fig. 2.17 (a).

The setup of the FOCES tank branch is more complex, owed to the stability requirements of the spectrograph. Since the lines that supply the FOCES tank traverse the FOCES room at a length of several meters, the variations of the room temperature may imprint on the temperature of the pressurized air before the air is injected into the temperature-stabilized FOCES tank. To reduce negative influences of the pressurized air temperature on the stability of the temperature control in the FOCES tank and box, the pressurized air temperature is stabilized by means of an aluminum heat exchanger (Fig. 2.14, top right) before entering the tank.

The heat exchanger (Fig. 2.15 b) is connected to the liquid cooling system used for the CCD camera, where the coolant is kept at a constant temperature (see Sec. 2.2.5). The pressurized air and the liquid coolant are passed through two separate but thermally coupled compartments of the heat exchanger, which provides a large contact area without direct contact of the media, thereby smoothing out possible temperature variations. To further diminish the imprinting of the room temperature variations, all tubes and connections before the heat exchanger are insulated with two layers of insulation fleece, while the parts after the heat exchanger are insulated with the same two-layer fleece and an added layer of Armaflex® foam.

A temperature sensor at the air entrance of the heat exchanger (Fig. 2.14, top right) was installed to measure the variation of the air temperature inside the tubes. A second temperature sensor just before the air is introduced into the tank (Fig. 2.14, bottom center) allows to monitor the effect of the heat exchanger and the insulation.

Following the temperature treatment are a pressure regulator and a vented shut-off valve (Fig. 2.14, right). The latter serves as a pressure release in case the FOCES tank branch is out of operation, during which the subsequent flow regulating valve needs to be relieved from any pressure to avoid damage.

The exact amount of air delivered to the FOCES tank is determined by the flow regulating valve (Fig. 2.14, bottom right). A PID controller measures the pressure in the tank and adjusts the flow rate through the valve to maintain a stable pressure level in the tank. Since the air inflow is compensating the tank leakage to reach a certain pressure, it is useful to also have control over the leak rate of the tank. A part of the leakage happens at the hull joints and other fittings of the hull, but additionally a needle valve is available (Fig. 2.14, bottom left) through which air can escape. This way, the leak rate can be adjusted so the consumption of pressurized air does not exceed the supply rate of the observatory's compressor.

For safety reasons, a further shut-off valve is installed before the tank (Fig. 2.14, bottom right). Furthermore, the tank is fitted with a blow-off valve (Fig. 2.14, left) which opens in case of an extreme overpressure in the tank. This is to avoid any damage to the tank itself, which in the worst case would result in a rupture of the hull joints.

Inside the FOCES tank, the end of the tube that is injecting the air is equipped with a sound dampening device (Fig. 2.14, bottom). It consists of two parts: a small industrial-grade sound dampener directly inserted into the tube, which is in turn enclosed in a plastic canister with small holes distributed over its surface. Apart from the reduction of vibrations, the dampening device brings the benefit of creating a diffuse air flow rather than a directed jet. This reduces the risk of the build-up of convection zones or heat pockets due to the air flow and favors a more uniform distribution and mixing of the air.

Four pressure sensors are measuring the pressure in the tank (Fig. 2.14, bottom left), two with low and two with high measurement resolution, and one low resolution sensor monitors the ambient pressure in the room (Fig. 2.14, bottom right). All of the sensors are read out by individual and independent readout units (Fig. 2.14, bottom).

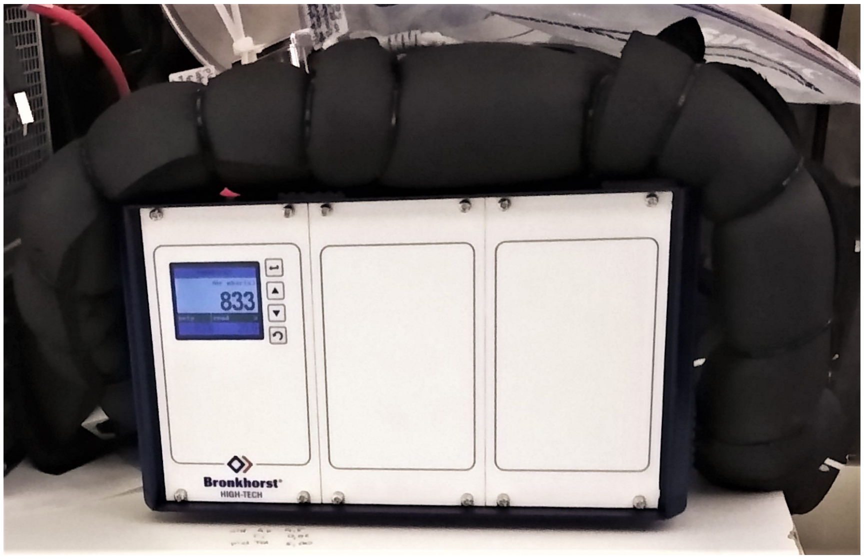

Figure 2.16: Bronkhorst E-8000 unit for controlling the pressure in the FOCES tank. A part of the insulated tube is also shown (black).

Pressure controller

For the control of the pressure in the FOCES tank, a *Bronkhorst E8101* PID controller (Fig. 2.16) in combination with a *Bronkhorst EL-FLOW Select* regulation valve is used.

The principles of a PID control loop are described in Sec. 2.2.3. However, the implementation of the control is differing slightly from the description in Sec. 2.2.3: the value C_P serves as scaling factor for all three control components, while C_I and C_D are given in seconds and correspond to the time interval used for the integration and differentiation, respectively.

In contrast to the temperature controllers, the Bronkhorst pressure controller does not offer an automated routine to find the best PID coefficients. Instead, the optimal values for the application at hand are supposedly chosen by the manufacturer already at the factory. It was noted however that in reality the preset PID values still needed to be improved in order to reach a pressure stability of $<0.1\,\mathrm{hPa}$.

For the manual tuning of the PID values, different strategies were tested. The recommended one starts with resetting the controller to the factory settings. After that, the manual tuning process described in *Temperature Control - Tuning a PID (Three Mode) Controller - manual* (2021) (method A) is followed, with each following step depending on the observed behavior of the pressure in the tank. In summary, the approach is based on finding the first setting that produces oscillations and then adjusting the values until the oscillations vanish.

Compared with the thermalization of the spectrograph, the exchange of the pressure inside and outside the tank is a fast process. Therefore, the derivative part of the PID control does not have to be very strong or can even be equal to zero.

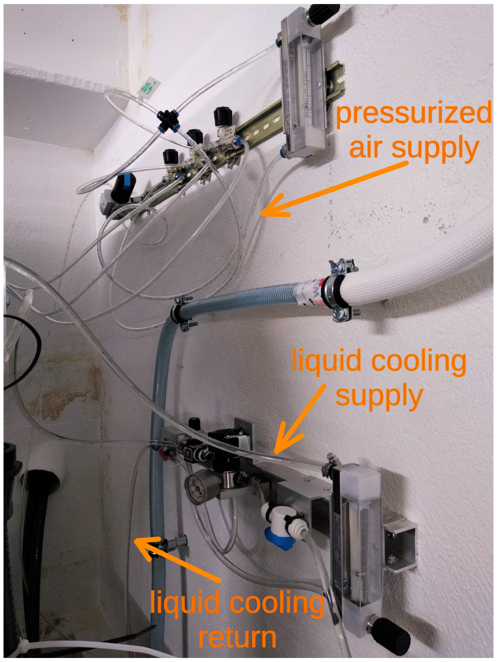

(a) LFC branch of the pressure control and liquid cooling systems.

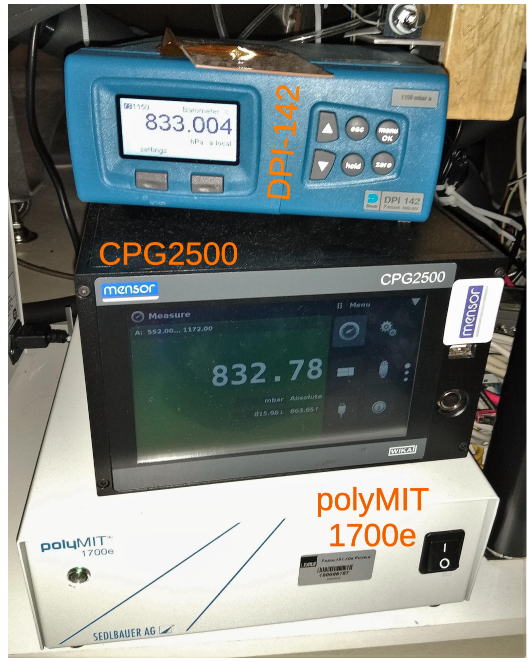

(b) High-accuracy pressure sensors *DPI-142*, *CPG2500* and isolating transformer *polyMIT 1700e*.

Figure 2.17: Components of the pressure control system of FOCES.

Pressure sensors

A total of four pressure sensors are available in the FOCES tank (Fig. 2.14). Figure 2.17 (b) shows the two sensors *GE Druck DPI-142* (top) and *Mensor CPG2500* (center), which both have a high measurement accuracy on the 0.1 hPa level. The two sensor units are connected to the FOCES tank by a tube and measure the pressure transmitted by the tubing inside their main housing.

The *DPI-142* sensor features an analog output with a 0 to 10 V signal, which is used as input for the pressure controller. Since the controller expects a signal with only 0 to 5 V, a special cable that includes a voltage divider was manufactured to connect the two devices.

A *Tecsis P3276* pressure transducer was originally chosen for operation with the pressure controller, however it has been noticed that its measurement accuracy of only 2.75 hPa is not sufficient to fulfill the pressure stability requirements in regular operation. Therefore, it has been replaced by the *DPI-142*, but is still available as backup control sensor. In contrast to the high accuracy sensors that have tube fittings, this sensor is installed directly inside the FOCES tank on one of the rails for the optical bench.

For fast and uncomplicated readout, a *Wiesemann & Theis 57713* web-thermo-hygro-barometer is also used to obtain pressure measurements in the FOCES tank. Its accuracy of 2.5 hPa is similar to that of the *Tecsis P3276*. The sensor is placed on top of the FOCES box that contains the optical bench.

Furthermore, an identical *Wiesemann & Theis 57713* unit is used to monitor the ambient pressure in the room, which gives the possibility to have a direct comparison of the values in and outside of the tank.

All devices used for the pressure control and monitoring are connected to the observatory network and can be controlled remotely.

2.2.5 Liquid cooling

The science CCD camera of MaHPS is operated at a temperature of −80 °C. To reach and maintain this temperature, the camera is equipped with a five-stage Peltier cooling element, from which the excess heat is removed by means of a liquid coolant. In order to keep the temperature of the coolant as stable as possible and avoid influences on the thermal stability of the spectrograph, part of this work was to develop an extended liquid cooling system.

Branch structure

Similar to the pressure control system, the liquid cooling system also consists of different branches, as shown in Fig. 2.18 (gray, blue and green). However, the liquid cooling is designed as closed circuit with a water-to-water cooler as centerpiece. A water-to-water cooler efficiently transfers heat from a warm liquid to another, colder one and thereby allows to control the temperature of the warmer liquid.

For the FOCES liquid cooling system, the observatory's facility water system is used as cold liquid. The facility water is a glycol-based coolant, which has a mean temperature of ∼8 °C (see also Sec. 2.2.3). A pressure regulator and flow meter (Fig. 2.18, top left) allow to adjust the pressure and flow rate in the facility water branch, respectively. While the limitation of the pressure is rather a safety measure to avoid excessive stress on the tubes and joints, which in turn reduces the probability of leakage, the choice of the flow rate influences the maximum cooling capacity of the cooler.

On the other side of the cooler, a coolant specifically designed for sensitive electronics is used at a process temperature of 16 °C. A splitter separates the LFC branch (Fig. 2.18, green) from the CCD camera branch (blue). Shut-off valves in each branch create the possibility to operate the branches independently, so that in case of a failure, leakage or general maintenance the other part of the cooling system can still be run.

The LFC branch supplies the LFC with cooling liquid, which is fed through the baseplates of the optical tables (Fig. 2.17 a). After passing through a pressure regulator and flow meter, the coolant traverses the LFC baseplates (Fig. 2.18, center) in order to provide the FPE length control mechanism with a stable temperature. As the thermal expansion of the FPEs plays a critical role, the liquid cooling helps to attenuate the influence of room temperature variations on the FPE control stability, making the LFC more reliable. A mechanical flow indicator is installed after the LFC to easily spot any potential blockage of the flow.

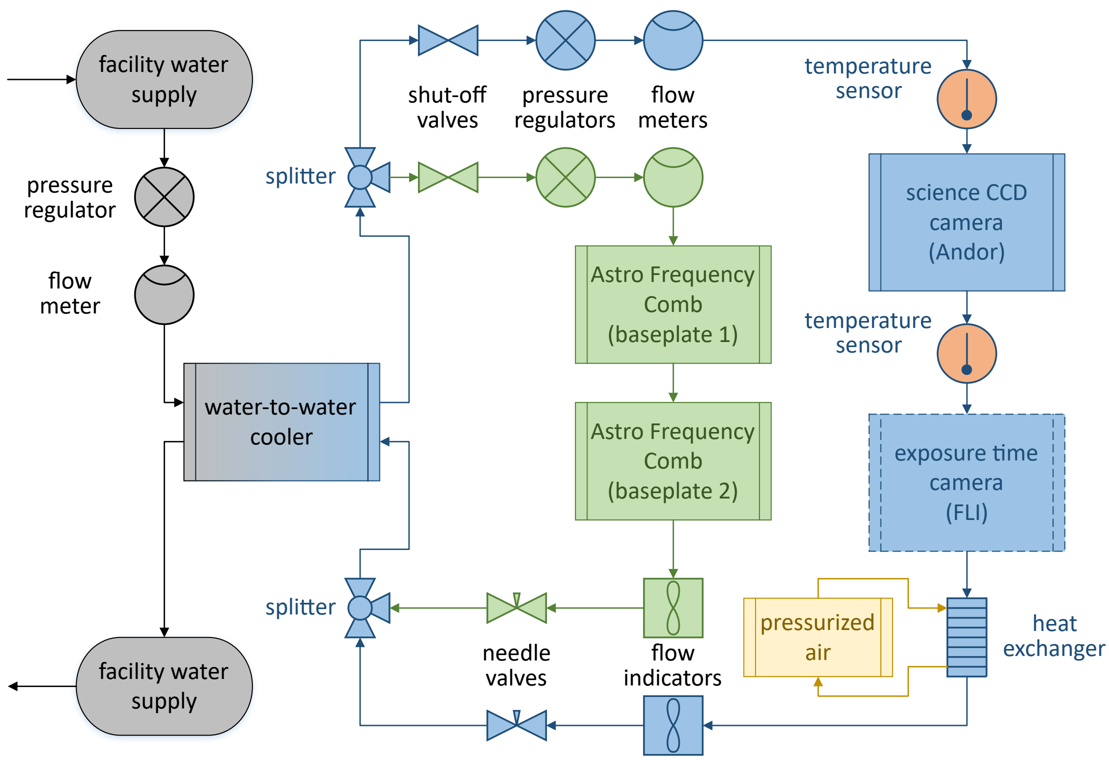

Figure 2.18: Schematic of the liquid cooling system for FOCES and its subsystems. Graphic taken from Fahrenschon et al. (2020).

The structure of the CCD camera branch (Fig. 2.18, blue) is in parts similar to that of the LFC branch. A pressure regulator and flow meter are installed before the critical parts (Fig. 2.18, top), as well as a flow indicator at the end of the branch (Fig. 2.18, bottom). Since the CCD camera is such an essential part of the spectrograph, temperature sensors in its coolant supply and return lines (Fig. 2.18, right) are available to monitor the stability of the coolant temperature. After passing through the science CCD camera, the coolant is used for cooling a second, smaller CCD camera. This camera is part of the exposure time monitor, which is already installed, but not yet in active use (see Sec. 2.3). In a last step, the coolant is used to stabilize the temperature of the pressurized air in the heat exchanger (see Sec. 2.2.4) before being returned to the water-to-water cooler.

The design with two parallel branches of the coolant circuit brings the necessity to balance the flow rate of the branches. If no adjustment is made, the coolant flow would concentrate on the branch with the bigger internal cross-section, leaving the other branch with basically no flow rate. To this end, both branches are fitted with a needle valve (Fig. 2.18, bottom center) and the flow can be distributed such that both branches get the amount of coolant needed.

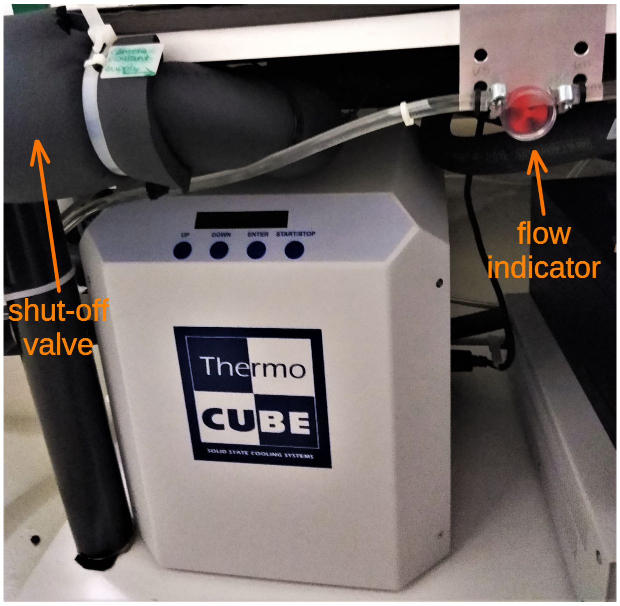

(a) The water cooler providing the liquid cooling.

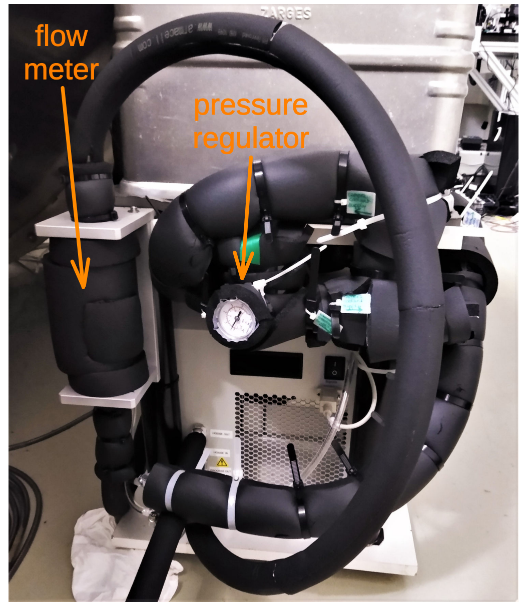

(b) Facility water tubing with Armaflex® insulation (black).

Figure 2.19: Components of the liquid cooling system of FOCES.

Water-to-water cooler

The central water-to-water cooler of the liquid cooling system is a *ThermoCube 400L* (Fig. 2.19 a), manufactured by *Solid State Cooling Systems*. This cooler has a cooling capacity of 400 W and a temperature control stability of 0.05 K, which is provided by an integrated temperature controller.

As the cooler is operated continuously, a long-lived centrifugal pump was chosen. Furthermore, the device is specially prepared for operation at temperatures below 10 °C, so the facility water can be utilized. An auto-restart software makes sure that the cooler starts the temperature control automatically after being turned on, be it regularly or irregularly, e.g. in the case of a power outage.

Coolant circuit

When a cooling circuit is designed, one issue that needs to be addressed is the potential for galvanic corrosion. If two different metals are connected over a liquid that contains electrolytes, the metals act as electrodes, resulting in the stripping of material from the one metal and deposition on the other one. Consequences could be a leakage due to the corrosive destruction on the one hand, or on the other hand the blockage of a part because of the material deposition.

Therefore, the choice of the so-called wetted materials is crucial when setting up a system with a long lifetime. For the FOCES cooling system, the wetted parts all consist of aluminum or non-corrosive materials like plastic. As additional safety measure, a coolant was chosen that contains an inhibitor for galvanic processes. The employed coolant, *innovatek Protect IP* in the application mix with 75% distilled water, is a glycol-based coolant suited for temperatures as low as $-12\,°C$. It is specifically designed to cool electronic devices, offers special properties like foam and bubble reduction, and is recommended by the manufacturer for use with the *Andor* CCD camera.

The regular setpoint of the coolant is $16\,°C$, which is a compromise to suit both the CCD camera and the LFC. The cooling of the CCD camera is more efficient at lower coolant temperatures, while at the same time the thermal stabilization of the LFC FPEs is limited at $\sim 15\,°C$ by the absolute range of the FPE adjustment motors.

Facility water branch

The temperature of the facility water lies at about $8\,°C$ all year round, meaning that the tubes, fittings and regulators take on this temperature. Since that temperature usually lies well below the dew point of the room, given the typical range of room temperature and humidity values, water condenses on those surfaces. In order to avoid damage to the electrical equipment caused by water running along the tubes or dropping from any fittings, the surfaces are insulated by a layer of Armaflex® foam, wherever possible. Figure 2.19 (b) shows some of the insulated parts, where even the flow meter (left) and pressure reducer (center) are completely covered, with removable pieces for reading the gauges.

The coolant used in the facility water circuit is a mixture of distilled water and glycol, owing to the fact that a part of the circuit runs through the telescope dome, where icing protection is required for the winter season. As a side effect, the high glycol concentration lubricates and thus protects any moving parts and prevents the formation of organic contamination like algae.

The water-to-water cooler is not equipped with a pump on the facility water side, instead the pressure on the facility water supply line is used to move the facility coolant. The cooling capacity of the water-to-water cooler directly depends on the flow rate of the facility water. The flow rate specified by the manufacturer of the water-to-water cooler for reaching the targeted cooling capacity of 400 W is 3.8 l/min or 1.0 gallon/min, which can be adjusted at the flow meter.

2.2.6 Guiding system

To make sure that the observed star is always centered on the fiber entrance optics, a guiding system is required. The fiber shaker ensures that the light distribution at the fiber exit is less sensitive to the exact modes that the light is coupled into, however another base property of optical fibers is the conservation of the angle under which the light was coupled in. In order to avoid the detection of false signals due to varying angles of the imaged light, the guiding system takes care that the coupling is done consistently.

In Fig. 2.20, the guiding system and the coupling optics are shown. The fiber to the spectrograph is sitting behind a small mirror with a hole in the center. The light passing

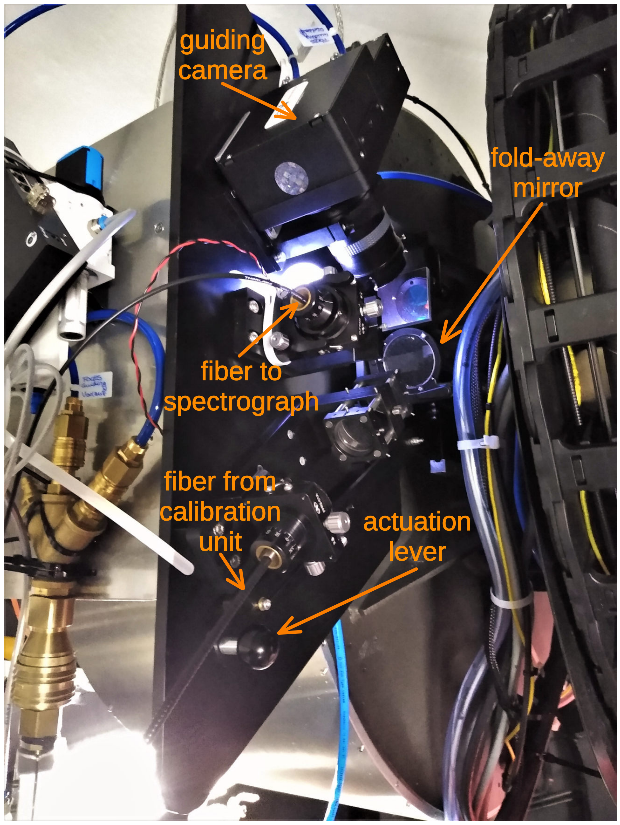

Figure 2.20: Optics installed in the telescope Nasmyth focus for the fiber pickup of the telescope light and the guiding system.

through the hole is coupled into the fiber, while the outer part is reflected onto a CCD camera, henceforth referred to as *guiding camera*.

The guiding camera takes images of the ring-shaped light with a typical exposure time of 5 to 10 s. Immediately after readout, the image is processed with a so-called *four sector guiding* to evaluate the positioning of the star. To this end, the image frame is divided into four sectors, centered at the hole, and the flux in each sector is measured. By comparing the fluxes, the direction and amplitude of the correction that may be needed for the telescope position is determined.

The pickup optics and guiding system, as well as the calibration fold-away mirror are mounted on a common baseplate at the telescope's Nasmyth focus (Fig. 2.20). Between the telescope mount and the baseplate, a derotator is installed to compensate the rotation of the telescope's field-of-view when an image is taken. However, since only the light from one star is coupled into the spectrograph and any spatial information is destroyed by the fiber shaker, the derotation is not needed. A further argument for the deactivation of the derotation function are the mechanical influences on the coupling optics. When the derotator has different positions, gravity acts differently on the mounting structures, leading to a slight bending that cannot be neglected. To guarantee a reproducible coupling of the light, a fixed derotator position for the operation of MaHPS is defined. Additionally, the mechanical effects show a dependency on the direction from which the defined position is set, so also the rotation direction for reaching said position is fixed.

2.2.7 Lightning protection

Due to the location on top of a mountain at the fringe of the Alps, the observatory is subject to frequent thunderstorms, especially in the summer months. Direct lightning strikes are a threat to the electrical and electronic equipment due to the immense electrical stress. While this problem can be dealt with – at least to some extend – by using surge-protected connectors, another more challenging problem are the large electrical fields that are induced by a lightning hit, even if it is only nearby.

The electrical fields result in a difference in the potential between cables or electronic devices at different positions. If there is a conductive connection between two points with different potential, a compensating current will be induced, which can be strong enough to damage electronic devices. The risk of being exposed to such a harmful potential difference increases with the distance between the two end points of the connection.

For MaHPS, several measures are taken to mitigate damages from lightning strikes. First, the power for all electric appliances is distributed radially from three central points and the devices which are connected to each hub are arranged as close together as possible (see shelf in Fig. 2.21). The power strips chosen as hubs feature a built-in surge and overload protection. Interconnections between the hubs, e.g. by data cables, are avoided to keep the maximum length of a conductive chain as small as possible. When it was not possible to use a cable with the bare minimum length, longer cables are installed but rolled up to decrease the effective length.

Furthermore, alternatives to copper cables are used in some places. The data connection of the CCD camera is realized with an optical fiber by employing a USB-to-fiber converter and the HLE2 is connected to the observatory's network via WiFi.

The devices installed inside the FOCES tank cannot be altered in their position to be close to the power supply. To protect them from lightning damage, their conductive connections are packed inside an aluminum box (Fig. 2.21, left) with a dedicated power supply line, which is equipped with an inline surge protected voltage filter. A more detailed description of the lightning protection box is given by Kellermann (2021). On the whole length between the box and the tank, the cables are surrounded by a copper mesh tube (Fig. 2.21, center) which is connected to both the box and the tank hull to provide shielding against any external electrical fields.

2.3 Future prospects

MaHPS has started regular science operation already in 2019 and this work describes the status of the instrument as of the date of submission. Nevertheless, numerous improvements and extensions can still be made in the future.

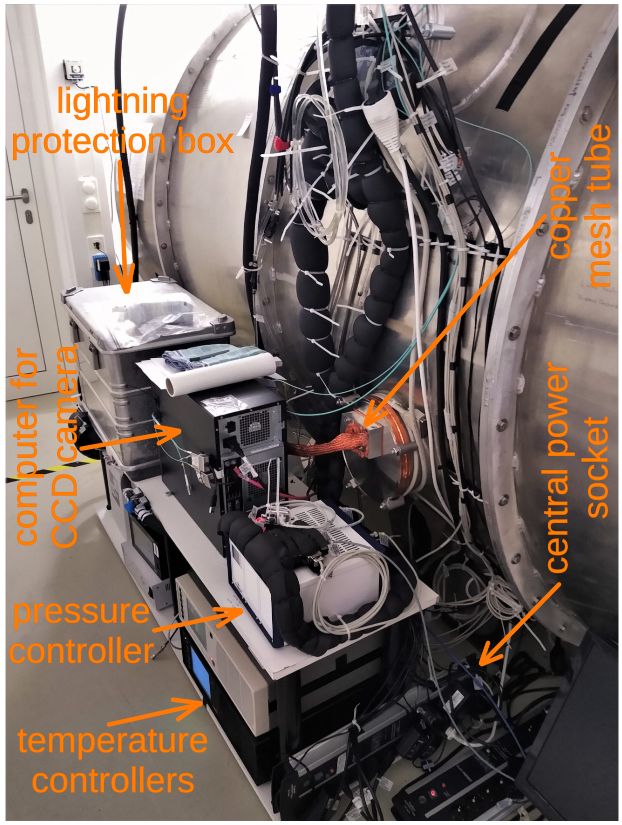

Figure 2.21: The shelf containing all relevant controllers, sensors and other electronic devices for FOCES operation.

2.3.1 First ring

The highest impact on the operation and performance of MaHPS lies in the installation of the so-called *1st ring* (Krecker et al. 2020). The 1st ring is a device designed to facilitate the switching between different instruments by providing a motorized central mirror mount. All parts of MaHPS that are to date installed on the baseplate at the Nasmyth focus of the telescope (Fig. 2.20), including the fiber pickup, guiding camera and calibration light path, will be integrated fully into the 1st ring.

In Sec. 2.2.2 the manually actuated foldaway mirror for the sequential calibration is presented. However, this solution is not optimal since the manual interaction is a potential source of errors. The 1st ring provides a fixed light path for this, so the reproducibility is improved and the calibration routine before the night can be executed fully automatically. It also opens the possibility to choose a calibration order in which the wavelength calibration exposures are taken closer in time to the science exposures to minimize errors in the wavelength calibration.

Furthermore, the 1st ring is equipped with a so-called *telescope simulator*, which reproduces the telescope's optical path, especially in terms of occultations like that of the mount of the secondary mirror. The calibration light for the sequential calibration is fed through the telescope simulator so its light path resembles that of the science light even better, reducing systematic calibration errors.

When observing targets at low elevations, the image of the star suffers more heavily from atmospheric dispersion. This is an effect due to the variation of the refractive index of the atmosphere with wavelength, which gets stronger as the light passes the atmosphere at a longer distance. Atmospheric dispersion causes the telescope image of a star to be spread out to a small spectrum rather than a single disk with all wavelength overlapping. This is important to consider when centering the star's image on the fiber pickup using the guiding camera. The 1st ring contains a filter wheel in front of the guiding camera with several standard broad-band filters, which can be used to optimize the flux coupled into the spectrograph for the wavelength region that is most interesting for the science application at hand.

2.3.2 FOCES exposure monitor (FOX)

The determination of the timestamp of an exposure also effects the RV precision. With exposure times as long as 30 min, the incoming flux from the star can undergo large variations during a single exposure, e.g. due to passing clouds or changes of the star's elevation. In these cases, using the simple midpoint of the exposure as a timestamp can introduce errors in the RV measurement, because the measured position of the spectral lines is given by the mean of the time distribution with which the flux arrived. Thus, the time coordinate of the mean arrival time of the photons needs to be used, otherwise errors of several m/s can occur.

Identifying the correct time coordinate for an exposure is possible by using an exposure monitor which tracks the incoming flux at a higher time resolution than the spectrograph itself. The FOCES exposure monitor (*FOX*) is designed to handle this task. A part of the light from inside FOCES is picked up by FOX, fed through an optical fiber, passed through a low-resolution prism and finally imaged with a dedicated CCD camera. However, although the FOX hardware is already installed, it is not in regular operation yet due to the lack of software implementation.

Once in operation, FOX provides further benefits to the operation of MaHPS. On the one hand, it can serve as warning mechanism to protect the MaHPS science CCD camera from unwanted saturation during an exposure. By comparing the fluxes on the MaHPS and FOX detectors, it is possible to determine a level at which the MaHPS detector would saturate and a readout or abortion of the exposure can be triggered. Unfortunately, to date the control software of the MaHPS CCD camera does not support a triggered readout, so an abortion with the loss of all data collected so far during the exposure is the only option. On the other hand, the low-resolution prism of FOX allows to record a spectrum and measure the flux in different wavelength bands individually. Large wavelength gradients in the flux can be observed e.g. when clouds pass the field-of-view or when the atmospheric conditions change rapidly. The information about the wavelength-dependent flux behavior then helps to obtain a mean flux arrival timestamp that is adapted to both the observing conditions and the most interesting wavelength regions of the science project.

2.3.3 Other modifications

Besides the 1st ring and FOX, other modifications are planned for MaHPS. One such modification is the use of optical fibers with an octagonal core to carry the science light from the telescope to the spectrograph. In contrast to the round-core fibers currently used, octagonal fibers feature a much more efficient internal mode scrambling, reducing the influence of coupling inconsistencies at the fiber entrance to a level that is more suitable for the 1 m/s regime.

In terms of improving the RV precision that can be achieved with MaHPS, an extension of the wavelength range of the LFC is in preparation. Newly developed hardware allows to extend the LFC spectrum significantly towards blue wavelengths, to an overall LFC range of about 420 to 680 nm, which means that more spectral orders can be used in simultaneous calibration mode. This allows to obtain RV measurements with an increased precision due to better statistics of a single measurement.

Concerning the long-time operation stability of MaHPS, a planned addition is a humidity control facility for the pressure control system. The pressurized air used for supplying the FOCES tank is dried in the very first step, however as a result the humidity inside the tank permanently lies at a very low level ($< 5\%$). On the long term, that might pose a problem to the tank interiors, especially the glues used to attach various parts. Reintroducing at least some humidity just before the air enters the tank would help to prevent glue failures and other related problems.

All in all, many improvements can and will still be made to MaHPS with the aim to improve the RV precision and handling of the instrument. The listing presented here should not be regarded as complete or mandatory, since the instrument as well as the observatory are subject to constant changes caused by a multitude of factors, some of them more foreseeable than others. Nevertheless, at the current state of MaHPS, the operation in the few m/s regime is feasible and the modifications that are already under way will further improve the precision and long-term reliability.

Chapter 3

Environmental stability of MaHPS

In this chapter, the stability of MaHPS is evaluated by means of a number of different measurements. As a significant part of the analysis was already published in Fahrenschon et al. (2020), the relevant excerpts will be cited and marked accordingly. The conduction of the measurements, the analysis of the data, as well as the creation of the published text and graphs are all my own work, except where explicitly stated otherwise.

To reduce interruptions of the reading flow, the special marking of small changes that do not affect the content of the cited text was omitted. This concerns the altered table and figure numbering, references to literature, as well as the way numbers, units and ranges are displayed. Wherever additional information is necessary, footnotes are inserted into the cited text.

3.1 Requirements

As stated in Sec. 2.2, stability requirements for the temperature and pressure control of MaHPS have been defined on the base of simulations (Tab. 2.2). The overall goal is to reach RV precisions on the level of $\leq 1\,\mathrm{m/s}$ when using the simultaneous calibration mode of MaHPS, in order to have a competitive instrument for exoplanet science.

One challenge for the stability of the temperature and pressure control systems is the shared volume of the FOCES tank. According to the general gas equation ($pV = NkT$) for a closed volume, where V and N are constant, any variation of either the temperature or the pressure of the contained gas is inevitably linked to a change of the other quantity. Although the FOCES tank is not exactly a hermetically closed system, the very limited thermal and pressure exchange with the ambient still gives rise to complications illustrated by the general gas equation. Therefore, both control loops influence each other and a balance between the two has to be found.

3.2 Stability measurements

"The stability was measured both in terms of pressure and temperature variations, and as shifts of the spectra of [...] [the] calibration sources on the CCD chip. Since RV measurements of exoplanets and exoplanet candidates will be the main application of the spectrograph, the measurements are presented in RV units and discussed with a special focus on this science field." Excerpt from Fahrenschon et al. 2020, p. 7.

3.2.1 Temperature and Pressure Control Stability

"Temperature and pressure values are measured by a multitude of sensors at different locations inside the spectrograph room and the spectrograph's enclosure, as described in Sec. 2.2. All temperature and pressure sensors are read out with a 5 s interval with the exception of the pressure sensor in the spectrograph room [WUT-room], which is only read every minute. The sensors used for the precise temperature measurements shown here are optimized for stable relative measurements on scales of <0.001 K and are not calibrated in their absolute values. For that reason, overall offsets between the sensors on the scale of ~0.5 K are natural and do not necessarily indicate real temperature differences, but relative trends are reliable." Excerpt from Fahrenschon et al. 2020, p. 7.

setting	air conditioning unit	setpoint T_{room}	setpoint T_{tank}	setpoint T_{box}	setpoint P_{tank}
1	AC V1	22 °C	23.5 °C	24.0 °C	833 hPa
2	V1	19 °C	inactive	inactive	inactive
3	V1	19 °C	21.5 °C	inactive	833 hPa
4	V2	19 °C	21.5 °C	inactive	833 hPa
5	V2	19 °C	21.5 °C	inactive	inactive
6	V2	20 °C	inactive	inactive	833 hPa

Table 3.1: The different combinations of temperature and pressure setpoints used to obtain stability measurements with MaHPS. Adapted and expanded based on Fahrenschon et al. (2020).

Due to the changing availability of components of the temperature components over the course of time, the measurements presented in this chapter were made with different configurations of the temperature control system. Table 3.1 lists the configurations that were used, along with the setpoints of the individual control loops.

Uncontrolled temperature propagation

For the interpretation of the stability measurements it is interesting to distinguish between temperature variation effects that are caused by the temperature control system and those

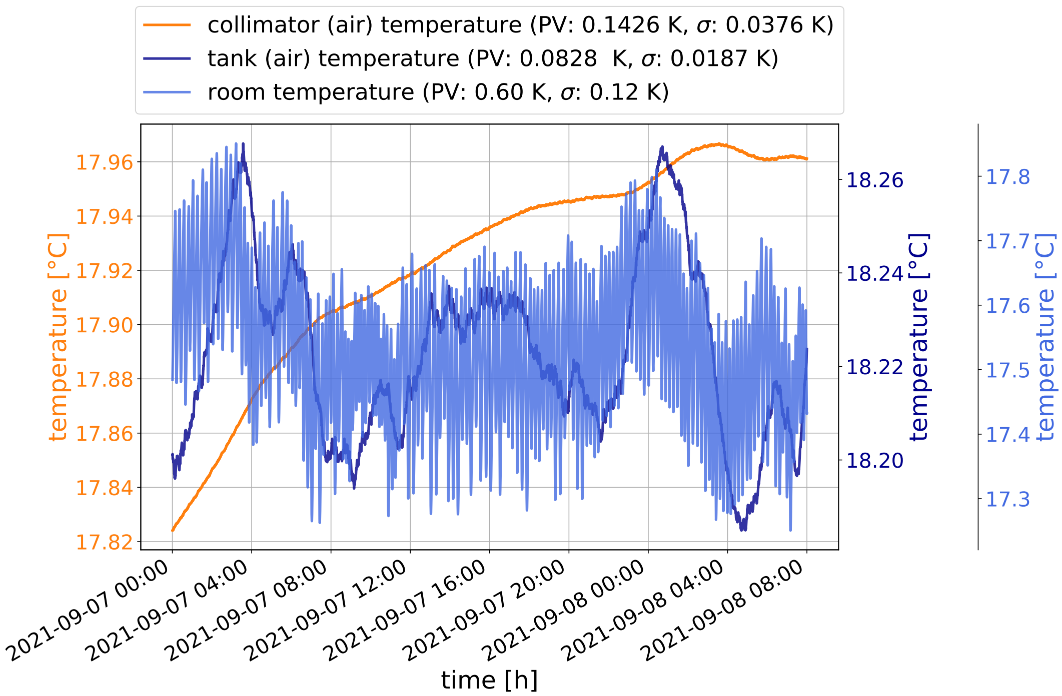

Figure 3.1: Temperature time curve over 32 h during a period when the temperature control in both the tank and the box were deactivated. Air temperature was measured between the two collimating mirrors (3A-2, orange), in the FOCES tank (3C-2, dark blue) and in the room (3D-1, light blue). The peak-to-valley (PV) variation and the standard deviation of the measured values in the displayed time interval are given in the legend. Setting 6 from Tab. 3.1 was used for this measurement.

that can be observed without any control, simply due to the insulation of the shell structure. The relevant characteristic values are the typical time delay and amplitude of temperature drifts that can be observed between two layers.

During a period when the temperature control was only active in the FOCES room, using AC V2, but not in the FOCES tank or box (Tab. 3.1, setting 6), the propagation of changes in the room temperature through the different shells could be directly studied (Fig. 3.1). The room temperature variations (light blue) imprint on the temperature in the tank (dark blue) with a delay of ∼30 to 45 min at an overall amplitude that is about 1/7 of the original amplitude.

The additional insulation of the FOCES box gives rise to a time offset with respect to the room temperature of ∼4 h. However, this is just a rough ballpark estimate, as the temperatures in the box (Fig. 3.1, orange) are extremely washed out, making it hard to identify any features for the measurement. An estimation of the damping factor was not possible due to the overall additional drift that was picked up by the sensors in the box.

Short-term stability

> "Single exposures of a science object with [...] [MaHPS] typically have exposure times between 15 to 30 min. The limit on the shorter end is given by the brightness of the target stars, whereas the upper limit was determined as a trade-off between detector specific noise and the expected signal strength from faint stars. The simultaneous calibration method does not allow to trace systematic shifts of the spectrum on the CCD during one exposure, so a good intrinsic stability of the spectrograph on the timescale of one exposure is desired.
>
> Figure 3.2 shows an example for the typical temperature (top) and pressure (bottom) variations in the FOCES spectrograph tank during one night of observation. Setting 4 from Tab. 3.1 was used for this measurement, when the temperature in the room and the tank were actively controlled and the temperature control in the box was inactive. The temperatures shown in the top panel were measured with the sensors mounted at the grating [3B-2] (orange) and between the two collimating mirrors [3A-2] (dark blue) and read out by the temperature controller that is not connected to the heating mats (Fig. 2.8, [light] gray controller). Additionally, the room temperature (light blue) is plotted, for which the data was obtained with the PT100 sensor outside of the tank [3D-1] from the controller actively regulating the temperature in the tank.
>
> During the 12 h of measurement, the temperature at the grating (Fig. 3.2 top, orange) has a peak-to-valley variation of (0.0022 ± 0.0005) K. It exhibits a slow overall drift of $\sim$0.0015 K, along with faster variations that have an amplitude of $\sim$0.0006 K at periods of around 30 min. There are also very fast changes of the measured temperature with periods of only a few minutes and amplitudes of $\sim$0.0002 K. Although it might appear as noise, these are real temperature fluctuations caused by the temperature regulation input of the temperature controller.[7]
>
> The temperature between the collimating mirrors (Fig. 3.2 top, dark blue) shows similar behavior to the temperature at the grating. Its overall drift amounts to $\sim$0.0014 K with a slightly different trend in time. The 30 min variations have a significantly larger amplitude [compared to the variations at the grating] of $\sim$0.0012 K, particularly at the beginning of the series. Also, the very short fluctuations are more pronounced with $\sim$0.0004 K. This might indicate that the heat transport, most likely due to mixing processes in the air, is more efficient at the collimating mirrors, while the surrounding of the grating is thermally more inert. A comparably large volume of free air is available at that part of the optical bench, whereas the grating and its mounting, along with the heat shield, might decrease the efficiency of the heat exchange at the other end of the optical bench. The range of temperatures plotted for the grating and the

[7]This statement is a result of a direct comparison of the temperature measurement curve with the controller input power on short timescales.

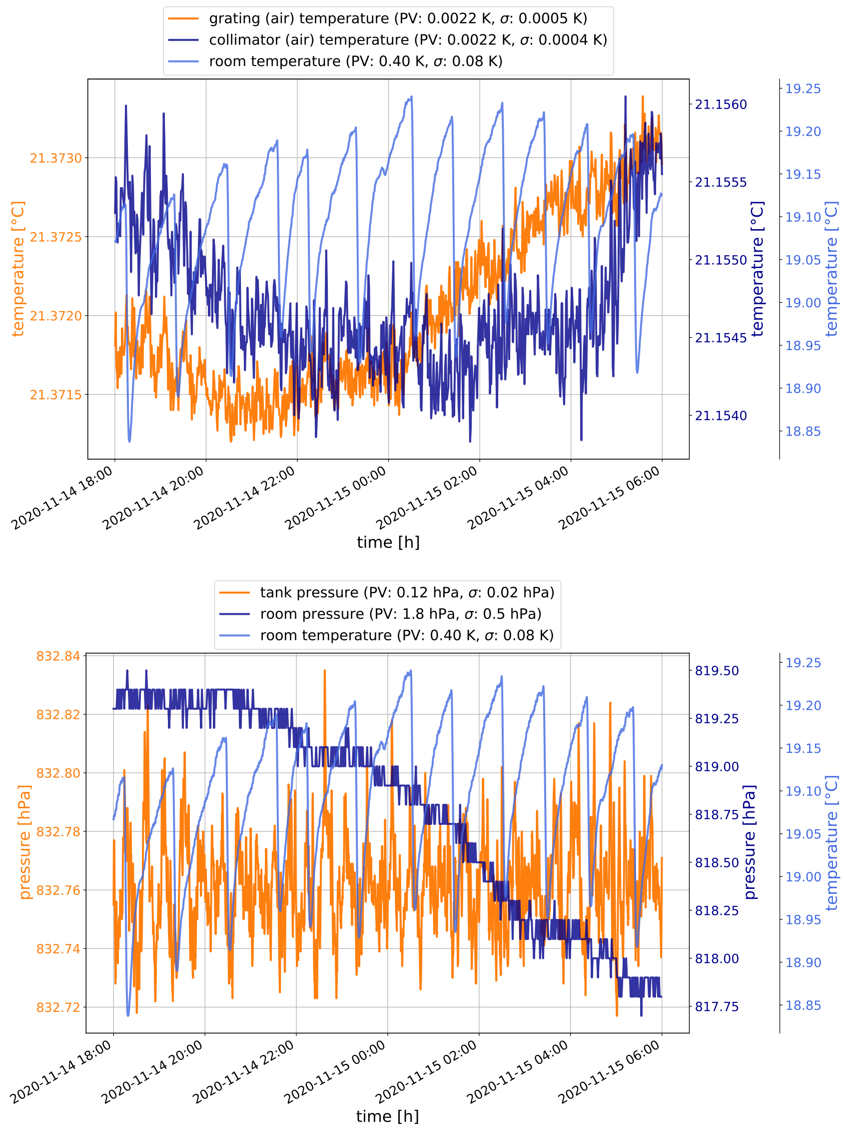

Figure 3.2: "Temperature and pressure time curve over 12 h during a night of observation. Top: Air temperature measured at the grating [3B-2] (orange), between the two collimating mirrors [3A-2] (dark blue), and the room temperature [3D-1] (light blue). For better comparison, the temperatures at the grating and the collimators are plotted using the same scale with an offset. Bottom: Pressure measured inside the FOCES tank [CPG2500] (orange), environmental pressure in the spectrograph room [WUT-room] (dark blue), and the room temperature [3D-1] (light blue). The peak-to-valley (PV) variation and the standard deviation of the measured values in the displayed time interval are given in the legend. Setting 4 from Tab. 3.1 was used for this measurement, when the temperature in the room and the tank were actively controlled and the temperature control in the box was inactive." Excerpt from Fahrenschon et al. 2020, p. 9.

collimator sensor in Fig. 3.2 (top) were chosen as equal, to allow for better visual comparison. Only an offset of the two scales is used to account for the lack of absolute calibration of the sensors.

The room temperature (Fig. 3.2 top, light blue) is controlled with a peak-to-valley variation of 0.4 K and periods between 45 to 90 min. There are no hints of the signature of the room temperature in the temperature sensors in the box, indicating that there is no thermal coupling of the spectrograph to the room temperature at this timescale.

In the bottom panel of Fig. 3.2, the orange curve shows the pressure inside the tank as measured by the high resolution sensor independent of the control loop [CPG2500] (see Fig. 2.14). The pressure in the spectrograph room (dark blue) was measured by the low resolution sensor available in the room [WUT-room].

The pressure inside the spectrograph tank is controlled to a total variation of (0.118 ± 0.017) hPa. Variations of about 30 min, like the ones seen in the temperatures, dominate the amplitude of the pressure fluctuations. The higher-frequency variations on timescales of few minutes only have an amplitude of $\sim$0.02 hPa. Although the pressure in the room changes by 1.8 hPa during the 12 h of this measurement, there is no drift visible in the tank on this timescale.

The temperature variations shown here satisfy the requirements from Tab. 2.2 well, although various forms of drifts and variations are present. The pressure controls in the tank are missing their specification slightly with variations that are on the timescale of one exposure or shorter. This could potentially be a source for small systematic errors in the RV determination, because shifts of the spectrum on the CCD during a single exposure cannot be resolved with the simultaneous calibration method.

Using active control of both temperature and pressure levels in a closed volume results in the coupling of both control loops. The variations with very short periods on the order of a few minutes are caused by this coupling of the temperature and pressure control systems. However, if the variations are fast enough and have overall drifts well below the specifications in Tab. 2.2, no overall shift of the spectrum is expected in one exposure. Since our control setup satisfies this, the precision of the RV measurements of single exposures should not be affected in a significant way." Excerpt from Fahrenschon et al. 2020, pp. 8–10.

Long-term stability without HLE

"RV observations for exoplanet science are typically not carried out with a few nights of observation, but require observing the same object repeatedly over an extended period of time. This is especially important when looking for Earth-like planets with periods on the order of hundreds of days.

In Fig. 3.3 the stability of the temperature (top) and pressure (bottom) over a total of 42 days [. . .] [is] shown.[8] The structure and content of the plots is equivalent to Fig. 3.2.

The temperature at the grating [3B-2] (Fig. 3.3 top, orange) is stable to a level of 0.045 K. The temperature variation between the collimating mirrors [3A-2] (dark blue) has a smaller amplitude of only 0.033 K. In general, the curve of the grating temperature shows less sharp edges than the temperature at the collimators when there is a sudden change of the temperature drift. When the temperature has a clear drift for several days, the slopes of the grating temperatures are steeper than those of the collimator temperatures. This fits together well with the behavior on short time scales and the impression that at the grating temperatures are more inert.

The room temperature [3D-1] (Fig. 3.3 top, light blue) changes by 2.3 K in the shown period. The parts of the room temperature curve that appear as a thin line were times when the room temperature dropped below the regulation range limit of the air conditioning unit. At the other times, the regulation pattern of the air conditioning unit is not resolved in this plot and appears as broader or more noisy line. The room temperature is affected by the outside temperatures and general weather conditions at the observatory because of the spectrograph room's comparably exposed location. In the second half of this measurement, a sudden and short spur of the room temperature can be seen. This was caused by a person doing maintenance works in the spectrograph room for about 5 h.

On the depicted timescale of 42 days, the temperatures in the spectrograph clearly follow the room temperature trends. However, as already shown in Fig. 3.2 (top), these drifts in general are slow and on the order of several hours.

The pressure stability inside the spectrograph tank [CPG2500] (Fig. 3.3 bottom, orange) is measured to be (0.490 ± 0.033) hPa. The amplitude of the peak-to-valley variations is dominated by a number of events when the pressure in the tank experienced a sudden increase or decrease and was quickly corrected by the controller. Most of the time, the pressure varies with an amplitude of $\sim$0.1 hPa and an overall drift of $\sim$0.06 hPa. The pressure in the room [WUT-room] (dark blue) has a total variation of 24.5 hPa, reflecting the outside weather conditions. The behavior of the pressure in the tank does not appear to be correlated with the room pressure at this timescale.

Both the temperature and the pressure controls do not meet the stability specified in Tab. 2.2 on a timescale of several weeks. Since the variations are slow, calibration exposures at the beginning of each night should be able to account for that behavior." Excerpt from Fahrenschon et al. 2020, p. 10.

Furthermore, as the working requirements from Tab. 2.2 contain conservative safety

[8] This measurement was taken before the activation of the HLE unit.

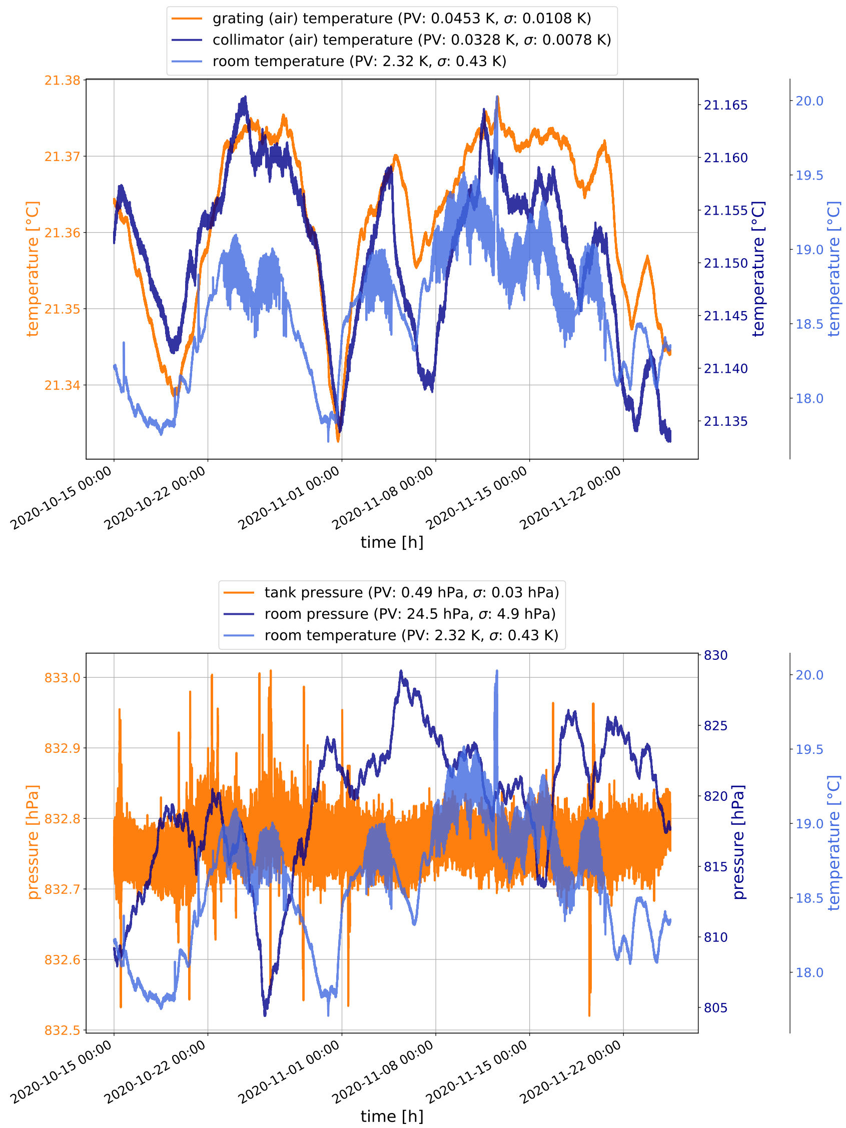

Figure 3.3: "Temperature and pressure time curve over 42 days. Top: Air temperature measured at the grating [3B-2] (orange), between the two collimating mirrors [3A-2] (dark blue), and the room temperature [3D-1] (light blue). For better comparison, the temperatures at the grating and the collimators are plotted using the same scale with an offset. Bottom: Pressure measured inside the FOCES tank [CPG2500] (orange), environmental pressure in the spectrograph room [WUT-room] (dark blue), and the room temperature [3D-1] (light blue). The peak-to-valley (PV) variation and the standard deviation of the measured values in the displayed time interval are given in the legend. Setting 4 from Tab. 3.1 was used for this measurement, when the temperature in the room and the tank were actively controlled and the temperature control in the box was inactive." Excerpt from Fahrenschon et al. 2020, p. 11.

margins, missing the temperature and pressure control requirements doesn't necessarily result in falling short of the RV stability goal.

The length of the shown measurement of 42 days was chosen as it was a period without any interruptions of the control loops, e.g. by maintenance works. Nevertheless, it is representative also for other periods of time. An exception are disturbances like restarts of the control systems, after which further observations are delayed for a brief period until the typical stability level is reached again.

Long-term stability with HLE2

Figure 3.3 illustrates the need of additional heat dispersion to reach a better regulation behavior of the AC unit for the room temperature. The measurement was taken during a time when outside temperatures were already low, but when HLE1 was not activated yet. In Fig. 3.4, an analogous measurement of 38.5 days at a later time is shown, immediately after HLE2 was installed, with a dissipated heat load of 700 W.

The variation of the grating temperature (3B-2, Fig. 3.4 top, orange) has an amplitude of 0.052 K, while the temperature amplitude at the collimators (3A-2, dark blue) is slightly less with 0.043 K. The room temperature (3D-1, light blue) varies with 2.3 K and continuously shows the characteristic regulation pattern of AC V2, which appears in the plot as broadened line. This demonstrates that HLE2 is indeed fulfilling its purpose to keep the AC unit inside the limits of its working range.

The stability of the pressure in the tank (CPG2500, Fig. 3.4 bottom, orange) is measured to be 0.50 hPa despite the room pressure variation (WUT-room, dark blue) of 29.2 hPa. For both the pressure and the temperature control, the conclusions drawn from the measurement without HLE are also valid here.

In direct comparison with the measurement shown in Fig. 3.3, the temperature and pressure variations obtained after the installation of HLE2 are slightly larger, but still on a similar level. Bearing in mind that the data series without any HLE is from late autumn, while the HLE2 measurement was taken in a sunny spring, the small disagreement may well be due to the considerable difference in outside conditions. In general, it could be noticed that the stability of the temperature and pressure control loops tends to downgrade slightly in hotter outside conditions. However, the differences are still acceptable and summer is anyways not the main observing season at the Wendelstein observatory, since extremely short nights and frequent unfavorable weather conditions naturally put a limit to the available observation time.

Both from Fig. 3.3 (bottom) and Fig. 3.4 (bottom), the impression of a correlation between the pressure (dark blue) and the temperature (light blue) in the room arises. The delay between the two is on the order of 40 to 60 h. When looking at the top panels, it becomes obvious that the same behavior is also imprinted on the temperatures inside the FOCES box, although with a largely dampened amplitude.

A check of the data collected by the meteorological station of the observatory shows that the room pressure and the outside pressure are identical, with basically no delay or damping between the two, as would be expected. The outside temperature follows the

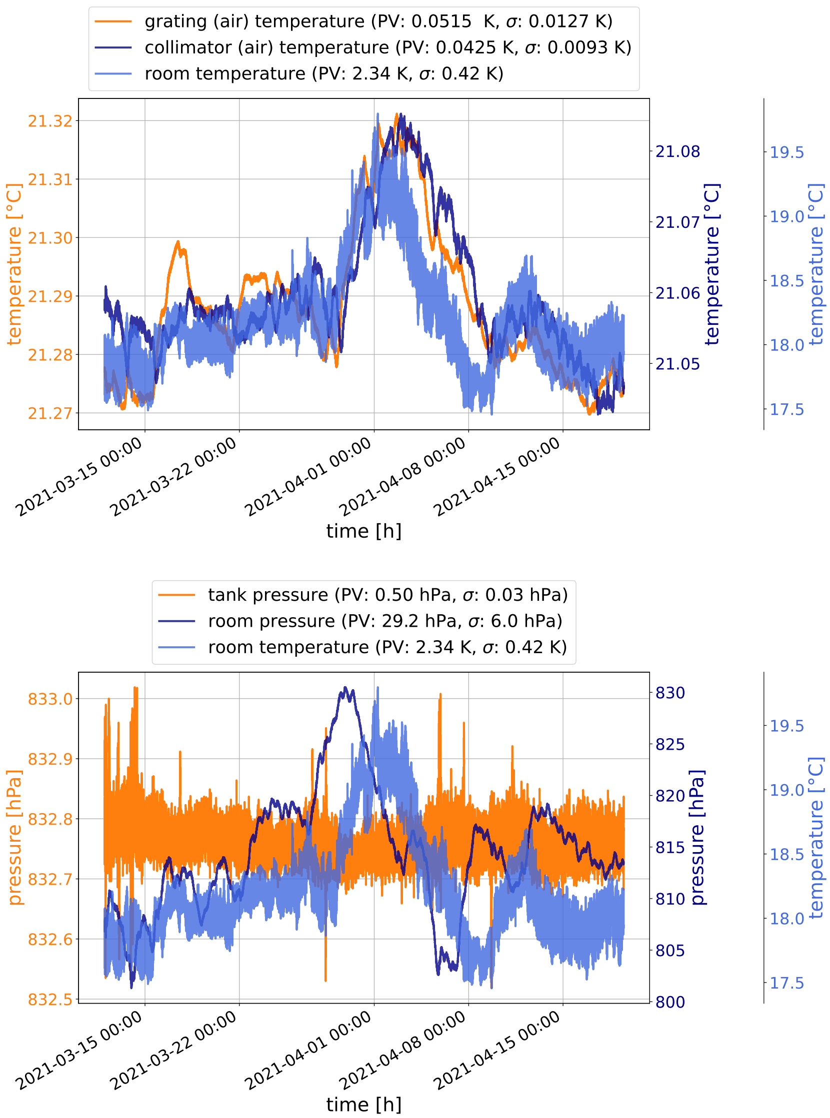

Figure 3.4: Temperature and pressure time curve over 38.5 days. In addition to Fig. 3.3, HLE2 was active and dissipating heat with a power of 700 W. Top: Air temperature measured at the grating [3B-2] (orange), between the two collimating mirrors [3A-2] (dark blue), and the room temperature [3D-1] (light blue). For better comparison, the temperatures at the grating and the collimators are plotted using the same scale with an offset. Bottom: Pressure measured inside the FOCES tank [CPG2500] (orange), environmental pressure in the spectrograph room [WUT-room] (dark blue), and the room temperature [3D-1] (light blue). The peak-to-valley (PV) variation and the standard deviation of the measured values in the displayed time interval are given in the legend. Setting 4 from Tab. 3.1 was used for this measurement, when the temperature in the room and the tank were actively controlled and the temperature control in the box was inactive.

overall pressure trend with an offset of about 24 h and the temperature of the FOCES room follows after that, with a total delay of 40 to 60 h relative to the outside pressure variations. The room temperature trend in turn affects the FOCES box temperatures at the collimator and grating, which show a typical offset on the order of 12 to 24 h relative to the room temperatures.

This finding also explains why the short-term stability measurement (Fig. 3.2) does not seem to be affected by the temperature correlations and at the same time underlines the importance of the daily wavelength calibration. Furthermore, compared to the measured temperature variation propagation without any temperature control in the tank and box (Fig. 3.1), a stability improvement is clearly seen. The difference of the time delays implies that the temperature drifts measured with active temperature control are caused by the controller, which cannot completely compensate the variations at such long timescales because of the enormous thermal inertia of the FOCES box.

The primary cause for these relations lies in the weather, since high pressure conditions are usually accompanied by higher temperatures than low pressure conditions. The delay between the two phenomena is due to the different timescales on which the pressure and temperature exchanges happen. The thermal inertia of the spectrograph room's walls and the rock surrounding it give rise to the additional delay of the room temperature with respect to the outside temperature. Furthermore, the temperature variations in the room are already dampened by a factor of $\sim$10, which is partly due to the AC unit and partly to the natural insulation.

As these slow temperature drifts are not visible at a significant level in the temperature sensors that are mounted inside the FOCES tank (3C-1 and 3C-2), the behavior of the sensors at the grating and the collimators could be a hint to a mechanism that thermally couples the FOCES box directly to the room temperature. One possibility of heat transport might be the rail mount onto which the optical table of the spectrograph is attached, since the rails are fastened directly to the tank structure. However, thermally isolating the optical bench mount is not feasible, as insulation materials typically cannot support the large weight of the optical bench. Nevertheless, as long as the drifts are slow and the amplitude is small enough, a good overall RV stability can be achieved with regular calibrations.

3.2.2 Wavelength Shifts With Temperature

> "It is crucial to understand how temperature variations of the air or of mechanical or optical components in the spectrograph can cause an imprint on the measured RV signals. Measurements with [...] [the *ThAr*] calibration lamp were made with different settings of the temperature control system to check how the spectrograph reacts to temperature variations." Excerpt from Fahrenschon et al. 2020, p. 10.

The characteristics of a *ThAr* lamp are described in Sec. 1.2.5. For the following measurements, the *ThAr* lamp was chosen to be used over the LFC with the better intrinsic precision for several reasons: First, due to its extreme intrinsic brightness, it allows to take spectra with a higher cadence than the LFC. Second, the analysis of the collected data is more straightforward, since the wavelength identification of each line is given unambiguously by the line distance and intensity distribution. Additionally, taking long exposure series degrades the PCF of the LFC quickly, which significantly shortens the lifetime of the PCF, ultimately resulting in a failure of the LFC and necessary maintenance by a specialist.

> "The analysis of the shifts of the *ThAr* spectra presented in the following was made in several steps. First, the wavelength calibration for all frames in one series was obtained with the General Astronomical Spectra Extractor[9] [...] [(GAMSE)] (L. Wang et al. 2016, 2017). For that, the optimum wavelength solution was determined in the first three frames of the series, then this solution was applied to all other frames. In the same step, the 2D echelle spectrum was extracted to individual 1D line spectra for each echelle order. Second, the shift of each individual order was obtained by computing the cross-correlation function[10] (CCF) with the corresponding order of a reference file, which [...] [was chosen] to be the first exposure of each series. A Gaussian function was then fit to the CCF peak to obtain the position of the maximum of the CCF and thus the shift of the spectrum. The shifts of all orders were then converted to RV units. Finally, for each exposure the RVs of all orders were combined to a weighted mean value, with each order's result weighted by the error of the fit to the CCF function. The scatter between all orders gives the error bars for each exposure." Excerpt from Fahrenschon et al. 2020, p. 12.

Open tank environment

> "A 1.75 h series of measurements with the *ThAr* lamp was made when the FOCES tank was open because of work on the hardware. Setting 2 from Tab. 3.1 was used, meaning that [...] [AC V1] was used for active control of the room temperature, all other temperature control loops were inactive.[11] Exposures of the *ThAr* spectrum were taken every 98 s with an exposure time of 1.2 s, while the temperature sensors were read in a 3 s interval.
>
> Figure 3.5 shows the resulting spectral shift of the *ThAr* exposures (orange). The individual data points of this series are connected by a line in order to highlight the overall trend. The room temperature (light blue) and the air temperature measured inside the spectrograph box at the grating (dark blue) are also shown.

[9]GAMSE is a software package for the automated reduction, *ThAr* wavelength calibration and 1D extraction of the raw CCD frames produced by MaHPS. It was developed and implemented by L. Wang. See Sec. 4.1 for a more detailed description.

[10]Section 4.2 gives a thorough description of the CCF method.

[11]As the tank was not closed, also the pressure control was inactive.

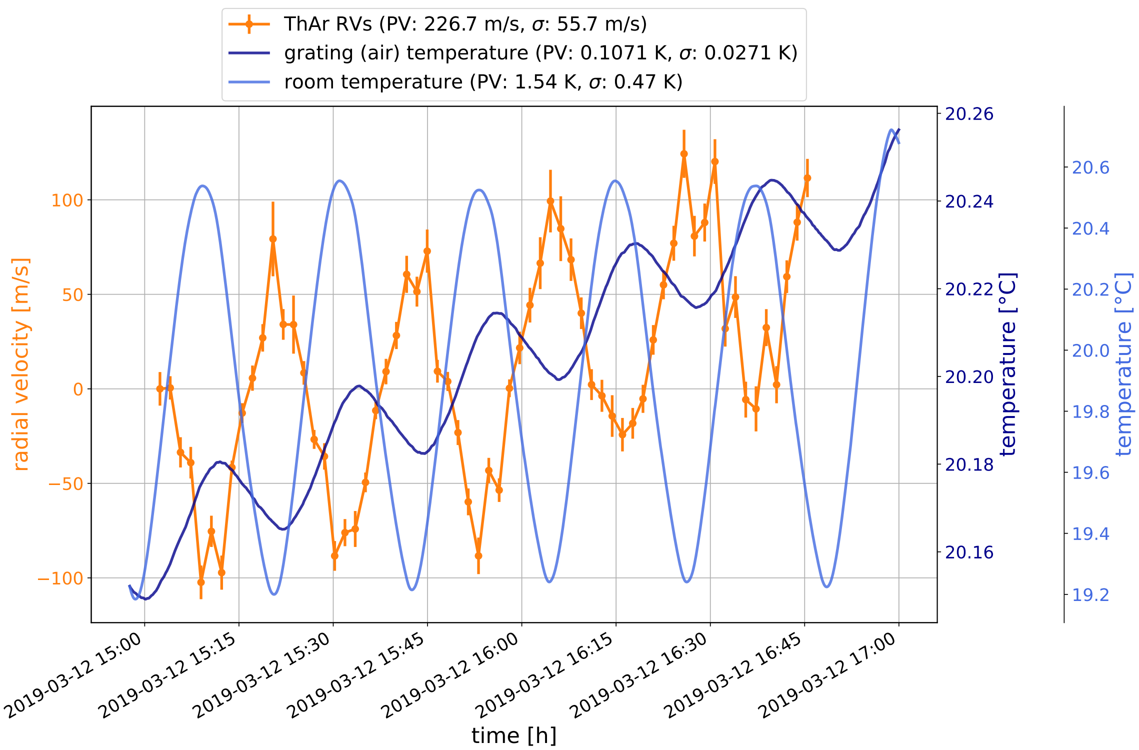

Figure 3.5: "Drift of the spectrum of a *ThAr* lamp on the spectrograph's CCD detector (orange circles), compared to the behavior of the air temperature at the grating [3B-1] (dark blue line) and the room temperature [3D-1] (light blue line) over 2 h. The shift of the weighted average of all echelle orders of each individual exposure is given in RV units, relative to the first exposure. The peak-to-valley (PV) variation and the standard deviation of the measured values in the displayed time interval are given. Setting 2 from Tab. 3.1 was used for this measurement, when the spectrograph tank was open and only the room temperature was actively controlled." Excerpt from Fahrenschon et al. 2020, p. 13.

The room temperature [3D-1] (Fig. 3.5, light blue) shows a very regular variation with an amplitude of 1.54 K and a period around 20 min. The temperature at the grating [3B-1] (dark blue) exhibits an overall drift of 0.11 K, that is modulated by a signal with the same period as the room temperature. The amplitude of this signal is ∼0.02 K and appears to have a small lag in time relative to the room temperature. The behavior of the shift of the *ThAr* spectrum again shows the same period, at an amplitude of about 150 to 180 m/s, where the *ThAr* spectra experience an additional redshift when the room temperature is falling. The *ThAr* spectrum also seems to be subject to an overall drift of ∼50 m/s in total.

The similarity of the periods measured with the temperature sensors and in the *ThAr* spectra in Fig. 3.5 is a strong evidence for a direct correlation between the spectral shifts and the temperature changes. Considering that the grating temperature and the spectral shifts experience an overall drift in the same direction, it is likely that there is a time delay between the temperature variation and the spectral shift, rather than the two behaviors being anti-correlated. The time delay seems to be of the order of ∼10 min, but the possible addition of any number of natural multiples of the period to the delay [cannot] be excluded from this measurement.

The presence of the time delay between the temperature and the spectral variation suggests that the root cause for the spectral shifts does not lie in the air temperatures directly. Mechanical movements due to temperature changes of the grating or its mounting are more probable, because their thermal inertia would result in a delayed reaction on air temperature variations.

This measurement reinforces the argument that temperature stabilization is needed for reliable RV measurements. If the spectrograph would be operated in this configuration, the precision of a single exposure of ∼30 min would be on the level of about 100 to 200 m/s. Simultaneous calibration with the AFC would not be able to improve the measurement quality in this case." Excerpt from Fahrenschon et al. 2020, p. 12.

Three layer temperature control

"All three layers of [...] [the] temperature control concept are actively controlled during the measurement presented here. Using the temperature control setting 1 from Tab. 3.1, consecutive exposures of the *ThAr* spectrum with exposure times of 1.5 s were recorded with a cadence of 218 s in a total of 10 h. The readings of the temperature sensors were logged with a 3 s interval.

The shifts of the *ThAr* spectra are shown in Fig. 3.6 (orange), along with the room temperature [3D-1] (light blue) and the temperature at the grating [3B-2] (dark blue). The spectral shift amounts to 57 m/s and is completely due to a slow drift. The room temperature is controlled to an amplitude of 1.2 K and

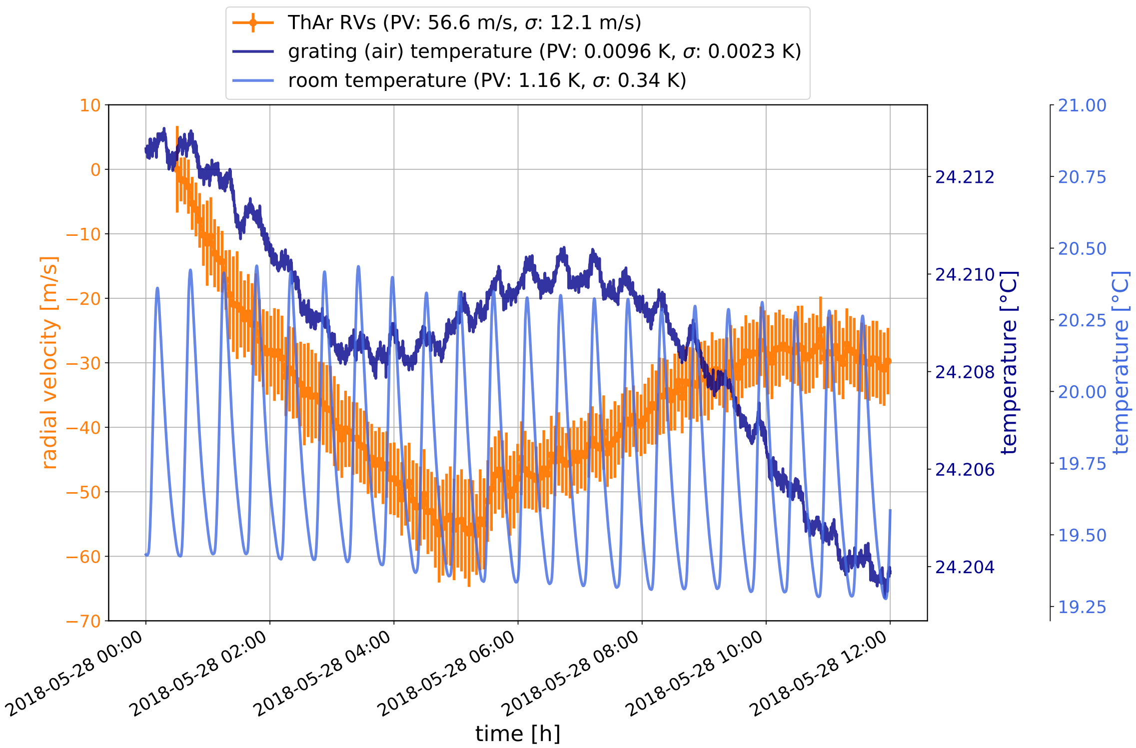

Figure 3.6: "Drift of the spectrum of a *ThAr* lamp on the spectrograph's CCD detector (orange circles), compared to the behavior of the air temperature at the grating [3B-2] (dark blue line) and the room temperature [3D-1] (light blue line) over 12 h. The shift of the weighted average of all echelle orders of each individual exposure is given in RV units, relative to the first exposure. The peak-to-valley (PV) variation and the standard deviation of the measured values in the displayed time interval are given. Setting 1 from Tab. 3.1 was used for this measurement, when the temperatures of the room, the tank and the box were all actively controlled." Excerpt from Fahrenschon et al. 2020, p. 14.

shows a similar overall behavior as in Fig. 3.5. The grating temperature experiences a total temperature change of 0.01 K in a long overall drift. Additionally, shorter variations with amplitudes of ∼0.0008 K at a period of ∼30 to 40 min are measured.

The short variations of the grating temperature (Fig. 3.6, dark blue) coincide with the variations of the room temperature (light blue) and therefore most probably are directly related. The amplitude of these variations in the grating temperature is damped by more than three orders of magnitude, compared to the room temperature amplitude.[12] In the *ThAr* spectra, no shifts with significant amplitudes are apparent at this timescale, indicating that the spectral shift is not coupled to the room temperature at the 10 m/s level of precision.

[12]This measurement shows that the design goal of the shell structure, which is to provide damping of

A correlation is possible between the drift of the *ThAr* spectra (Fig. 3.6, orange) and the grating temperature. The spectral shift could be a smoothed and delayed version of the overall slow drift of the grating temperature. This strengthens the impression from Fig. 3.5 that the shifts in the spectra are caused by more thermally inert components than the air in the spectrograph. However, with the measurement shown here a clear confirmation of this correlation is not possible.

The behavior of the temperature at the grating shown here fulfills our requirement of <0.01 K (Tab. 2.2). In total, the drift of the *ThAr* spectra is a smooth and slow curve with a RV variation between 3 to 12 m/s on the 30 min timescale. However, from this measurement it is not possible to confirm whether the RV stability goal of ≤1 m/s during a single exposure can be reached with this temperature control concept. The reasons for this are the intrinsic precision limits of the *ThAr* lamp and the definition of the stability requirement, which is based on the simultaneous calibration method with the AFC." Excerpt from Fahrenschon et al. 2020, pp. 12–14.

Two layer temperature control

"A third *ThAr* lamp exposure series was made using setting 3 from Tab. 3.1. This represents a configuration with only two layers in which the temperatures are actively controlled. The innermost layer, the FOCES box, stabilizes its temperature only by the insulation layers towards the surrounding layer (the FOCES tank). The series has a duration of 12 h, the exposure time for the *ThAr* frames was 3.5 s and a time interval of 306 s was chosen between individual exposures. The readout interval of the temperature sensors is 3 s.

In Fig. 3.7, the shift of the *ThAr* lines on the detector (orange), the room temperature [3D-1] (light blue) and the temperature at the grating [3B-2] (dark blue) are given. The spectral shifts amount to 50 m/s in a relatively slow drift behavior. The grating temperature exhibits an overall drift of 0.020 K, while the room temperature varies with an amplitude of 1.7 K. In this measurement, the behavior of the room temperature differs from that in the previous measurements (Fig. 3.5 and Fig. 3.6). The regular pattern of the temperature is interspersed with phases when the temperature is drifting away to lower values. This is due to the fact that the [...] [AC V1], which was in use during this measurement, reached the limit of its operation range.

The spectral shifts (Fig. 3.7, orange) seem to follow the overall trend of the room temperature (light blue), with a delay of about 30 min. The shorter temperature variations with a period of around 30 min do not seem to affect the spectral shift much, at least at the level of precision of a *ThAr* lamp. The temperature

the temperature variations by a factor of 10 for each shell (Sec. 2.2.3), is easily fulfilled.

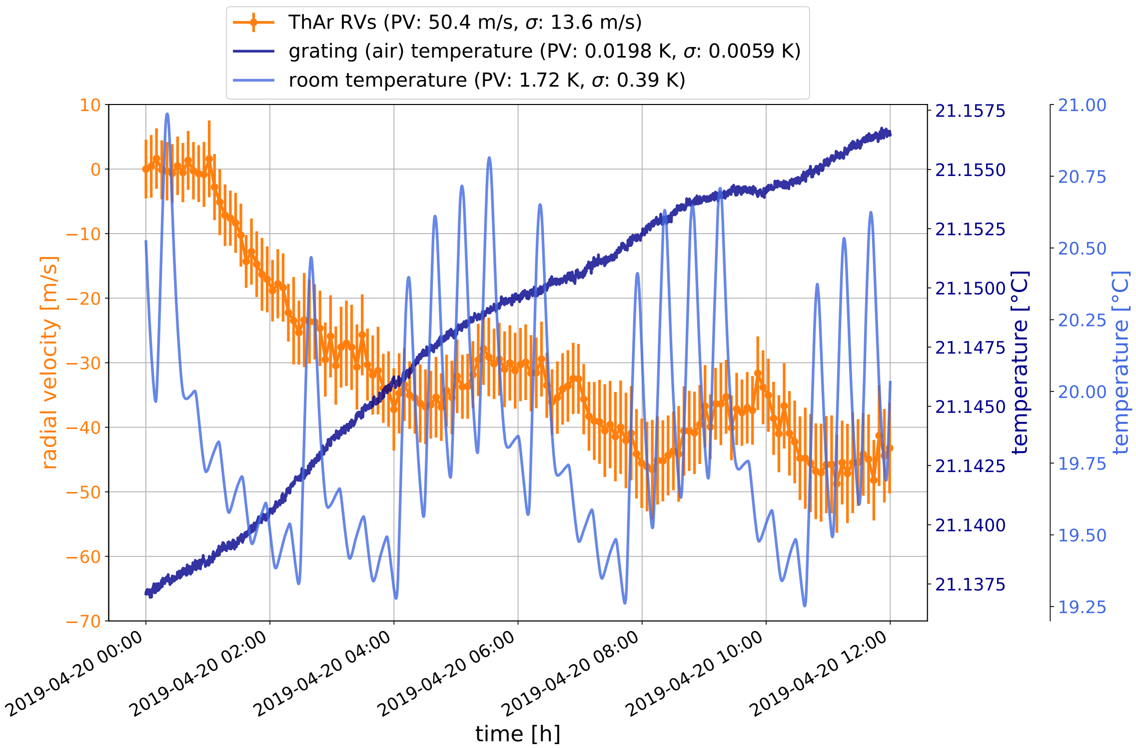

Figure 3.7: "Drift of the spectrum of a *ThAr* lamp on the spectrograph's CCD detector (orange circles), compared to the behavior of the air temperature at the grating [3B-2] (dark blue line) and the room temperature [3D-1] (light blue line) over 12 h. The shift of the weighted average of all echelle orders of each individual exposure is given in RV units, relative to the first exposure. The peak-to-valley (PV) variation and the standard deviation of the measured values in the displayed time interval are also given. Setting 3 from Tab. 3.1 was used for this measurement, when the temperature in the room and the tank were actively controlled and the temperature control in the box was inactive." Excerpt from Fahrenschon et al. 2020, p. 15.

at the grating (dark blue) is not showing any similarities or possible correlations with the room temperature, nor with the RV shifts.

The grating temperature seems to be decoupled from the apparently correlated drifts in room temperature and spectral shift. This suggests that there might be a heat transport process affecting the spectrograph's stability other than by mixing of the air inside the tank, e.g. a direct thermal contact of the optical bench to the outside of the spectrograph tank.

The drift of the grating temperature in this configuration (setting 3) is clearly larger than the specification from Tab. 2.2. However, the *ThAr* shifts are slower and about 10% smaller than those measured with temperature setting 1 (Fig. 3.6). The shifts on the timescale of a single exposure are between 2 to 10 m/s, but also here a final confirmation of the RV stability requirement is not possible because of the limited *ThAr* precision.

All in all, the thermal exchange between the FOCES box and the tank appears to be a slow process because of the several layers of insulation and the high thermal load inside the FOCES box (optical bench and large optics). This allows for a short-term stability near the precision limit of the *ThAr* lamp, especially on the timescale of single exposures during an observation. In all of these measurements, no correlation with the pressure control in the spectrograph could be seen. Therefore, we can assume that the pressure stability is not affecting the RV measurements at precisions on the 10 m/s scale, although the values of the requirements (Tab. 2.2) are exceeded by about 20%." Excerpt from Fahrenschon et al. 2020, pp. 14–16.

3.2.3 LFC Calibration Stability

The previous measurements demonstrate that the intrinsic RV precision limitations of the *ThAr* lamp do not allow to probe the $\leq$1 m/s precision regime. To verify that this precision can indeed be reached by simultaneous calibration with the LFC[13], dedicated measurements were made and are presented in this section.[14]

"The wavelength calibration of the AFC spectra is obtained in several steps with the [Munich Analyzer for Radial Velocity Measurements with B-spline Optimized Templates[15] (*MARMOT*) software package (Kellermann 2021; Kellermann et al. 2020)]: A reference *ThAr* exposure is used to identify the wavelength of each single AFC emission line in the first frame of a series. Then, the line

[13]For details on the LFC and the simultaneous calibration method, see Sec. 1.2.5 and Sec. 2.2.2, respectively.

[14]The collection and analysis of the LFC data presented in this section were done by H. Kellermann. The creation of the figures and text from the publication, as well as the interpretation of the results is my own work.

[15]*MARMOT* is a software package for the LFC wavelength calibration and RV determination of MaHPS spectra that have been already reduced with the *GAMSE* software package. It was developed and imple-

position on the CCD chip is determined in all frames of the series relative to the position in the first (reference) frame. This step is done for all AFC lines independently. To obtain the shift of an echelle order, the mean of the shifts of the individual lines, weighted by the signal-to-noise ratio of the lines, is calculated. The mean of the results for all orders, weighted by the total flux in each order, gives the overall shift of a frame. " Excerpt from Fahrenschon et al. 2020, p. 16.

Calculating the error for the AFC spectrum is very time-consuming due to the large number of lines in the spectrum, which each have an individual error in the fit of the line position. Therefore, a conservative estimate for the errors, based on the typical spread of the RV shift between all echelle orders, is used for each AFC exposure. Furthermore, the errors in the determination of the emission line centers are dominated by photon noise rather than by changes of the line profile, because the intrinsic line width of the AFC is much narrower than the instrumental broadening, resulting in an approximately constant line profile even on long timescales.

The slit mask in front of the fiber ends of the science and calibration fiber features a different slit opening size for the two fibers, in order to ensure that the spectra are well separated on the CCD detector (Kellermann et al. 2016, 2019). Given that photon noise scales with the number of received photons, which is directly related to the light collection area, the error bars for the AFC spectra taken via the science or the calibration fiber need to be scaled accordingly. The area of the science fiber slit is larger than the area of the calibration fiber slit by a factor of 1.57, so the error bars of the calibration fiber data are inflated with this factor.

"In Fig. 3.8, a 5 h series of simultaneous AFC exposures is presented. Each frame was recorded with an exposure time of 120 s at an interval of 218 s. For better visualization of trends, the individual data points are connected by lines. In the top panel, the spectral shifts of the light from the science fiber (orange) and from the calibration fiber (light orange) are displayed separately. In the bottom panel, the difference of the two shifts (sci − cal) is depicted in orange. Both panels show the temperature measured at the grating [3B-2] (dark blue) and the pressure in the spectrograph tank [CPG2500] (light blue), which were recorded every 5 s. The temperature was controlled with setting 5 from Tab. 3.1 during the measurement, which corresponds to the two layer setup.

Both the science and the calibration fibers undergo the same overall drift (Fig. 3.8, orange). The amplitude of this drift is slightly larger in the science fiber (45.6 m/s) than in the calibration fiber (43.5 m/s). The grating temperature (dark blue) shows a drift of 0.0076 K, while the pressure in the tank (light blue) varies by 0.27 hPa. A correlation between the grating temperature and

mented by H. Kellermann. See Sec. 4.3 for a description of the functionalities utilized here and Kellermann (2021) for an in-depth presentation of *MARMOT*.

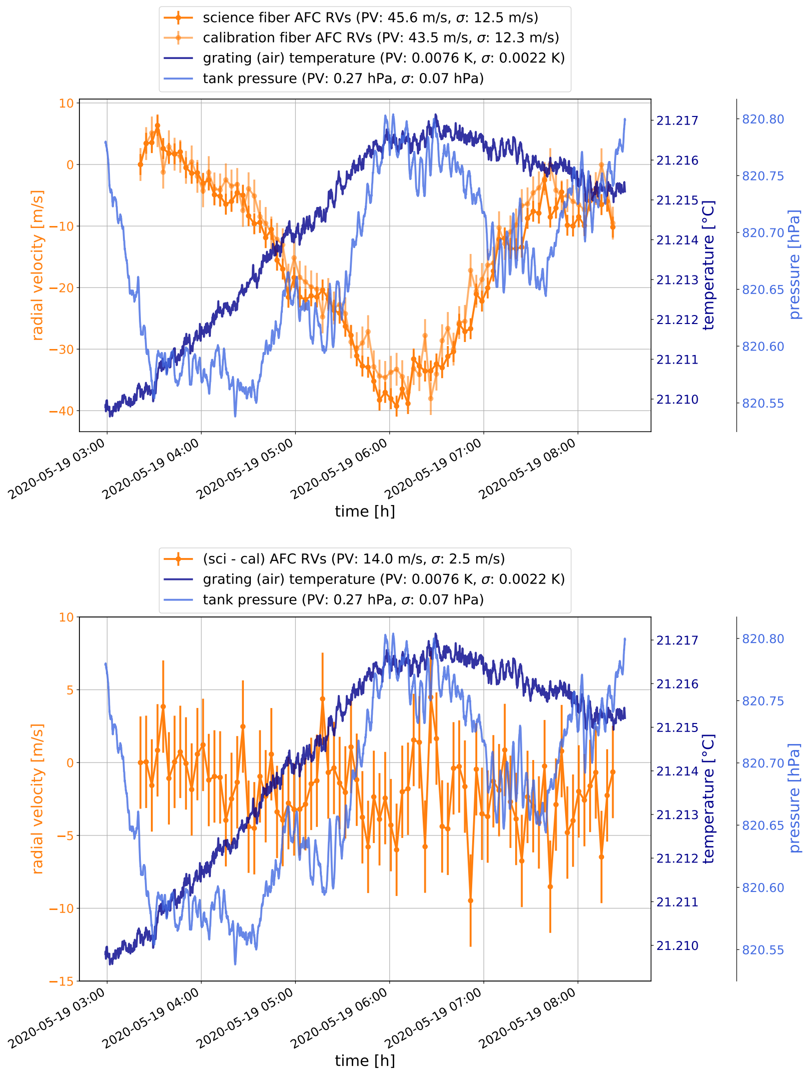

Figure 3.8: "Series of AFC exposures over 5 h, with light of the AFC fed into the science and calibration fiber simultaneously. The shift of the weighted average of all echelle orders of each individual exposure is given in RV units, relative to the first exposure. Top: shift of the spectrum from the science fiber (orange circles) and from the calibration fiber (light orange circles) on the spectrograph's CCD detector, bottom: difference (sci − cal) of the shift of the two AFC spectra (orange circles). Both panels: air temperature at the grating [3B-2] (dark blue line) and pressure in the tank [CPG2500] (light blue line). The peak-to-valley (PV) variation and the standard deviation of the measured values in the displayed time interval are also given. Setting 5 from Tab. 3.1 was used for this measurement, which corresponds to the two layer setup [and a deactivated pressure control.]" Excerpt from Fahrenschon et al. 2020, p. 17.

the spectral shift can neither be confirmed nor rejected from this measurement. The behavior of the pressure does not seem to be related to the RV shifts.

The difference between the science and calibration fiber (Fig. 3.8 bottom, orange) exhibits some scattering with an amplitude of 14.0 m/s [peak-to-valley]. Only a small overall drift of ∼2.5 m/s is visible, however that is not a significant finding considering the size of the error bars of 3.2 m/s. The scattering of the difference between the two fibers is mainly on the order of the error bars, but it seems that at the turning point of the overall spectral drift, the difference between the fibers has slightly larger absolute values. This could be an indication that the light paths of the two fibers are stable relative to each other when a drift is present, but behave slightly different when the environment changes. The turning point of the spectral shift coincides with the maxima of both the grating temperature (dark blue) and the pressure curve (light blue), but the presented measurements do not allow to distinguish whether one of the two is causing the spectral shift to change direction. Overall, the assumption that the shifts in both fibers exhibit the same behavior seems justified.

On the 30 min timescale of a single exposure of a scientific observation, a stability of the order of ∼3.2 m/s is achieved, which is limited by the scatter between individual orders. It should be noted that the real errors of one frame could be smaller, but an analysis of the actual error of the position of each single AFC line has to be made. If several consecutive exposures of a science object are made and combined, it is possible to reach the ≤1 m/s RV precision target." Excerpt from Fahrenschon et al. 2020, pp. 16–18.

Chapter 4

Data reduction

The MaHPS CCD camera produces unprocessed (*raw*) images in the common Flexible Image Transport System (FITS) format. Due to the technical characteristics of CCD detectors, some treatment of the raw images is required before they can be used for a scientific analysis. The term *reduction* is often used to summarize these steps, but may also include any subsequent treatment of the data, depending on the context.

In order to measure spectral shifts in wavelength or RV units, several more steps in addition to the basic CCD reduction are necessary: the individual one-dimensional(1D) spectrum[16] of each echelle order needs to be extracted from the 2D image frames, a wavelength calibration has to be made, and finally the shift of the spectra with respect to a reference has to be determined.

Several software packages were utilized in this work to obtain the final RV measurements from the raw CCD frames. This chapter gives an outline of the strategies, functionalities and algorithms of the employed packages.

4.1 GAMSE

The General Astronomical Spectra Extractor (*GAMSE*) is a software package which was developed in-house by L. Wang et al. (2016). The purpose of GAMSE is to obtain a 1D spectrum for each echelle order with a *ThAr* based wavelength calibration from the raw CCD frames. To this end, it comprises functions for the reduction of the raw FITS files, the extraction of the echelle orders to 1D spectra, and the wavelength calibration of the obtained spectra based on ThAr lamp exposures. Additionally, an error propagation of the measured fluxes in all spectra is made, the implementation of which was part of Kellermann (2021).

In this work, GAMSE is applied but no considerable contribution was made to the development and implementation. Therefore, only an outline of the data treatment by

[16] In this context, the term *1D spectrum* is used to describe a spectrum that gives a discrete flux distribution as function of wavelength bins, in this case given by the wavelength bins associated to each pixel along the dispersion axis.

GAMSE is given and the reader is referred to L. Wang et al. (2016, in prep.) and Kellermann (2021) for the necessary mathematical and statistical foundations, as well as any other details. Information necessary for the understanding of the presented processes for readers unexperienced with CCD image reductions is given in footnotes.

GAMSE was developed for the reduction of MaHPS data, initially carrying the name Echelle Data Reduction Software 2 (*EDRS2*), and is loosely based on the deprecated reduction pipeline *EDRS*, which was used for FOCES at the Calar Alto Observatory. Despite the well-defined application, GAMSE is programmed in a modular and flexible way to offer an easy adaption to other telescopes and instruments.

The primary use case for GAMSE is to run automatically after each night of observation without any user input. For this reason, the order of execution of the reduction steps as well as the parameters used in the reduction are fixed, which as a further benefit also guarantees the comparability of the collected data from different nights. It is however possible to tweak the parameters by the means of a configuration file, if a reduction deviating from the default is desired. Common instructions for the use of GAMSE are summarized by Kellermann (2021).

The overall reduction flow of GAMSE is shown in Fig. 4.1. For each night, the collected data are analyzed individually to produce the wavelength calibrated 1D spectra. To this end, all raw FITS frames of a given night get listed in the so-called *observing log*. The type of each exposure is automatically determined based on the filename[17] and the exposures are grouped accordingly into four groups:

- **Bias** frames: exposures with no illumination of the detector and exposure time 0 s,
- **Flat** frames: exposures of a flat lamp with a smooth (*flat*) black body spectrum without any prominent features,
- **ThAr** frames: exposures of the *ThAr* lamp as wavelength reference,
- **Science** frames: exposures that contain either or both light from the scientific object and the LFC.[18]

4.1.1 CCD reduction

Once the images are grouped, the classic CCD reduction steps begin. As these are standard processes in CCD imaging, plenty of general background information is available in the literature (e.g. Howell 2006), and only a basic description is given here. The specific formulations chosen for GAMSE are presented by L. Wang et al. (2016) and L. Wang et al. (in prep.).

[17]The filename of each MaHPS frame contains information about the frame type, encoded in a alphanumeric string code. The convention used for this code is documented in Kellermann (2021).

[18]Note that as GAMSE only performs a *ThAr*-based wavelength calibration, exposures of the LFC, even without any other scientific spectrum, are also considered as *science* frames.

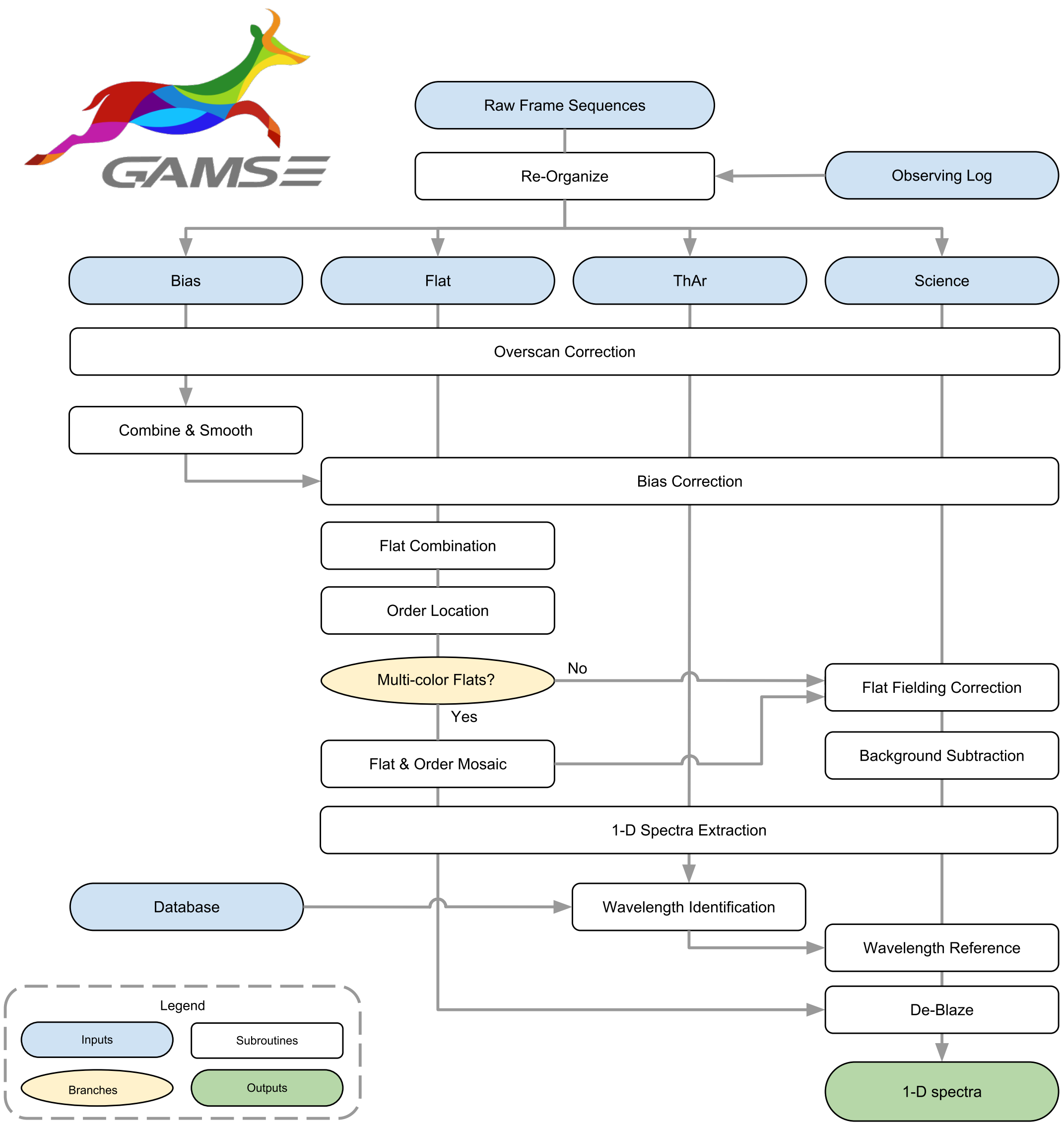

Figure 4.1: Flowchart of the GAMSE software for reduction of the MaHPS spectra. Graphic taken from Kellermann (2021).

Overscan and bias correction

As first step, the bias count level[19] is corrected in all exposures, regardless of their group, based on the count level in the overscan region of the detector.[20] After that, all bias frames are combined and subsequently smoothed with a 2D Gaussian kernel, which exposes the underlying bias structure[21], to obtain a so-called *master bias* frame. A correction for said structure is then applied to all frames of the three remaining exposure groups.

Flat treatment

As soon as the bias correction is done, the flat fielding process is started, which aims to compensate the intrinsic sensitivity differences between the individual pixels of the CCD chip[22] and correct for fringing effects caused by the detector coating.[23] A further purpose of the reduction of the flat exposures is the detection of the position of each individual order in the frame.[24]

Figure 4.1 illustrates the individual steps for the flat treatment: the flat exposures with identical exposure times are combined and used as base for the location of the echelle orders. The orders are curved and not distributed regularly in the image plane because of the prisms' dispersion characteristics and optical distortions of the CCD camera. Therefore, the position and shape of each order needs to be determined (*traced*), based on cross-sections through all orders at defined distances. Polynomials of second order are then used to describe the order locations.

As shown in Fig. 1.14, the effective throughput and thus the sensitivity of an echelle spectrograph depends on the wavelength and decreases drastically towards the blue wavelengths. Additionally, the black body temperature of the employed flat lamps usually lies well below the effective temperature of the observed stars, further decreasing the available signal in the blue regions. Therefore, the calibration strategy of MaHPS contains exposure series of the flat lamp with several different exposure times. The regions that are illumi-

[19] For technical reasons, a bias voltage is applied to the CCD detector, causing an elevated but exposure time independent count level for every pixel. This level typically shows a statistical variation, but also changes with time and detector temperature. Therefore, it has to be corrected for each frame individually.

[20] The overscan region is a part of the detector chip that contains regular pixels, but is covered in some manner, so that the isolated bias signal can be measured. In order to avoid contamination from the spill-over of nearby uncovered pixels and charge persistence effects, only the overscan which is read out before the rest of the image and restricted to the blue half of the detector is used.

[21] The structure of the bias arises from mechanical stress and other inhomogeneities over the detector area. For MaHPS it has a saddle-like shape, varies slowly with time and can be assumed to be constant for a single night, but not between different nights.

[22] Usually, when taking a flat exposure the whole CCD chip is irradiated homogeneously to correct the sensitivity variations over the complete detector area. However, as it is not possible to obtain such an image with MaHPS due to the dispersing elements, the flat lamp is instead illuminating all echelle orders and only the area covered by the orders is corrected.

[23] Especially at near-infrared wavelengths, the light falling onto a CCD detector suffers from strong interference effects with the coating, due to its finite thickness. See Kellermann (2021) for an example.

[24] The location of the echelle orders is specific to spectroscopic observations, it is not part of the classic CCD reduction but inserted here to reflect the structure of GAMSE.

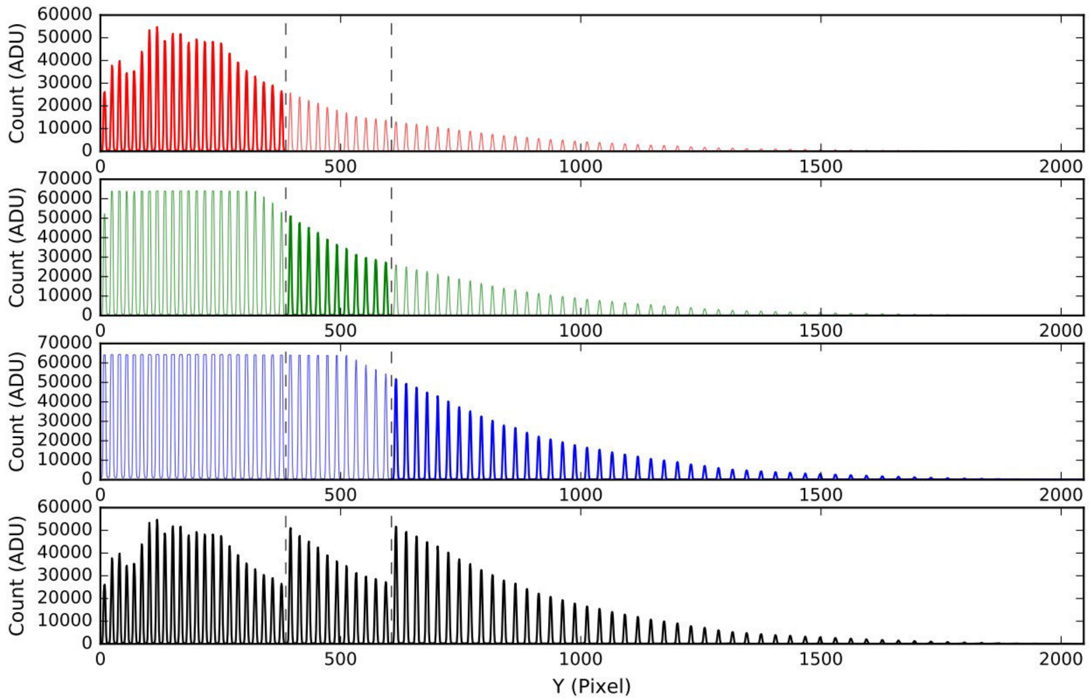

Figure 4.2: Illustration of the mosaic process for the master flat creation of GAMSE. Top three panels: central cross-section through all echelle orders of the combined flat frames with exposure times from short (red) to long (blue); bottom: central cross-section of the resulting flat mosaic. The dashed lines indicate the stitching borders. Orders with shorter wavelengths are located on the MaHPS detector at positions with higher y-axis pixel count. Graphic taken from L. Wang et al. (2016).

nated best are selected based on signal-to-noise ratio (SNR) measurements and stitched together to a mosaic along curved lines between the echelle orders (Fig. 4.2).

If flats with only one exposure time are available, the combination of those frames is used as *master flat*, otherwise the mosaic is chosen to act as master flat. Subsequently, the correction of the pixel-to-pixel variations with the master flat is carried out in all science frames. Regions of the science frames with particularly low signal level are excluded from the correction, because in those cases the relative error of the measured flux grows significantly (Kellermann 2021).

4.1.2 Spectroscopy-specific reduction

While the steps described above as classic CCD reduction are common to any data recorded with CCD detectors, exposures of echelle spectra need to undergo further treatment for their analysis. GAMSE features functions for the subtraction of a background of scattered light, for the extraction of spectra from 2D to 1D and for a first wavelength calibration.

Background subtraction

The information content of echelle spectra lies in the individual echelle orders, which are imaged on the detector. However, the detector also records light from any other sources, which may lie in between or overlap with the orders, in the worst case altering the measured fluxes and thus spectral line positions or depths. Stray light is the main cause for such a background signal, originating e.g. from scattering at imperfect optical surfaces or the surrounding mechanical components. The intermediate slit (Fig. 2.1) blocks a large amount of the stray light, but some scattered light still reaches the detector and requires dedicated treatment.

Since the distribution of the scattered light is smooth, GAMSE performs a background correction by modeling the shape and intensity of the stray light by the interpolation of brightness measurements between the orders. To reduce the influence of flux measurement errors, a two-stage smoothing of the obtained model is done.

The exact shape of the background model depends on the transmission characteristic of the atmosphere as well as the spectral type of the observed objects, so it is computed freshly each night for each individual object that was observed. To this end, a spectrum of each observed object without simultaneous wavelength calibration is needed. Once the wavelength-dependent brightness distribution model is obtained for a given object and observation date, it is scaled to the overall brightness of each single science exposure and subtracted.

It has to be noted that the background subtraction of GAMSE does not incorporate any correction of the sky background. While this was possible in the former FOCES setup featuring a dedicated sky fiber, this option was removed in favor of a better instrument stability. As a consequence, several conditions need to be met during an observation to safely neglect the sky background: the observed object should be at a safe distance[25] from the Moon, should not be near the horizon in twilight conditions, and conditions with increased atmospheric scattered light should be avoided, e.g. cloudy skies combined with strong moonlight.

Order extraction

For further use, the spectra of the individual orders are extracted, so that a 1D spectrum is obtained for each 2D order strip on the detector. To this end, GAMSE employs the extraction method developed by Horne (1986). The polynomial coefficients determined during the order location process are used to find the pixels belonging to a given echelle order, then the 2D region is collapsed in the cross-dispersion direction.

The collapsing of the orders is done by summing the row of pixels that is perpendicular to the dispersion direction. In principle, one should also take into account that due to the nature of echelle spectrographs, the image of the slit is slightly tilted with respect to the cross-dispersion direction and so are the spectral lines. However, if the tilt angle is

[25] The choice of the safety distance lies in the professional judgment of the observer, as it depends on the atmospheric conditions, the elevation of the Moon and the object, and other factors.

neglected, the extracted spectrum is slightly degraded in terms of resolution, but there is no RV measurement error introduced.

Since the edges of the orders usually do not coincide with the edges of the pixels, the partial illumination of the pixels has to be considered in the extraction process. When computing the sum of each pixel column, smaller weights are applied for the pixels at the edges of the order.

ThAr-based wavelength calibration

The wavelength calibration of the 1D spectra obtained with GAMSE is performed based on *ThAr* emission line spectra. In Fig. 4.1 (bottom), the necessary steps for wavelength calibrating the science spectra are summarized: The *ThAr* exposures are compared with a database[26] of known *ThAr* lines, which allows to identify their wavelengths and generate a wavelength-to-pixel map that is then applied to all science frames.

Due to the large intrinsic discrepancies between spectra of different *ThAr* lamps (see Sec. 1.2.5), the first time a certain lamp is used for a given instrument, a manual identification of the lines has to be done. The manual identification for the MaHPS *ThAr* lamp is provided with GAMSE and serves as input for the automatic line identification algorithm. More details about this process are given by L. Wang et al. (2016, in prep.).

After the detection of the *ThAr* lines in the calibration frames of a night, the function that best describes the distribution of the central wavelengths of the emission lines is determined. This is done by using a 2D polynomial that is spanned in the coordinate space of physical orders o as one dimension and pixels along the physical orders p as other dimension (L. Wang et al. 2016):

$$\lambda(p, o) = \sum_{m,n} C_{m,n} p^m o^n. \tag{4.1}$$

The parameters m and n are the order of the polynomial in the pixel and physical order direction, respectively. Further input parameters for the fitting procedure are the number of iterations i, the σ-clipping[27] coefficient c_σ and the pixel range $[x_1, x_2]$ that is used in the fit for all orders. The values of all parameters listed here are defined in the configuration file of GAMSE, with the exception of the pixel range, which is hard-coded.

In the scope of this work, an extensive test of the fitting parameters for the wavelength calibration was conducted to obtain an optimized parameter set that can be used as default for MaHPS reductions with GAMSE. For the test, an arbitrary choice of a night in which the calibration routine was executed regularly was made and this same dataset, consisting of four *ThAr* exposures, was used for all analysis runs. In each run, one of the six

[26]The *ThAr* database used for GAMSE is based on the database for EDRS, but has been extended with additional line information that was manually collected.

[27]The σ-clipping is performed every time a fit was made. The standard deviation (σ) of the residuals of the fit and the data is computed and any data points deviating from the fit by more than $c_\sigma \cdot \sigma$ are cut away. For each iteration of the fit, the procedure is repeated.

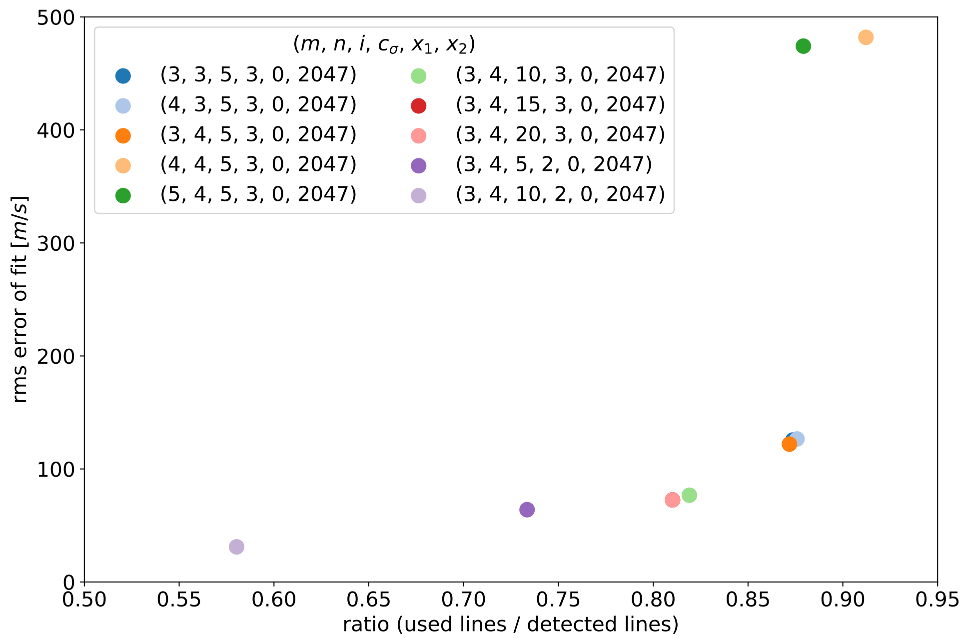

Figure 4.3: Test of different parameter sets for the ThAr wavelength fitting routine of GAMSE with focus on the best orders of the polynomial (m, n) and number of fit iterations i. The points for $i = 15$ (red) and $i = 20$ (pink) overlap perfectly.

fitting parameters $(m, n, i, c_\sigma, x_1, x_2)$ was changed to observe the effect on the wavelength calibration.

The quality of the wavelength calibration is evaluated in terms of the root mean square (rms) error of the fit to the data, where a smaller rms error indicates a more precise wavelength calibration. In the regular reduction flow of GAMSE, the wavelength fit is performed for all four available *ThAr* frames, but only the solution with the smallest rms error is chosen to be used and subsequently applied to the science frames. Similarly, in this test to find the best parameter set, only the results with the best rms error for a given parameter set are compared with each other.

Since a σ-clipping is employed, the rms error should not be used as the only reference, because in unfavorable cases the clipping of too many lines may cause the fit to converge to a solution that does not fully represent the true wavelength distribution over the whole detector area. Therefore, the fraction of lines that contribute to the fit is utilized as second indicator of the fit quality. If two or more *ThAr* frames from the same reduction produce equal rms error values[28], the frame in which more lines contributed to the fit is chosen, both in this analysis and in the regular GAMSE reduction.

[28]The number of significant figures for the rms error of the fit is limited, which is why the equality of rms error values is not unusual to occur.

Figures 4.3 and 4.4 show the results of the tests as plots of the rms error of the fit against the percentage of lines that were still included after the last σ-clipping iteration, with respect to the total number of detected lines. The rms error of the wavelength fit is computed by GAMSE in wavelength units, but for a more intuitive understanding of the impact on the RV precision it has been converted to RV units here. One should keep in mind that the rms error gives a measure for the average error of each individual *ThAr* line. Since per order the information about the line position of many lines is combined, the actual RV measurement precision can be better than the values given in the plots.

For the results shown in Fig. 4.3, parameters m and n were varied first to find the polynomial orders that can best represent the wavelength distribution. Shown are possible combinations of $m \in [3, 5]$ and $n \in [3, 4]$. Any values outside of these ranges result in rms errors that are orders of magnitude larger and therefore not suited. The fraction of used lines does not change significantly with the choice of the fit orders, so the tuple $(m, n) = (3, 4)$ with the best overall rms error of 122 m/s and 87.2% of the lines used was adopted for the rest of the analysis and chosen as default for GAMSE.

In a second step, the number of iterations i was varied while keeping the rest of the parameters the same (Fig. 4.3). It can be observed that with a higher number of iterations more lines are excluded from the fit, but at the same time the rms error decreases. After a certain amount of iterations, the fit converges and no further lines are excluded, which in Fig. 4.3 can be seen as perfect overlap of the points for $i = 15$ (red) and $i = 20$ (pink). The point of convergence for this parameter set is at an rms error of 73 m/s and a used line fraction of 81.0%.

Adopting a stricter σ-clipping coefficient of $c_\sigma = 2$ instead of $c_\sigma = 3$ results in the rejection of more lines, but a further improvement of the rms error (Fig. 4.3, purple). This is not surprising, as it can be generally expected that the fit quality improves as more and more lines are clipped away. However, as noted above, care should be taken that enough lines remain for the fit to represent the actual wavelength distribution.

While in the reductions shown in Fig. 4.3 all pixels along the physical orders were used with $(x_1, x_2) = (0, 2047)$, Fig. 4.4 (top panel) presents the results of excluding regions at the beginning (x_1) or the end (x_2) of each order. At the edges of the CCD detector area, a significantly larger deviation of the line positions from the fit is found (Fig. 4.5 top), probably caused by mechanical distortions of the CCD chip. As these deviations can deteriorate the fit for the regions that are not distorted, the affected regions should be excluded.

As starting point, the parameter set $(m, n, i, c_\sigma, x_1, x_2) = (3, 4, 5, 3, 0, 2047)$ was chosen, which is also part of Fig. 4.3. Note that the scaling of the axes is different for Fig. 4.3 and 4.4. Since the deviation effect is larger at the x_1 edge of the detector than at the x_2 edge, different step sizes of 50 and 20 pixels, respectively, were chosen to explore the optimum cut level. The best result with a rms error of 111 m/s is found for $x_1 = 100$ (orange) and no further improvement can be seen when excluding more than the first 100 pixels. Additionally excluding the pixels on the other edge produces the smallest rms error of 108 m/s when starting from $x_2 = 1987$ (red).

Using the result $(x_1, x_2) = (100, 1987)$, an analysis of the influence of the number of

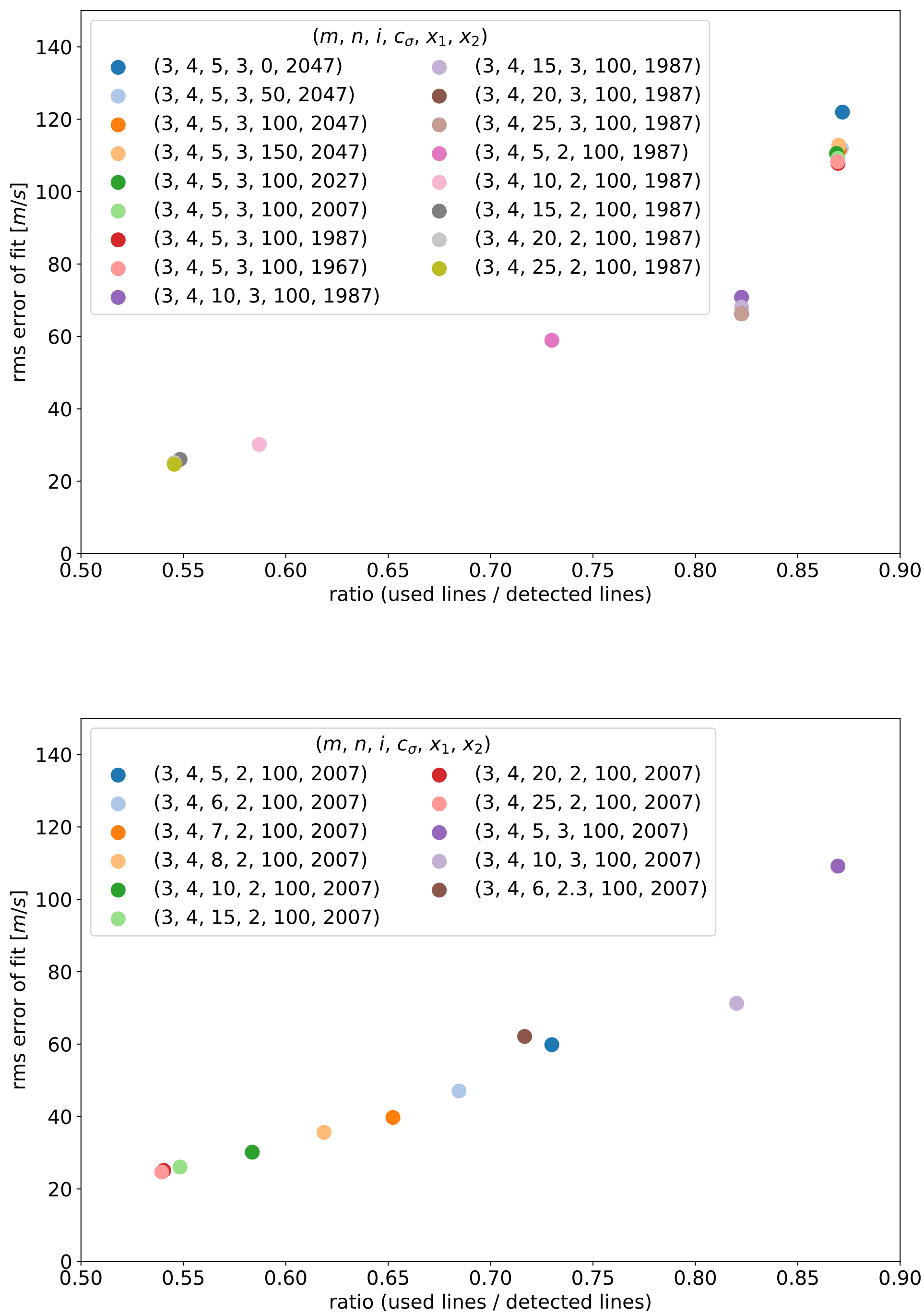

Figure 4.4: Tests of different parameter sets for the ThAr wavelength fitting routine of GAMSE with focus on the pixel cuts (x_1, x_2), number of fit iterations i and σ-clipping coefficient c_σ. Scaling of the axes differs from Fig. 4.3.

iterations i on the fit was carried out afterwards (Fig. 4.4, top panel). To this end, the number of iterations was increased in steps of 5 until convergence was reached. This was the case at $i = 20$ for both $c_\sigma = 3$ (brown) and $c_\sigma = 2$ (gray, yellow), although the converged rms error values and used line percentages differ significantly for the two σ-clipping coefficients. While the first has a rms error of 66 m/s and 82.3% used lines, the latter reaches 25 m/s rms error by using only 54.6% of the detected lines. Since there is little difference in the results for a pixel cut at $x_2 = 1987$ (Fig. 4.4, top panel, red) and $x_2 = 2007$ (light green), the decision concerning the default value for the GAMSE reduction was made in favor of having a larger number of pixels contributing to the fit: $(x_1, x_2) = (100, 2007)$.

Figure 4.4 (bottom panel) shows a further comparison of the fit quality for varying i and c_σ when adopting the pixel limits $(x_1, x_2) = (100, 2007)$. Based on these results, the number of iterations was determined so at least 2/3 of the detected lines are kept in the fit, which is the case for $i = 6$ (light blue, 47 m/s rms error at 68.5% used lines percentage). The adopted value for c_σ was slightly raised to $c_\sigma = 2.3$ (brown) in order to allow for a safety margin, as the calibration data from other nights differ slightly from the dataset used in this test.

All in all, the final choice of default parameters for the GAMSE wavelength fitting routine is $(m, n, i, c_\sigma, x_1, x_2) = (3, 4, 6, 2.3, 100, 2007)$, indicated by the brown point in Fig. 4.4 (bottom panel). With this parameter set, a typical rms error $\sim$60 m/s with about 72% of the lines contributing to the fit can be achieved, also when using calibration data from other nights.

As mentioned before, the rms error of the fit is a measure for the uncertainty of the wavelength solution for each single line of the *ThAr* lamp. However, this statement only holds if the wavelength calibration error of the spectral lines in each physical order is uncorrelated and does not show any residual structure. Figure 4.5 shows the residuals of the wavelength calibration fit for the best parameter set $(m, n, i, c_\sigma, x_1, x_2) = (3, 4, 6, 2.3, 100, 2007)$ to verify that the distribution is indeed statistical.

In the top panel of Fig. 4.5, the residual values between the fit and the measured line positions are plotted in pixel coordinates along the orders. The residuals of all individual echelle orders are stacked in order to emphasize possible structures along the dispersion direction. At the left edge of the top panel, the distortion effect of the CCD chip can be recognized as correlated deviation from the fit. A hint of such a distortion can also be seen at the right edge, although with a much smaller amplitude. Lines that are depicted with an open circle were excluded from the fit, either due to the pixel cuts at the edges or because of the sigma clipping, where the dashed lines indicate the 1σ, 2σ and 3σ level, respectively. Taking into account only the filled circles, which contribute to the fit, no structure can be discerned and the distribution indeed appears statistical.

The bottom panel of Fig. 4.5 shows the same residuals, but ordered by the aperture, each of which corresponds to a physical order. This allows to get an impression of the fit quality in the cross-dispersion direction. The lines detected in a given spectral order are all displayed with one color, which is also used for the top panel. The lines used in the fit are again shown as filled circles and do not show evidence for a problematic residual structure. Only the apertures with the highest numbers show a degraded fit quality due to the fact

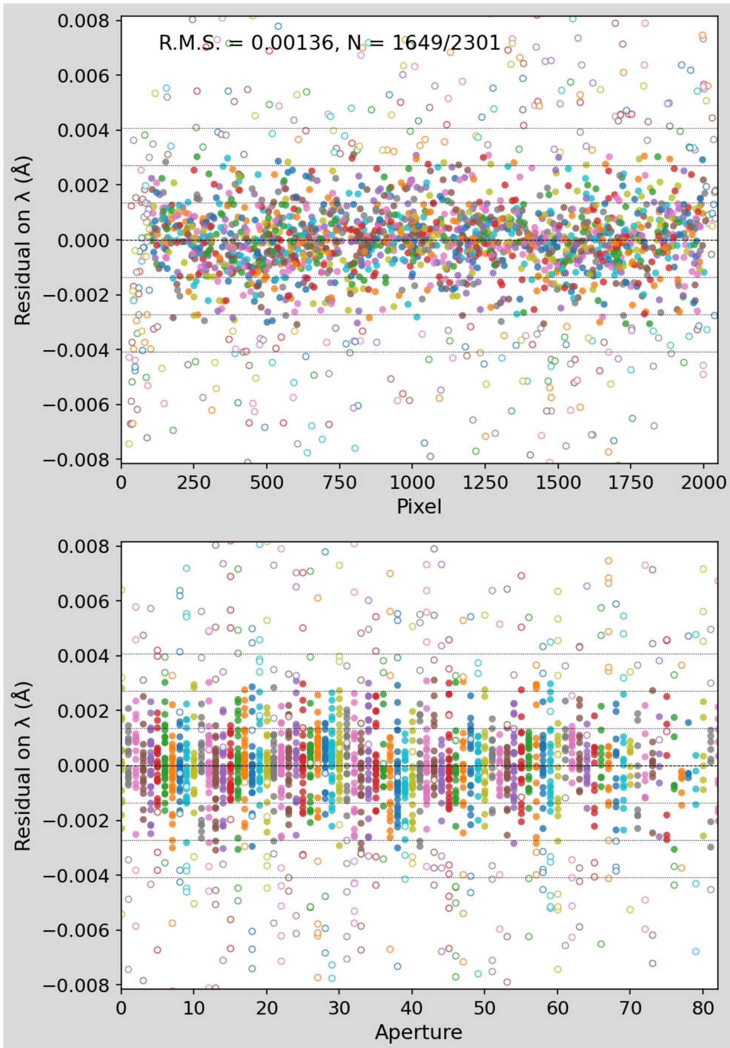

Figure 4.5: Residuals of the GAMSE wavelength calibration fit obtained with the final set of parameters $(m, n, i, c_\sigma, x_1, x_2) = (3, 4, 6, 2.3, 100, 2007)$, for the same frame that produced the brown point in Fig. 4.4 (bottom). Each circle represents a *ThAr* emission line that was detected. Top: residuals of each order along the pixel axis, all orders stacked; bottom: residuals per order (aperture). Open circles denote lines that were detected, but excluded from the fit, while all filled circles contribute to the fit. The horizontal lines give the 1σ, 2σ and 3σ values of the residual distribution. The rms of 0.001 36 Å corresponds to a RV of ∼62 m/s (at 656 nm); N gives the number of lines used in the fit over the number of lines detected in this frame. Graphic automatically generated by GAMSE (L. Wang et al. 2016).

that there are only few lines available and some of them are extremely bright, saturating the CCD and thus preventing any useful position determination.

When applying the obtained wavelength calibration to the science frames, the residual rms error of $\sim$60 m/s, which is clearly too large for the desired exoplanet measurements, is transferred to the spectral lines of the science spectrum. But since the assumption of uncorrelated errors in the wavelength calibration fit seems reasonable if the distorted regions are carefully excluded, the information of all lines in one order can be statistically combined to reach a smaller overall error. For example, to reduce the RV error originating from the wavelength calibration for a single order to a level of 15 m/s or 10 m/s, a total of 16 or 36 lines are needed, respectively. Those numbers are common for stars of stellar types F, G or K, which are mainly observed with MaHPS. Nevertheless, other sources of errors of the RV measurements exist and need to be considered as well in the analysis of scientific spectra.

In the automated reduction flow of GAMSE, the wavelength calibration is evaluated for each of the *ThAr* frames, using the parameter set determined here. The fit with the smallest rms error, or the largest number of contributing lines in case of a degeneracy, is then utilized as wavelength reference for all science spectra. The *ThAr* calibration exposures are typically taken at the beginning of the night, meaning that any drifts or changes of the instrument during the night are not corrected. This is only possible by using the information of the LFC in an analysis with the MARMOT software package (Sec. 4.3).

4.1.3 Output files and format

For each recorded FITS frame in the ThAr or science frame group, GAMSE produces a new FITS frame that contains the individual 1D spectra of all orders as a binary table. An optional de-blazing function for the normalization of the echelle orders is available at the end of the GAMSE reduction, intended for science applications that do not require such a high precision of the RV measurements as exoplanet science. However, the de-blazing is not part of the default GAMSE reduction, since the required actions are not flux-conserving and prone to systematic errors regarding the spectral line positions. The exact format of the stored data is described in detail by Kellermann (2021).

Further outputs are produced by GAMSE to help verifying the success of the reduction or facilitate spotting issues if the reduction fails. In the very first reduction step, the observing log is compiled, which contains some simple statistics for all frames that are part of the reduction. That is helpful when e.g. checking for frames that might be oversaturated or not exposed at all. Additionally, a log file is made during the execution to track any errors in case the reduction fails.

In several steps of the reduction, report plots are created that allow to visually inspect the reduction quality and result. This encompasses plots of e.g. the 2D structure of the bias, the position of all echelle orders that were detected or the residuals of the wavelength calibration fit. It is advisable to verify the plots presenting the 2D background model, as once in a while discrepancies between the used model and the actual background light distribution occur. In such a case, a different background reference frame, for instance recorded in a different night, has to be provided.

After GAMSE was applied to the obtained data, the information about the wavelength shift of the spectra has to be obtained with other means. In the following, the two software packages used for this purpose are featured.

4.2 IRAF package `rv`

The Image Reduction and Analysis Facility (IRAF) is an extensive software system developed at the National Optical Astronomy Observatory (NOAO). IRAF is a general-purpose software suite that comes with a multitude of software packages for the reduction and analysis of data from the astronomical context (Tody 1986, 1993).

A few words of caution are in place before advancing in the description of the data analysis, because IRAF has originally been developed about three decades ago. First, the official development and support by NOAO has ceased and although there is still a community providing ongoing support and service, the packages are no longer updated content-wise to incorporate new methods. Furthermore, the age of IRAF leads to more and more compatibility problems with current hardware and operating system architectures.

Nevertheless, IRAF has the advantage of providing ready-made solutions for almost any problem concerning astronomical data. IRAF is therefore still a helpful tool to quickly generate meaningful results without the effort of implementing completely new routines or searching extensively for other existing software. This work made use of IRAF functionalities only for measuring RV shifts of *ThAr* exposure series[29] (Sec. 3.2.2), for which obtaining results with minimized effort was desired. For the remaining analyses, the modern and more specialized software solution MARMOT (Sec. 4.3) was used.

The available packages for IRAF cover a large variety of data analysis steps and science purposes, such as the classic CCD reduction, the photometry of point and extended sources, or the plotting and fitting of data. There are also several packages for the analysis of echelle spectra, out of which the *Radial Velocity Analysis* (`rv`) package by Fitzpatrick (1993) was employed in this work.

4.2.1 The cross-correlation function (CCF)

A widely distributed way to measure RV shifts in 1D spectra is by means of the cross-correlation function (CCF). For computing the CCF, two spectra are artificially shifted with respect to each other in defined wavelength or pixel intervals (Fig. 4.6). The area enclosed under both the curves is then computed and gives a measure for the similarity of the curves. The values obtained for each wavelength or pixel step are recorded and give the CCF, which has a maximum at the shift where both curves match best. By determining the position of the maximum, the RV shift can be immediately measured.

[29]The scripts and additional files necessary for the IRAF reduction as done in this work are provided under `https://github.com/vfahrens/MaHPS_scripts` for download.

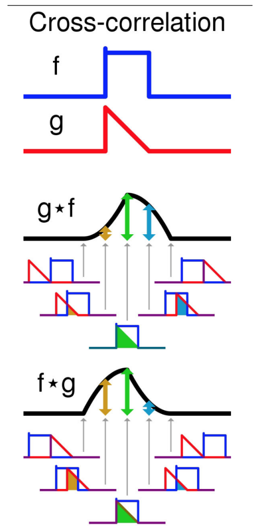

Figure 4.6: Illustration of the computation of the cross-correlation function (CCF) for two arbitrary continuous functions f and g. Graphic taken from Wikimedia.[30]

Mathematically, the cross-correlation function is defined as the convolution of a function $y(m)$ with the complex conjugate of a second function $x(m)$, as function of the relative shift n between the two:

$$CCF(n) = (x \star y)(n) = \int_{-\infty}^{\infty} x^*(m) y(m+n) dm, \tag{4.2}$$

where both $x(m)$ and $y(m)$ are continuous functions in m. In this case, the CCF can be calculated as an integral, corresponding to the interpretation of the area under both curves (Fig. 4.6).

However, the spectrograph only returns discrete spectra for which the wavelength axis is binned by the pixels of the detector. This binning is linear in the logarithm of the wavelengths ($\ln\lambda$), so that a bin n of a spectrum with N pixels is described by (Tonry and Davis 1979)

$$n = A \ln \lambda + B, \tag{4.3}$$

where A and B are scaling factors and $n \in [1, N]$ holds for the bin number. The formulation of the non-continuous CCF for two spectra $x(m)$ and $y(m)$ is then given as (Tonry and Davis 1979):

$$CCF(n) = (x \star y)(n) = \sum_{m=-\infty}^{\infty} x(m) \cdot y(m-n). \tag{4.4}$$

[30]This graphic was created by user *Cmglee* (Wikimedia Commons) and is available for free use under the *Creative Commons license CC-BY-SA-3.0* (2021).

When using the CCF to measure spectral shifts, one of the input spectra is in general used as reference spectrum, also called the template. This template can be of either natural or artificial origin, like an observed spectrum with a good SNR or a synthetic spectrum computed from a stellar model. For the analysis of the *ThAr* exposure series, the first spectrum of the series is used as template, because only the relative spectral shift is of interest.

If the CCF is computed for two spectra that have lines with a Gaussian line profile, the CCF also has a Gaussian shape. In general, the overall CCF shape reflects the line shape characteristics of the input spectra. Since the measured line profiles are never truly Gaussian due to components like the instrumental line profile or stellar effects, the CCF also deviates from the perfect Gaussian form. Especially deviations from symmetric line profiles affect the CCF to become asymmetric as well, but at the same time the CCF provides an efficient way to quantify such line asymmetries. Because these deviations of the CCF from a Gaussian profile are small, a Gaussian function is typically fit in order to determine the position of the maximum.

An important characteristic of the CCF when measuring shifts of spectra is that all spectral lines contribute information to the result. Broad and deep lines have a higher contribution than narrow and shallow ones, since they have a larger impact on the area under the graphs. For this reason, some lines have to be excluded from the CCF in order to not bias the RV measurement. This concerns on the one hand strong lines that do not originate from the stellar spectrum, like atmospheric absorption lines, and on the other hand lines with large wings, e.g. the stellar H_α absorption line for solar-type stars. Since the *ThAr* spectra analyzed here do not have such features, no exclusion was necessary and all parts of the spectrum could be used.

4.2.2 `fxcor`: a CCF routine for IRAF

The `rv` package of IRAF allows to obtain shifts of spectra in radial velocity units by calculating the cross-correlation function (CCF) for given wavelength calibrated spectra and determining the position of the CCF's maximum. The task that comprises the whole process is called `fxcor`. In the following, an overview of the data analysis with `fxcor` as it was executed for this work is given. Both the `rv` package and the `fxcor` task feature many more functionalities than used in this work, details about which can be found in the literature and documentation of the `rv` package (Fitzpatrick 1993; Alpaslan 2009).

It has to be pointed out that in favor of a better RV measurement precision, the CCF is calculated order-wise and the resulting RVs are afterwards combined to one RV for each frame. Merging the spectra of all orders before the computation of the CCF would require interpolation in wavelength regions that are recorded in two adjacent orders or extrapolation for wavelengths that lie in the gaps between orders. Both cases occur in MaHPS spectra and are a source of possible RV errors.

Data input format

The extracted 1D spectra obtained with GAMSE are used as input for the `fxcor` analysis. However, the data input format expected by IRAF differs from the output format of GAMSE, which is why a conversion script was written as part of this work. The most important criterion in the development of the converter is the conservation of all information from the GAMSE output files concerning the wavelength calibration information in order to keep the full quality of the data.

In the GAMSE output format, for each echelle order of the spectrum the values for both the flux and the wavelength are stored pixel-by-pixel in separate lists. These lists, along with similar lists that contain other information not of relevance here (see Kellermann (2021) for more details), form the body[31] of the binary FITS table.

In contrast to that, IRAF requires the wavelength calibration information to be in the header of the FITS file. Therefore, in the conversion script the wavelength data is read from the GAMSE frames and reformatted as strings to be used in the header. The binary table format used by GAMSE cannot be read by the IRAF routines, so completely new FITS files need to be generated.[32]

A further complication arises from the sheer length of the strings containing the wavelength calibration data, with 2048 data points for each of the 84 echelle orders. The FITS format does not support headers with such a large number of entries, so for each order a new extension, which basically acts as individual FITS frame, of the main FITS frame is created. The resulting *multi-extension FITS file* (MEF) has an empty main body and one extension for each order, with the wavelength information in the headers and the flux data in the corresponding bodies.

CCF and error calculation

For calculating the CCF, `fxcor` makes use of the algorithm by Tonry and Davis (1979). The CCF is computed at steps of 1 pixel, corresponding to steps of ~2100 m/s for MaHPS, order-wise for all echelle orders in one frame and all frames of the *ThAr* exposure series. A Gaussian function, along with a linear background component, is fit to determine the position of the maximum. The width in which the Gaussian was fit to the CCF was chosen to be fixed to 15.0 pixels, which in an empirical test gave the best result. The fitting width should not be confused with the full width half maximum (FWHM) of the Gaussian, which could freely vary in a range from 3 to 21 pixels. The actually measured FWHM after the fit is typically around 8 pixels.

In order to avoid negative influences of the blaze function of the spectrograph (compare Fig. 1.17) on the precision of the RV measurement, the blaze function normally has to be removed to obtain flat spectra. In the case of the analysis of the *ThAr* exposures, this is

[31] A FITS file always consists of a header, which typically contains auxiliary information in the form of text strings, and a body, which contains the actual data of the measurement.

[32] A script to automatically convert spectra from GAMSE to IRAF data format was compiled as part of this work. Under `https://github.com/vfahrens/MaHPS_scripts` the script and additional files are provided to the public.

not possible as the emission line spectrum does not have a continuum that would allow to measure the blaze function. Therefore, the blaze function removal is skipped in the analysis of the *ThAr* spectra, which is not a problem because anyway only the overlap of the emission lines contributes to the CCF.

Since the CCF is calculated only at discrete steps in pixel space, a rebinning of the input spectra might be necessary. If this is the case, `fxcor` automatically rebins the spectra to a reference scale that is determined by the user. To guarantee the best consistency of results, the template's binning was chosen as reference.

As input for the CCF, both for the template spectrum and the spectrum that is matched, only the pixel region $[200, 1848]$ is used. On both sides of all orders, 200 pixels are cut away for two reasons: On the one hand, these regions suffer from mechanical distortion of the chip (see Sec. 4.1.2), and on the other hand the SNR is very low compared to the rest of the order because of the blaze function.

In the *ThAr* series reduction, the shifts between the individual spectra are relatively small (<1 km/s or < 0.5 pixels[33]) and consequently the peak of the CCF is expected to be close to zero. The used spectra have a high signal to noise, resulting in a CCF peak with a large amplitude that can be easily distinguished from the background. Furthermore, since the emission line pattern from the *ThAr* lamp is not periodic, there should be no significant side peaks that the algorithm might mistake for the main CCF peak. Consequently, the search window parameters remained undetermined in order to not manipulate the measurements with the knowledge of the expected peak position.

Along with the measurement of the RV shift as the position of the CCF maximum, `fxcor` also delivers an error of the measured RV. This error is not derived statistically, but is an empiric approximation. The formulation employed by `fxcor` is given by Tonry and Davis (1979). It is based on the assumption that errors in the position measurement of the CCF peak are caused by a superposition of the perfect CCF peak with an antisymmetric disturbing function, which can be directly obtained from the measured CCF. The RV measurement error can then be estimated from the relative amplitude of the disturbing function with respect to the CCF peak, the number of pixel bins used in the correlation and the power spectrum of the CCF.

Output files and format

The standard output of `fxcor` consists of three files:

- a text file, containing the measured RVs, errors and some additional information;
- a log file, containing information about the fitting of the CCF, like the coefficients of the fit functions;
- a graphical file, containing a plot of the CCF function and the fit.

[33] The conversion from velocity to pixel space was made via the standard Doppler formula and the wavelength interval $\Delta\lambda$ per pixel, as given by the spectral resolving power. The reference wavelength was chosen to be that of the H_α transition at 6562.8 Å.

Out of the three, the text file is the one that is of most interest, because it contains the actual measurement results. The other two files, at least in the scope of this work, served mainly to review the fitting process and track possible errors.

In the output text file, for each spectrum that was correlated with the template, the measured shift is given in pixels and velocity. The `fxcor` task additionally offers RV values that are corrected for the barycentric motion of the Earth, however for the analysis of the *ThAr* exposure series such a correction is not needed, because only the shift relative to the first exposure is relevant.

The RV values for each frame of the *ThAr* series as shown in Fig. 3.5-3.7 are finally obtained by calculating the weighted mean of all orders. As weighting factors, the errors of the CCFs of the individual orders are used. The error bars of the combined RVs are calculated from the spread between all orders of one frame in the form of the standard deviation of the order-wise RV values.

4.3 MARMOT

The Munich Analyzer for Radial Velocity Measurements with B-Spline Optimized Templates (MARMOT) is a software package that was developed in-house specifically for further analysis of the *ThAr* wavelength calibrated 1D spectra produced by GAMSE (Kellermann 2021; Kellermann et al. 2020). The primary purpose of MARMOT is to obtain a RV value for each observed frame of the science object. It is designed in a modular way, so users can choose the most suitable functions for the data quality and the scientific problem at hand. Furthermore, MARMOT can be easily adapted to data formats from other instruments, similarly to GAMSE.

The following description of the MARMOT analysis is focused on the steps necessary to obtain the RV measurements shown in Chap. 6 for stellar spectra observed with MaHPS. A full description of the MARMOT routines is given by Kellermann et al. (2020) and Kellermann (2021).

The main functionalities of MARMOT include:

- performing an improved wavelength calibration based on simultaneous LFC measurements,
- calculating the barycentric correction due to the Earth's motion,
- creating high-quality templates by interpolation of a single or combination of several observed spectra,
- obtaining precise RV measurements for the input spectra.

Figure 4.7 outlines the data analysis process with the existing options the user can choose from. In contrast to GAMSE, the analysis of data with MARMOT is highly configurable, owing to different needs for different types of observed objects, quality of the data or science goals. Therefore, no standard reduction flow exists, but the desired choice and sequence of analysis steps needs to be specified by the user in a reduction script.[34]

As input, the 1D spectra produced by GAMSE are used, along with the GAMSE obslog files from the individual nights that contribute auxiliary data to the analysis. Additionally, variables and parameters relevant for the analysis can be specified in an initialization file.

The first steps in the RV analysis are applying the barycentric correction and masks to all frames. For the barycentric correction, the external package *barycorrpy* (Kanodia and Wright 2018) is utilized, which requires the precise location of the observatory, the coordinates of the observed target and the time at which the observation was made as input parameters. While the observatory's location has to be manually specified in the initialization file, the object's coordinates in the sky are automatically retrieved from the *SIMBAD* online database (Wenger et al. 2000) based on the object's name. *barycorrpy* then returns the barycentric correction in m/s for the given object and observation time, which is subtracted automatically from the RV that is computed for each order.

The time of observation that is used for each frame should resemble the mean arrival time of the photons, as motivated in Sec. 2.3.2. Since to date there is no exposure time monitor that allows to track the distribution of the incoming photons, MARMOT uses the plain mid-time between the start and end of each exposure, accepting that errors might be introduced to the measured RV by this. The timestamp of the mid-time of the exposure serves as input for the barycentric correction routine.

A dedicated mask file allows the user to exclude regions from the analysis. The exclusion can be specified in different ways, so different causes of contamination of the observed spectra can be taken into account. It is possible to exclude regions by wavelength, which is useful e.g. for atmospheric (*telluric*) lines that are superimposed on the stellar spectrum, by pixel range, in case there are known bad regions on the detector, or by complete orders.

For the analysis of the data presented in Chap. 6, all physical orders outside of the range $[76, 133]$ were excluded because of a low SNR. A wavelength mask was generated for the remaining orders from a typical atmospheric absorption spectrum. All wavelengths that are affected by telluric absorption lines with a depth of at least 10% of the surrounding continuum emission are listed in the mask file and were not used in the analysis. In addition, the physical order 87, which contains the broad H_α absorption feature, is also excluded from further use. Lastly, only pixels inside the range $[200, 1850]$ are allowed to contribute to the analysis due to the CCD distortion at the edges.

4.3.1 LFC-based wavelength calibration

The GAMSE reduction only makes use of the *ThAr* spectra to obtain a wavelength calibration for all spectra. Since the *ThAr* exposures used for this are only taken at the beginning of the night, errors might be introduced to the measured RVs due to instrumental drifts and other changes of the wavelength position on the detector. However, in order to achieve

[34]The scripts and initialization files, as well as additional files necessary for the MARMOT reduction as done in this work, are provided under `https://github.com/vfahrens/MaHPS_scripts` for download.

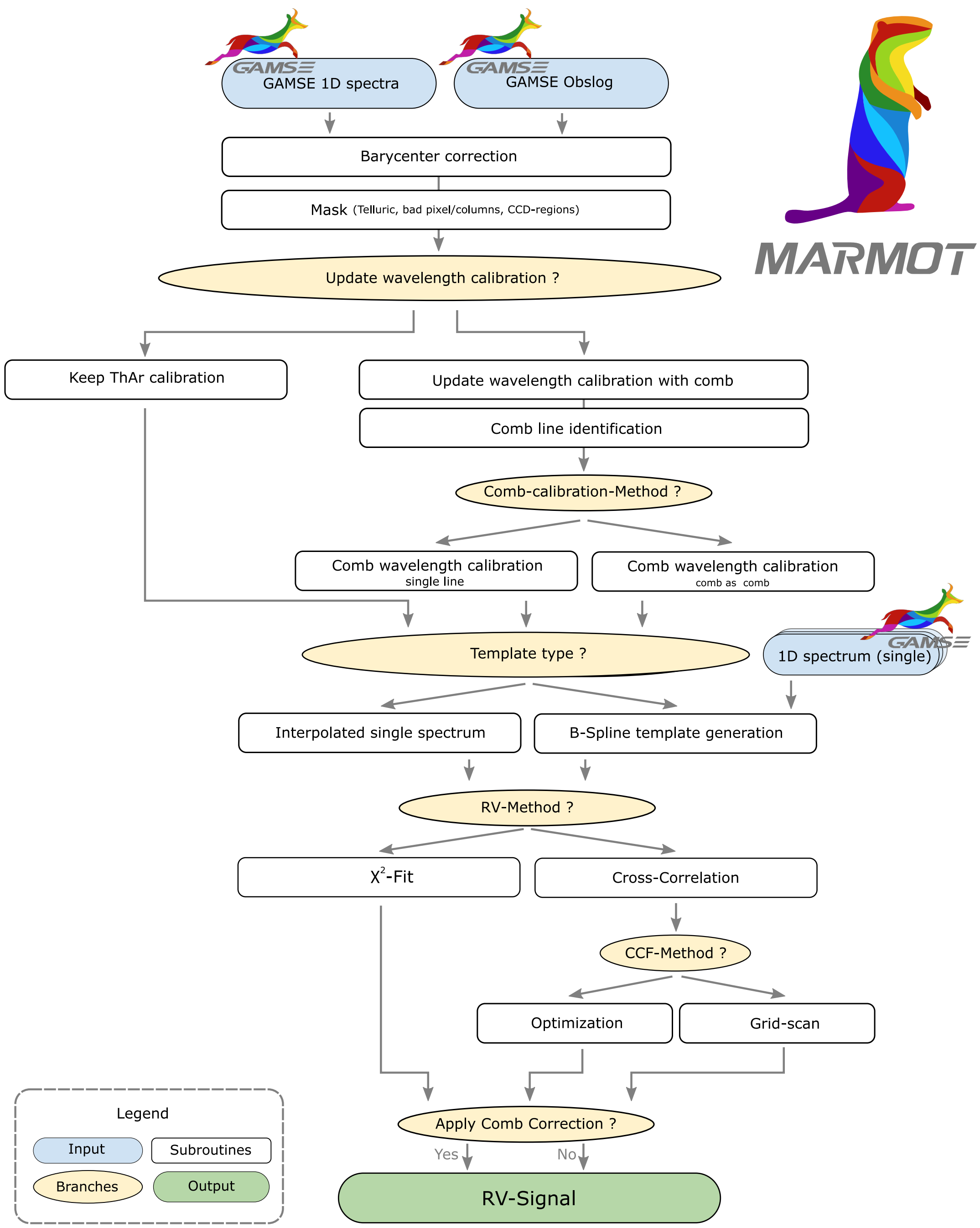

Figure 4.7: Flowchart of the MARMOT software package for LFC calibration and RV calculation of 1D spectra. Steps where a user decision has to be made are shown in yellow. Graphic taken from Kellermann (2021).

RV precisions on the few m/s level, information from simultaneous calibration with the LFC has to be utilized. MARMOT offers the possibility to improve the wavelength calibration of GAMSE by additionally analyzing the shift of the LFC lines between individual exposures.

The LFC-based wavelength calibration is performed by finding the center of each LFC line, identifying its true wavelength and measuring the shift. Because of the nature of the LFC, the wavelengths of the LFC lines are precisely known. Given that the instrumental drift of the spectrum during one night is only a small fraction of a pixel, the *ThAr* wavelength calibration of GAMSE can be utilized to identify the LFC lines and directly measure the difference of each line's true position to that determined with the *ThAr* calibration.

MARMOT features two different methods to measure the shift of the LFC (Fig. 4.7). On the one hand, a Gaussian can be fit to each LFC line individually and the determinations of the line centers are then combined per order to get the overall shift. On the other hand, since the spectral function of the LFC is known, a direct best fit of the spectrum of each order can be performed. The latter method yields slightly more precise results, however it requires more computation time, as the number of free parameters for the fit is large. Since the LFC-based wavelength calibration was not applied in this work, further discussion of the two methods is omitted. Details on the implementation of both methods and the advantages and disadvantages of one over the other are given by Kellermann (2021).

Once the shifts between the true LFC line position and the measured position are determined, there are different possibilities of how to correct the RV measurement, depending on the chosen method for the shift measurement. The first possibility is probably the most obvious: The shifts of all lines are averaged for the complete frame and the result is subtracted from the measured RV shift of the science spectrum. For the second method, a completely new wavelength calibration is computed from the knowledge about the true LFC line positions and subsequently assigned to the science spectrum. The last option also involves a new wavelength calibration, but the model of the LFC's spectral function is used instead of the fit position of each line.

As stated in Tab. 2.1, the LFC spectrum covers only a part of the spectral range of MaHPS, so not for all orders the improved LFC wavelength calibration is available. During the analysis of the RV data for this work, an important finding was made: if the data generally feature a comparably low SNR, either because of the faintness of the object or a deliberately short exposure time in favor of a better time resolution, it is advantageous to give up the gained wavelength calibration precision of the LFC and instead make use of a larger number of *ThAr* calibrated echelle orders to improve the measured RV by statistics. Consequently, for the RV results shown in Chap. 6, no LFC-based wavelength calibration was performed.

4.3.2 Template generation

A critical part in the RV measurement process is the choice and generation of the template spectrum, as it serves as reference for all science spectra. For precise RV measurements, the best possible match of the spectral features between the template and the science spectra is desired, so synthetic spectra are in general less suited than observed spectra, in the best case of the exact same star. However, observation-based templates only perform better than synthetically generated ones as long as the SNR is excellent and any systematically perturbing features like telluric absorption lines or cosmic rays are masked or removed reliably.

The general approach followed by MARMOT, in comparison to other RV determination routines like `fxcor`, is to avoid using binned template spectra because sampling effects between the template and science spectra might worsen the RV measurement. Instead, the template spectrum is parametrized and only the coefficients of the function representing the spectrum are stored. In this way, the template can be evaluated at any given wavelength without further effort.

MARMOT makes use of observed spectra as templates by applying noise suppression methods and thus improving the quality of the template. Two options are available for that (Fig. 4.7): interpolation of a single spectrum or combination of several observed spectra with a B-spline[35] optimization algorithm. The latter is more robust against spurious or variable features like noise, cosmic rays or telluric absorption lines, but at the same time requires a significant amount of computing power. The first option of a single interpolation can be calculated more quickly, but is more prone to errors in the final RV measurement.

For this work, due to the low SNR of the obtained datasets the creation of B-spline templates was chosen. The B-spline template optimization of MARMOT is based on the method by Zechmeister et al. (2018) and thoroughly described by Kellermann (2021). The spectra that contribute to the template are treated before the combination. On the one hand, the spectra are naturally shifted with respect to each other because of the different time of observation, which is compensated by subtracting the barycentric correction and allowing for a linear shift in $(\ln \lambda)$. On the other hand, in one order the total brightness as well as the brightness distribution over the wavelengths may vary between the used exposures, caused by differences in the atmospheric conditions or exposure times, for which a polynomial of order 2 is applied along the dispersion direction. The input spectra are then jointly fit with the B-spline function to obtain the template parametrization.

In order to obtain templates with an efficient reduction of noise and other disturbing features, a minimum of three observed spectra has to be combined. In a typical reduction, between four and eight spectra are chosen, using a larger number than that does not significantly improve the template anymore.

4.3.3 RV measurement methods

Two different methods for measuring the RV shift of a spectrum relative to the template are offered by MARMOT (Fig. 4.7): either by using a CCF (see Sec. 4.2.1) or by performing a χ^2-optimized fit of the template to the data. While the latter tends to deliver more precise

[35] A B-spline is a fitting function that consists of a configurable number of control points, which represent the overall shape of the function, and the parts in between the control points, where independent polynomial functions are fit. MARMOT employs a uniform distribution of $N_{pixels}/2$ control points and polynomials of order $l = 2$ (Kellermann 2021).

results because the intermediate step of fitting the obtained CCF to determine the position of the maximum is not required, the computational effort needed is larger. Additionally, the CCF method has proven to be more robust for spectra with low SNR, which is the reason why it was applied to the spectra shown in this work.

The necessity of using flattened spectra for the CCF computation and therefore removing the blaze function from the individual orders was already discussed in Sec. 4.2.2. This step is done automatically by MARMOT by fitting the continuum emission and dividing the observed spectrum with the obtained function.

When using the CCF method for RV measurements, the determination of the position of the maximum of the CCF is the most critical step. As noted in Sec. 4.2.1, the observed line profiles and therefore the CCF are never perfectly Gaussian, possibly causing errors in the RV determination. MARMOT features two different methods for obtaining the CCF maximum (Fig. 4.7), either by employing the classical approach of calculating the CCF at given RV steps and fitting a Gaussian function plus a background component, or by inverting the CCF values and applying a minimizing algorithm to find the best match.

Although the influences of noise and the pixel binning structure are reduced in the template by the B-spline method, they are not removed entirely and some information still remains in the template spectrum. When the CCF with the science spectra is computed, in some unfavorable cases the CCF is superimposed with a periodic ringing feature, oscillating around the Gaussian shape of the CCF, caused by those remainders. As a consequence, the minimizer method may produce an incorrect result for the CCF maximum if a side maximum is found. Such a behavior has been observed for the data presented in Chap. 6, therefore the RV measurement was performed with the Gaussian fit method, since it partly averages out the ringing feature.

4.3.4 RV errors

One of the drawbacks of the CCF method for RV determination is that is does not deliver an error with the RV measurement, because the uncertainty of the fit of the Gaussian to the CCF does not represent the true error between the maximum of the CCF and the true RV shift. In the `fxcor` routine, the error is estimated based on the asymmetric noise component of the CCF (Sec. 4.2.2), however assumptions about the noise spectrum and the cause of the errors need to be made for that. MARMOT offers different error estimation methods, so the user can decide which one represents the properties of the used data and therefore the expected errors best.

Similarly to the method used for the analysis with `fxcor`, the final RV measurement error for each frame can be obtained by calculating the spread between the individual orders. In this case, the errors of the individual CCF fits are not relevant if a simple average of all orders is used for the RV value. However, this may lead to an additional error in the final RV value on the one hand and overestimation of the corresponding error on the other, if the result of one or several orders deviates strongly from the rest. The preferred way to obtain the final RV values for each frame that was analyzed is therefore to compute the weighted average of all individual echelle orders of that frame.

The first error estimator of MARMOT, which was chosen to be utilized in this work, is based on Monte Carlo simulations. For each order of the frame that is analyzed, the SNR is determined and spectra with an identical SNR but randomly fluctuating noise are generated. This is done by adding noise with either a Poisson or Gauss distribution at the correct scaling to the template spectrum. For each resulting "random noise" spectrum, the CCF and its maximum is determined and the standard deviation of all results gives the error for this order.

The number of spectra generated for the error estimation can be specified by the user, where 100 iterations have been found to produce a realistic error estimate. The disadvantages of this method are that a fixed noise distribution has to be chosen, which might not resemble the true noise perfectly, and that the overall computation time increases significantly because of the need to create the random noise spectra.

The other error estimation methods implemented in MARMOT are based on methods from the literature developed by either Bouchy et al. (2001) and Artigau et al. (2018) or Murphy et al. (2007). Since they were not used in the scope of this work, the reader is referred to Kellermann (2021) for a description.

In general, it has to be noted that there is no perfect method for determining the CCF position error. Additionally, the quality of the error estimators depends on the SNR and the exact spectral characteristics, like the depth and density of spectral lines in one order. The most suitable method therefore has to be chosen based on the application and data quality at hand.

As an auxiliary function, MARMOT offers the possibility to measure the SNR of a spectrum of a given physical order, which is utilized for the creation of spectra with artificial random noise. The SNR determination uses pixels 400 to 1600, corresponding to the central part of the order where the blaze function has its maximum. All the data in this pixel range are used, regardless of whether parts may be excluded from further analysis by a mask, e.g. due to contamination. In Chap. 6, the median SNR of a night of observations is cited as a quality estimator. This number was obtained by calculating the median SNR of the physical orders 85, 86, 89 and 90, where the overall maximum of the incoming flux is located, for each frame from that night. The median of the list of frame-wise SNRs was then taken as indicative number for the data quality of that night's observation run.

Chapter 5

The Rossiter-McLaughlin (RM) effect

The Rossiter-McLaughlin (RM) effect occurs when a body transits in front of a star, thus blocking a part of the light from the stellar surface. Because the star rotates, one half approaches the observer and the other one recedes, consequently the halves appear blue- and redshifted, respectively. The transiting body then may block light from only one half, which results in a change of the spectral line profile that can be measured as center-of-mass shift.

This concept was first theorized a long time before precision spectroscopic instruments were available. Nevertheless it was already proposed as a means to distinguish between contributions to the profile of the spectral lines originating from either rotational broadening or the effect of thermal broadening (Holt 1893). A first observational hint was found in a binary star system by Schlesinger (1910), before it was unambiguously measured by Rossiter (1924) and McLaughlin (1924), in honor of which the effect was named.

Due to the limited precision of stellar spectroscopy in the beginning of the 20th century, observations were restricted to binary stars that have a RV amplitude typically on the order of 10 to 1000 km/s. The RM effect served mainly to constrain stellar parameters like the rotational velocity, mass, size, density or the limb darkening effect of the stars.

As the first exoplanets were discovered, the RM effect experienced a sudden rise in popularity in the rapidly growing community of exoplanet scientists. The reason is that the RM effect allows to constrain the angle of a planet's orbit relative to the spin axis of its host star and from that, conclusions about the possible formation history of planetary systems can be drawn.

The first RM effect caused by an exoplanet transit was measured by Queloz et al. (2000) for the star HD209458 (Fig. 5.1). To date, measurements for about 170 planetary systems are available and the number is continuously growing. The insights from the statistical distribution of orbit orientations are an essential way to validate planet formation models and learn about the evolution of systems due to interactions between multiple bodies.

Before the first exoplanet detections, planet formation models were based solely on the information available from the Solar System, which suggested that planets are formed in

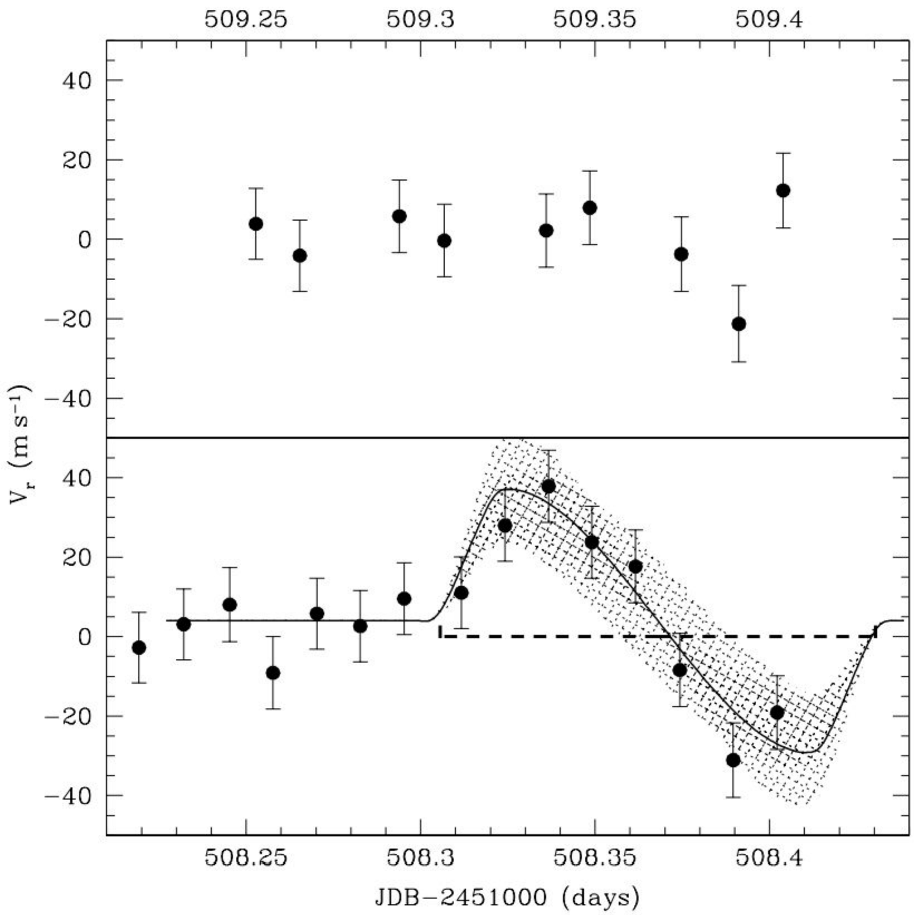

Figure 5.1: The RM effect for HD209458, the first planetary system with a measurement of the RM effect. The RV signal of the orbital motion of the planet is already subtracted. Top: measurement during a non-transiting phase; bottom: measurement during a transit of the planet. The best fit model of the RM effect (solid line) and the duration of the transit (dashed line), determined from photometric transit measurements, are given. The gray shaded area indicates the 1σ uncertainty level of the fit. Graphic taken from Queloz et al. (2000).

a disk of dust and gas around the central star. This disk would lie in the equatorial plane of the star, perpendicular to the star's spin axis, and consequently the planets would orbit the star in the same plane due to the conservation of angular momentum. These so-called aligned or co-planar orbits were thought to be prevalent in all planetary systems (e.g. Hatzes 2016b).

Small rocky planets form in the inner region, close to the host star, while giant gaseous planets have to form in the outer regions, where the stellar radiation is not strong enough to blow away small particles. Given that in the Solar System the giants are orbiting the Sun at much larger distances than the small planets, it was therefore assumed that exoplanetary systems have a high chance to strongly resemble the Solar System as this initial architecture is likely to be maintained over long periods of time. However, when the first exoplanets were detected this paradigm had to change because most of the newly detected objects were close-in Jupiter-like planets which must have undergone some kind of migration from their outer formation region to their later stable orbit close to the host star.

An additional challenge to the traditional models was posed by the first detection of a planet that orbits its host star with a significant inclination towards the stellar spin axis on a misaligned orbit, which was the case for HAT-P-7 (Narita et al. 2009; Winn et al. 2009). By observations of the RM effect, it is possible to characterize the orbit orientations of exoplanets and thus gain a better understanding of the mechanisms that affect the geometry of planetary systems, giving rise to the large variety of planetary system architectures known today.

In this chapter, first the projected obliquity λ, the observable tied to the RM effect, is introduced and the relation of λ with the physically relevant angle ψ, the true obliquity angle, is discussed. After that, the formation of the RM effect is described and factors influencing its shape and amplitude are highlighted. Additionally, a short overview of alternative measurement methods that allow to recover λ is given. The statistical distribution of the sample of exoplanets for which λ has been measured is presented and possible interpretations are given. The chapter is concluded with the presentation of observations of the RM effect with MaHPS for three exoplanet systems.

5.1 The projected obliquity angle

With the RM effect, it is possible to measure the so-called *projected obliquity angle* λ[36], also known as the *spin-orbit alignment angle*, which is a geometrical property of an exoplanet's orbit around its host star. Figure 5.2 illustrates the definition of the angle λ in the case of a star that is hosting a planet. For simplicity, only this special case is considered in the following, although the same definitions apply for any gravitationally bound two-body system, e.g. binary stars.

[36]The common symbol for the projected obliquity angle in the literature is λ or sometimes β, where $\lambda = -\beta$. This convention is adopted for the whole chapter, however it is emphasized that λ here is completely unrelated to the previous chapters, where it was used as symbol for the wavelength.

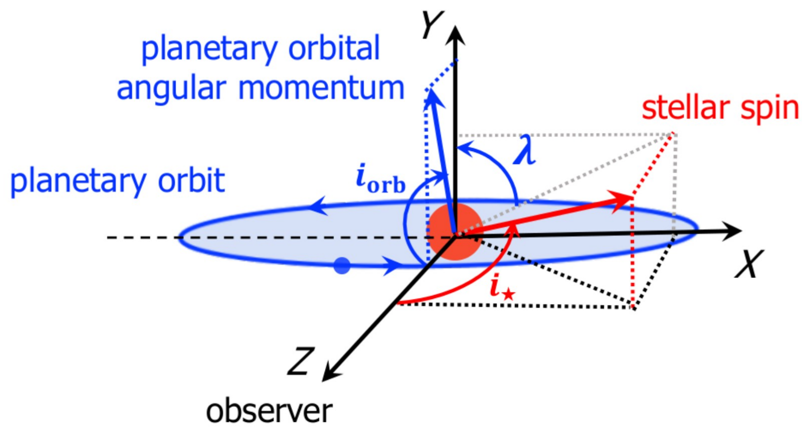

Figure 5.2: The geometry of the projected obliquity angle λ. The spin vector of the star (red) and the normal vector of the planet's orbit (blue) are inclined with respect to the z-axis (LOS) by the angles $i_\star$ and i_{orb} (in this work: i_S and i), respectively. The y-axis is chosen so that the planet's orbit normal vector lies in the y-z-plane. λ is the angle between the POS-projection of the stellar spin (gray dotted line) and the POS-projection of the orbit normal, which coincides with the y-axis. Graphic taken from Sasaki and Suto (2021, in press).

One can choose a Cartesian coordinate system such that the x- and y-axis lie in the POS, while the z-axis points towards the observer and coincides with the LOS (Fig. 5.2). The observed star sits in the origin and rotates around its own spin axis (red), which is generally inclined towards the LOS by an angle i_S (denoted with $i_\star$ in Fig. 5.2).

The planet's orbit has an orbital angular momentum vector which points in the direction of the orbit normal (Fig. 5.2, blue). For convenience, the direction of the y-axis is chosen to be the same as the projection of the planetary angular momentum vector onto the POS. As a result, the orbital angular momentum vector lies in the y-z-plane of this coordinate system. The inclination angle i of the orbit normal is measured relative to the LOS, as indicated in Fig. 5.2 (blue, denoted with i_{orb}), and is identical to the orbit inclination introduced in Sec. 1.1.1.

The projected obliquity λ is then given by the angle between the projection of both the stellar spin axis and the planetary orbital axis onto the POS. In Fig. 5.2, this corresponds to the angle between the gray dotted line and the y-axis. By convention, λ is measured in the direction away from the projected stellar spin axis and $\lambda \in [-180°, 180°]$.

It should be noted that the exact choice of the coordinate system is arbitrary. Alternative coordinate systems are frequently used in the literature, e.g. where one of the coordinate axes coincides with the projection of the stellar spin vector instead of the projection of the orbit normal.

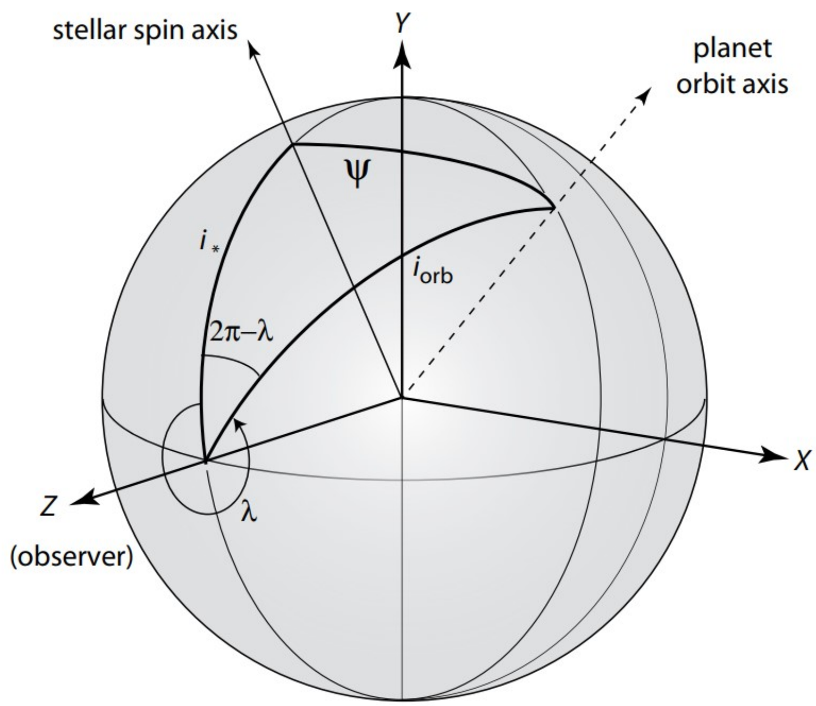

Figure 5.3: The geometric relation of the projected obliquity angle λ and the true obliquity angle ψ. Graphic taken from Perryman (2018).

5.1.1 The true obliquity angle

The RM effect only allows to measure λ, a projection of the actual relative inclination between the stellar spin vector and the planetary orbit normal. The angle between the two vectors before the projection onto the POS is called the *true obliquity angle* ψ (Fig. 5.3). The projected and true obliquity angles are related as (e.g. S. Albrecht et al. 2021):

$$\cos\psi = \sin i_S \sin i \cos\lambda + \cos i_S \cos i. \tag{5.1}$$

In contrast to λ, the convention for ψ is to choose the measurement direction such that $\psi \in [0°, 180°]$.

It should be mentioned that the term *obliquity* is also used in other contexts to designate relative orientations, e.g. for the inclination between a body's rotation axis and its orbit normal. The most prominent example for such a case is the 23.4° inclination of the Earth's rotation axis, but those topics have to be clearly distinguished from the geometry relevant for the RM effect.

In analogy to planetary masses measured with the RV method, which have a degeneracy with the orbital inclination as $v\sin(i)$, a measurement of λ can only constrain the value of ψ by a certain amount, unless information on both the orbital and the stellar spin inclination angles is available. As the RM effect requires a transiting planet, the orbital inclination i

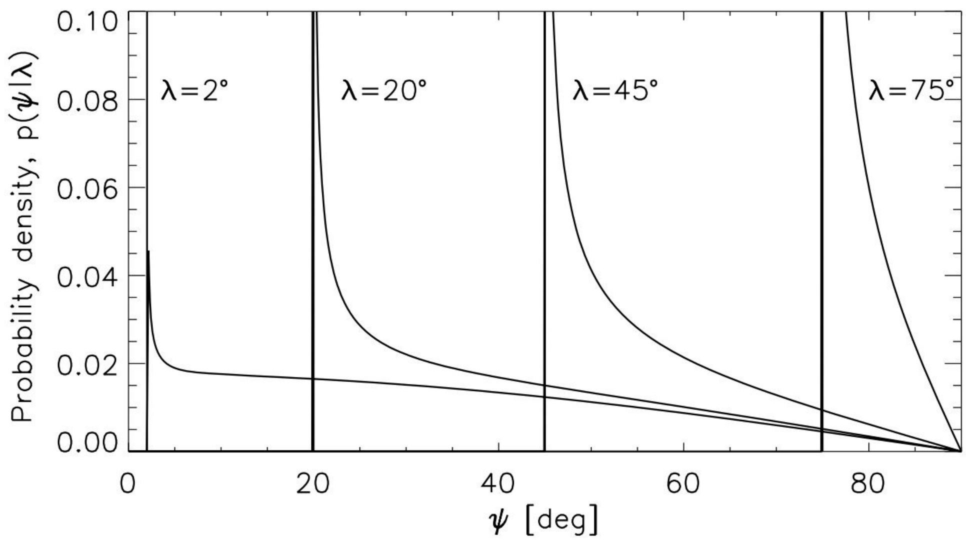

Figure 5.4: The probability density of ψ values for a selection of λ values. For the calculations shown here, the assumptions of $i = 90°$ and a random distribution of ψ were made. Graphic taken from Fabrycky and Winn (2009).

(labeled as i_{orb} in Fig. 5.3) has to be close to 90° and a measurement is typically available from photometric transit observations. However, the inclination of the stellar spin axis i_S (or i_* in Fig. 5.3) can take any value and is unknown in the majority of cases, since direct measurements are complicated (see Sec. 5.3.2 and Sec. 5.4.1). Nevertheless, the most valuable information for planet formation models is the one contained in the physical angle ψ instead of λ, so a consideration of the constraints on ψ for a given value of λ is necessary.

Fabrycky and Winn (2009) analyzed the probability density distribution for ψ in dependence on a given value of λ, shown in Fig. 5.4 for selected λ values. In this case, the assumptions of an edge-on orbit of the planet with $i = 90°$ and a random distribution of ψ values are made. While the first assumption is somewhat justified due to the planet's transit, the latter is possibly unphysical. There may exist mechanisms that favor certain orientations, e.g. aligned orbits with a concentration around $\psi = 0°$, leading to deviations from the random distribution. Nevertheless, the choice of random ψ value distribution was made by Fabrycky and Winn (2009) because it is free from assumptions and preferences of specific mechanisms that prefer some ψ values over others.

As can be seen in Fig. 5.4, any measurement of λ directly gives a lower limit of ψ in the form of $\psi \geq \lambda$. This hard limit only vanishes for λ values close to 90° if $i \neq 90°$ holds for the orbital inclination (Fabrycky and Winn 2009).

Additionally to the lower limit, there is a peak of the probability distribution in Fig. 5.4 at each measured value of λ. A wing extends from the peak towards $\psi = 90°$, owing to the assumed random distribution of ψ. The width of that peak varies, depending on whether λ is small, where it is very sharp, or whether λ is large, in which case the peak is significantly broadened. Based on that, the following interpretation of Fig. 5.4 can be made: as the measured value of λ approaches 90°, it is more probable that ψ is close to λ, while inversely for small λ the constraint on ψ is weaker.

5.2 The RM effect

The RM effect appears as an anomaly in the observed spectral line profile of a rotating star, caused by a transiting companion[37] that is obscuring a part of the stellar surface. It allows to measure the projected obliquity λ, because the time-evolution of the anomaly during the transit depends on λ. For this reason, the RM effect is widely used to determine the alignment between exoplanets and their host stars.

Figure 5.5 illustrates the formation of the RM effect for an exoplanet transiting its host star on an aligned orbit. In the top row, the photometric representation of the transit is shown for three different phases of the transit, representative for the whole process. The three phases are: early transit stage (left), middle of transit (center), and late transit stage (right). The stellar surface has a gradient in its color and brightness from the edges towards the center due to the limb darkening effect, where less flux is contributed from the outer zones. As a consequence, the amount of light blocked by the planet is not constant during the transit, but varies as a function of the planet's distance to the center of the stellar disk.

The second row of Fig. 5.5 illustrates the transit from a spectroscopic perspective. The star's rotation causes one half of the star to approach the observer, resulting in a blueshift of the photons from this half, and the other half to recede from the observer, resulting in a redshift. Since the stellar rotation is a symmetric contribution to the broadening of the spectral lines (see also Sec. 1.2.3), blocking some of the light from a certain part of the stellar surface, corresponding to a certain wavelength, immediately leads to a distortion of the spectral line profile. This behavior is observed as the RM effect.

Depending on the star's properties, the line profile distortion can be measured in two different ways: either as a resolved deformation (Fig. 5.5, third row) or as an unresolved change of the center-of-mass (bottom row) of the spectral lines. The former method is applied for stars with broad spectral lines due to a large rotational velocity and is called *Doppler tomography* (see Sec. 5.3.1).

For stars with a small rotational velocity, where rotation is not the dominant line broadening mechanism and the lines are generally narrow, the spectral lines are typically sampled by only a few pixels of the CCD detector. Therefore, it is not possible to directly resolve any line distortions. In addition, the distortions are affecting a larger portion of the overall line profile and the change of the flux is smaller (compare third and bottom row of Fig. 5.5). Nevertheless, instruments optimized for the detection of exoplanets with the RV method are well suited to measure the resulting variation of the center-of-mass of the spectral lines as anomaly of the classical RV curve. This is the method applied in this work for the observations obtained with MaHPS.

[37]For the rest of this work the companion is assumed to be an exoplanet, although the RM effect occurs also for transiting bodies of other nature.

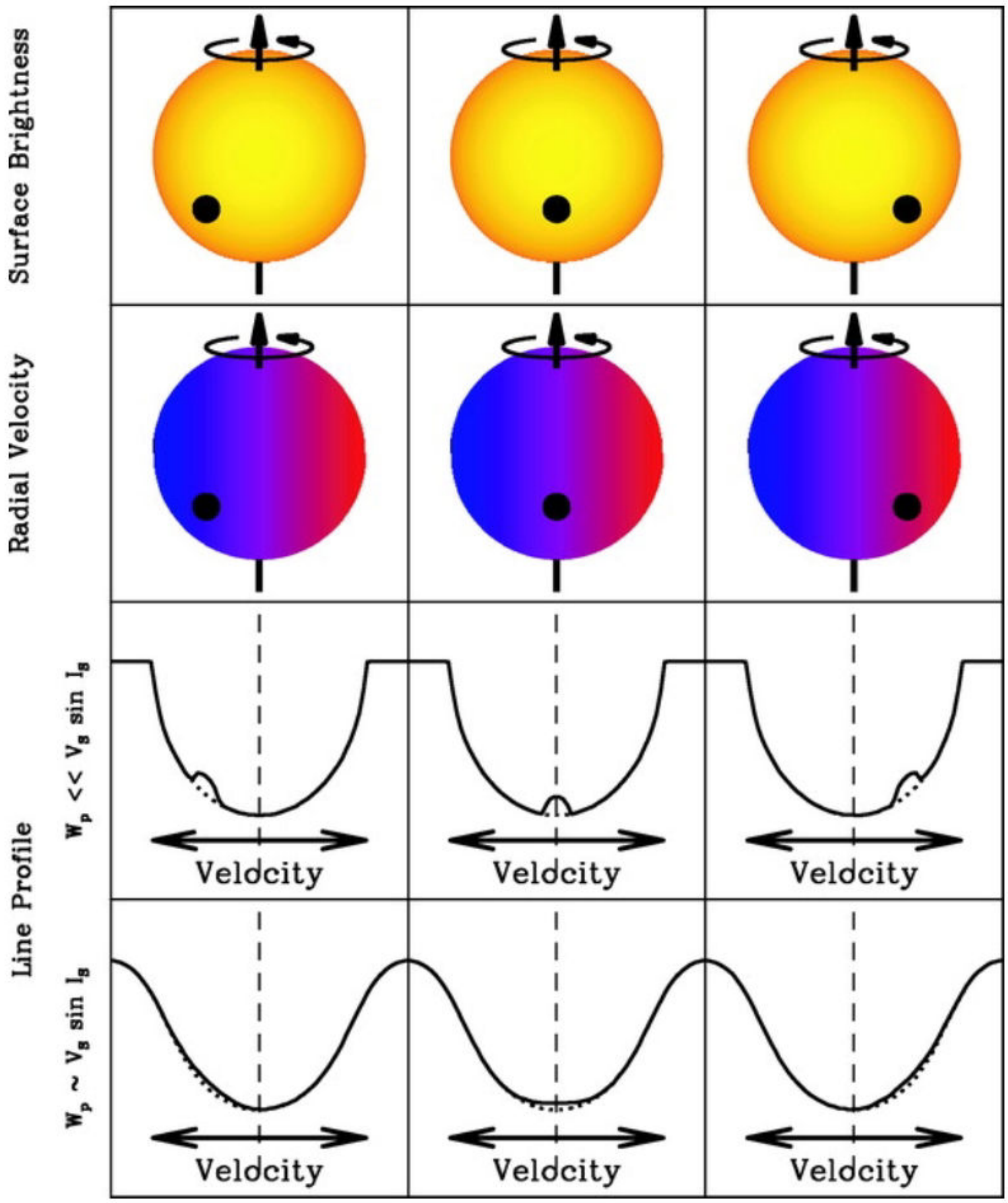

Figure 5.5: The formation of the RM effect as anomaly of the spectral line profile, caused by the transit of a planet. The three columns correspond to different phases during the transit: early stage (left), middle of transit (center), and late stage (right). Upper row: photometric view of the transit; second row: obscuration of blue- and redshifted parts of the stellar surface during the transit; third row: effect on spectral line profile for a rapidly rotating star (see Doppler tomography, Sec. 5.3.1); bottom row: effect on spectral line profile for a slowly rotating star. Graphic taken from Gaudi and Winn (2007).

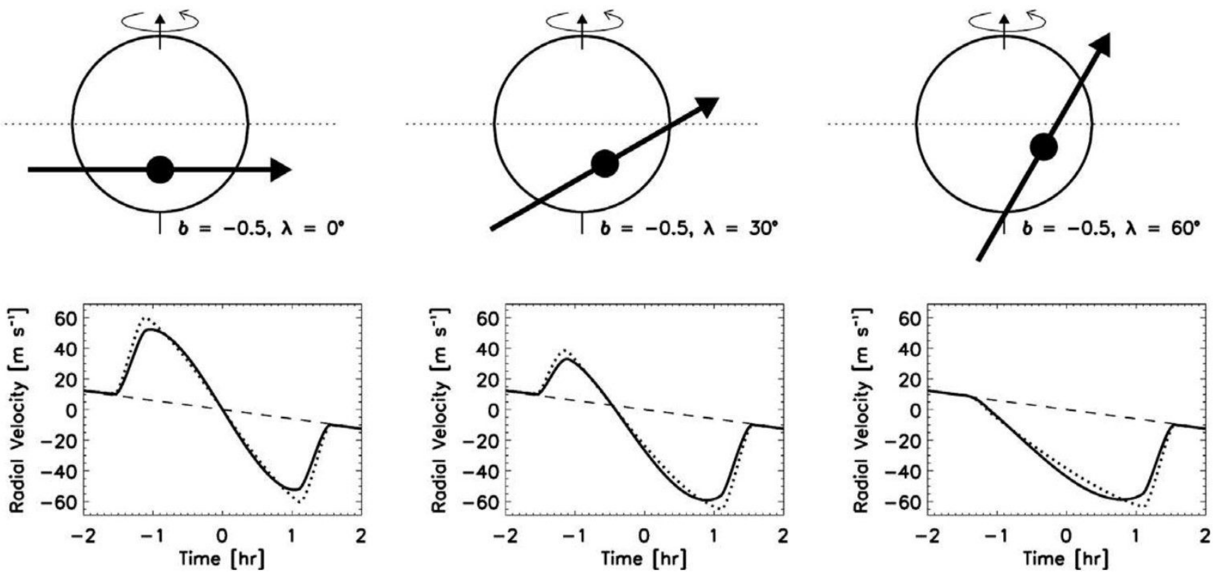

Figure 5.6: The RM effect caused by a planet with three different orbital alignment angles $\lambda = 0°, 30°$ and $60°$ (left to right). Top row: geometry of the transit, where b is the impact parameter; bottom row: corresponding shape of the RV anomaly when adopting a linear (solid line) or quadratic (dotted line) limb darkening model, with the classical RV curve due to the star's orbit around the common barycenter as comparison (dashed line). Graphic taken from Winn (2011).

5.2.1 Examples for the RM effect

It was already stated above that the RM effect allows to measure the projected obliquity λ via the shape of the time curve of the line profile anomaly. In the case of the center-of-mass method, the anomaly can be directly obtained by conducting RV measurements during the transit of the planet.

Examples for the RM effect signature are shown in Fig. 5.6 for different projected obliquities λ. In the top row, the geometry of the planet's orbit around the star is depicted, whereas in the bottom row the RV curve that would be measured for this particular configuration is given. Three different projected obliquity angles are included, from the aligned case with $\lambda = 0°$ (left) over a slightly misaligned orbit at $\lambda = 30°$ (center) to a significantly misaligned system with $\lambda = 60°$ (right).

To facilitate the direct comparison of the three cases, the transit geometries were chosen such that they produce identical photometric light curves (Winn 2011). This is realized by adopting the same impact parameter[38] $b = -0.5$ for all cases, meaning that the planet doesn't cross the disk centrally, but the distance of the closest approach to the center is equal to half the radius of the star (Fig. 5.6, top row).

[38] The impact parameter b indicates the smallest distance of the planet to the center of the disk of the stellar surface during the transit. It is given in units of the stellar radius, so $b = 0$ corresponds to a central transit and $b = 1$ corresponds to the planet grazing the stellar disk at the very edge.

During the transit of the planet, the line profiles of the spectral lines are distorted, however this effect is superimposed with the shift of the spectral lines due to the star's Keplerian motion around the common barycenter with the planet, which is responsible for the classical periodical RV curve (Fig. 5.6, dashed line). Thus, the RM effect always has to be regarded as deviation relative to the classical RV curve. As the transit duration is much shorter than the orbital period of the star, only a small fraction of the Keplerian RV signal is typically shown in the plots of the RM effect, which in most cases can be well approximated by a straight line. In some publications, the RV curve of the RM effect is given after the subtraction of the Keplerian RV component, removing the overall RV trend from the plot.

The exact shape of the RM effect is not only determined by the blocked wavelengths, but also by the overall brightness of the part of the stellar disk that is obscured. One factor that needs to be considered when describing the brightness distribution of the stellar disk is the limb darkening effect. Typical ways to formulate the limb darkening are to assume an either linear or quadratic decrease of the brightness from the center towards the edge of the disk. Figure 5.6 (bottom row) shows the direct comparison of the RM effect when adopting a linear (solid line) or a quadratic (dotted line) limb darkening law.

The most common case of an orbit aligned with the stellar spin axis ($\lambda = 0°$) is presented in the left column of Fig. 5.6. While the planet transits the half of the star approaching the observer, a part of the blueshifted light is blocked, displacing the center-of-mass of the spectral lines towards redder wavelengths and causing a deviation of the measured RVs towards positive values. Conversely, as the planet transits the receding half, a relative blueshift of the spectral lines is measured. Because the planet's velocity is approximately constant during the transit and the planet transits both halves of the star on an equal distance, the resulting curve of the RM effect is symmetric.

Slightly misaligned orbits, as shown in the central column of Fig. 5.6 for $\lambda = 30°$, produce asymmetric signals with a displacement of the measured RVs in both directions. There are also transit geometries for which the RV curve is displaced exclusively in one direction, for instance the last example in Fig. 5.6 (right column) with $\lambda = 60°$ and $b = -0.5$, where only a blueshift is detected. In such cases, only one half of the star is obscured during the transit, so the additional RV shift due to the RM effect does not change its sign.

5.2.2 Modeling the RM effect

In order to obtain λ from observations of the RM effect, a model is needed that can be fit to the data. This model consists of three major components: the transit geometry, the velocity map of the stellar disk and the brightness distribution over the stellar surface. For building an accurate model of the stellar disk with respect to the velocity and intensity distribution, extended knowledge of the star's properties is required.

Since in some situations an estimate of the expected signal amplitude is sufficient, e.g. when evaluating whether RM effect observations of a certain object are feasible, a simple approximation can be made. Neglecting the variation of the intensity and velocity over the different parts of the stellar disk, the maximum amplitude of the RM effect $|\Delta v_R|$ is roughly given as (Winn 2010):

$$|\Delta v_R| \approx \left(\frac{R_P}{R_S}\right)^2 \sqrt{1-b^2}\,(v_{rot}\sin i_S)\,. \tag{5.2}$$

Here, R_P/R_S is the planet-to-star radius ratio, b is the impact parameter and $v_{rot}\sin i_S$ is the rotational velocity of the star, projected onto the LOS. R_P/R_S and b describe the transit geometry and are available from photometric transit observations. Relying on data collected with a different observation technique here does not pose a problem, because spectroscopic observations of the RM effect are expensive in observational time compared to transit photometry. Consequently, blind surveys for the RM effect are not feasible and the RM effect so far only has been measured for planets that are known to show a transit. Thanks to large-scale photometric transit surveys like TESS or WASP[39], a large amount of transit data has become publicly available over the last years and can serve as basis for RM effect observations.

The value of the rotational velocity $v_{rot}\sin i_S$ needed for Eq. 5.2 is not available from photometry, but requires some spectroscopic information. Nevertheless, most bright stars are historically well-studied and measurements of $v_{rot}\sin i_S$ are therefore typically available in the literature. Additionally, some photometric transit surveys feature a large database of reconnaissance spectra for the discovered planetary candidates, as spectroscopic follow-up observations are routinely made to reject possible false positive detections. One example is the *Tillinghast Reflector Echelle Spectrograph* (TRES), which provides spectra for a large portion of planetary candidates from the TESS survey in the Northern sky (e.g. Bieryla et al. 2021). An automated data reduction pipeline measures $v_{rot}\sin i_S$, among other stellar parameters, at a precision sufficient for estimating $|\Delta v_R|$ with Eq. 5.2.

When analyzing data of the RM effect to obtain the obliquity of a planet's orbit, a more exact formulation of the RV displacement due to the RM effect is needed, because Eq. 5.2 does not contain any information on λ. The RV anomaly Δv_R as a function of the planet's position (x, y) on the stellar disk can be generally formulated as (e.g. Montet et al. 2020):

$$\Delta v_R = \frac{\int I(x,y)v(x,y)dS}{\int I(x,y)dS}, \tag{5.3}$$

where $I(x, y)$ is the intensity of the stellar surface as function of the position on the disk, $v(x, y)$ is the radial velocity of the stellar surface as function of the position, and the integral is made over all parts of the disk that are visible to the observer. Information on λ is encoded in the position (x, y) of the planet.

Generating exact or good approximate models for $I(x, y)$ and $v(x, y)$ is a demanding task, as they need to consider a range of effects that influence the brightness distribution of the stellar disk or the velocity component along the LOS as function of position on the

[39] *WASP* is the *Wide-Angle Search for Planets*, a full-sky survey for transiting exoplanets, carried out by two fully robotic ground-based telescopes, one located in the Northern Hemisphere at the island of La Palma (Spain), the other situated in the Southern Hemisphere in South Africa.

stellar surface. There are different ways to obtain analytical or numerical formulations of $I(x, y)$ and $v(x, y)$, which incorporate different effects and contributors to the intensity and velocity distribution. The most widely used formulations include those by Ohta et al. (2005), Giménez (2006), Hirano et al. (2010) or Boué et al. (2013).

The derivation of such models is out of the scope of this work, instead a discussion of the individual contributions to the velocity (Sec. 5.2.3) and intensity distribution (Sec. 5.2.4) is given in order to enable a thorough understanding of the related influences on the measured RV curve. Furthermore, the model used for the analysis in Chap. 6, which is based on the `starry` package by Luger et al. (2019) and was applied to the RM effect by Bedell et al. (2019), Montet et al. (2020), and Johnson et al. (2021, subm.), will be outlined.

Before further discussion, it has to be mentioned that different RV observation techniques lead to slightly differing RV values when measuring the RM effect. This is due to the fact that the RM effect causes a change of the line profile, which should be fit in order to obtain exact results, as is done for Doppler tomography. When employing the center-of-mass method however, it's not possible to fit the line profile because the number of data points per line is not sufficient.

At the currently prevailing RV precisions, the difference between fitting the line profile and measuring the center-of-mass is small enough to vanish inside the error bars, but it has to be kept in mind that these RV results are technically not exact. Additionally, there is a small difference in the obtained RV values for spectra with simultaneous (emission source) calibration and absorption gas cell calibration, due to the way the line center is determined. For the first, CCFs or lately χ^2 fitting are used to recover the relative shift of the spectrum relative to a template (see Sec. 4.3.3), while for gas cells the stellar template spectrum is multiplied with the gas spectrum and convolved with the point spread function[40] (PSF) of the instrument in order to make a comparison with the observed spectrum (e.g. Butler et al. 1996). A detailed discussion of this topic and RM effect models that are customized for each detection methods are given by Boué et al. (2013).

5.2.3 Velocity distribution of the stellar disk

Stellar rotation is the basis for the RM effect. The key parameter describing the rotation of a star is $v_{rot} \sin i_S$, which gives the velocity component along the LOS of the velocity vector at the star's equator. There is a degeneracy with the inclination of the stellar rotation axis i_S, in analogy to the RV measurement of the mass of an exoplanet, caused by the property of the RV method to be sensitive only to motions in the direction of the LOS.

During a transit in front of the star, the exoplanet usually does not only cover the edge of the star, but also the inner parts where the rotational velocity along the LOS is

[40]The point spread function (PSF) is the function that describes the actual light distribution recorded at the detector when observing an ideal point source at infinite distance from the observer. The PSF consists of several components, like the atmospheric spreading of the light distribution from a delta function to a disk (typically described with an Airy function), the imaging properties of the telescope's and the instrument's optics, as well as possible obstructions of the light path, often present due to the mounting structures of the optical element.

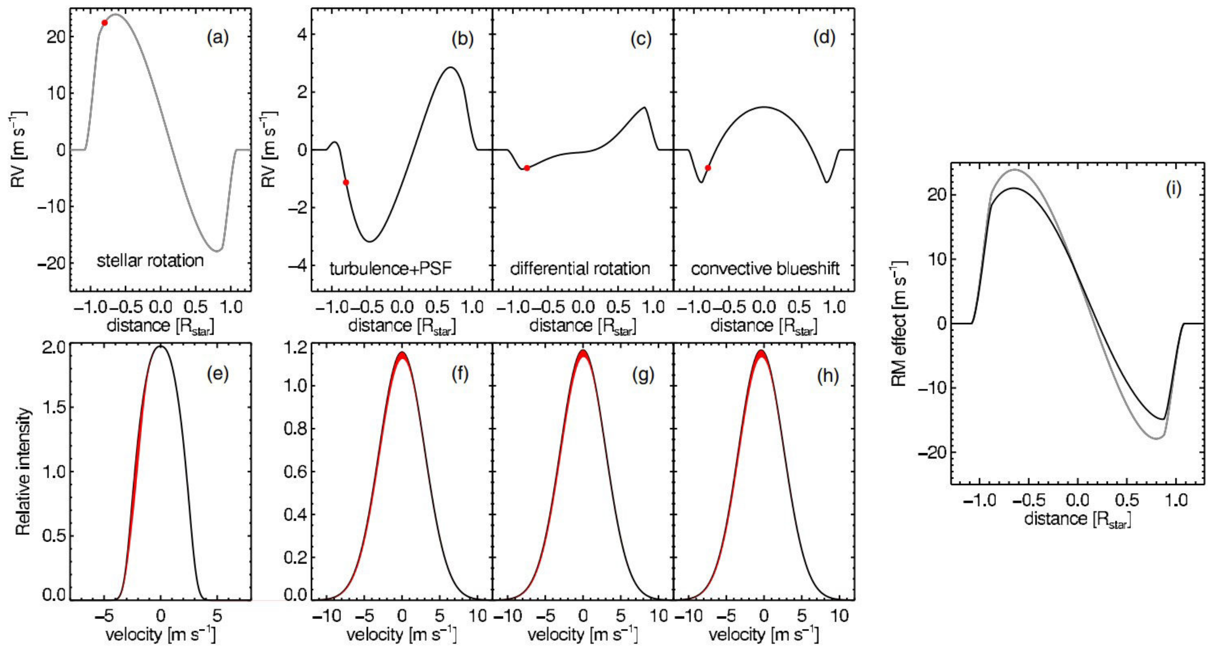

Figure 5.7: The RM effect signature (panels a-d) and spectral line profile distortion (panels e-h) caused by different components of the velocity field on the stellar surface for a planet-star system with parameters $\lambda = 40°$, $v_{rot} \sin i_S = 3\,\mathrm{km/s}$, $R_P/R_S = 0.12$, and $b = 0.2$. The red areas in panels (e-h) correspond to the amount of light blocked by the planet at the transit phase shown by the red dot in panels (a-d), exaggerated by a factor of 4 for visibility. Panel (a) and (e): stellar rotation contribution, assuming a rigid rotator; (b) and (f): combined influence of turbulence and PSF broadening; (c) and (g): contribution from differential rotation; (d) and (h): symmetrical contribution from the convective blueshift; (i): overall RM effect with all contributions combined (black line), compared to the curve from rigid rotation alone (gray line, same as a). Graphic taken from S. Albrecht et al. (2012).

smaller. If the star is assumed to exhibit rigid rotation, then the LOS velocity v_z at any given position (x, y) on the stellar surface disk, in a coordinate system where the stellar rotation axis coincides with the y-axis (Fig. 5.3), is determined by (e.g. Gray 2005):

$$v_z = x\ \Omega\ \sin i_S, \tag{5.4}$$

with Ω being the angular rotation velocity of the star. In this scenario of rigid rotation, only the distance of the planet perpendicular to the stellar rotation axis, projected to the POS, has an effect on v_z. Considering the special case of the planet obscuring the stellar disk at the equator and the very edge of the disk, where $x = R_S$, then Eq. 5.4 yields $v_z = R_S \Omega \sin i_S = v_{rot} \sin i_S$.

Figure 5.7 (a) illustrates the RV signal of the RM effect which is caused solely by the rigid rotation of the host star. Assuming constant brightness over the stellar disk, the RV curve is completely determined by four parameters: $\lambda = 40°$, $v_{rot} \sin i_S = 3\,\mathrm{km/s}$,

$R_P/R_S = 0.12$, and $b = 0.2$. Note that the RM effect curve is asymmetric because $\lambda \neq 0°$ and that the x-axis of the plot is given in units of the stellar radius R_S, indicating the planet's spatial position instead of the transit time. In most cases, the transit of the planet is short enough so that uniform motion during the transit is a good approximation, making the distance and time coordinates interchangeable.

The effect of the occultation on the spectral line profile when regarding only rigid rotation is shown in Fig. 5.7 (e). The black line gives the regular line profile and the red area indicates the missing intensity when the planet is located at the transit position indicated by the red circle in the panel above. For better visibility, the red area is exaggerated by adopting $R_P/R_S = 0.24$, which is also true for Fig. 5.7 (f-h).

In Fig. 5.7 (e), the width of the spectral line is determined only by rotational broadening and the remaining velocity field components (f-g) further broaden the line. For stars with higher $v_{rot} \sin i_S$, the initial line profile is broader and at the same time the peak intensity decreases, washing out the spectral line. As a result of that, the error in the determination of the line center increases, giving intrinsically larger error bars for RV measurements of stars that have higher rotation velocities. The rotation velocity can even be the dominant line broadening mechanism and the main driver of uncertainty, as is the case for instance for the star HAT-P-2, which was observed as part of this work. Therefore, although the amplitude of the RM effect scales at least partly with $v_{rot} \sin i_S$, rapidly rotating stars are often not suited for measurements with the center-of-mass method.

As stars are not built from rigid material, the velocity field is not fully described by rigid rotation. Further effects like differential rotation, turbulence and general dispersions of the velocity or temperature are a source of errors if they are neglected.

Differential rotation

Assuming rigid rotation with $v_{rot} \sin i_S$ is a simplification used to express the velocity field of the stellar disk to the first order. In reality, the angular velocity Ω of a star is not constant over the stellar disk since stars are not rigid bodies, so a modified description of the rotational velocity is needed. Differential rotation causes the angular velocity Ω to vary depending on the distance to the equator. If a differential rotation behavior similar to that observed for the Sun is assumed, the angular velocity is a function of the latitude l (e.g. Short et al. 2018, App. C):

$$\Omega(l) = \Omega_{eq} \left(1 - \alpha \cos^2 l\right), \tag{5.5}$$

where Ω_{eq} is the rotational angular velocity at the star's equator and $\alpha = (\Omega_{eq} - \Omega_{pol})/\Omega_{eq}$ is the (linear) shear parameter with Ω_{pol} being the angular velocity at the star's pole. Substituting Eq. 5.5 into Eq. 5.4 yields the RV for a given position on the stellar disk with the effect of differential rotation included.

In general, stars are rotating more slowly at the poles than at the equator. Typical values for the shear parameter are for instance $\alpha \approx 0.163$ for the Sun (e.g. Sasaki and Suto 2021, in press) and $\alpha = 0.278 \pm 0.093$ for HD189733 (Cegla et al. 2016), for which RM effect observations are presented in Sec. 6.2.

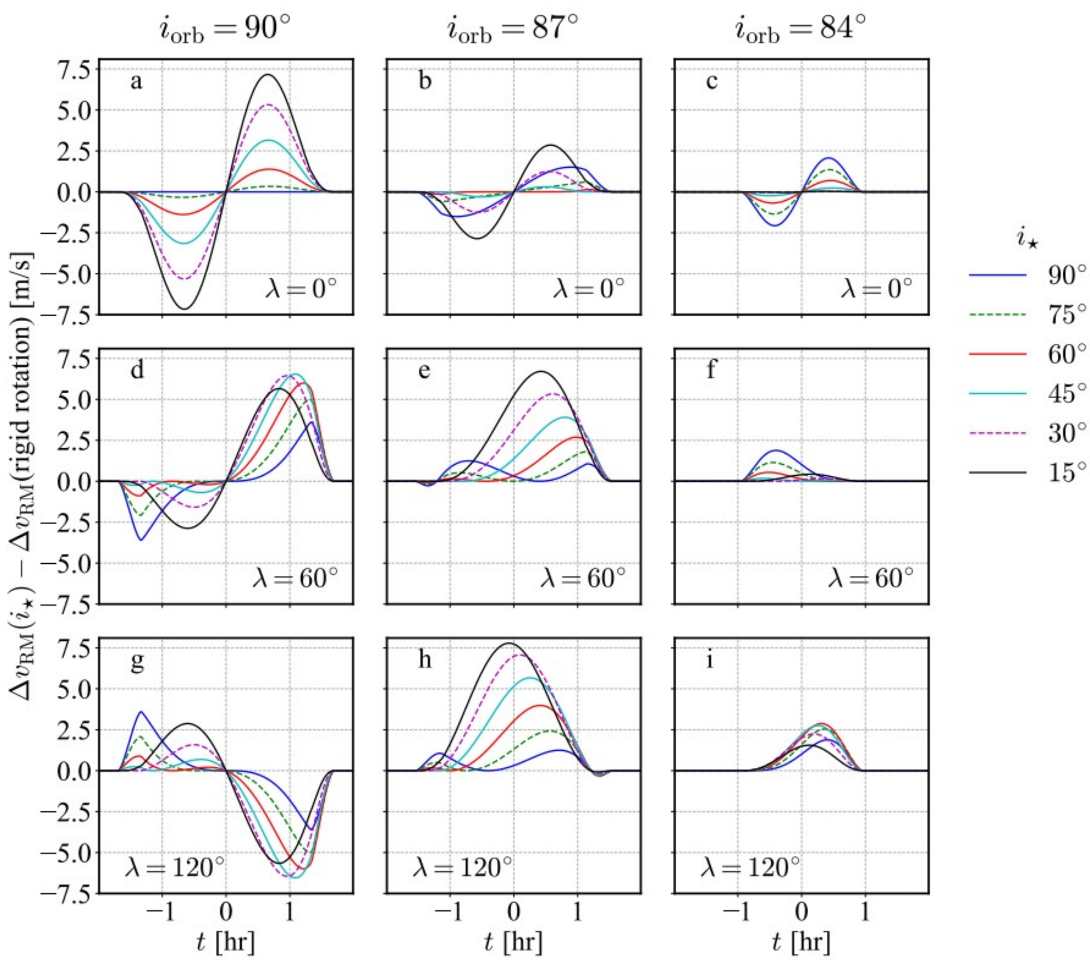

Figure 5.8: The contribution of differential rotation to the RM effect, isolated from the rigid rotation contribution, as function of λ (top to bottom), i_{orb} (left to right, in this work: i) and $i_\star$ (colored lines, in this work: i_S), assuming solar shear parameters $\alpha_2 \approx 0.163$ and $\alpha_4 \approx 0.121$. Graphic taken from Sasaki and Suto (2021, in press).

The dependence of Eq. 5.5 on the latitude l implies that for transits along or parallel to the equator of the star, the differential rotation only causes a time-independent influence on the measured RVs. The influence becomes time-dependent and increases in amplitude as the planet passes over more latitudes during a transit, which is a function of the obliquity λ, the inclination of the stellar rotation axis i_S and the inclination of the orbit i.

Figure 5.8 illustrates how the shape and amplitude of the differential rotation effect changes with λ, i_S, and i. Here, Sasaki and Suto (2021, in press) employ an extended formulation for the differential rotation, which has the form $\Omega(l) = \Omega_{eq}\,(1 - \alpha_2 \cos^2 l - \alpha_4 \cos^4 l)$. Overall, the RV signal caused by differential rotation decreases with decreasing i and increasing i_S. The latter relation can be understood as the lines of equal latitudes on the star's surface appear closer together when looking at the star from a more pole-on orientation, corresponding to the case of a small i_S. A transiting planet will then consequently traverse more latitudes than for a star with $i_S = 90°$.

In Fig. 5.7 (c), the additional RV signal due to differential rotation for the presented transit geometry with $\lambda = 40°$ is shown. A solar-like shear parameter $\alpha \approx 0.163$ is adopted. In this example, the amplitude is relatively small with $\Delta v_R < 2\,\mathrm{m/s}$, less than 10% of the total RV signal amplitude. Nevertheless, Fig. 5.8 demonstrated that the amplitudes of the differential rotation components can also take larger values and cannot simply be neglected.

When rigid and differential rotation are combined, the velocity field on the stellar disk can be analytically expressed with a formalism that is given for instance by Short et al. (2018) and utilized in the `starry` package (Montet et al. 2020):

$$v(x, y) = \Omega_{eq}\,(Ax + By)\left(1 - \alpha\,(-Bx + Ay + Cz)^2\right), \tag{5.6}$$

where x, y are the Cartesian coordinates on the stellar disk in the coordinate system of Fig. 5.2, with the planet orbit normal along the y-axis. Furthermore, $z = \sqrt{1 - x^2 - y^2}$ and A, B, C are coefficients that are needed to describe the geometric orientation of the stellar rotation axis, the orbital axis of the planet, and the LOS relative to each other (Montet et al. 2020):

$$\begin{aligned} A &= \sin i_S \cos\psi; \\ B &= \sin i_S \sin\psi; \\ C &= \cos i_S. \end{aligned} \tag{5.7}$$

Keeping in mind that ψ and λ are related via Eq. 5.1, it becomes clear that $v(x, y)$ is indeed a function of λ. The parameters that can be fit with the approach outlined here are λ, i_S, v_{rot} and α (Bedell et al. 2019). The presence of differential rotation in principle allows to disentangle v_{rot} and i_S, however in most real cases the influence of differential rotation on the RV curve disappears in the error bars, only allowing to fit $v_{rot} \sin i_S$ as one combined parameter (Hirano et al. 2011).

The `starry` package used for the analysis in this work allows to analytically calculate $v(x, y)$ by transforming the polynomial in Eq. 5.6 to a sum of spherical harmonics, which can be more efficiently evaluated at any given position (x, y). The exact details of this procedure are found in Luger et al. (2019) and Montet et al. (2020).

Turbulence

The turbulent motion of plasma on the stellar surfaces contributes to the broadening and displacement of the spectral lines as observed in RV measurements. Two different types of turbulence can be distinguished, which have to be treated each in a unique way: microturbulence and macroturbulence.

Microturbulence arises from turbulence cells with a size considerably smaller than the mean free path length of a photon emitted by the star. The effect on the line profile is a symmetric broadening of the spectral lines, similar to thermal broadening, as one averages over a large amount of photons and turbulence cells that are statistically distributed. The broadening by microturbulence can be expressed as Gaussian with width ξ, which is typically of the order of $\xi \sim 1$ to 2 km/s (Gray 2005). In order to obtain an accurate representation of the intrinsic line profile, the microturbulence broadening needs to be convolved with the Gaussian for thermal line broadening (Hirano et al. 2011).

Macroturbulence in contrast is caused by turbulence cells that are larger than the mean free path length of a photon, so all photons from that cell take on the cell's overall velocity. When integrating over the complete stellar surface, which contains many macroturbulence cells, the effect appears as further line broadening (e.g. Gray 2005), however if the stellar disk is not regarded in its entirety, for instance because a small portion is blocked during the transit of a planet, a small RV shift of the line profile is the result.

While microturbulence causes a line broadening that is independent of the position on the projected stellar disk, macroturbulence produces a signal that varies over the stellar disk because its amplitude depends on the angle of the LOS relative to the stellar surface (e.g. Gray 2005; S. Albrecht et al. 2012). This can be intuitively understood when considering a convection cell, where the radial motion of the material is clearly much more pronounced than the tangential motion. If such a cell is located in the center of the stellar disk, RV measurements would pick up the radial motion component, however if the cell was located at the disk edge, only the smaller tangential velocity of the material can be measured.

One possibility to parametrize macroturbulence is by employing a broadening function with width ζ_R and ζ_T, which represent the average velocity of the radial and tangential component of macroturbulence, respectively. A common approach is to assume both parameters to have the same value $\zeta = \zeta_R = \zeta_T$ and the exact magnitude of ζ can be determined from empirical relations with the effective temperature of the star (e.g. S. Albrecht et al. 2012).

The influence of macroturbulence on the RV curve of the RM effect can be obtained by integrating both the radial and tangential component over the whole stellar disk and subtracting the areas that are occulted by the planet (S. Albrecht et al. 2012). A quantitative example for the variation of the RV curve with different macroturbulence parameters is shown in Fig. 5.9 (top panel) for the planetary system XO-3. The RV curve when employing the macroturbulence parameter initially chosen for this system (black line) is shown together with the RV curves obtained with a ζ values that is 30% smaller (red line) or larger (blue line). The bottom panel gives the relative deviation of the RV curves with modified ζ from the initial model.

Although the adopted macroturbulence parameters in Fig. 5.9 change by as much as 30%, the difference in the RV curves is only of the order of a few m/s or a few percent of the total amplitude of the RM effect. While the RM effect could in principle be used to measure ζ (S. Albrecht et al. 2012), Fig. 5.9 makes clear that this is not feasible for the majority of observations, as the error bars of the RV determination are typically of a comparable size. Vice versa, as long as the ζ chosen for the modeling of the RM effect is in the correct order of magnitude, which can be assumed when using one of the empirical relations, there should be no negative influence on the measurement of λ or other parameters from the observed RV curve.

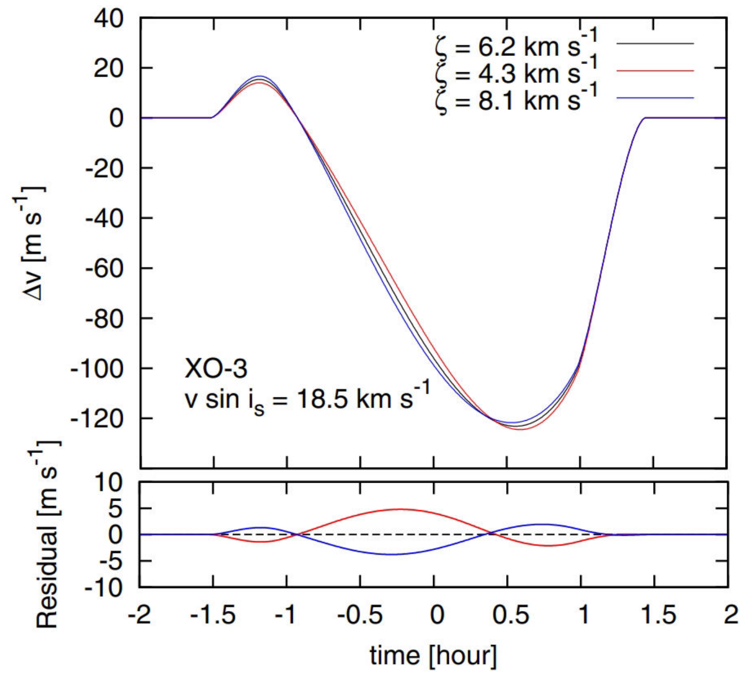

Figure 5.9: Variation of the RV curve of the RM effect due to macroturbulence. Black: macroturbulence parameter ζ determined empirically from the temperature of the star XO-3; red: reduction of ζ by 30%; blue: increase of ζ by 30%. Top panel: expected RV curve of the RM effect for all three cases; bottom panel: deviation of the blue and red line from the black reference curve. Graphic taken from Hirano et al. (2011).

Micro- and macroturbulence are not incorporated in the formulation of $v(x, y)$ used in the `starry` package (Montet et al. 2020). However, for the RV measurements with MaHPS presented in Chap. 6, the error bars of the individual RV data points are relatively large compared to the overall amplitude of the RM effect, easily absorbing any uncertainties from not considering turbulence effects.

Other line broadening mechanisms

Further mechanisms that cause spectral lines to appear broadened, but are not associated with a shift of the position of the line center, are briefly summarized here.

The line broadening due to the instrumental profile of a spectrograph, also called PSF broadening, can be approximated by a Gaussian, the width of which is dependent on the resolution of the spectrograph. Typical values for the PSF broadening are 3.6 km/s for a spectrograph with resolving power $R \sim 45000$, or 1.9 km/s at $R \sim 90000$ (Hirano et al. 2011). The combined effect of both PSF broadening with a magnitude of 2.2 km/s and macroturbulence with $\zeta = 3$ km/s on the RV curve of the RM effect is shown in Fig. 5.7 (b). The change of the corresponding line profile is given in panel (f).

In addition to the line broadening due to the star's temperature, rotation and tur-

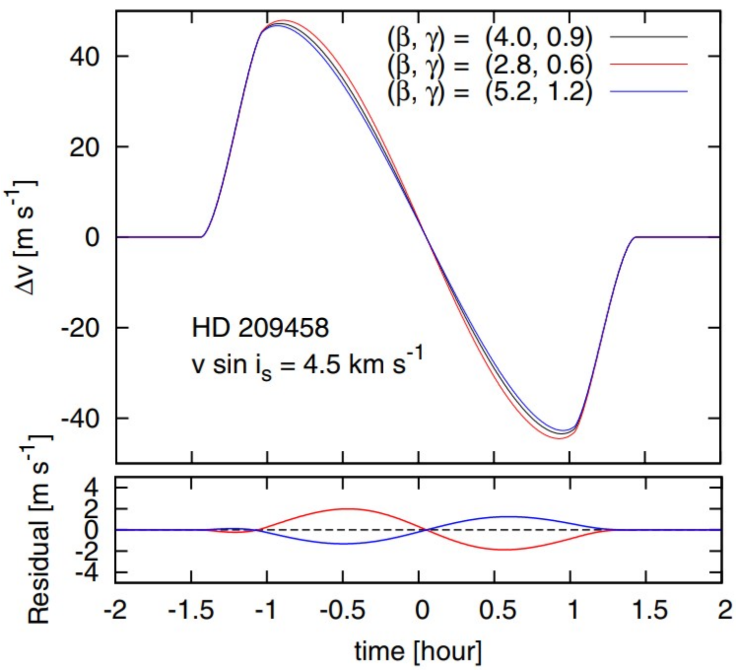

Figure 5.10: Variation of the RV curve of the RM effect due to Gaussian and Lorentzian line broadening mechanisms with width β and γ, respectively. Black: line broadening parameters (β, γ) as determined for HD209458; red: reduction of (β, γ) by 30%; blue: increase of (β, γ) by 30%. Top panel: expected RV curve of the RM effect for all three cases; bottom panel: deviation of the blue and red line from the black reference curve. Graphic taken from Hirano et al. (2011).

bulence, minor contributions come from collisional (pressure) broadening and the Zeeman effect, causing a splitting of the atomic energy levels. These broadening terms are small compared to the effects listed in the beginning and can be incorporated by using a Lorentzian function with a small width of $\sim$1 km/s (e.g. S. Albrecht et al. 2012), which is convolved with the Gaussian profile from the other broadening mechanisms.

Figure 5.10 (top panel) displays how the RM effect varies as the widths of the Gaussian function representing microturbulence (β) and the Lorentzian function representing the broadening caused by collisions and Zeeman splitting (γ) are modulated. Similar to Fig. 5.9, the initially adopted widths (black line) are reduced or increased by 30% (red and blue line), resulting in a RV difference of a few m/s (bottom panel).

Convective blueshift

The effects previously discussed mainly manifest themselves as broadening of the spectral line profile. In contrast, the convective blueshift causes an overall shift of the spectral line center towards smaller wavelengths, as the name already implies. The convective motion of material at the star's surface leads to a blueshift of photons emitted by material rising towards the surface and a redshift of photons emitted by material falling back towards the star's center. If the amount of emitted photons would be equal for both scenarios, a symmetric velocity distribution contributing as a further line broadening would be the result. However, the rising material is hotter and thus also brighter than the falling components, producing an excess of blueshifted photons in the form of an asymmetry of the spectral line profile.

The exact shape of the line asymmetry due to the convective blueshift is a function of the position on the stellar disk, as convection is mainly a radial motion. Areas at the edge of the star show only a small signature of the convective blueshift, while the effect is maximized at the center of the disk, where the motion is parallel to the LOS. When measuring relative RV shifts of a star, the convective blueshift can be ignored as long as one integrates over the same part of the stellar disk, in which case the line asymmetry is kept constant. For the RM effect, the contributing stellar disk area changes as the planet blocks different parts during its transit. Therefore, an additional RV signal due to the changing line asymmetry is expected.

A good approximation of the convective blueshift can be made by assuming that the maximum blueshift, measured at the disk center, decreases with $\cos\theta$ towards the disk edge, where θ is the angle between the LOS and the normal vector of the considered surface element (Shporer and T. Brown 2011). It has to be noted that the RV shift caused by the convective blueshift is only depending on the distance from the center of the stellar disk and is completely independent of λ or $v_{rot} \sin i_S$. Therefore, the convective blueshift always produces a symmetric RV variation, regardless of the transit geometry of the system, as illustrated for example in Fig. 5.7 (d) for a convection velocity as observed in the Sun.

A detailed discussion of the influence of convective blueshift on RM effect measurements is given by Shporer and T. Brown (2011). The conclusion from that consideration is that, for stars typically observed in RV observations, the RV variation during a transit due to the convective blueshift is of the order of $\sim$1 to 2 m/s. The overall amplitude scales with the temperature of the star, as the convection flows are generally faster for hotter stars and therefore the blueshift is more pronounced. Given that the RV signal from the convective blueshift is symmetric but the curve of the RM effect may be asymmetric, it is possible that λ measurements are slightly biased towards orbits that are polar or well-aligned. Nevertheless, the convective blueshift effect is still small compared to the size of the error bars of most RM effect observations and an incorporation into the RV models is only needed for extremely high-precision observations.

5.2.4 Intensity distribution of the stellar disk

The curve of the RM effect depends not only on the velocity field $v(x, y)$ on the stellar surface, but also on the intensity distribution $I(x, y)$, as stated in Equation 5.3. The intensity is a function of the position on the stellar disk, but also contains time-variable components. A summary of the most relevant effects is given in the following.

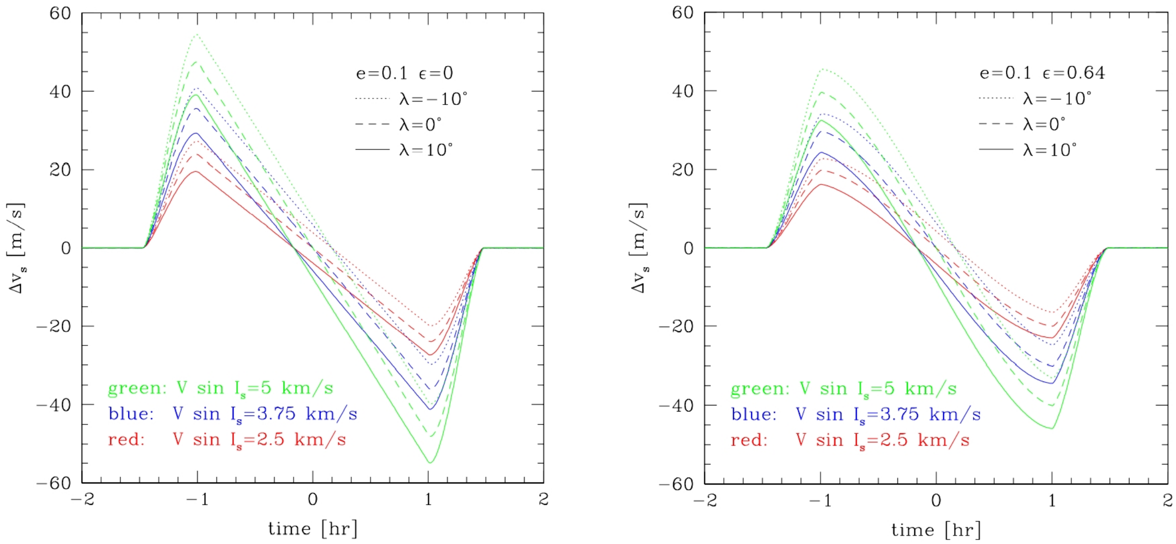

(a) RM effect without limb darkening. (b) RM effect with linear limb darkening.

Figure 5.11: Comparison of the RV curve expected from the RM effect without limb darkening (a) and with linear limb darkening (b) adopting $c_1 = 0.64$. The color of the curves indicates the used rotational velocity $v_{rot} \sin i_S$ and the line style corresponds to different alignment angles λ. Graphic taken from Ohta et al. (2005).

Limb darkening

The most important effect that has to be considered when modeling the intensity distribution for the RM effect curve is the limb darkening, the fact that stars appear darker at the edge of the disk than at the center. Different formulations are proposed in the literature to mathematically express the intensity variation as a function of the distance to the center (e.g. Short et al. 2018). The most commonly used limb darkening models for transiting exoplanets are the linear and quadratic forms given by:

$$I(\mu) = I_0 \left(1 - c_1(1-\mu)\right) \qquad \text{linear;} \qquad (5.8)$$

$$I(\mu) = I_0 \left(1 - c_1(1-\mu) - c_2(1-\mu)^2\right) \qquad \text{quadratic.} \qquad (5.9)$$

Here, I_0 is the intensity of the star at the center of the disk, c_1 and c_2 are the intrinsic limb darkening coefficients of the observed star and $\mu = \sqrt{1-r^2}$ parametrizes the distance to the disk center with the normalized radial coordinate $r = \sqrt{(x^2+y^2)/R_S^2}$.

Limb darkening has to be included when modeling the RM effect, because the amount of light contributed from different positions on the stellar disk varies, resulting in a different magnitude of the center-of-mass shift of the spectral lines as the planet blocks different areas. Figure 5.11 shows a comparison of the RV curve due to the RM effect without any limb darkening (a) and with a linear limb darkening, adopting $c_1 = 0.64$ (Ohta et al. 2005).

The rotational velocity of the star (green, blue and red colors) and the orbital alignment of the planet (solid, dashed and dotted lines) are also varied. In this particular case, the amplitude change of the RV signal is of the order of $\sim$5 to 10 m/s, emphasizing the necessity to take limb darkening into account.

Similarly to the convective blueshift, limb darkening is independent of the transit geometry, leading to a symmetrical RV signal that is superimposed to the possibly asymmetrical velocity shift due to the RM effect.

The limb darkening effect implemented in `starry` makes use of the quadratic formulation (Eq. 5.9) in the q_1, q_2 notation proposed by Kipping (2013), where

$$\begin{aligned} q_1 &= (c_1 + c_2)^2\,; \\ q_2 &= \frac{c_1}{2\,(c_1 + c_2)}. \end{aligned} \tag{5.10}$$

The reason for this choice of limb darkening coefficients is that the complete physically allowed parameter space is contained in $q_1, q_2 \in [0, 1]$, allowing for a more efficient way to determine the coefficient values in a fit.

Since the quadratic limb darkening is expressed by a polynomial of order 2, it can be easily transformed into a spherical harmonic of 2nd degree (Montet et al. 2020; Luger et al. 2019). This has the advantage that a fully analytical model is used that gives everything needed to evaluate the integrals in Eq. 5.3. The analytical property of the functions for $I(x, y)$ and $v(x, y)$ is even preserved in the `starry` approach of employing spherical harmonics, as the multiplication of two spherical harmonics yields another spherical harmonic of a higher degree, in this case of degree 5.

Star spots

Irregularities in the brightness of the stellar surface, like dark star spots or bright plages[41], impact the intensity distribution function of the stellar disk $I(x, y)$. As a further complication, such phenomena are typically time-variable, as they have lifetimes on the order of several days to weeks while at the same time being coupled to the star's rotation period, when the side affected by star spots rotates into or out of view.

One effect of star spots on RV measurements is a time-variable change of the slope of the RV curve of Keplerian motion, parametrized by K. When conducting measurements of the RM effect, the underlying orbital component of the RV curve therefore can be subject to errors. Using values of K determined from observations of the planet's orbit in other nights than that of the transit could have negative effects on the measurement of λ, which is why K is usually included in the RM effect model as a free fitting parameter (S. Albrecht et al. 2012).

[41] Star spots and plages are parts of the stellar surface that are darker or brighter, respectively, than the surrounding regions. The two are often observed in conjunction with each other, with plages typically surrounding star spots. As both phenomena can be described similarly and only the sign of the intensity change needs to be inverted, in the following only star spots will be considered.

RV measurements during the transit of the planet are also affected by star spots and can lead to errors in the determination of λ as large as $\sim 30°$ to $40°$ (Oshagh et al. 2016, 2018). In general, the effect is stronger if the transiting planet is small, has good alignment or the host star is young and thus more active.

Figure 5.12 shows the difference between the signal of the RM effect without (red line) and with (blue line) a star spot, after subtraction of the Keplerian RV signal. If the transiting planet does not cross the star spot (Fig. 5.12 a), the deviation during the transit is small with a few m/s and larger just before and after the transit, owing to the alteration of the Keplerian signal. In case the planet traverses over the star spot (Fig. 5.12 b), an additional deformation of the RM effect curve with an amplitude of $\sim$10 m/s can be observed.

The influence of star spots on RV measurements can be reduced by employing suitable observation strategies. Possibilities are to either conduct spectroscopic and photometric observations in parallel, which allows to derive a model of the currently present star spots from the photometry data set, or to carry out RV measurements for several transits of the planet at a time separation on the order of months, so the effects of the star spots can be averaged out. A further option lies in executing RV measurements in infrared instead of optical bands, where star spots are generally much less pronounced (Oshagh et al. 2016, 2018).

In this work, star spots were neglected in the model for $I(x, y)$, as the error bars of the obtained data are larger than the influence of star spots. However, `starry` allows to include star spots as additional spherical harmonics if a more precise analysis of RV data is desired (Luger et al. 2019).

Wavelength dependence

The exact description of the RM effect with Eq. 5.3 depends on the wavelength which is considered. As the observations for this work were made at a wavelength range fixed by the utilized instrument and no data sets from other instruments were used, the wavelength dependence is not a factor. Nevertheless, it is presented for completeness.

The reason for the wavelength dependence, or chromaticity, is twofold: On the one hand, the impact of star spots on the form of $I(x, y)$ strongly varies with the wavelength, as the intensity of star spots rapidly decreases when observing at longer wavelengths. On the other hand, the integral over the visible parts of the stellar disk in Eq. 5.3 directly depends on the apparent size of the planet, which may be subject to change for different wavelengths, for instance due to absorption features in the planet's atmosphere.

The influence of star spots, or more generally stellar activity, on the RV curve of the RM effect can be seen in Fig. 5.13. The RM effect during a transit of V1298 Tau was observed simultaneously with different instruments covering various wavelength regions. The chromaticity of the RM effect is especially stressed by the direct comparison of RV measurements with the PEPSI spectrograph, split into a short wavelength (yellow points) and long wavelength (light blue points) optical path, where systematic effects due to different instrumentation can be ruled out (Johnson et al. 2021, subm.). Both the slope of the RV

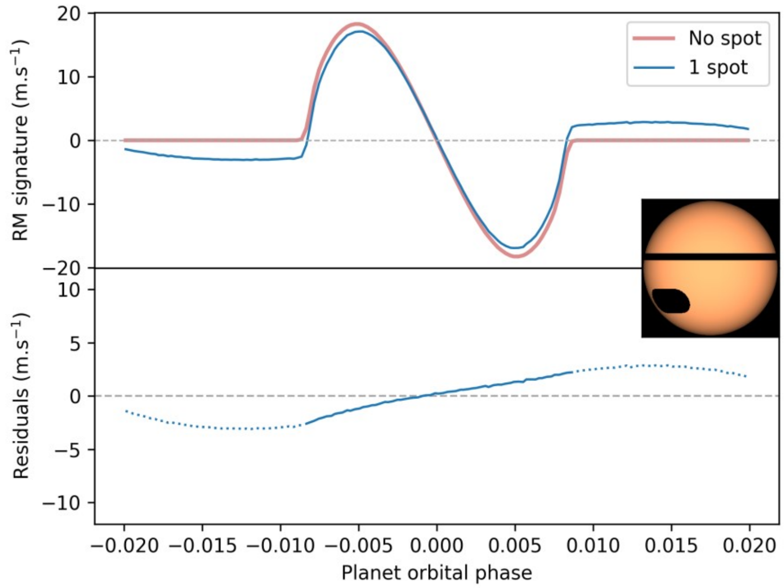

(a) The planet transit trajectory and the star spot are separated.

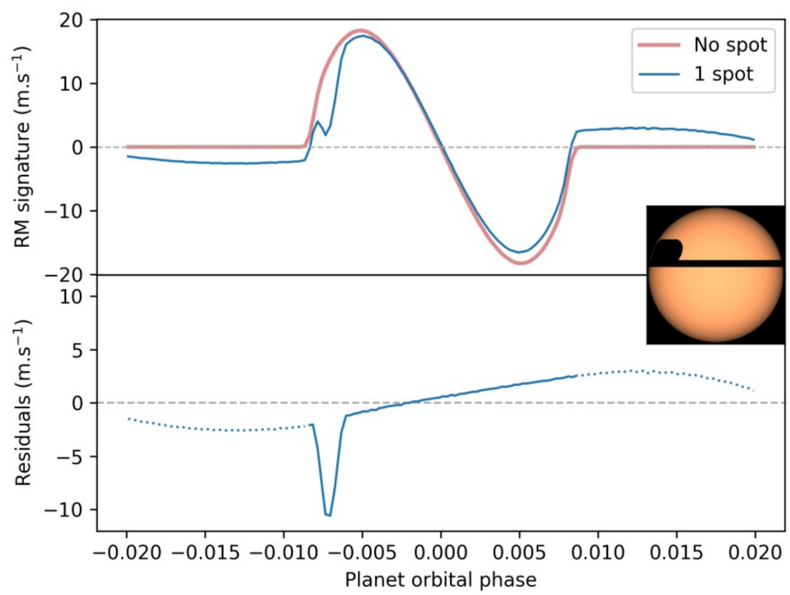

(b) The planet transit trajectory crosses over the star spot.

Figure 5.12: The RV curve caused by the RM effect, with the Keplerian signal of the planet subtracted, if no star spot (red) or a single star spot (blue) is present. Top panel: RV signal for both cases; bottom panel: deviation of the RV signal with one star spot from the curve without any star spots. Graphical inset: representation of the geometry of the transit and the star spot, integrated over the complete transit duration. The star spot is assumed to be circular and appears elongated due to the time integration. Graphic taken from Addison et al. (2021).

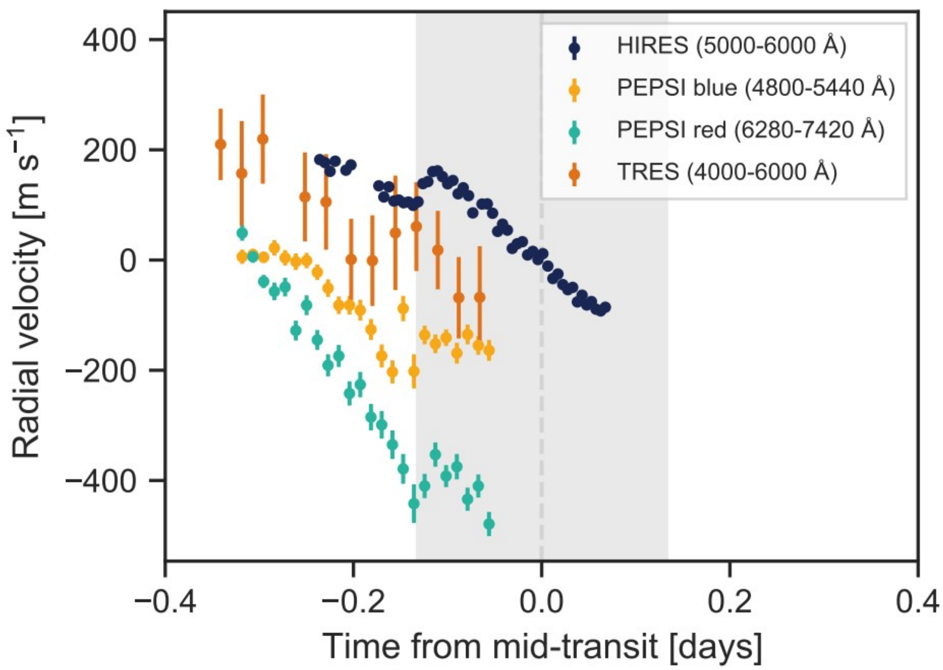

Figure 5.13: RV measurements for the RM effect of V1298 Tau with four different instruments, illustrating the wavelength dependence of the RM effect. For each instrument the approximate wavelength region that was used for the analysis is indicated. Gray area: time of transit. Graphic taken from Johnson et al. (2021, subm.).

curve and the amplitude of the RM effect are differing, making clear that when combining data from several instruments, effects from the varying wavelength coverage have to be taken into account.

The fact that the planet's apparent radius increases if absorption features are present in its atmosphere alters the RV curve of the RM effect and can be exploited to conduct atmospheric studies. This analysis is currently mostly restricted to broad atmospheric features due to the available data quality, nevertheless it is possible to roughly determine properties like the atmospheric temperature, as has been done for instance by Di Gloria et al. (2015). The new generation of spectrograph with extremely high RV precision will allow to make more detailed studies of the extend of the atmosphere or the elements that are present (Borsa et al. 2021).

5.3 Alternative methods to measure obliquity

Measuring the RM effect as RV anomaly in the form of a center-of-mass shift of spectral lines is not the only way to obtain the alignment of a planet's orbit with the spin axis of its host star. A selection of other methods that have been used successfully to obtain λ or ψ is briefly presented in the following.

5.3.1 Doppler tomography

Historically, the RM effect was discovered as an anomaly of the RV curve resulting in a shift of the lines. Doppler tomography builds on the same physical foundations as the center-of-mass method (Fig. 5.5, third panel), but allows to obtain the alignment angle of the planet's orbit for star that are hot and rapidly rotating. In these cases, the center-of-mass method fails to produce meaningful results as the uncertainties due to the severely broadened line profiles grow too large.

The large rotational velocities that inhibit traditional RV measurements enable Doppler tomography, because the extreme broadening of the spectral lines results in a resolved line profile. The light blocked by the transiting planet shows as a bump or dent in the line profile, sometimes called the *Doppler shadow*, which travels over the line profile as the planet travels over the stellar disk as illustrated in Fig. 5.5 (third panel) (e.g. Perryman 2018).

An example of a Doppler tomography measurement of a planetary transit is shown in Fig. 5.14. In the upper panel, the time evolution (bottom to top) of the line profile during the transit is plotted with the moving Doppler shadow of the planet clearly visible in the upper curves. As it can be hard to make out the small deviations from the line profile by eye, typically the modeled or observed mean line profile without any planet signature is subtracted and the residuals are displayed as color-coded velocity maps, as can be seen in the bottom panel (e.g. Gandolfi et al. 2012). The diagonal track from left to right in the lower panel corresponds to an aligned orbit with $\lambda \sim 0°$, whereas a planet on a polar orbit with $\lambda \sim 90°$ would result in a nearly horizontal track.

5.3.2 Transit photometry

While the determination of the obliquity with both the center-of-mass method and Doppler tomography relies on spectroscopic observations, constraints on λ can also be inferred from photometric data. In the following, a selection of photometric approaches is presented that have already yielded obliquity measurements for a number of planets.

Spot-crossing anomaly

Star spots and other inhomogeneities of the stellar surface brightness distribution do not only impact the measured RVs during a transit, but are also visible in the photometric data. In the photometric transit curve, an increase of brightness is registered as the planet crosses a star spot, called the *spot-crossing anomaly*.

A typical situation for hot Jupiters with short orbital periods P is that both the rotation period of the star and the lifetime of a star spot are several times larger than P. As a result, a possible star spot stays present on the visible hemisphere during several transits, but its position is moving because of the stellar rotation. However, star spots don't change their latitudinal position relative to the equator, making them good tracers for the rotation direction and thus the spin axis of the star. When several subsequent transits are observed,

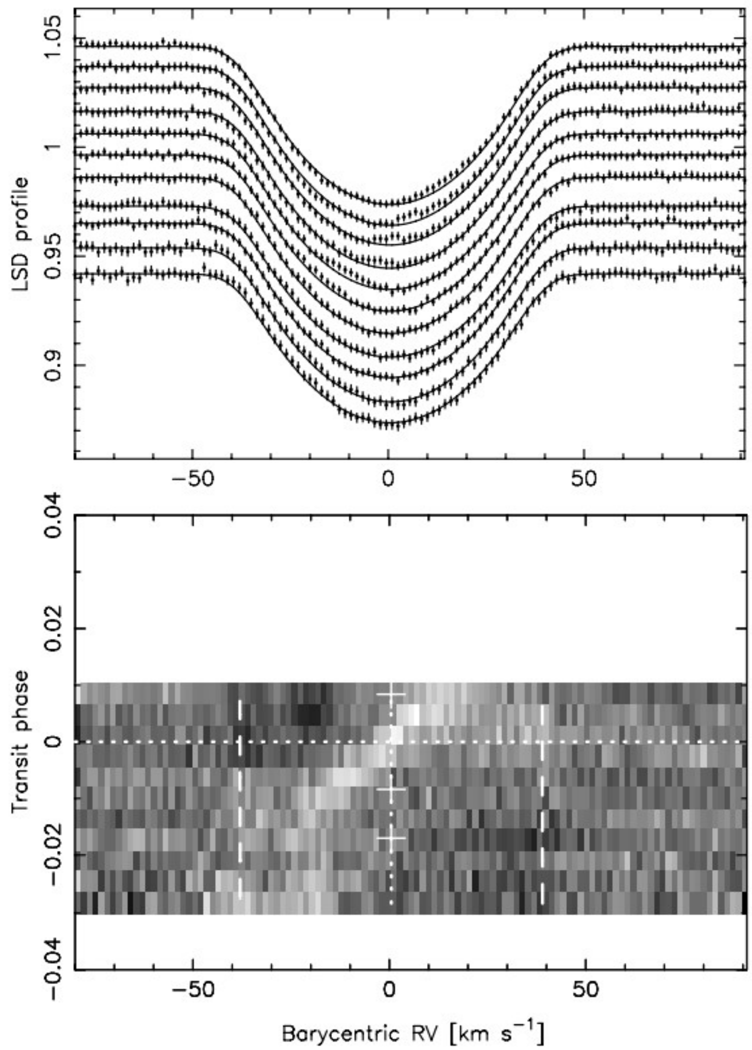

Figure 5.14: Doppler tomography of CoRoT-11. Top panel: series of spectral line profiles observed during the transit (black points, time progression from bottom to top) and best-fitting model of the line profile out of transit (solid line), including limb darkening and rotational broadening. The transiting planet's signature can be seen in the upper curves moving from left to right. Bottom panel: Same time series from bottom to top, after subtraction of the best-fit model from the data, the gray scale corresponds to the deviation from the model with brighter patches indicating larger deviations. The transit signature of the planet is visible as bright diagonal streak. Horizontal dotted line: mid-time of transit; vertical dotted line: velocity zero point in the rest frame of the barycenter of the CoRoT-11 system; vertical dashed lines: $v_{rot} \sin i_S$ of CoRoT-11, corresponding to the maximum possible RV amplitude during the transit; crosses, bottom to top: time of first contact of the planetary and stellar disk, time of first complete overlap between the two disks, and time of last complete overlap. The final transit phase when all overlap between the two disks vanishes is not covered by the observation. Graphic taken from Gandolfi et al. (2012).

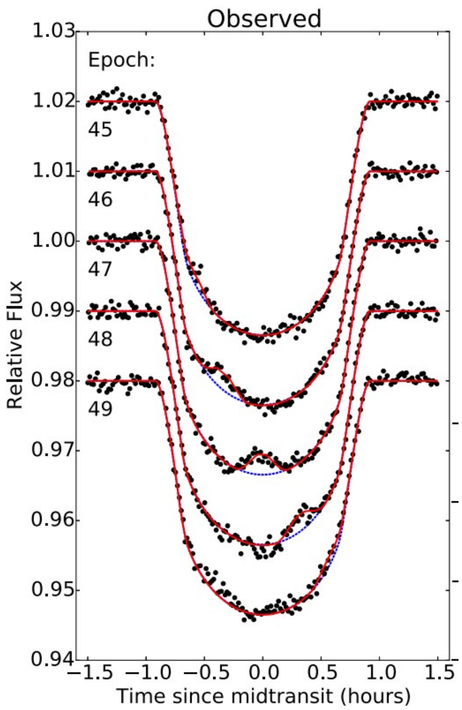

(a) The spot-crossing anomaly for a single star spot in five consecutive transits (top to bottom), which moves across the stellar disk, resulting in different positions in the transit curve. Blue: model of the transit lightcurve without star spots; red: best fit to the observed lightcurve with a star spot. Graphic taken from Dai et al. (2017).

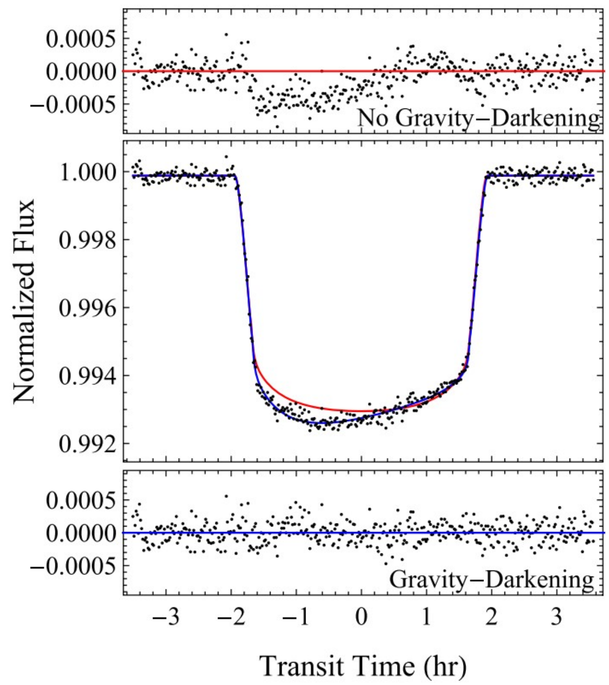

(b) The distortion of the transit lightcurve due to gravity darkening, where the planet transit begins in a bright region (pole) and ends at a darker region (equator). Red: model of the transit lightcurve without gravity darkening; blue: best fit to the observed lightcurve with gravity darkening. Top panel: residuals of the data for the lightcurve wiithout gravitational darkening; bottom panel: residuals for the lightcurve including gravity darkening. Graphic taken from Ahlers et al. (2020).

Figure 5.15: The influence of the spot-crossing anomaly (a) and gravity darkening (b) on the photometric transit curve of a planet.

an investigation of whether the planet crosses the same spot multiple times, illustrated in Fig. 5.15 (a), allows to constrain the obliquity. If the planet indeed crosses one or more star spots, the time when such a spot is crossed can be directly related to the position on the disk and the geometry of the transit trajectory on the stellar disk can be obtained (e.g. Sanchis-Ojeda et al. 2013).

The overall achievable precision of λ when using the spot-crossing anomaly depends strongly on the number of star spots. Detections of single spots can produce results more precise than observations of the RM effect, as the stars observed with the spot-crossing anomaly show at least a certain level of activity that systematically downgrades the RV measurement precision. But then, the spot-crossing measurement precision also suffers if a star is too active and many spots are present, because several distinct patterns of star spots may produce ambiguous results (e.g. Dai et al. 2017; Sanchis-Ojeda et al. 2011). Additionally, since the motion of the star spots on the stellar disk is perpendicular to the star's spin axis, the spot-crossing method is more sensitive to aligned than to misaligned orbits.

Gravity darkening

For rapidly rotating stars that are oblated due to the high rotational velocity, the surface temperature at the equator is lower than at the poles, causing a brightness decrease from the poles towards the equator. This effect is called *gravity darkening* and can be observed as a distortion of the transit light curve (e.g. Ahlers et al. 2020), as depicted in Fig. 5.15 (b).

The shape of the gravity darkening distortion during the planet's transit is on the one hand a function of the inclination of the stellar rotation axis i_S relative to the LOS, and on the other hand also of the projected obliquity angle λ. Since the planetary orbit inclination i is anyway known from the transit data, it is possible to immediately obtain the true obliquity ψ using Eq. 5.1.

A big advantage of the gravity darkening method is that it allows to observe stars that are extremely hot, for which the RM effect cannot be measured. Contrary to the spot-crossing method, observations exploiting gravity darkening are more sensitive to polar or highly misaligned orbits than to aligned ones, however it is not possible to distinguish between prograde and retrograde orbits (Ahlers et al. 2020).

All in all, photometric methods for obtaining obliquity angles pose attractive alternatives for spectroscopic measurements, especially as smaller telescopes can be used for the observations. Nevertheless, these methods come with their own systematic deficiencies, ultimately limiting their application.

5.4 Obliquity statistics

The detection of hot Jupiters on misaligned orbits, such that have a significant inclination towards the stellar spin axis, gave rise to a rethinking concerning the mechanisms that dictate the formation and evolution of planetary systems. As the projected obliquity was measured for more and more planets, the statistical distribution of the values also became a relevant factor that planet formation and evolution models needed to be able to explain, especially since a considerable number of planets with misaligned orbits was discovered.

A variety of migration and interaction mechanisms that could potentially justify the observed distributions is available, forming two groups: those that lead to significantly misaligned orbits, and those that result in aligned orbits. The most widely-known mechanisms in the misaligned group are:

- **primordial misalignment**, which designates a misalignment already of the protoplanetary disk before planet formation, due to interactions with nearby stellar companions as in a binary system or a dense star-forming region (e.g. Lai et al. 2011);

- **planet-planet scattering**, caused by gravitational interactions of planets during close encounters in a multiple system (e.g. Chatterjee et al. 2008);

- **the Lidov-Kozai mechanism**, which is a result of periodical perturbations of the planet's orbit around its host star by a distant third body, like a binary companion, resulting in a shrinkage of the planet's orbit size and increased misalignment (e.g. Fabrycky and Tremaine 2007);

- **secular resonance crossing**, an effect observable if a more massive outer planetary companion is combined with a disappearing protoplanetary disk (e.g. Petrovich et al. 2020).

The latter three mechanisms are commonly summarized as *high-eccentricity migration* (e.g. S. Wang et al. 2021), as they all rely on interactions that massively increase the eccentricity of the planet's orbit. This causes close passages of the planet to the host star, during which the orbit size and eccentricity are successively reduced due to damping effects. From these examples, it becomes clear that the orbit size, its eccentricity and the misalignment angle are often not isolated parameters, but come hand in hand. If the orbit has an unexpectedly small size, the probability is high that also the eccentricity and the misalignment have unusual values.

In contrast to that, mechanisms belonging to the group of aligned orbits are:

- **disk migration**, where the planet experiences gravitational interaction, torque and drag from the protoplanetary disk (e.g. Kley and Nelson 2012);

- **tidal interaction**, an effect where the planet induces tides in its host star, which efficiently removes angular momentum from the planet's orbit, reducing the overall orbit size, eccentricity and potential misalignments (e.g. Lai 2012);

- **in-situ formation**, meaning that close-in massive planets could have formed already at the small observed distances to their host star if certain special conditions are met (e.g. Boley et al. 2016).

Measurements of λ or ψ with the current state of instrumentation are mostly limited to hot Jupiters. Figure 5.16 shows a recent census by S. Wang et al. (2021) of all detected planets (gray), plotted by orbital period and planet mass, with the ones highlighted that have alignment measurements available (purple). The $\sim$170 planets with a determined λ correspond to roughly 3% of the total number of planets detected by the RV or transit method. This makes clear that the statistical distribution of the available measurements might not be able to fully represent the true distribution of alignment angles, besides being subject to the same systematic limitations as the RV and transit methods.

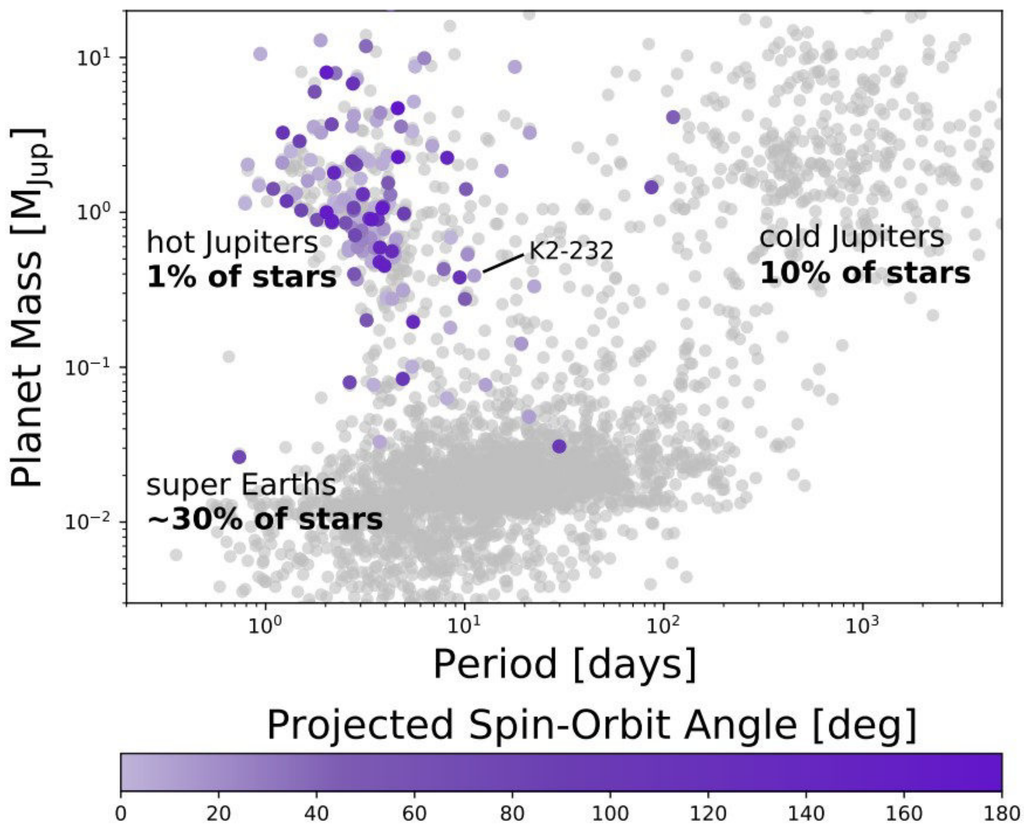

Figure 5.16: Current census of all known exoplanets (gray) and exoplanets with a measurement of λ (purple), plotted by orbital period and planetary mass. Most of the planets with measured λ belong to the group of hot Jupiters. Graphic taken from S. Wang et al. (2021).

Figure 5.16 reveals that the population of hot Jupiters is relatively well sampled, while there is little to no obliquity information available for planets in the other populations. Consequently, all interpretations of the statistical distribution of λ only apply to the group of hot Jupiters. The formation and evolution history of other planets, for which completely different physical processes may be dominant, cannot be constrained in a relevant manner from λ measurements yet.

Before further discussion, it has to be noted that the sample for which λ measurements are available is affected by certain biases. As the value of λ cannot be known or estimated before a measurement, it is unlikely that the sample is biased a priori towards certain values of λ. However, there are selection and detection biases due to the stellar properties of the host star. For instance, it is much more straightforward to measure the RM effect for relatively cool stars with narrow lines, which rotate slowly, instead of rapidly rotating, hot stars. This has to be kept in mind when making an interpretation of the statistical distribution.

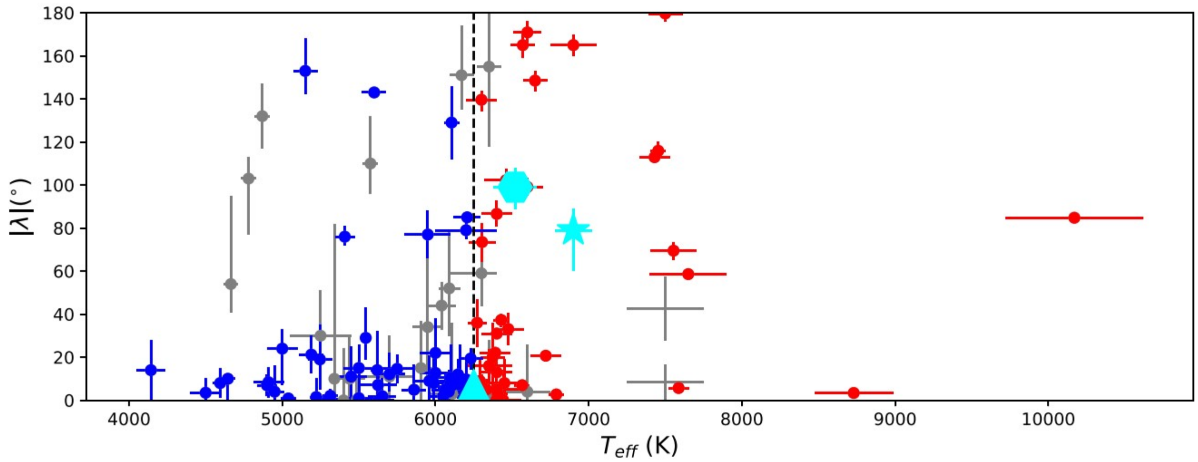

Figure 5.17: Distribution of measured λ values plotted over the stellar temperature T_{eff}. The vertical dashed line indicates the Kraft break at $T_{eff} \approx 6250\,\mathrm{K}$, where stars transition from slow rotation (lower T_{eff}) to fast rotation (higher T_{eff}). Blue: stars below Kraft break; red: stars above Kraft break; cyan: measurements from Addison et al. (2018); gray: systems with uncertainty of $\lambda > 20\%$. Only hot Jupiters are included. Graphic taken from Addison et al. (2018).

In order to investigate the physical processes behind planet formation and evolution, it is useful to observe possible correlations of the measured spin-orbit alignment with the star's and the planet's properties. A selection of such correlations is presented in the following.

5.4.1 Correlation with host star temperature

One interesting correlation concerning the spin-orbit alignment is the one between λ and T_{eff}, the host star's temperature. Figure 5.17 shows the relation for the sample of hot Jupiters, defined by limits on the orbital period ($P < 10\,\mathrm{d}$) and the planetary mass ($0.3\ M_{Jup} < M_P < 13\ M_{Jup}$). Measurements of λ with an error bar larger than 20% are grayed out.

The dashed line in Fig. 5.17 at $T_{eff} \approx 6250\,\mathrm{K}$ is called the *Kraft break*. At this temperature, which corresponds to a stellar mass of roughly $1.4\ M_{Sun}$, a transition of the internal structure of stars occurs. Stars with lower temperatures (blue) feature extended convective zones in their outer layers, whereas stars above the Kraft break (red) only have thin convective layers, if any (e.g. Winn et al. 2010). This impacts the rotational velocity of the star, which is in general small for stars cooler than that boundary and larger for hotter stars. The reason for this behavior is found in the magnetic braking effect, which occurs in the cooler stars due to strong magnetic fields generated by the convective motion of the plasma. As the magnetic fields are strong enough to force ejected material, for instance from stellar winds, to rotate with the star, the star's angular momentum gets dispersed

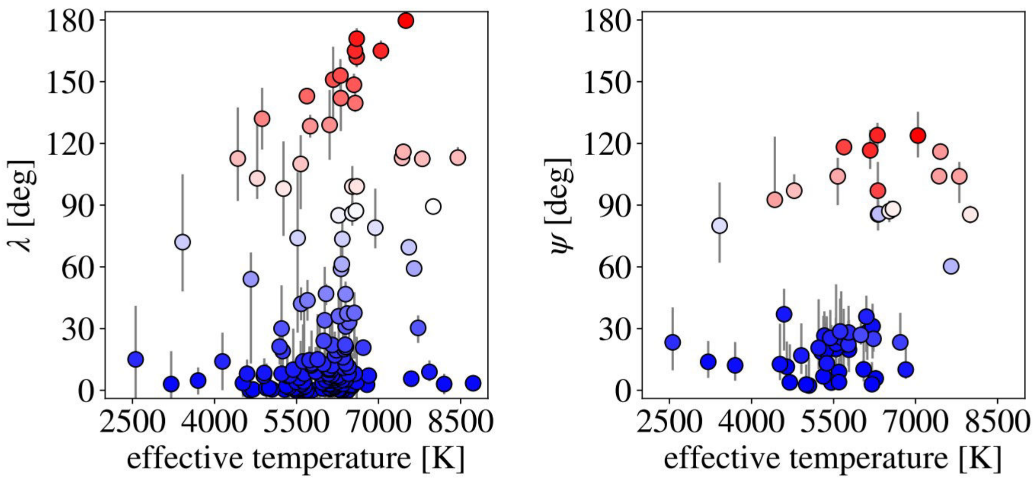

Figure 5.18: Distribution of measured λ (left panel) and ψ (right panel) values plotted over the stellar temperature T_{eff}. In the right panel, only stars with an available estimate of the stellar inclination i_S are included. The color coding in both panels corresponds to the λ value of each system. Graphic taken from S. Albrecht et al. (2021).

and the rotation is slowed down (e.g. Maeder 2009).

In Fig. 5.17, the planets hosted by stars above the Kraft break are found to have a significantly larger chance of being misaligned, with $|\lambda| \gtrsim 20°$, than those below the Kraft break, where there seems to be a stronger preference for aligned orbits. Please note that some of the stars near the break have error bars in T_{eff} that would put them on the other side of the break. Additionally, in reality the temperature of the Kraft break is not exactly fixed at $T_{eff} \approx 6250\,\mathrm{K}$, but may vary around this value depending on factors like the star's composition and evolutionary stage.

As stated previously, the variable relevant for physically modeling planet formation and evolution is ψ rather than λ. For a conversion, knowledge about the inclination of the stellar spin axis i_S is required, a quantity that is not straightforward to measure. Nevertheless, a number of results have become available during the past years, which were collected and analyzed by S. Albrecht et al. (2021). Figure 5.18 shows the statistical distribution of λ and ψ as function of T_{eff}, the latter for a total 57 systems with i_S measurements. The methods exploited to obtain the measurements or estimates of i_S used for Fig. 5.18 are:

- combining measurements of the projected rotational velocity $v_{rot} \sin i_S$ with the stellar radius R_S and the rotation period of the star P_{rot} in the relation

$$\sin i_S = (v_{rot} \sin i_S)/v_{rot} = v_{rot} \sin i_S \cdot P_{rot}/(2\pi R_S), \tag{5.11}$$

  which produces only an estimate of i_S since effects like differential rotation of the star are completely neglected, but requires less observational effort than the other methods (e.g. Winn et al. 2007a);

- asteroseismology, which relies on acoustic oscillations of Sun-like stars that result in periodic variations of the intensity, producing a characteristic pattern in a frequency analysis of the intensity variation that strongly depends on i_S (e.g. Gizon and Solanki 2003);

- the gravity-darkening method, suitable for rapidly rotating stars that are oblated due to the high rotational velocity and therefore are cooler and less bright at the equator than at the poles, observable as a distortion of the transit light curve as a function of i_S (e.g. Ahlers et al. 2020).

The three different methods contributed a total of 51, one, and five data points, respectively, to Fig. 5.18 (right panel).

The left and right panel of Fig. 5.18 present the measured λ and ψ values, respectively. The data points are color coded by the λ value, from blue for $\lambda = 0°$ to red for $\lambda = 180°$, to allow for a direct comparison. While the data points of misaligned orbits seem to be more or less evenly distributed over the whole range of possible λ values (left), the misaligned orbits form a population between $\psi \sim 90° - 120°$ for the ψ values (right), clearly distinct from the aligned orbits between $\psi \sim 0° - 30°$.

Overall, the consideration of ψ instead of λ also confirms the impression that misaligned orbits are more common around hotter stars, even though the statistical sample is considerably smaller. The tendency of planets around cool star to have aligned orbits can have different reasons. On the one hand, it is possible that migration mechanisms which conserve the planetary alignment are preferred for cooler host stars. On the other hand, the migration processes could be the same, but there might exist some mechanism for the cooler stars, which efficiently realigns the planetary orbit with the star's spin axis on a relatively short timescale after the planet got misaligned during its migration.

In fact, tidal interactions of hot Jupiters with the massive convective shell of cool host stars provide such a possibility of re-alignment. Because large amounts of angular momentum and inertia can be transferred from the planet to the star's convection zone, misalignments are suppressed, resulting in aligned orbits (Lai 2012). Beyond that, tidal interactions can also lead to polar orbits with $\psi \sim 90°$ if special conditions are met, as demonstrated e.g. by Lai (2012). This could explain part of the concentration of the misaligned planets in Fig. 5.18 (right), however this does not apply for the hot stars, where a convective zone is absent.

More recent data sets support the relevance of tidal interactions as they show slight evidence that the increase of misalignment starts slightly below the Kraft break, at temperatures around $T_{eff} \sim 6000\,\mathrm{K}$ (e.g. X.-Y. Wang et al. 2021, subm.). This could indicate that the mechanism responsible for the preferred alignment of planetary orbits is indeed related to the convective zones and some minimum thickness for the convection layer exists, which is required for tidal dissipation to be effective.

A further possible cause for preferring polar orbits if a misalignment is present are interactions of the observed planet with a third body in the planetary system, like an additional planet. These interactions can be either chaotic or resonant, depending on the

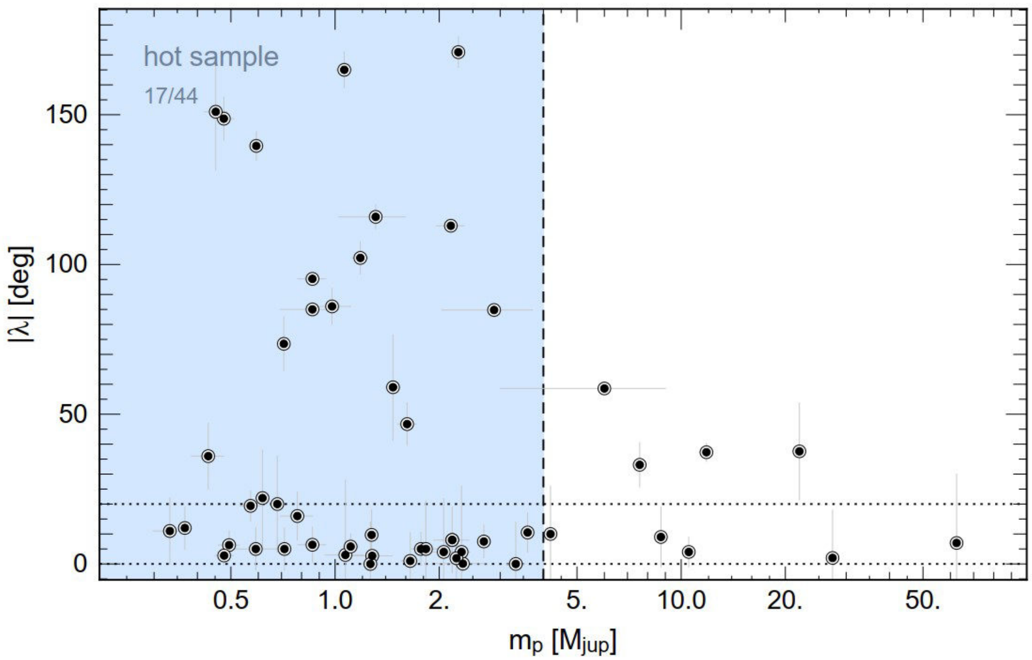

Figure 5.19: Distribution of measured λ values for all host stars above the Kraft break plotted over the planet's mass M_P. The horizontal dotted lines indicate the region of aligned orbits ($|\lambda| \leq 20°$). The vertical dashed line at $M_P \sim 3.5\ M_{Jup}$ separates the populations with strong misalignment (left, blue area) and weak misalignment (right). Graphic taken from Triaud (2018).

geometry of the three-body system. In the latter case, the inclination of one body can be amplified until it reaches a semi-stable configuration on a polar orbit (S. Albrecht et al. 2021). However, the still limited statistical sample doesn't allow a conclusive interpretation regarding those mechanisms yet and further measurements are needed to improve the overall understanding of the involved processes.

5.4.2 Correlation with planetary mass

The mass M_P is one of the most fundamental physical properties of an exoplanet. The formation and evolution history of a planet may change significantly depending on its mass, a relation which can be investigated and specified by regarding the distribution of λ as function of M_P. This is shown in Fig. 5.19 for all stars above the Kraft break, here called the *hot sample*.

It can be observed that a certain mass limit exists, below which λ spans the whole range of possible values, but above which only moderate misalignments occur. In Fig. 5.19, this is indicated by the vertical dashed line corresponding to a planetary mass of $M_P \approx 3.5\ M_{Jup}$. The reason for this change in the misalignment distribution is still under debate. A number of attempts for explanation exist, which include for instance the argument that heavy planets are more inert when gravitationally interacting with other bodies, so they are possibly less affected by processes like planet-planet scattering, which would result in heavily misaligned orbits (Hébrard et al. 2011). A different proposal is that the mass of the planet is so high that it induces a tidal interaction with the host star, even if the host star doesn't have a convective shell (Dawson 2014).

Owing to the small sample size, the exact value of the boundary has a large uncertainty and more measurements of massive planets are needed to refine the results. Given that there are only a handful of λ measurements available for planets above $M_P \approx 3.5\ M_{Jup}$, it might even be possible that the trend shown in Fig. 5.19 disappears in a more extensive data set. In any case, the finding of the different λ distributions for low-mass and high-mass planets orbiting hot stars from the currently available data set is statistically relevant and hints towards different formation and evolution histories, which needs to be further investigated in the future.

5.4.3 Correlation with relative orbit size

During the formation and evolution of planetary systems, the conservation and dissipation of angular momentum plays a crucial role. The angular momentum of Jupiter-like planets on far-out orbits, at their place of formation, is significantly larger than that of hot Jupiters. Consequently, in order for such a planet to reach a stable close-in orbit, some of the angular momentum needs to be transferred or dispersed.

As the angular momentum of the planet can be related to the size of its orbit, it is useful to investigate Fig. 5.20, where the distribution of λ is given as a function of the relative orbit size a/R_S. Here, only cool stars below the Kraft break are included, called the *cold sample*. Normalizing the size of the orbit a with the stellar radius R_S is justified to obtain a better comparison, as even with the restriction to the cold sample there is still a large variety in the radii of the host stars, which at the same time puts a natural lower limit to possible orbit sizes.

In Fig. 5.20, two distinct populations separated at $a/R_S \sim 12$ (dashed line) can be recognized. Above this value, the observed planets show a wide distribution in obliquities. Furthermore, most of the orbits larger than $a/R_S \sim 12$ feature large eccentricities, which is represented in Fig. 5.20 by the solid lines and the small dots, corresponding to the planet's smallest distance to the star. Below this boundary (red shaded area), all planets with the exception of one outlier are aligned at $|\lambda| \leq 20°$.

The fact that planets on wide orbits often have large eccentricities favors a mechanism called high-eccentricity migration (e.g. Anderson et al. 2015). During the pericenter passage, when the planet is closest to its host star and the gravitational and tidal interaction between the two is strong, angular momentum is transferred from the planet to the star, damping the orbit's misalignment and eccentricity. However, the timescales of the damping processes are relatively long compared to the timescales of direct tidal interactions for close-in stars.

According to high-eccentricity migration, it is therefore expected that the planets with $a/R_S \gtrsim 12$ in Fig. 5.20 will undergo further evolution to become close-in planets on cir-

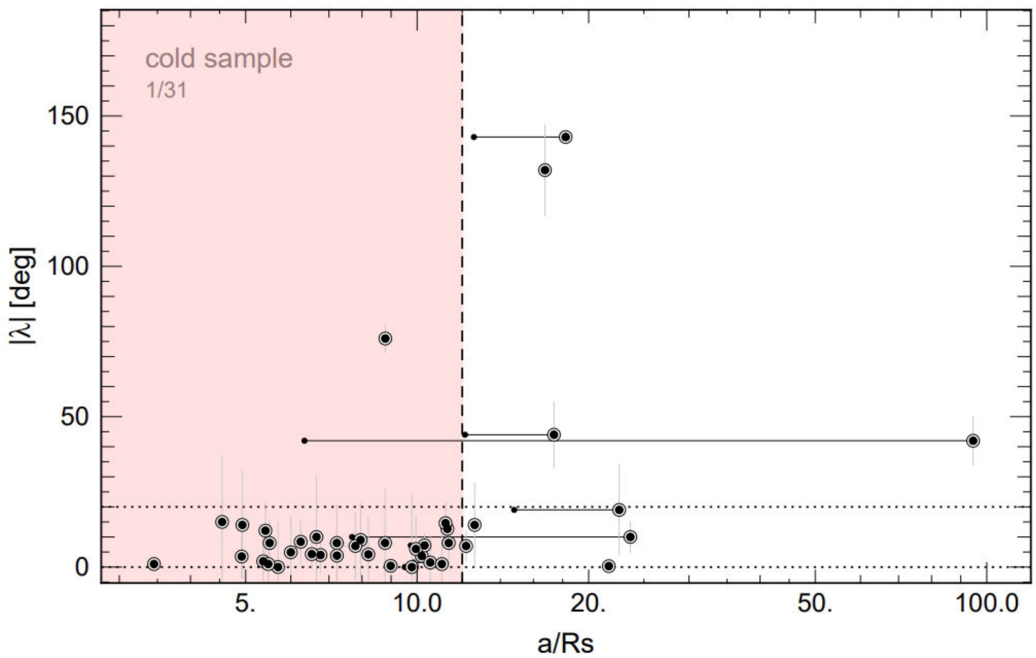

Figure 5.20: Distribution of measured λ values for all host stars below the Kraft break plotted over the planet's relative orbit size a/R_S, given by the orbital semi-major axis in units of stellar radii. The horizontal dotted lines indicate the region of aligned orbits ($|\lambda| \leq 20°$). The vertical dashed line at $a/R_S \sim 12$ separates the group of well-aligned planets (left, red area) from those with strong misalignments (right). The solid lines indicate eccentricities, with the small dots representing the semi-minor axis distance. Graphic taken from Triaud (2018).

cular orbits themselves. In general, it is assumed that at distances $a/R_S \lesssim 10 - 15$ tidal interactions between the planet and the host star become the dominant mechanism, as suggested by the transition between the two populations in Fig. 5.20 (e.g. Anderson et al. 2015).

Two special cases from Fig. 5.20 need to be further discussed. On the one hand, there is a planet on a wide orbit ($a/R_S \sim 21$) with good orbital alignment and a very small eccentricity. In this case, the planet could have formed already at this distance from its star (in-situ formation) or be the result of a disk migration process (Triaud 2018). Considering that the host star of this planet is relatively young (Anderson et al. 2015) supports this claim, however more such cases on wide but aligned orbits have to be studied to reach conclusive results.

On the other hand, the planet with $|\lambda| \approx 80°$ at a relatively small distance could indicate that this particular planetary system features some special conditions where other mechanisms than tidal interaction are relevant. Therefore, further investigation of this system is required, but also the observation of a larger statistical sample is needed to evaluate whether misalignments could be more common for close-in orbits, but the sample

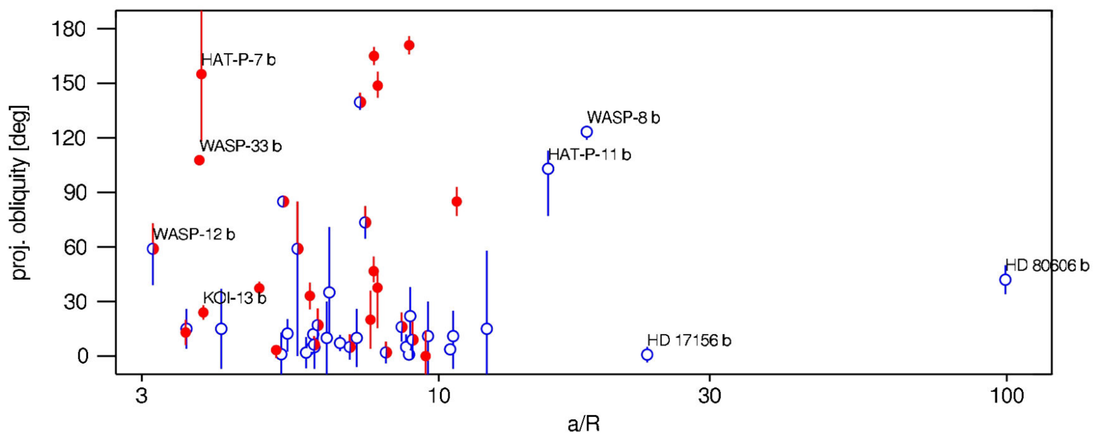

Figure 5.21: Distribution of measured λ values plotted over the planet's relative orbit size a/R_S (same as Fig. 5.20), for stars both below (blue open circles) and above (red filled circles) the Kraft break. Mixed symbols indicate stars that could lie on either side of the Kraft break due to uncertainties in T_{eff}. Graphic taken from S. Albrecht et al. (2012).

of λ measurements is not good enough yet to represent the true distribution.

Figure 5.21 compares the λ distribution by orbital distance of the cold sample (blue open circles) with that of the hot sample (red filled circles). The stars above the Kraft break all host planets on orbits with $a/R_S \lesssim 12$, but with a much wider variation of the measured λ values. Due to the lack of convective zones in hot stars, the angular momentum cannot be dissipated as efficiently as for cool stars due to tidal interaction (e.g. Triaud 2018). Therefore, the timescale for the re-alignment of the planetary systems is much larger, which is reflected by the large number of misaligned orbits that are observed.

All in all, the planet migration that we observe is most likely a combination of different individual mechanisms, where the dominating mechanisms could be different for hot stars and cool stars. While for cool stars mechanisms like tidal interaction, disk migration and high-eccentricity migration seem to be preferred, there are hints that for hot stars planet-planet scattering plays a more significant role, which leads to a wide distribution of λ values. This can be understood as hot stars on the one hand do not have convective layers and on the other hand blow away more disk material in the inner regions, making both tidal interaction and disk migration less powerful.

5.4.4 Correlation with system age

As discussed already for the previous relations, there exist certain mechanisms that change the alignment or misalignment of a planet's orbit over the course of time. Consequently, it is informative to look at the relation of the measured λ values with the age of the systems (Fig. 5.22).

The gradual decrease of orbital misalignment due to tidal interaction and high-eccentricity migration leads to the expectation that old systems should show smaller λ values

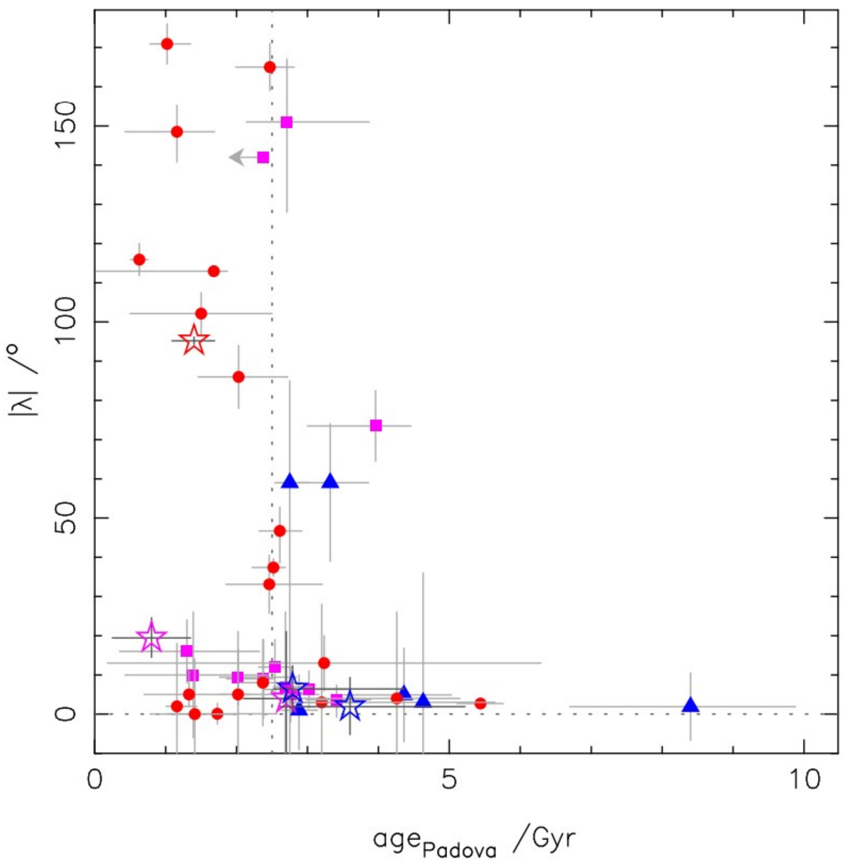

Figure 5.22: Distribution of measured λ values for all host stars with $M_S \geq 1.2M_{Sun}$ plotted over the age of the host stars. The vertical dashed line at ~ 2.5 Gyr separates the group of young, frequently misaligned planets (left) from the older ones with better orbital alignment (right). Blue: stars with $T_{eff} < 6150\,\mathrm{K}$; pink: stars with $6150\,\mathrm{K} \leq T_{eff} \leq 6350\,\mathrm{K}$; red: stars with $T_{eff} > 6350\,\mathrm{K}$. Stellar age estimated with the Padova models by Marigo et al. (2008). Graphic taken from D. J. A. Brown et al. (2017).

than younger ones. Figure 5.22 includes λ measurements for host stars with $M_S \geq 1.2M_{Sun}$ and suggests a transition (dashed line) between the young population with a wide variety of λ and the old population with more aligned orbits at roughly 2.5 gigayears (Gyr). However, the correlation is considerably weaker than in the cases presented before and the sample is not very large, leading to large uncertainties in the transition age (D. J. A. Brown et al. 2017).

Nevertheless, the distribution of λ in Fig. 5.22 supports the insights from the correlations of λ with the effective temperature T_{eff}. Planets around cool stars ($T_{eff} < 6150\,\mathrm{K}$, blue) tend to be more aligned, which can be explained by the presence of convective layers in such stars. In contrast to that, hot stars ($T_{eff} > 6350\,\mathrm{K}$, red) typically don't feature convective zones, however it is possible that they form convective layers at advanced age, which would in turn lead to more aligned orbits (D. J. A. Brown et al. 2017). This can

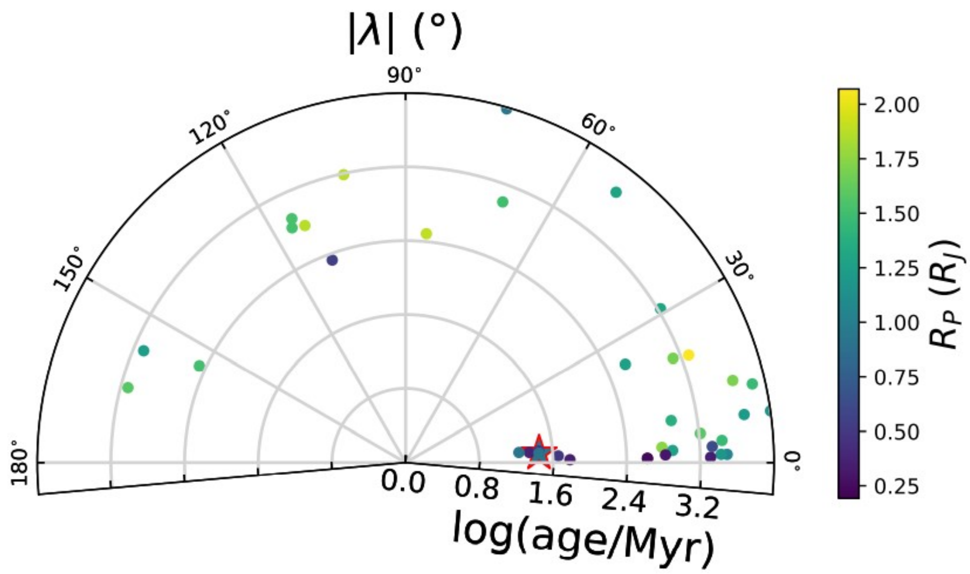

Figure 5.23: Distribution of measured λ values plotted over the age of the host stars. There is a distinct group of very young, extremely well-aligned planets at ages $\sim 15 - 60$ Myr. The color coding corresponds to the planet size. Graphic taken from Johnson et al. (2021, subm.).

be observed in Fig. 5.22 for hot stars older than ~ 2.5 Gyr, possibly confirming the importance of convection zones for the alignment of planetary systems. The planets orbiting stars in the zone of uncertainty around the Kraft break ($6150\,\mathrm{K} \leq T_{eff} \leq 6350\,\mathrm{K}$, pink) show a mixed behavior.

Recently, evidence has been found that in extremely young systems planets are likely to be aligned and the probability to find systems with a significant primordial misalignment is low. Figure 5.23 shows a distinct population of such young planets at ages < 100 megayears (Myr) with extremely small values of λ. This is in line with the picture of planet formation in a disk of dust and gas confined to the host star's equatorial plane and indicates that the mechanisms causing substantial misalignment, such as planet-planet interactions, only take effect after a few hundred Myr (Johnson et al. 2021, subm.).

It is important to note that the young sample shown in Fig. 5.23 is small and thus may fail to represent the actual distribution of λ values for young planets. Furthermore, there is no information available about the alignment of objects in the transition zone between ages $\lesssim 100$ Myr and $\gtrsim 250$ Myr. Concluding a robust explanation of the origin and evolution of the alignment distribution for young planets is therefore currently not possible but would require more observations.

5.4.5 Systems with small planets

The ultimate goal of exoplanet science is to be able to describe the formation and evolution of all types of planets, even small rocky ones similar to Earth. To achieve that, measure-

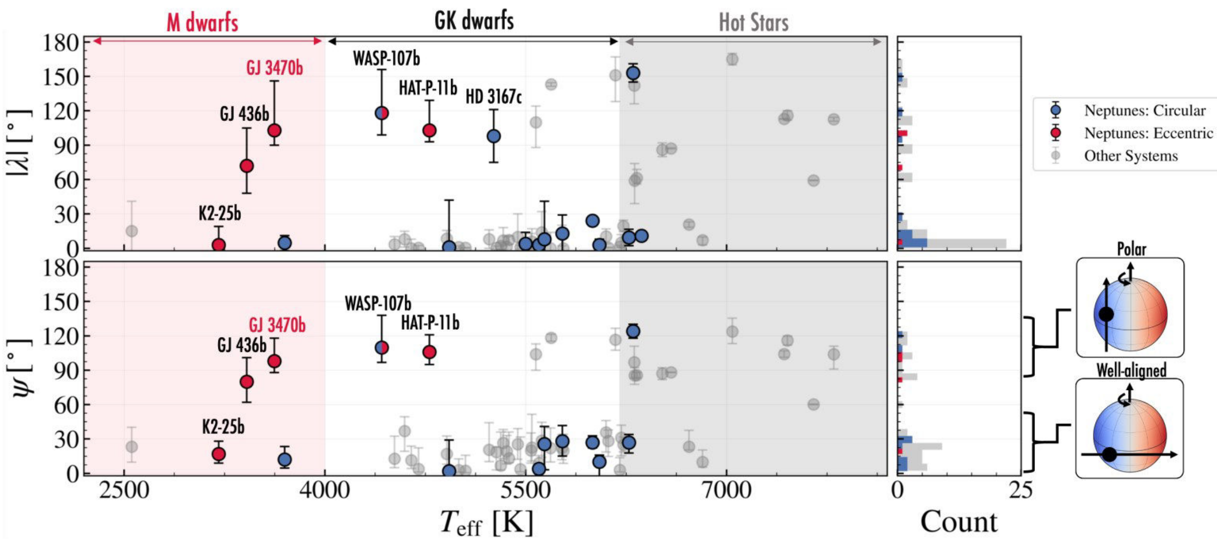

Figure 5.24: Distribution of measured λ (upper panel) and ψ (lower panel) values plotted over the stellar temperature T_{eff} for Neptune-type planets with $M_P \in [0.03, 0.16]M_{Jup}$ or $R_P \in [0.14, 0.55]R_{Jup}$. In the lower panel, only stars with an available estimate of the stellar inclination i_S are included. The color coding highlights whether the orbits of the planets are circular($e \leq 0.1$, blue) or eccentric ($e > 0.1$, red). Gray symbols indicate the distribution of hot Jupiters from Fig. 5.18 (S. Albrecht et al. 2021). Graphic taken from Stefansson et al. (2021, subm.).

ments of the alignment of such planets are crucial. As of today, measuring λ for Earth-like planets is not possible, but may become feasible in the near future as 30 m class telescopes and spectrographs with precisions well below 1 m/s are taken into operation.

Despite the more challenging measurement, the sample of planets smaller and less massive than Jupiters with λ measurements is slowly growing. A substantial group form Neptune-type objects on relatively close-in orbits, called *warm Neptunes*, which cover an intermediate region between Earth-like and Jupiter-like planets, with typical masses and sizes of $M_P \sim 0.03 - 0.16 M_{Jup}$ and $R_P \sim 0.14 - 0.55 R_{Jup}$, respectively (Stefansson et al. 2021, subm.).

Figure 5.24 shows the distribution of λ (upper panel) and ψ (lower panel) for warm Neptunes as a function of the host star's effective temperature T_{eff}, similar to Fig. 5.18. The measurements included in this plot are additionally color coded by eccentricity of the orbit, with circular orbits ($e \leq 0.1$) drawn in blue and those with a significant eccentricity $e > 0.1$ shown in red.

The majority of Neptune-like planets shows an aligned orbit with a small eccentricity, but a significant number of planets are misaligned. The misaligned planets mostly feature large eccentricities and show a tendency to prefer polar orbits with $\psi \sim 80° - 120°$. The latter finding agrees with the trend observed for hot Jupiters from Fig. 5.18 (S. Albrecht et al. 2021), leading to the conclusion that warm Neptunes and hot Jupiters on misaligned

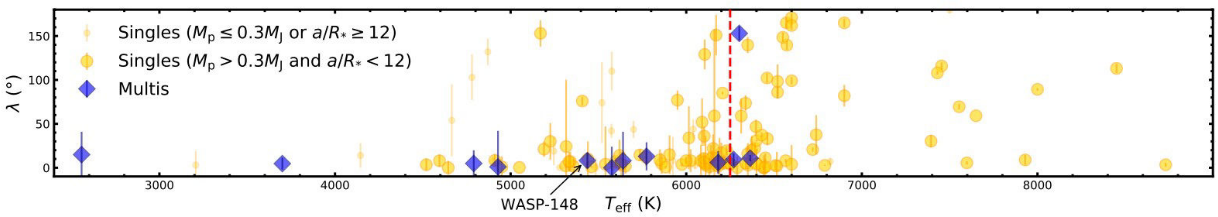

Figure 5.25: Distribution of measured λ values for single and multiple planetary systems plotted over the stellar temperature T_{eff}. Blue diamonds: systems with multiple planets; yellow large circles: systems with a single hot Jupiter; yellow small circles: systems with single planets other than hot Jupiters; red dashed line: Kraft break at $T_{eff} \approx 6250\,\mathrm{K}$. Graphic taken from X.-Y. Wang et al. (2021, subm.).

orbits possibly originate from similar mechanisms (Stefansson et al. 2021, subm.).

The significant eccentricity of most misaligned warm Neptunes allows to constrain the migration mechanisms to two plausible options, as Stefansson et al. (2021, subm.) demonstrate. On the one hand, high-eccentricity migration as proposed for hot Jupiters is able to explain the observed distribution of misalignment and eccentricity (Dawson and S. H. Albrecht 2021, in prep.). On the other hand, interactions with both the dissipating protoplanetary disk and massive planetary companions on further-out orbits also allow to obtain a similar distribution of λ and e (Petrovich et al. 2020).

Some indicators exist that the dissipating disk and companion interaction is the mechanism which is more relevant for warm Neptunes, like evidence for the presence of suitable companions (Stefansson et al. 2021, subm.), as opposed to hot Jupiters where high-eccentricity migration is dominating. However, from the current number and quality of measurements, it is not possible to determine conclusively whether one of the mechanisms is more important than the other. Further investigation concerning the formation history of warm Neptunes is ongoing in the exoplanet community, paving the way to an improved understanding of planetary systems with multiple smaller planets.

5.4.6 Systems with multiple planets

Interactions between individual planets in a planetary system play an important role in triggering possible misalignments, as discussed in the context of the previously presented correlations. Considering that systems with multiple planets are found to be very common, it is essential to examine the distribution of λ also for systems with confirmed multiplicity in order to develop realistic models for their formation and evolution.

When comparing multiple systems, two groups of planetary systems can be formed by considering the mutual inclination of the planets relative to each other. On the one side, there are systems with a good relative alignment, where all planets orbit the host star in a common plane of a few degrees. On the other side, it is possible that several planets could orbit the same host star with different orbital inclinations due to violent migration mechanisms like planet-planet interaction.

For a few multiple systems, constraints on the orbital alignment are available, shown in Fig. 5.25 (blue) as function of T_{eff}. For comparison, the results for systems with only a single known planet are also plotted (yellow), with large symbols for hot Jupiters and small symbols for planets attributed to other planet types. It should be noted that in most of the systems presented here, λ was only directly measured for one planet. For the other planets in those systems, often only the information on whether the orbits are mutually aligned is available, e.g. from transit photometry observations.

Apart from one exception, the multiple systems with obliquity measurements are all well aligned and co-planar rotation is observed. Therefore, mechanisms like high-eccentricity migration, which dominate the migration for hot Jupiters especially around hot stars and frequently result in misaligned orbits, are unlikely to play a significant role for multiple systems. One side effect would be the ejection of smaller planets, often leaving the hot Jupiter to be the only remaining planet. Nevertheless, some of the mechanisms causing misaligned orbits, especially for hot Jupiters, rely on interactions with other planetary or stellar companions. This leads to the possible conclusion that most planetary systems form as multiple systems, but the ejection or destruction of smaller planets due to violent interactions turns some of those systems to single planetary systems (X.-Y. Wang et al. 2021, subm.).

Figure 5.25 suggests that in multiple systems, there must have been a formation and evolution history without violent dynamical interaction between the planets. Furthermore, the one misaligned system provides little statistical significance for a second population with larger orbital obliquity, particularly as the different orbital orientation in this case could be explained by interactions with a nearby binary companion (X.-Y. Wang et al. 2021, subm.).

With the sample of multiple systems as of today, a strong preference of aligned and co-planar orbits is found, compared with the larger variation of λ in single planet systems (X.-Y. Wang et al. 2021, subm.). However, the multiple systems all lie close to or below the Kraft break (Fig. 5.25, red dashed line), making it difficult to distinguish between whether this effect arises from the planetary systems themselves or whether it might be related to stellar effects like tidal interaction (X.-Y. Wang et al. 2021, subm.). In addition, the lack of measurements for multiple systems above the Kraft break might be due to the general lack of multiple systems around massive stars, as they tend to host massive hot Jupiters which expel or destroy any other planets in the system. Further measurements would help to clarify these open questions regarding multiple planetary systems, which form a significant fraction of known planetary systems.

Chapter 6

MaHPS observations of the RM effect

The RM effect was measured for several objects with MaHPS as part of this work. The observations were intended both as performance tests of the instrument and proof of concept for potential future observational campaigns. Furthermore, measurements of the RM effect feature particular challenges in observation planning, like finding a suitable trade-off between the time resolution during the transit and the exposure time needed to reach an acceptable SNR. Gathering experience with the instrument in this context to assess which observations could be feasible in the future was a further aim of the RM effect measurements. In the following, the MaHPS measurements and their results are presented and discussed individually for each object.

6.1 Target selection

The three planetary systems HD189733[42], HD149026 and HAT-P-2 were chosen as observation targets. For all of them, spectroscopic measurements of the RM effect are available in the literature, an essential selection criterion to enable a comparison of the performance of MaHPS with other instruments and to ensure a realistic evaluation of the obtained data quality. Apart from the availability of reference measurements, the targets observed with MaHPS were chosen based on a number of additional factors outlined here.

The starting point for the object selection was the *Orbital Obliquity Catalogue*, which is a regularly updated online catalog of all published obliquity measurements for exoplanets as part of the *Transiting Extrasolar Planets Catalogue* (TEPCat) by Southworth (2011).

[42] Following the naming convention for exoplanets proposed by Hessman et al. (2010), which is widely adopted, an exoplanet is designated with the name of the host star, followed by a lower-case letter. The lower-case letter indicates the sequence of discovery of planets orbiting a common host, where the first discovery is denoted with "b", the second with "c" and so forth. When talking about the host star or the entire planetary system, the lower-case letter is omitted.

An automated preselection[43] was applied to the objects listed in the Orbital Obliquity Catalogue to exclude systems that are not observable with MaHPS based on their brightness and sky position, where only stars with an apparent magnitude[44] $mag < 9.5$ and declination coordinate $\delta > -30°$ were retained.

The magnitude limit is determined by the overall throughput of MaHPS and the maximum exposure time of 30 min, as observations of stars fainter than $mag \sim 10$ do not yield a useful SNR in a single exposure. In this particular case, a small margin towards brighter stars was applied to make sure that the SNR is sufficient even in slightly suboptimal weather conditions, because time resolution is a crucial parameter for RM effect measurements. The constraint on the sky position of the object follows from the geographic position of the observatory, since objects in the Southern Sky are not visible in general.

For the objects remaining after the preselection, the projected rotational velocity of the star $v_{rot} \sin i_S$ and the measured RV amplitude of the RM effect were obtained manually from the corresponding publications. In this step, all objects with a λ measurement only from Doppler tomography[45] were excluded, as they are most probably not suitable for measuring the RV with the center-of-mass shift method. Because the error bars of the RV measurements grow with increasing line broadening, it can be said as a rule of thumb that the limiting rotational velocity for high-precision (<10 m/s) RV observations with MaHPS is around ∼5 km/s. If the RV signal to be measured has a larger amplitude, it can be feasible to nevertheless collect spectra of stars with a higher rotational velocity and accept the larger error bars. For instance, in this work, spectra of HAT-P-2 with $v_{rot} \sin i_S \sim 23$ km/s were obtained, resulting in error bars of ∼60 m/s for a single exposure when measuring the RV with the center-of-mass method. However, whether observations of a target with a $v_{rot} \sin i_S$ value in that range are feasible depends on additional factors, like the overall number of spectral lines and the amplitude of the expected RV signal, and has to be evaluated in each case individually.

All observations shown here were carried out between November 2020 and April 2021, therefore stars not visible during that period were not considered further. Additionally, the measurement of the RM effect is only possible during a transit of the planet, so the transit scheduling tool *Tapir* (Jensen 2013) was utilized to determine the dates of the next transits for all objects still remaining.

The decision which target to observe in a given night was then made on a night-to-night basis by compiling a priority list of the objects showing a transit. An object was only included on the priority list if at least a certain fraction of the transit happened during night time. The limits for the minimum fraction were 75% for objects with a total transit duration of $t_{dur} \leq 3$ h and 50% for objects with $t_{dur} > 3$ h. In addition, there had to be at

[43]The script used for the automated target preselection is provided under `https://github.com/vfahrens/MaHPS_scripts` for download.

[44]The apparent magnitude system following Pogson (1856) is used here. Magnitude 1 corresponds to the brightest stars in the sky, whereas stars with magnitude 6 are barely visibly by eye. In general, a logarithmic scale is used where smaller numbers indicate brighter stars.

[45]There is a certain overlap between the applicability of measurements with the center-of-mass method and Doppler tomography, so a number of objects exist where both methods have been used.

least 1.5 h of observable non-transit time, before or after the transit, to be able to obtain reference RV measurements.

Eventually, the priority list was generated by ordering the remaining targets by the amplitude of the RV anomaly due to the RM effect, from large to small amplitudes. In the unlikely case that two objects showed comparable amplitudes, the rotational velocity of the star was used as additional criterion, where the star with the slower rotation and thus the narrower spectral lines was preferred. Furthermore, when a transit of one object was observed, several out-of-transit spectra without simultaneous calibration were taken in the next possible night, which served as spectral templates.

The final factors influencing the target choice were the weather conditions at the observatory and targets of other instruments with higher priority. Whenever the telescope schedule allowed, the transit with the highest priority for that night was observed, resulting in the set of the three objects presented here.

6.2 HD189733

The RM effect for HD189733 has first been measured by Winn et al. (2006), which made it the third overall planetary system with a RM effect detection. Independent observations with a different instrument (Triaud et al. 2009) and several re-analyses of the available data sets (Cegla et al. 2016; Collier Cameron et al. 2010; Casasayas-Barris et al. 2017) make it one of the best studied systems regarding the RM effect and the determination of the obliquity.

6.2.1 System characteristics

The system parameters of HD189733 as obtained and collected in the latest published analysis by Casasayas-Barris et al. (2017) and used for the analysis of the measurements with MaHPS are summarized in Tab. 6.1.

The host star is a K-type star on the main sequence[46] with $T_{eff} = (5040 \pm 50)\,\mathrm{K}$ (e.g. Winn et al. 2006) with a mass of $0.806 \pm 0.048\ M_{Sun}$. It lies well below the Kraft break, rotates slowly at $v_{rot} \sin i_S = (3500 \pm 1000)\,\mathrm{m/s}$ and shows signs of stellar activity (e.g. Triaud et al. 2009), so for high-precision RV measurements the influence of stellar spots should be taken into account. The planet orbiting HD189733 is a typical hot Jupiter, being slightly larger ($1.138 \pm 0.027\ R_{Jup}$) and more massive ($1.144 \pm 0.056\ M_{Jup}$) than Jupiter on a very close orbit with a period of $\sim$2.2 d. The duration of the transit is $t_{dur} = (1.84 \pm 0.04)\,\mathrm{h}$.

The alignment of the planet's orbit has been found to be close to $0°$ with a high precision, the latest value being $(-0.31 \pm 0.17)°$ (Casasayas-Barris et al. 2017). Additional information on the stellar inclination angle i_S is available from photometric star spot

[46]The term *main sequence* indicates the position of the star in the Hertzsprung-Russel diagram, which corresponds to its evolutionary stage. Stars on the main sequence are in the main phase of hydrogen burning.

parameter	value	reference
P	$(2.218\,575\,67 \pm 0.000\,000\,15)$ d	a
T_0 [BJD]	$2\,454\,279.436\,714 \pm 0.000\,015$	a
e	0 (fixed)	a
a	$0.031\,00 \pm 0.000\,62$ AU	a
i	$(85.7100 \pm 0.0023)^{\circ}$	a
$v_{rot} \sin i_S$	(3500 ± 1000) m/s	a
λ	$(-0.31 \pm 0.17)^{\circ}$	a
i_S	$92^{+12}_{-4}{}^{\circ}$	a
K	(205.0 ± 6.0) m/s	a
T_P [BJD]	$2458334.64^{+0.51}_{-0.50}$	b
ω	90° (fixed)	a
R_P/R_S	0.1513 ± 0.0072	a
a/R_S	8.84 ± 0.27	a
T_{eff}	(5040 ± 50) K	a
R_P	$1.138 \pm 0.027\ R_{Jup}$	a
M_P	$1.144 \pm 0.056\ M_{Jup}$	a
R_S	$0.756 \pm 0.018\ R_{Sun}$	a
M_S	$0.806 \pm 0.048\ M_{Sun}$	a
b	$0.703^{+0.029}_{-0.033}$	b
t_{dur}	(1.84 ± 0.04) h	b
RV jitter	$16.5^{+4.6}_{-3.1}$ m/s	b
V-band magnitude	7.648	c

Table 6.1: Parameters of HD189733 and its exoplanet as used for the analysis in this work. References: a) Casasayas-Barris et al. (2017); b) Addison et al. (2019); c) Koen et al. (2010).

observations by Dumusque (2014), who calculated ψ, using the λ value by Triaud et al. (2009), to be $(4^{+18}_{-4})^{\circ}$, giving further evidence for a well-aligned orbit.

As HD189733 is a comparably bright star with a V-band magnitude of 7.6 (Tab. 6.1), studies that rely on excellent SNR observations to further characterize the planet have been carried out, for instance concerning temperature gradients on the planet's surface (Heng et al. 2015) or atmospheric winds at high altitudes (Louden and Wheatley 2015).

6.2.2 MaHPS Observations

HD189733 was observed in two nights. In the first night (2020-11-06), the transit was recorded, whereas in the second night (2020-11-09) a series of template spectra out of transit were taken. The characteristics of the obtained data sets as well as the observing conditions are summarized in the following.

Transit (2020-11-06)

Observations of HD189733 with MaHPS were carried out in the night starting 2020-11-06, yielding a total of 19 spectra during and around the transit. The first exposure was a test frame, which served to estimate a suitable exposure time for the following observations, with an exposure time of 100 s and without simultaneous calibration. All remaining frames were recorded with simultaneous calibration using the LFC. At an exposure time of 900 s, a median SNR of 86 was reached (see Sec. 4.3 for the determination of the value).

The sky in that night was free from clouds and the airmass[47] during the observation ranged from 1.1 to 2.9. Two potential complications can arise from such a large airmass: on the one hand, the strength of telluric absorption lines in the stellar spectrum is significantly increased, on the other hand, atmospheric dispersion can introduce some drift or offset of the measured RVs.

The observation run of HD189733 on 2020-11-06 started right after sunset. The first exposure of the series was taken before astronomical twilight[48], giving rise to a small chance that the first frame could be contaminated with remaining sunlight. In that night, the Moon had an illumination of 66% and rose around the midtime of the series, but its elevation relative to the horizon stayed below 20° during the whole observation, so contamination of the frames with scattered light from the Moon is very improbable.

At the end of the transit phase, a technical issue with the telescope occurred, which resulted in an interruption of the automated tracking of the star while the exposure was still running. The correction of that error required to restart the telescope and make a new pointing to the star. Since the frame taken during that time received almost no light from the star, it was excluded from the analysis.

Templates (2020-11-09)

Template spectra of HD189733 without simultaneous calibration were obtained on 2020-11-09 with an exposure time of 1800 s each. Four spectra with a median SNR of 162 were recorded. Since time resolution is not an issue for the template spectra, the exposure time was chosen to be larger than that of the transit observations in order to get best SNR possible, because the data quality of the template has a direct effect on the error of the CCF method.

During the template observations on 2020-11-09, no clouds were in the sky, but the

[47]The airmass is a unitless number indicating the length of the light path through the atmosphere. It is defined to be 1 if the light is falling in perpendicular to the Earth's surface, for instance if a star is located exactly at zenith, directly above the observer. The value of the airmass increases for shallower incidence angles, so that light from a star at a lower altitude, for example with an airmass of 2 (or an altitude of 40°), traverses the atmosphere on a path that is twice as long as if the star was positioned at zenith.

[48]Astronomical twilight denotes the time in the evening and morning, when the Sun is positioned 18° below the horizon. The night time between astronomical twilight is considered to be completely dark, historically based on the fact that the faintest star became visible by eye at that time. Spectroscopic measurements are often less sensitive to the remaining scattered sunlight in the atmosphere after sunset, allowing for a start of observations slightly earlier than astronomical twilight, and vice versa before sunrise.

ambient humidity was relatively high, which could possibly cause the telluric absorption features of H_2O to appear stronger. A generally conservative masking of the areas where such a contamination is expected allowed to rule out any negative effects in this analysis. The airmass for the four exposures ranges from 1.1 to 1.3.

The observations on 2020-11-09 were also taken at the very beginning of the night, with the start of the first exposure coinciding with astronomical twilight. The Moon remained well below the horizon during the complete observation run, so no contamination of the collected spectra with sunlight is expected.

6.2.3 Data analysis

The observations of HD189733 were reduced using the in-house pipelines GAMSE and MARMOT (description in Sec. 4.1 and Sec. 4.3, respectively).

Reduction with GAMSE

GAMSE was executed automatically after each night of observation with the default parameters as quoted in Sec. 4.1. Table 6.2 lists the frames that were used for the background correction of the exposures with simultaneous calibration, along with the *ThAr* exposures that were chosen as basis for the wavelength calibration.

night	background reference	exposure time [s]	wavelength reference	exposure time [s]	rms [Å]
2020-11-06	20201106_0106	100	20201106_0048	19	0.00139
2020-11-09	—	—	20201109_0048	19	0.00139

Table 6.2: Reference frames used for the background correction and *ThAr* wavelength calibration of GAMSE for the HD189733 data. For nights in which all exposure were taken without simultaneous LFC calibration, no background correction is performed.

The fact that the background reference frame 20201106_0106[49] was taken with only 100 s exposure time, while the rest of the spectra in that night were exposed for 900 s, could introduce a small systematic error in the extracted fluxes. Considering that all exposures using this frame for the background correction were taken in one night and that the shape of the background only changes slowly with time, the overall error due to the different exposure times is expected to be negligible, since only relative RV measurements are conducted. However, in order to avoid such error sources for other observations, in each night a frame without simultaneous calibration should be taken at the same exposure time as the remaining frames.

[49]Each frame recorded with MaHPS follows the same naming convention. The date of the observation night is followed by a numeric frame ID, starting with 0001 for the first exposure, including calibration exposures. The full filename additionally contains information about the instrument and hardware revision, as well as about the type of exposure. For conciseness, only the date and frame ID are given here and in the following.

Reduction with MARMOT

The reduction of the data with MARMOT in order to obtain RVs from the wavelength calibrated spectra was made using a script, which contained all necessary MARMOT commands, and an initialization file, where the parameters for the reduction were specified.[50] The relevant parameters for the reduction are summarized in Tab. 6.3.

	HD189733	HD149026	HAT-P-2
included orders	76, 84 to 133	76, 84 to 133	76, 84 to 133
excluded orders	$87, 88, 91, 96, 97$	$87, 88, 91, 96, 97$	$87, 88, 91, 95, 96, 97$
number of frames used for template	3	4	7
template SNR	288	225	176
template barycentric correction	$-22\,119$ m/s	$14\,499$ m/s	$11\,792$ m/s
wavelength calibration method	*ThAr*	*ThAr*	*ThAr*
CCF center measuring method	Gaussian	Gaussian	Gaussian
pixel range for CCF	$[200, 1850]$	$[200, 1850]$	$[200, 1850]$
σ-clipping coefficient	2.0	1.75	2.0
σ-clipping iterations	4	3	2
RV combination method	mean, no weights	mean, no weights	mean, no weights
median error bar size	12 m/s	21 m/s	61 m/s

Table 6.3: Parameters used for the MARMOT reduction of the observation data of HD189733, HD149026, and HAT-P-2.

A list of physical orders is excluded from the RV analysis, as they are affected either by broad stellar absorption features or heavy contamination with telluric absorption lines. However, additional orders to those listed in Tab. 6.3 may be rejected during the analysis, based on the excluded wavelength regions specified in the mask file.

The template was generated from three individual frames and has an approximate SNR of 288. As the template is only available as a continuous parametrized function, the SNR of the template cannot be determined in the same way as for the discrete spectra that were binned with the detector pixels. To obtain the SNR of the template spectra, the strategy outlined in the following was applied.

In case the noise of a spectrum is dominated by photon noise and therefore follows the distribution of a Poisson function, the error F_{err} of the measured flux F for a single detector pixel can be approximated as:

[50] The script and initialization file, as well as additional files necessary for the MARMOT reduction of HD189733, are provided under `https://github.com/vfahrens/MaHPS_scripts` for download.

$$F_{err} \approx \sqrt{F} = \sqrt{N_{phot}}, \tag{6.1}$$

where N_{phot} is the number of photons collected in that pixel. By definition, the SNR is the quotient of the flux and the flux error. Using the approximation of Eq. 6.1, this simplifies to:

$$\mathrm{SNR} = \frac{F}{F_{err}} \approx \frac{F}{\sqrt{F}} = \sqrt{F}. \tag{6.2}$$

For all MaHPS spectra used in this work, it was verified that Eq. 6.1 holds to a level better than 3%, which is satisfying the 2σ confidence interval of 4.5%, and therefore the SNR can be obtained with Eq. 6.2. The SNR of the template spectrum for a single order was calculated by first summing up the number of photons from all frames that contribute to the template for each pixel, then calculating the mean N_{phot} in each order, using the summed fluxes for all pixels between $[200, 1850]$. Finally, the square root of the mean value was taken to get the order-wise template SNR as stated in Eq. 6.2. The overall template SNR was determined analogously to that of the observed frames, by calculating the median of the order-wise SNR of orders 85, 86, 89 and 90.

It has to be noted that the B-spline fit performed during the creation of the templates additionally smooths out noise features, so the method described here will yield template SNR values that are systematically underestimated.

Figure 6.1 shows an example of a spectrum of HD189733 (blue line and orange data points), as recorded for physical order 90 on 2020-11-06 with MaHPS, in direct comparison with the template (green line). The gray-shaded areas correspond to wavelength regions that have been excluded from further analysis in the mask file. The overall amplitude of the template, here plotted in the form of CCD counts, results from the fit during the template generation and doesn't carry any physical information. In Fig. 6.1, the template amplitude was divided by a factor of 4 to adjust it to the amplitude of the observed spectrum and facilitate visual comparability. During the data reduction with MaHPS, the amplitude of the template is automatically scaled to best fit that of the data, as stated in Sec. 4.3.

The reduction of noise in the template while keeping the spectral features is demonstrated in Fig. 6.1. The template SNR for order 90 is 279, whereas the SNR of the measured spectrum is only 85, a value representative for the complete observation run of 2020-11-06. To make a direct comparison of the binned measured spectrum with the continuous template possible, the template is discretized for Fig. 6.1 by evaluating the template function only at the wavelength coordinates of the observed spectrum.

In addition to the difference in SNR, Fig. 6.1 clearly reveals a wavelength shift between the template and the measured spectrum, which is caused by the motion of the Earth around the Solar System's barycenter. The barycentric correction necessary to take this effect into account is applied to the spectrum and the template at a later stage.

The frames with and without simultaneous calibration were treated identically in this reduction, since no use of the additional wavelength calibration information of the LFC was made. The reason for this decision was the benefit from including more orders than

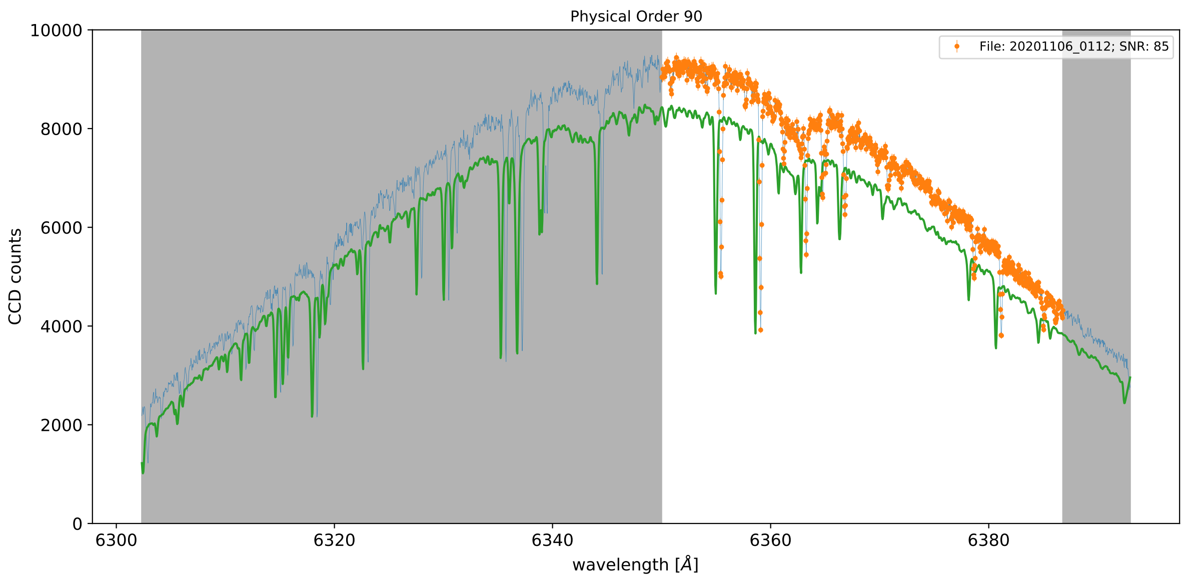

(a) Spectrum of the complete physical order 90.

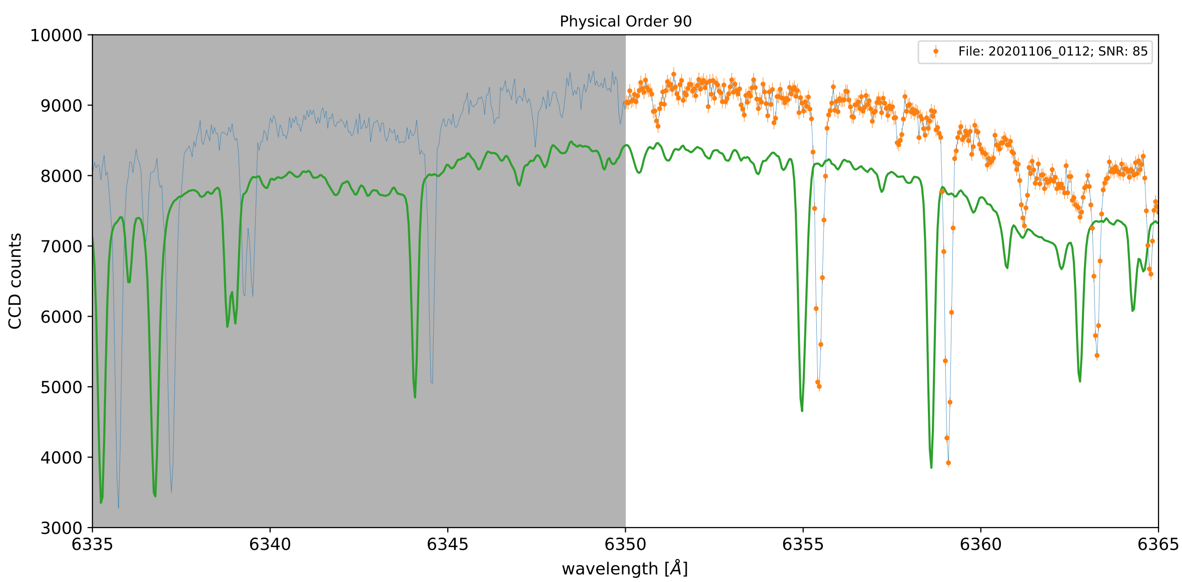

(b) Zoom of physical order 90 to the wavelengths 6335 to 6365 Å.

Figure 6.1: Example of a recorded spectrum of HD189733 for physical order 90, compared with the used template. Blue line: recorded spectrum, extracted with GAMSE; green line: B-spline template from MARMOT pipeline, evaluated at the same wavelengths; orange points: data points of the spectrum contributing to the CCF calculation, error bars are the flux error of each pixel calculated by GAMSE; gray areas: wavelength regions excluded in the mask file. The flux of the template is scaled down by a factor of 4 for better comparability.

covered by the LFC, that was greater than the gain in RV precision for the limited number of orders which contain LFC calibration light.

To obtain RV measurements for the single orders, the CCF method of MARMOT was chosen. The χ^2 fitting method was found to produce less stable results for low SNR data as in this work. Further details on the data reduction procedure with MARMOT are given in Sec. 4.3.

After getting a RV measurement for each order of all frames of HD189733 from MARMOT, a frame-wise combination of the RV of all individual orders was made by applying a σ-clipping to the order-wise results and calculating the mean of the remaining RV values. The median of the RVs of all orders served as reference for the σ-clipping, the applied coefficient and number of iterations are given in Tab. 6.3.

It should be noted that the σ-clipping coefficient and iterations have to be adjusted for each object individually, since the difference in the stellar spectra, e.g. due to a difference in the spectral type of the stars, results in a significantly different distribution of the typical RV errors between the orders. The frame-wise RVs are typically obtained as the weighted mean of the order-wise results, where the inverse of the RV error of each order is used as weighting factor. In this work, the mean for each frame was calculated without using weights, because orders with a large deviation from the remaining orders and therefore probably large errors were rejected by the σ-clipping.

The error bars for each frame's RV measurement were then determined from the spread between the orders remaining after the σ-clipping as the standard deviation of the order-wise RVs, divided by the square root of the number of contributing orders. As indicative number of the precision of the obtained frame-wise RVs, the median of the error bar size is given in Tab. 6.3.

Plotting the RV model and data

The RV curve that is theoretically expected for the RM effect of HD189733 is calculated with the `starry` package. However, as discussed in Sec. 5.2, the results are affected by several modeling imperfections. Therefore, instead of using a single model with a fixed parameter set, a sample of multiple different models that reflects the uncertainty of the input parameters is plotted.

The sample of RV curve models is generated in the following way: First, each model input parameter is obtained from the literature, in the form of the measured value P_m and the associated error bars e_{P_m} for the example of the orbital period P. It is then assumed that the statistical distribution of the measurement error follows a Gaussian function, which is described with peak position P_m and width e_{P_m}. The value of P used in the model is then randomly drawn from this distribution. The other parameters are determined equivalently. In case the measurement of a parameter has asymmetric errors, the larger of both values is adopted as width of the distribution. This procedure is repeated to acquire 100 random sets of parameter combinations, each of which is then provided to `starry` for the calculation of the model RV curve.

The measurement values and errors used for the generation of the random parameter sets are given in Tab. 6.1. In addition to that list, a few more parameters are required for the RV curve model, for which no measurements are available. This concerns on the one hand the limb darkening parameters q_1 and q_2, which are relevant for the intensity distribution $I(x, y)$ of the stellar disk. A uniform distribution with boundaries $q_1, q_2 \in [0, 1]$ is assumed for both parameters, which is justified by the fact that the parameter space of q_1, q_2 is designed to be uniform and only values between 0 and 1 are allowed physically, as proposed by Kipping (2013) and outlined in Sec. 5.2.4. For the calculation of the velocity field $v(x, y)$ of the stellar disk, on the other hand, the linear shear parameter α is required to take into account differential rotation. A Gaussian with peak position $\alpha_m = 0.0$ and width $e_{\alpha_m} = 0.5$ is applied.

The complete sample of the modeled RV curves is plotted together with the data points from the observations of HD189733 with MaHPS, so an impression of the involved uncertainties can be gained. The model curves are sampled with a much larger time resolution, however for a direct comparison of the recorded data with the model the binning of the measured RV curve in terms of the exposure time has to be considered. Therefore, the model RV curves are also shown binned with the exposure time.

To obtain the binned model RV curve, the finely sampled time coordinates of the model are divided into chunks that have the length of the exposure time. For each chunk, an expected RV value and its associated error are calculated. The RV value is generated by determining the median of the 100 RVs for each single time coordinate in that chunk and subsequently taking the mean of the median RVs of all time coordinates. While the distribution of the RVs of the individual models per time step is statistical and the median gives a good representation of the true value, the mean has to be used for the combination of all time steps in one chunk, as the exposure during an observation corresponds to an integration of the incoming signal. The RV error of each binned RV value is obtained by calculating the standard deviation of all individual model RVs in one bin, without taking the median per time step first, in order to reflect the statistical uncertainty of the models and the changes of the RV curve during one exposure.

In the generation of the model RV curves, the RV baseline, which represents a RV offset of the complete curve relative to zero velocity at mid-transit time, is a further parameter that cannot be directly measured. RV measurements from measured spectra can show such offsets for various reasons. If the wavelength reference frame of the template differs from the observations, a systematic offset is introduced. This can be the case if synthetic spectra are used as templates or if a template from measured spectra is not corrected for the relative motion of the observer to the Solar System's barycenter (see also Fig. 6.1).

When using observed spectra of the same star as templates, the baseline RV is expected to be around 0 m/s, since constant offset terms like the peculiar velocity of the star are automatically canceled out in the RV determination process. Therefore, the baseline for all RV model curves was chosen to be 0 m/s.

In this work, the barycentric correction was not applied to the template spectrum before its creation or calculating the CCF. Instead, the barycentric correction term for the template was calculated as the mean of the barycentric RV corrections for the individual exposures contributing to the template and subtracted from the frame-wise RV values obtained from the MARMOT reduction. Although the barycentric correction value from this method is not exact, since the template is not generated as a simple mean of the used frames, it is still a good estimator if all template frames were collected in the same night. For HD189733, the barycentric correction amounts to $-22\,119\,\mathrm{m/s}$ (see Tab. 6.3).

Additional sources for RV curve offsets are instrumental offsets, like drifts of the instrument between nights or inconsistencies in coupling the stellar light into the fiber (see Sec. 2.3.3). These effects vary on a night-to-night basis with a typical amplitude on the order of several $10\,\mathrm{m/s}$, the exact value of which is not known a priori. Furthermore, the template exposures are usually obtained at an arbitrary phase of the orbit and in the process of the template generation they are combined to a common wavelength reference, which may correspond to any phase of the orbit, giving rise to another offset. While this contribution is constant between different observation nights, it still has to be taken into account here, as the observation data are directly compared to a model with a defined zero point. To correct effects like that outlined here, for each night, a nightly RV offset of the data set is determined.

The RV offsets specific to each night are calculated by subtracting the median of the binned RV values of the models from the median of all RV measurements in that night, only taking into account the bins of the model where a measurement is available. The latter is necessary to account for cases when e.g. only half of the transit phase was observed, but the model is calculated for the complete transit. The RV offset value is subject to statistical variations, as the comparison of the measured data is made with a sample of 100 randomly drawn RV curve models. To account for those variations, the procedure of calculating the RV offset is repeated 100 times, each time with a fresh set of RV curve models, and subsequently the median of all RV offsets is calculated. This median is subtracted from the observed RVs to finalize the zero point correction of the RV data. The uncertainty of the RV offset is determined as the standard deviation of all individual offset values.

object	night	RV offset	note	median data error bar size	baseline error
HD189733	2020-11-06	$(153.6 \pm 0.9)\,\mathrm{m/s}$	a	$12.3\,\mathrm{m/s}$	$3.7\,\mathrm{m/s}$
HD149026	2021-03-05	$(5.9 \pm 0.8)\,\mathrm{m/s}$		$20.3\,\mathrm{m/s}$	$7.0\,\mathrm{m/s}$
	2021-03-08	$(-12.1 \pm 1.1)\,\mathrm{m/s}$	b	$20.5\,\mathrm{m/s}$	$8.9\,\mathrm{m/s}$
	2021-04-23	$(-19.4 \pm 0.8)\,\mathrm{m/s}$	c	$19.4\,\mathrm{m/s}$	$6.3\,\mathrm{m/s}$
	2021-04-26	$(9.8 \pm 0.7)\,\mathrm{m/s}$		$22.1\,\mathrm{m/s}$	$6.6\,\mathrm{m/s}$
HAT-P-2	2021-02-24	$(-958.7 \pm 3.3)\,\mathrm{m/s}$		$55.2\,\mathrm{m/s}$	$28.9\,\mathrm{m/s}$
	2021-02-25	$(-911.9 \pm 3.0)\,\mathrm{m/s}$		$60.8\,\mathrm{m/s}$	$25.6\,\mathrm{m/s}$

Table 6.4: RV offsets between the RV model and the RV data, as well as median error bar size of the data and resulting baseline error for the individual nights of observation with MaHPS for all three objects. Notes: a) last 7 frames excluded from RV offset determination due to systematic offset; b) last 6 frames excluded from RV offset determination due to systematic offset; c) last 4 frames excluded from RV offset determination due to restart of the guiding system.

Table 6.4 contains an overview of all nightly RV offsets for the objects observed in this work. For HD189733, the last seven data points from 2020-11-06 were excluded from the offset calculation, as they are with high probability affected by a further systematic offset due to the restart of the telescope. The offset value of $(153.6 \pm 0.9)\,\mathrm{m/s}$ can be mainly attributed to the phase difference at which the templates were recorded. Unfortunately, it is not possible to draw conclusions about the magnitude of instrumental effects from this single measurement.

The last required parameter for the RV models is the error of the baseline, reflecting intrinsic measurement errors related to factors like the signal strength of the individual exposures. Given that the template is the reference for the RV determination, the baseline error should correspond to the expected RV measurement error if only the template was the only source of errors. Therefore, the size of the baseline error was estimated by scaling the median error bar size of the observed data of one night with the ratio of the data SNR divided by the SNR of the template. The resulting baseline errors for all objects are given in Tab. 6.4.

In the RV model calculation, the baseline error is assumed to follow a Gaussian distribution. For HD189733, the baseline parameter overall is specified as $(0.0 \pm 3.7)\,\mathrm{m/s}$. The template-based error bar of $3.7\,\mathrm{m/s}$ is almost identical to the observational RV error achieved with MaHPS for spectra of the planet host star 51 Peg of $3.6\,\mathrm{m/s}$ (Kellermann 2021). In the observation of 51 Peg, spectra with extremely high SNR were obtained, allowing the conclusion that the errors of $3.6\,\mathrm{m/s}$ reflect the intrinsic precision of the instrument and the data reduction methods. That a similar value is reached with the template for HD189733 indicates that the template is of such a good quality that using additional frames in its generation would not result in a further significant improvement of the RV precision.

6.2.4 Results

The MaHPS RV measurements of the RM effect of HD189733 for the observation conducted on 2020-11-06 are shown in Fig. 6.2 (blue points). The sample of the modeled RV curves (orange lines) and the RVs of the model curves, binned to the exposure time of the observation (red points), are plotted for comparison.

Overall, the RV measurements obtained here follow the expected RV signal within the error bars, with the exception of the very first data point, which is the test exposure with a shorter than regular exposure time of only 100 s. The SNR of that frame is extremely low at ~ 30, potentially explaining the large deviation from the other RV measurements. In addition, there is a chance that the exposure could be contaminated with remaining sunlight after sunset, forming a further possible degradation of the RV measurement accuracy and precision.

The case of the first data point in Fig. 6.2 demonstrates that it is possible to obtain RV values from MARMOT even for very weak stellar spectra, however the reliability of such results should be doubted. The error bars of this data point are clearly underestimated by at least a factor of 2, which could be a result of using the spread between the orders

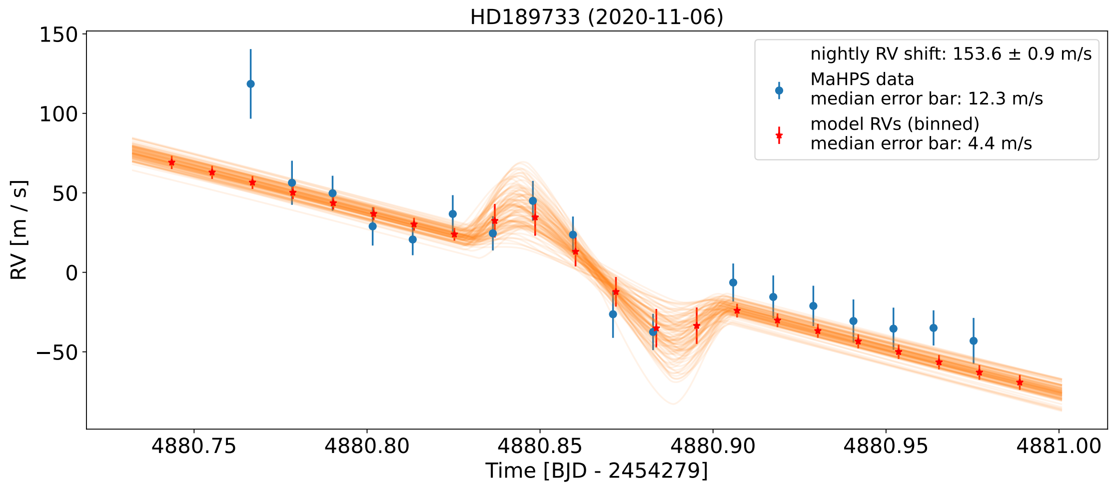

Figure 6.2: RV curve of the HD189733 transit observations with MaHPS (blue points), the sample of RV curve models (orange lines) and the binned RV curve models (red points), which are representing the uncertainty of the literature parameter set for HD189733. Data from 2020-11-06.

as error estimator, in combination with the σ-clipping of the order-wise RV distribution. When the RV distribution is not clearly peaked, but rather random due to the low SNR, it is possible that RV values off from the true RV are preferred, if several data points form a concentration by chance. Instead, computing the weighted average for the frame-wise RVs of low flux data can provide a method to avoid this kind of complications, at least to a certain degree.

Right at the end of the transit in Fig. 6.2, there is a data point missing due to a telescope failure. While the data points collected before and during the transit match the modeled RV curves, the data points recorded after the transit feature the same slope as the RV models, but seem to show a consistent, systematic offset of about 15 to 20 m/s. This offset is probably caused by the re-pointing of the telescope, in which case a small change of the angle could have happened, under which the stellar light is coupled into the fiber, resulting in a small overall shift of the slit image on the detector. Simultaneous calibration is not capable of correcting such an offset, as the optical path of the LFC light via the calibration fiber is not affected by a fresh telescope pointing. A possibility to mitigate fiber coupling errors is the use of fibers with octagonal cores as mentioned in Sec. 2.3.3.

A further interesting factor during the measurement series shown in Fig. 6.2 was the airmass at which HD189733 was observed. The star was setting during the complete run, reaching an airmass of 1.5 just as the tracking of the telescope failed. After the observations were continued, the airmass rapidly climbed to a maximum of 2.9 as the star approached the horizon. Owing to the increased absorption from the atmosphere, the SNR in the last three exposures declined from $\sim$80 to $\sim$60. Despite the drop in recorded intensity and the thick atmospheric layer that the light of the star traversed, no impact on the RV

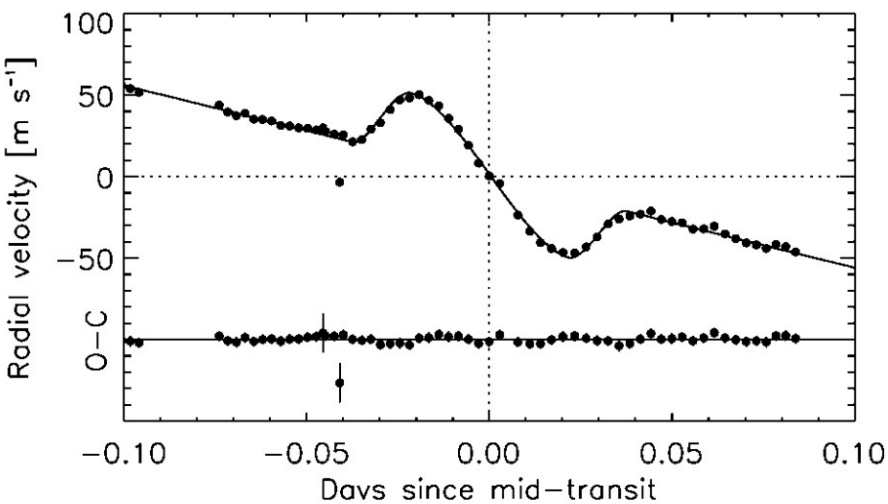

Figure 6.3: RV data of the RM effect for HD189733, obtained during a single transit with HIRES at the Keck I 10 m telescope. Black points: RV measurements; solid line: best fit model. Top part: RV curve around the transit phase; bottom part: residuals between the model and the data. Graphic taken from Winn et al. (2006).

measurements in the form of an additional drift or shift can be seen.

Other MaHPS observations, for instance with the goal to determine the orbital RV curve of a planet-hosting star, have adopted a maximum allowed airmass of 1.5 to mitigate negative effects of the atmospheric dispersion effect. However, the RV series of HD189733 shows that this is not necessary, as long as the weather conditions allow observations at low elevations and the regions affected by telluric lines are thoroughly masked before the analysis.

Because a RV offset was introduced to the measurement series by technical issues and the RV anomaly of the RM effect is only sampled with five data points, it is unfortunately not possible to make an independent fit of the obliquity λ or any other parameters for HD189733. Nevertheless, Fig. 6.2 illustrates that even a single observation night can be enough to gain a first impression of the existence of a RV anomaly and whether a prograde or retrograde orbit is present.

6.2.5 Literature data

Measurements of the RM effect for HD189733 have been published by Winn et al. (2006), Triaud et al. (2009), and Casasayas-Barris et al. (2017). The RV data and fit models are given in Fig. 6.3, Fig. 6.4, and Fig. 6.5, respectively.

The first RM effect measurement series for HD189733 by Winn et al. (2006) was obtained with an exposure time of 180 s and yielded an SNR of ~300. The errors from photon noise for each individual exposure on average were found to be 0.8 m/s, but the error bars used for the fit were enlarged to 3 m/s, a value obtained from RV data recorded out of tran-

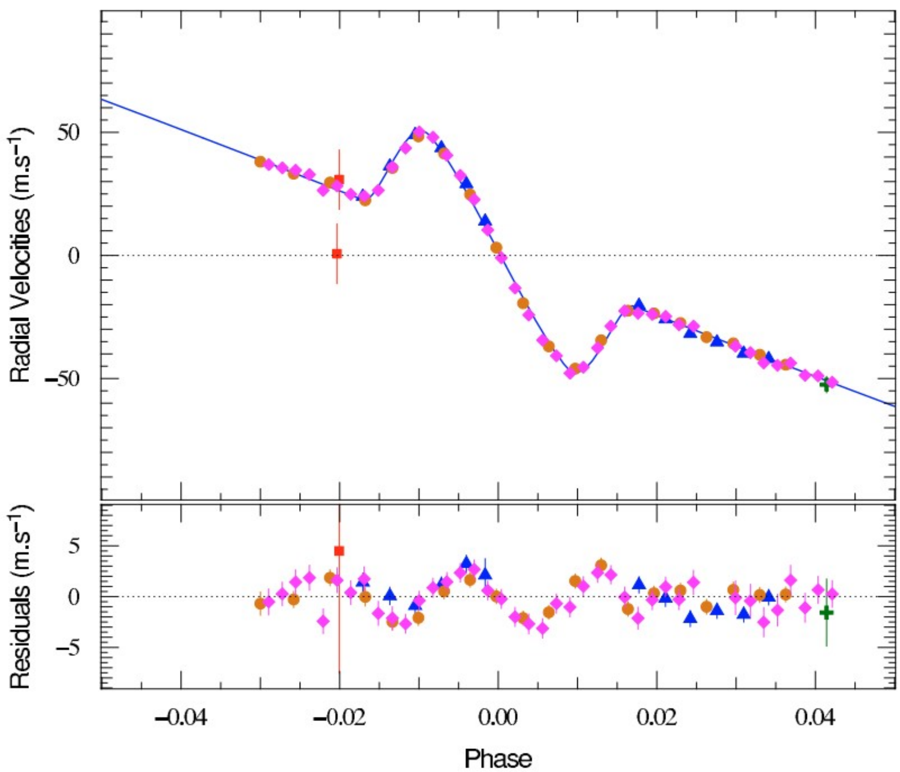

Figure 6.4: RV data of the RM effect for HD189733, obtained during three transits with HARPS at the ESO La Silla 3.6 m telescope. Pink diamonds, blue triangles, orange circles: RV measurements of the three observation runs; blue solid line: best fit model to the combined data set; red squares, green crosses: RV data from other instruments for sampling the barycentric motion of HD189733. Top panel: RV curve around the transit phase; bottom panel: residuals between the model and the data. Graphic taken from Triaud et al. (2009).

sit, to account for stellar effects causing additional RV uncertainties. The residuals of the best fit (Fig. 6.3, bottom) show a pattern appearing like an oscillation with an amplitude larger than the error bar size.

Further observations of the RM effect for HD189733 were conducted by Triaud et al. (2009) for transits in three separate nights. Two of the three measurement series were sampled at a 630 s interval (Fig. 6.4, orange and blue) and one series was recorded with a higher sampling rate at 330 s (pink). The average error bar size due to photon noise for all exposures is 0.98 m/s. The residuals in Fig. 6.4 exhibit a significant oscillation-like behavior, similar to that found by Winn et al. (2006). The fact that the residual structure is identical for all three transits is a strong hint towards imperfections of the model fit to the data.

The RM effect analyses by Winn et al. (2006) and Triaud et al. (2009) were relatively early works and the models used for the RM effect have developed over the past years. Recently, a re-analysis of the HARPS data set, using the identical RV values and errors

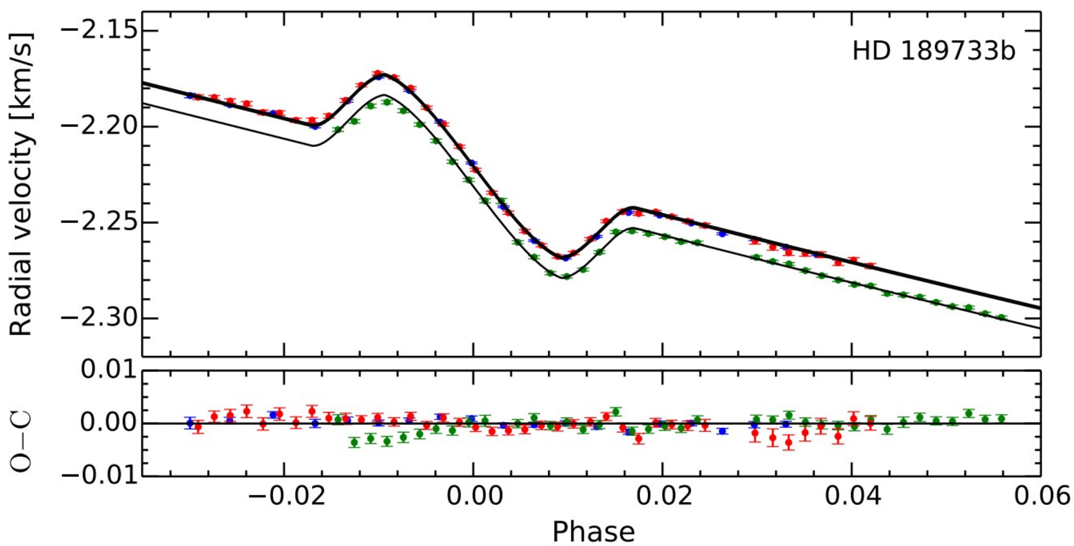

Figure 6.5: Re-analysis of the RV data of the RM effect for HD189733, obtained during three transits with HARPS at the ESO La Silla 3.6 m telescope by Triaud et al. (2009), compare Fig. 6.4. Red, blue, and green data points: RV measurements of the three observation runs; black solid lines: best fit models to all transits jointly but allowing for independent RV offsets. Top panel: RV curve around the transit phase; bottom panel: residuals between the model and the data. Graphic taken from Casasayas-Barris et al. (2017).

of Triaud et al. (2009), was made by Casasayas-Barris et al. (2017). The correlation in the residuals for the three transits that was found from the previous analysis has vanished (Fig. 6.5, bottom), indicating that the model used in this case is able to predict the RM effect with a better precision.

Comparing the RV curves in Fig. 6.3 to Fig. 6.5 with the observational data of MaHPS, given in Fig.6.2, immediately highlights the primary challenge of conducting RM effect investigations with MaHPS: obtaining spectra with high SNR at the best possible time resolution. The main limiting factor is the size of the telescope. The light collection area of HARPS and HIRES are larger by a factor of 3.3 and 25, respectively, which allows to reach better SNR for an individual exposure even at shorter exposure times. To overcome this handicap of MaHPS, the advantage of more flexible scheduling has to be exploited. Several transit observations in different nights need to be made for a single object, which afterwards can be combined statistically for a better RV measurements precision.

6.3 HD149026

HD149026 is the second[51] star-planet system for which the RM effect was detected and used to determine the obliquity (Wolf et al. 2007). A re-analysis of that dataset was carried out by S. Albrecht et al. (2012), because improved photometric measurements of HD149026 were available in the meantime (Carter et al. 2009).

6.3.1 System characteristics

Table 6.5 contains the system parameters of HD149026 that were adopted for the analysis of the RV measurements with MaHPS presented in the following.

parameter	value	reference
P	$(2.875\,888\,74 \pm 0.000\,000\,59)$ d	e
T_0 [BJD]	$2\,454\,456.787\,60 \pm 0.000\,16$	e
e	0.051 ± 0.019	d
a	0.0432 ± 0.0024 AU	d
i	$84.55^{+0.35}_{-0.81}$ °	b
$v_{rot} \sin i_S$	(7700 ± 800) m/s	a
λ	$(12 \pm 7)^\circ$	a
i_S	—	—
K	(39.22 ± 0.68) m/s	d
T_P [BJD]	$2\,463\,208.80 \pm 0.17$	d
ω	$(109 \pm 21)^\circ$	d
R_P/R_S	0.0507 ± 0.0009	a
a/R_S	$6.01^{+0.17}_{-0.23}$	b
T_{eff}	(6160 ± 50) K	b
R_P	0.718 ± 0.065 R_{Jup}	c
M_P	0.352 ± 0.025 M_{Jup}	c
R_S	1.45 ± 0.10 R_{Sun}	c
M_S	1.30 ± 0.10 M_{Sun}	c
b	$0.48^{+0.09}_{-0.15}$	e
t_{dur}	(3.230 ± 0.150) h	a
RV jitter	2.35 m/s	d
V-band magnitude	8.14 ± 0.01	f

Table 6.5: Parameters of HD149026 and its exoplanet as used for the analysis in this work. References: a) S. Albrecht et al. (2012); b) Carter et al. (2009); c) Wolf et al. (2007); d) Ment et al. (2018); e) Zhang et al. (2018); f) Høg et al. (2000).

HD149026 is a G-type subgiant[52] star (e.g. Wolf et al. 2007) with $T_{eff} = (6160 \pm 50)$ K and has a mass of 1.30 ± 0.10 M_{Sun}. It lies very close to the Kraft break at 6250 K, and as expected from a star below the break it is a relatively slow rotator at $v_{rot} \sin i_S = (7700 \pm 800)$ m/s.

[51]The obliquity measurement of HD149026 was chronologically the second that was made, but before the publication of the discovery in a journal, RM effect measurements of a few other objects got published, among them HD189733.

[52]Subgiants are stars that have run out of hydrogen to burn in the core and are in a transition to become a giant star.

HD149026 hosts a close-in planet on a 2.9 d orbit, featuring a transit duration of (3.230 ± 0.150) h and a mass of $M_P = 0.352 \pm 0.025\ M_{Jup}$, roughly comparable to the mass of Saturn. Combining the mass with the planet's radius ($0.718 \pm 0.065\ R_{Jup}$) as obtained from photometric transit observations, the mean density can be estimated, which turns out to be higher than it would be expected for a gas giant, indicating a significant concentration of elements heavier than hydrogen and helium, probably in the form of a dense core (e.g. Carter et al. 2009; Zhang et al. 2018). The determination of the obliquity revealed an orbit orientation close to alignment with $\lambda = (12 \pm 7)^{\circ}$.

Since HD149026b shows an unusually high density and therefore is not a typical hot Jupiter, it has been extensively studied with photometrical methods to investigate properties such as the atmospheric temperature and composition (e.g. Carter et al. 2009; Stevenson et al. 2012) or the albedo, which is unusually high and potentially linked to the presence of clouds (Zhang et al. 2018).

6.3.2 MaHPS Observations

HD149026 was recorded in a total of five nights, with a total of four recorded transits (2021-03-05, 2021-03-08, 2021-04-23, and 2021-04-26) and one night of template spectra observations out of transit (2021-03-06). In the following, the characteristics of the obtained data sets as well as the observing conditions are summarized. To avoid confusion, the individual transits are labeled with letters A to D by the order of their observation.

Transit A (2021-03-05)

A transit of HD149026b was observed on 2021-03-05 in overall 13 exposures with exposure time 1200 s and simultaneous LFC calibration. A median SNR of 78 was achieved.

The night of 2021-03-05 was clear, but the start of the observation run was slightly belated due to ground-layer fog in the first half of the night. Owing to the ambient humidity, which stayed high during the complete run, the ventilation windows and doors of the telescope dome were kept closed and the AC was turned on for improved humidity control.[53] At end of the night, ground-layer fog formed again, but as the object was close to zenith at that time, there should be only a minor effect on the collected spectra. The airmass progressed from 1.4 to 1.0 during the observation and the object reached zenith at the end of the series.

The observation of HD149026b's transit was carried out in the second half of the night. The last five frames of the series were taken after astronomical twilight, the very last frame was even recorded after sunrise and was excluded from the analysis, because the spectrum of the Sun is visible with bare eye. Based on that fact, for the other four frames taken after astronomical twilight some contamination with the solar spectrum can be expected.

[53] In conditions of extremely high humidity, there is a risk of condensation on the telescope mirrors. If water condenses on the optical surfaces, the image of the star is blurred and the throughput is significantly decreased. Apart from that, the coatings of the reflecting surfaces can be damaged by moisture, therefore the humidity inside the dome needs to be controlled under such circumstances.

In that night, the Moon was illuminated to 51% and was visible at an elevation below 20° during complete run.

Templates (2021-03-06)

On 2021-03-06, four template frames of HD149026 with an exposure time of 1800 s were taken without simultaneous calibration. The median SNR for those spectra is 111.

In that night, some slight but persistent ground-layer fog was present, which also caused the humidity inside the dome to be rather high. During the observation run, the airmass for HD149026 was around 1.1 to 1.0.

All frames were obtained at end of night, with the exposure of the last frame starting after astronomical twilight. During the observation time, the Moon had elevations below 15°at an illumination of 39%.

Transit B (2021-03-08)

The second transit observation of HD149026b was made on 2021-03-08, yielding 17 spectra with simultaneous LFC calibration. At an exposure time of 1200 s, a median SNR of 98 for all frames combined was reached.

Similarly to the previous nights, there was a high humidity throughout the observation. The first exposure was taken at airmass 2.0, which continuously decreased as the star kept rising, until airmass 1.0 was reached for the last exposures.

All spectra were recorded in second half of the night. Obtaining out-of-transit reference spectra before the start of the transit was not possible, because the view was obstructed by the nearby broadcast antenna. The last four frames of the series were taken after astronomical twilight, with the last exposure being finished just before sunrise. The influence of the Moon can be safely neglected for this run, as it had a very low illumination of 20% and rose above the horizon only during the last few exposures.

Transit C (2021-04-23)

The transit observation on 2021-04-23 resulted in 15 exposures with simultaneous LFC calibration. One additional frame without simultaneous calibration was taken at the very beginning of the observation time and used in the analysis for the correction of the background stray light. All frames were recorded with exposure time 1200 s and have a median SNR of 73.

In that night, ground-layer fog formed around 00:00 UT, but quickly dispersed again. The airmass of HD149026 ranged from 1.4 to 1.0.

The observation of HD149026 started in the second third of the night and was continued until dawn. The last four frames were obtained after astronomical twilight, but the exposures were completed before sunrise. The Moon stood relatively high at 45° elevation when the series began and set at the end of the series. With a high illumination of 85% and a position on the sky relatively close to the target (72° Moon distance at 02:00 UT), there could be some contamination of the spectra with the reflected light of the Sun.

During the second half of the transit, the guiding camera failed and the automated object tracking of the telescope was stopped. In total, three exposures were affected by that error and are therefore excluded from the analysis.

Transit D (2021-04-26)

The last observation of HD149026 consists of 17 spectra of the transit with simultaneous LFC calibration and an extra frame without simultaneous calibration, taken at the end of the series, for the background correction. All frames have exposure time 1200 s and feature a median SNR of 67.

During the night of 2021-04-26, the sky was mostly clear with the occasional passage of cirrus cloud bands. The observation of HD149026 started at an airmass of 2.2, but the elevation of the star in the sky increased during the run to a final airmass of 1.0.

Since the nights at the end of April are significantly shorter than those at the beginning of March, when transits A and B were observed, the observation filled the complete night time. The run was started shortly after sunset but before astronomical twilight, which is why the first two frames could be affected by remaining stray light. The last exposure of the series was finished at astronomical twilight of the following morning. During the complete run, the Moon had an elevation between 15° and 35° and was in the full Moon phase with an illumination of 100%. Additionally, the angular distance between HD149026 and the Moon was small with only 57° (measured at 02:00 UT), so a potential contamination of the obtained spectra with reflected sunlight needs to be discussed.

A technical issue caused a telescope failure during the first exposure, causing a repositioning of the telescope onto the star while the exposure was still running. This exposure was included in the analysis, because there was no significant lack of flux in that frame.

6.3.3 Data analysis

The observations of HD149026 were reduced with the same methods as outlined for the observations of HD189733 (Sec. 6.2.3), using the in-house pipelines GAMSE and MARMOT (description in Sec. 4.1 and Sec. 4.3, respectively).

Reduction with GAMSE

GAMSE was executed automatically after each night of observation with the default parameters as quoted in Sec. 4.1. Table 6.6 lists the frames that were used for the background correction of the exposures with simultaneous calibration, along with the *ThAr* exposures that were chosen as basis for the wavelength calibration.

The data from nights 2021-03-05 and 2021-03-08 were re-reduced manually with the GAMSE pipeline, because in both nights an exposure of the star without simultaneous calibration was missing, inhibiting a correct background correction. In order for the routine to work properly, a frame without simultaneous calibration was copied from a different night's observation run. To that end, the frame with the best SNR from the closest possible

night	background reference	exposure time [s]	wavelength reference	exposure time [s]	rms [Å]
2021-03-05	20210306_0085	1800	20210305_0059	22	0.00133
2021-03-06	—	—	20210305_0045	12	0.00134
2021-03-08	20210306_0085	1800	20210308_0046	12	0.00133
2021-04-23	20210423_0079	1200	20210423_0056	22	0.00133
2021-04-26	20210426_0081	1200	20210426_0040	12	0.00137

Table 6.6: Reference frames used for the background correction and *ThAr* wavelength calibration of GAMSE for the HD149026 data. For nights in which all exposure were taken without simultaneous LFC calibration, no background correction is performed.

night was chosen, in this case 20210306_0085. The GAMSE reduction was then run again with all other parameters unchanged.

This approach is of course a possible source for systematic errors in the RV measurement and should be avoided by making sure that at least one frame without simultaneous calibration is recorded each night. Nevertheless, situations like the present one can happen for a variety of reasons, e.g. due to technical issues of the telescope or a sudden change of observing conditions. Therefore, the use of frames from other nights as background correction reference can be a necessary option and is tolerable if the time between the two nights and the difference in weather conditions is not too large.

Reduction with MARMOT

The reduction of the HD149026 data with MARMOT to obtain RVs from the wavelength calibrated spectra was made using a script, which contained all necessary MARMOT commands, and an initialization file where the parameters for the reduction were specified.[54] The procedure is identical to that for HD189733, with the set of parameters specific to HD149026 given in Tab. 6.3.

The template for HD149026 was generated from four individual frames and has a SNR of approximately 225.

Figure 6.6 shows an example of a spectrum of HD149026 (blue line and orange data points), as recorded for physical order 90 in the night of transit B (2021-03-08) with MaHPS, in direct comparison with the template (green line). The gray-shaded areas correspond to wavelength regions that have been excluded from further analysis in the mask file. The template SNR for order 90 is 223, whereas the SNR of the measured spectrum is 98, a value representative for the complete observation run of 2021-03-08.

In comparison with Fig. 6.1 for HD189733, the spectral lines in Fig. 6.6 for HD149026 are slightly broader. This becomes apparent e.g. when considering the spectral feature around 6338 Å in panel (b), which for HD189733 consists of a clearly resolved double peak,

[54] The script and initialization file, as well as additional files necessary for the MARMOT reduction of HD149026, are provided under `https://github.com/vfahrens/MaHPS_scripts` for download.

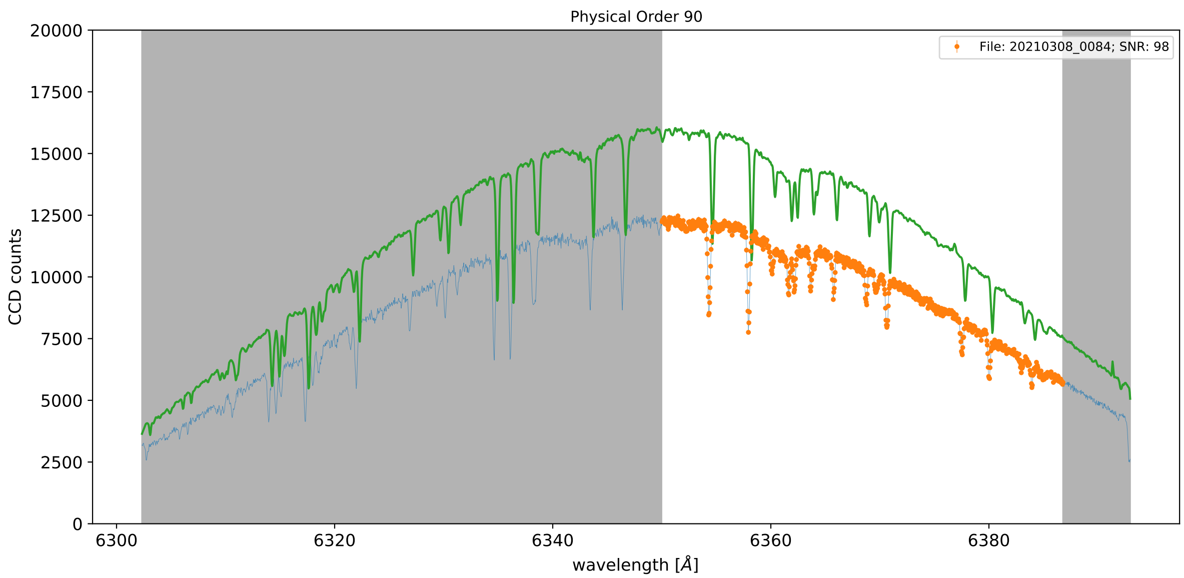

(a) Spectrum of the complete physical order 90.

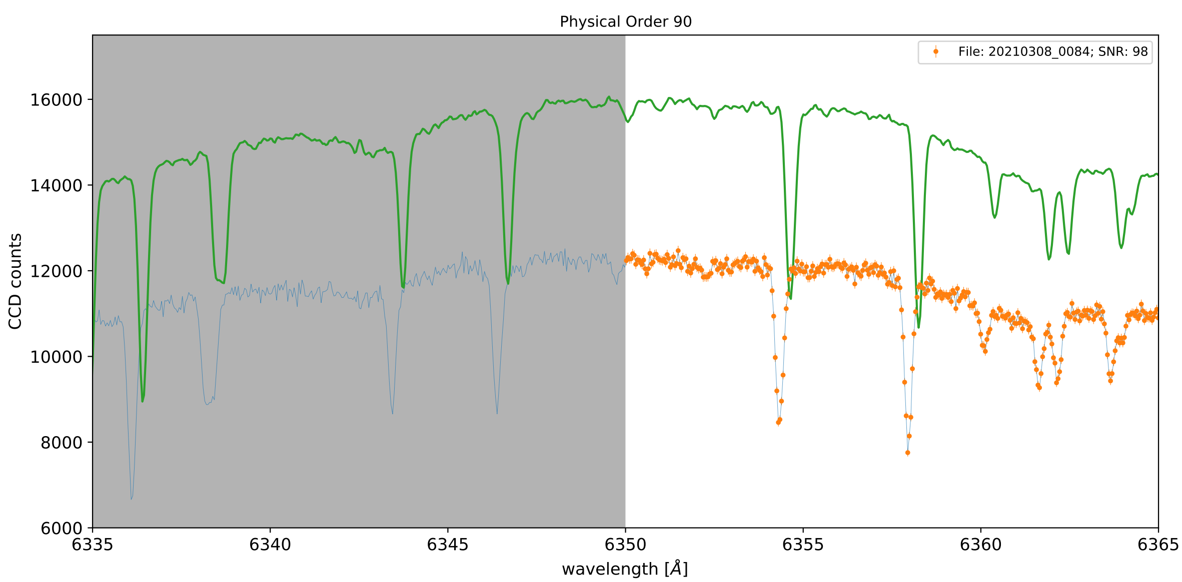

(b) Zoom of physical order 90 to the wavelengths 6335 to 6365 Å.

Figure 6.6: Example of a recorded spectrum of HD149026 for physical order 90, compared with the used template. Blue line: recorded spectrum, extracted with GAMSE; green line: B-spline template from MARMOT pipeline, evaluated at the same wavelengths; orange points: data points of the spectrum contributing to the CCF calculation, error bars are the flux error of each pixel calculated by GAMSE; gray areas: wavelength regions excluded in the mask file.

whereas for HD149026 the two peaks are blended into a single broad feature.

In this analysis, both the frames with and without simultaneous calibration were utilized, since no use of the additional wavelength calibration information of the LFC was made. As outlined in the description of the observations, several exposures were excluded from the analysis due to various issues. The affected frames were:

- `20210305_0102`, due to contamination with daylight, visible in the raw spectrum with bare eyes as additional spectral lines;

- `20210423_0088` to `20210423_0090`, due to a technical issue with tracking the star, so no stellar light reached the detector.

For the σ-clipping of the order-wise RV results of HD149026, the best coefficient found was 1.75 with a total of 3 iterations. With a median error bar of 20 m/s, the precision of the RVs for HD149026 is not as good as for HD189733 (12 m/s). However, this fact can be explained on the one hand by the broadened line profiles of HD149026 due to a faster rotation and on the other hand by the weather conditions during the observations, which were afflicted with fog and high humidity.

Plotting the RV model and data

For the generation of the RV curve models for HD149026, the same strategy as described in Sec. 6.2.3 for HD189733, was employed. A sample of 100 random parameter sets, to be used for the calculation of RV curves with `starry`, was obtained. The measurement values and errors of the input parameters are given in Tab. 6.5. In case a parameter features asymmetric errors, the larger value was adopted to get conservative estimate.

For the additional parameters q_1, q_2 and α, identical distributions as for HD189733 were assumed, with q_1, q_2 being uniformly distributed in $[0, 1]$ and α having a Gaussian distribution with peak and width 0.0 ± 0.5.

The barycentric correction of the template for HD149026 is 14 499 m/s (see Tab. 6.3). The RV offsets of the individual nights range from -19 to 10 m/s, indicating that the night-to-night variations of the instrumental RV offsets are on the order of at least 30 m/s.

For the baseline parameter of the RV model, (0.0 ± 8.9) m/s was adopted for the data set obtained on 2021-03-08, the errors for the other nights are listed in Tab. 6.4.

6.3.4 Results

HD149026 was observed during four transit phases, under varying conditions resulting in a large spread of SNR. For a better understanding of the measurement interpretations, the results of the observation runs are not presented chronologically, but in the order of highest to lowest SNR.

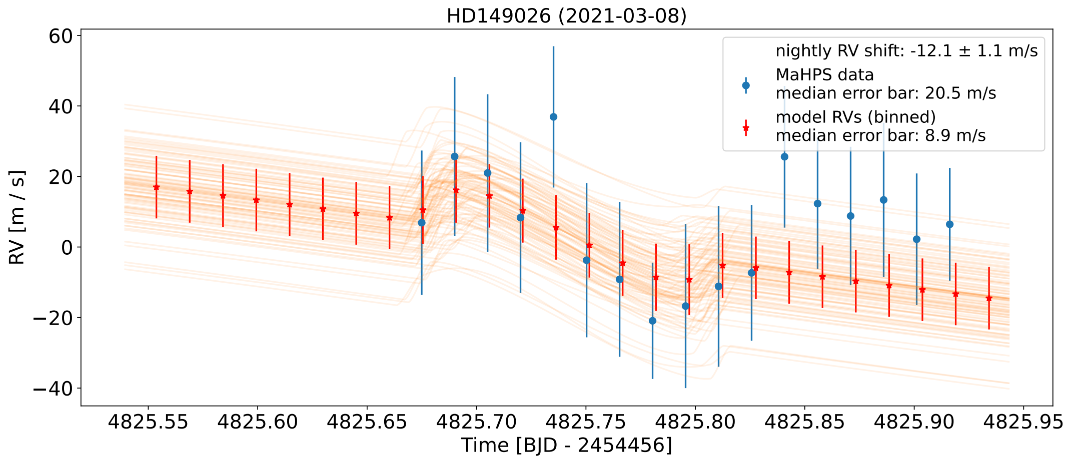

Figure 6.7: RV curve of the HD149026 observations of transit B (2021-03-08) with MaHPS (blue points), the sample of RV curve models (orange lines) and the binned RV curve models (red points), which are representing the uncertainty of the literature parameter set for HD149026.

Transit B (2021-03-08)

The MaHPS RV measurements of the RM effect of HD149026 for the observation conducted on 2021-03-08 are shown in Fig. 6.7 (blue points). The sample of the modeled RV curves (orange lines) and the RVs of the model curves, binned to the exposure time of the observation (red points), are plotted for comparison. The data was obtained with the highest SNR of the four transit measurements at ∼98.

During the transit, the data follow the model RV curves in Fig. 6.7, except for one data point. As during that exposure no conspicuous event was registered, neither in the weather nor in any control parameters of the telescope or the instrument, there is a high probability that this data point is a statistical outlier. Furthermore, it stands out that the in-transit slope of the RV curve and the overall RV amplitude of the RM effect are larger in the measurements than in the models. Whether this finding is true or only due to RV measurement errors cannot be conclusively argued, as the discrepancies are well inside the error bars.

The exposures recorded after the end of the transit, however, show a significant offset from the model curves, while still following the expected downward RV trend within the errors. When the observation run was started, the object was at airmass 2.0, rising as the run proceeded to reach a position near zenith with airmass 1.0 for the last exposures. Considering that, contamination from telluric lines or other atmospheric influences can be excluded as the reason for the RV offset, even though the humidity in that night was relatively high.

Instrumental effects like changes in the temperature or pressure stabilization of the spectrograph tank can also be ruled out as causes for the offset after the transit, as the temperature and pressure curves show a well-controlled behavior throughout the complete observation run.

The last four frames of the observation of HD149026 presented in Fig. 6.7 were obtained in between astronomical twilight and sunrise, giving rise to a chance of contamination of the stellar spectra with daylight. The SNR of these frames is slightly increasing from ∼98 to ∼109, supporting the presence of some additional and slowly growing amount of flux. However, the SNR increase does not allow to infer the origin of the flux, which could also be due to the object approaching zenith on the sky and the related decrease of atmospheric absorption.

Furthermore, in the night of transit B (2021-03-08) the Moon rose above the horizon at about the time when the transit ended and reached an elevation of about 10° at the end of the observations. The illumination of the Moon in this night was comparably low at 20%, which is why initially the assumption was made that spectral contamination with moonlight could be neglected. Consulting a sky map of the observation night immediately reveals that the angular distance of 78° between HD149026 and the Moon was almost entirely in the altitude direction, in other words the Moon was located exactly below the target. As the dome had to be pointed in that exact direction for executing the observation, the moonlight was able to directly enter the dome, even though the Moon was barely above the horizon. Therefore, the probability that the moonlight was scattered into the light path of the telescope is high and contamination with moonlight could well explain the discrepancies for the last six exposures in Fig. 6.7.

In reality, a combination of the effects just discussed is probably responsible for the offset in Fig. 6.7, but a determination of the exact contributions from the individual error sources is not possible from this data set.

Making a fit of parameters like λ to the RV data from this transit is not feasible because of the size of the error bars relative to the RV signal amplitude and the RV measurement errors in the frames out of transit. If spectra before the transit would have been available, it probably would have been possible to mitigate at least some of the negative influences. Unfortunately, no spectra could be obtained as the telescope's view of HD149026 was blocked by the broadcast antenna prior to the transit start time.

To statistically reduce the errors of the RV measurements during as well as out of transit, more observations are required. A total of three more transits of HD149026 were recorded as an attempt to improve the RV data quality by combining the data from different nights.

Transit A (2021-03-05)

The MaHPS RV measurements of the RM effect of HD149026 for the observation conducted on 2021-03-05 are shown in Fig. 6.8 (blue points). The sample of the modeled RV curves (orange lines) and the RVs of the model curves, binned to the exposure time of the observation (red points), are plotted for comparison.

The overall match between the RV data and the model curves in Fig. 6.8 is not convincing. About half of the data points during the transit seem to follow the RV anomaly at some offset, however this is merely an impression and not statistically significant, taking the size of the error bars into account. The SNR of this data set is substantially smaller than the

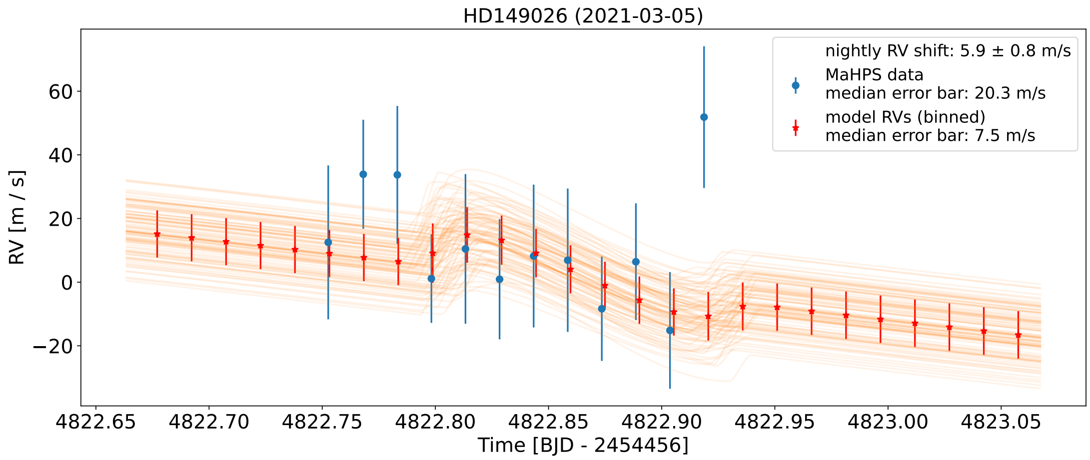

Figure 6.8: RV curve of the HD149026 observations of transit A (2021-03-05) with MaHPS (blue points), the sample of RV curve models (orange lines) and the binned RV curve models (red points), which are representing the uncertainty of the literature parameter set for HD149026.

SNR of the observations of transit B (2021-03-08, with SNR 78 and 98, respectively), so an overall larger scattering of the RV measurements of this transit is not surprising.

Instrumental effects like changes in the temperature or pressure stabilization of the spectrograph tank are with high probability not responsible for the mismatches in Fig. 6.8, as the temperature and pressure curves show a well-controlled behavior throughout the complete observation run.

A relatively high ambient humidity persisted throughout the night of transit A (2021-03-05), which in the beginning and the end of the night condensed into ground-layer fog. As the observations of HD149026 started at an airmass of 1.4 just as the fog had dispersed for the human eye, it is possible that the first frames suffer from contamination with strong H_2O absorption features, from a reduction of the recorded flux due to the scattering of star light away from the optical path, or from contamination with spectral features of light from other sources that is scattered into the optical path.

RV measurement errors due to strong telluric absorption lines can almost safely be ruled out, as the excluded regions in the mask file are defined conservatively exactly for this reason. If light from HD149026 was scattered away from the optical path by H_2O molecules or other particles, a smaller SNR would be obtained for the first frames, which is not the case. Therefore, that option is also improbable to cause the significant mismatch between the data and the models in Fig. 6.8.

Scattered light from other sources could indeed have contaminated the spectra of HD149026 in several ways. During the complete observation run of HD149026, the half-illuminated Moon was visible, first close to the horizon and in the end at an elevation of about 20°. In combination with high humidity or even droplets of condensed water in the atmosphere, moonlight can be efficiently scattered into the light path of the telescope,

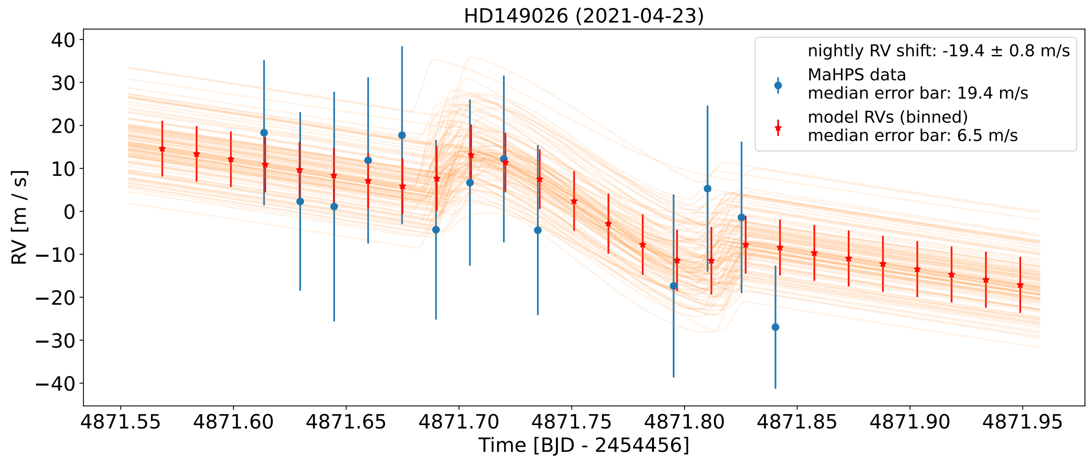

Figure 6.9: RV curve of the HD149026 observations of transit C (2021-04-23) with MaHPS (blue points), the sample of RV curve models (orange lines) and the binned RV curve models (red points), which are representing the uncertainty of the literature parameter set for HD149026.

causing a serious contamination of the spectra. The expected negative on the RV measurement of this scenario is larger as both the measured object and the Moon are at smaller elevations in the sky. This is the case for the beginning of the 2021-03-05 observation run and delivers a potential explanation for the large discrepancy especially before the start of the transit.

Further contamination of the obtained spectra was found for the last frames of the series. The last four data points in Fig. 6.8 were recorded between astronomical twilight and sunrise and the deviation of the last data point is without doubt caused by an additional RV signal from the solar spectrum.

It also should be mentioned that the frame used for the background correction of this series in the GAMSE reduction was taken from another night. That reference frame was observed at a low airmass in conditions with less ambient humidity and a smaller illumination of the Moon. Therefore, an additional error could be introduced to the RV determination, which is expected to be larger for the first exposures than the later ones shown in Fig. 6.8, as the difference in airmass and humidity is larger.

All in all, the mediocre atmospheric conditions and presence of bright objects that contaminate the HD149026 spectra from 2021-03-05 provide plausible explanations for the fact that the RM effect was not obtained for this transit.

Transit C (2021-04-23)

The MaHPS RV measurements of the RM effect of HD149026 for the observation conducted in the night of transit C (2021-04-23) are shown in Fig. 6.9 (blue points). The sample of the modeled RV curves (orange lines) and the RVs of the model curves, binned to the exposure time of the observation (red points), are plotted for comparison.

A detection of the RM effect cannot be claimed from the RV data presented in Fig. 6.9 as the scattering of the data points is too large, but the overall RV trend of the barycentric motion of HD149026 is obtained. The SNR of the spectra shown here is comparable to the SNR for the transit A data set.

In direct comparison with transit A, the deviations from the RV curve models appear to be more random for this measurement series, whereas the deviations for transit A are stronger at the beginning and the end of the series. This is an indication that the effects causing the errors in the RV measurements are distinct between the two transits.

The atmospheric conditions during the observation run shown in Fig. 6.9 were relatively good and can be ruled out as cause for the RV measurement imperfections.

Contamination of the HD149026 spectra with light from the Moon is a relevant factor, as the Moon was illuminated to 85% on 2021-04-23 and had a relatively small angular distance to the target of only 72°. The probability that moonlight entered the dome and was scattered into the optical path of the telescope is therefore relatively high.

A failure of the automatic object tracking during the second half of the transit caused the gap in the RV series shown in Fig. 6.9. The observations could be resumed at the time of astronomical twilight and continued until shortly before sunrise, indicating that the last four frames of the series could be contaminated with daylight. For the very last frame, a significantly higher SNR due to the additional flux is found, explaining the large deviation of that data point from the overall RV trend.

In contrast to transits A and B, instrumental effects that harm the RV precision need to be taken into account in this measurement series. During the observation run, the temperature and pressure curves did not show a well-controlled behavior. Instead, the pressure in the tank oscillated with an amplitude of ~0.1 hPa and a period of 20 to 30 min, which is only slightly out of the specification (Tab. 2.2) but nevertheless can possibly result in small random spectral shifts, especially when taking into account that the exposure time of the series was only 20 min.

The temperature measured at the echelle grating of MaHPS exhibited a slow drift of about 0.02 K over the course of the night or 0.01 K during the observations. As the drift is very steady, it is improbable that this effect contributes to the scattering of the RV measurements, however it could be responsible for a continuous trend in the RV data. From the stability measurements in Sec. 3.2.2, an overall RV shift of the order of 50 m/s would be expected for a temperature drift of 0.01 K, which is about the difference between the first and the last RV measurements of HD149026. It is therefore unclear whether the measured RV trend is a real RV signal from the star or due to the imperfect temperature control.

Since the RM effect measurement shown in Fig. 6.9 suffers from spectral contamination and instrumental stability issued, the effects of which cannot really be disentangled, it should not be combined with the measurement of transit B with the goal of improving the RV precision by statistics. Additionally, as the signal of the RM effect was not recovered, a parameter fit to the data is also not useful.

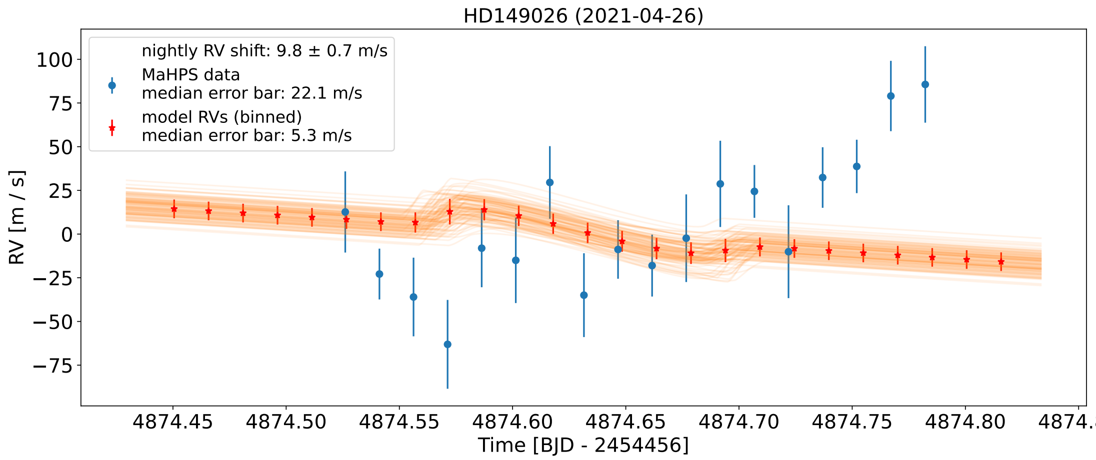

Figure 6.10: RV curve of the HD149026 observations of transit D (2021-04-26) with MaHPS (blue points), the sample of RV curve models (orange lines) and the binned RV curve models (red points), which are representing the uncertainty of the literature parameter set for HD149026.

Transit D (2021-04-26)

The MaHPS RV measurements of the RM effect of HD149026 for the observation conducted in the night of transit D (2021-04-26) are shown in Fig. 6.10 (blue points). The sample of the modeled RV curves (orange lines) and the RVs of the model curves, binned to the exposure time of the observation (red points), are plotted for comparison.

The RV data presented in Fig. 6.10 show neither the expected signature of the RV anomaly during the transit nor the overall RV trend. One potential cause could lie in the low SNR of about 67 that was obtained for the observations on 2021-04-26.

The weather conditions during the series of HD149026 spectra were unfavorable, as clouds were occasionally passing through the field of view. In addition, the Moon was in full phase and at a very small angular distance of 57°, so the spectral contamination is expected to be high for all frames of that night.

Similarly to the other transits of HD149026, the observations on 2021-04-26 were carried out until dawn, however the series did not extend until after astronomical twilight. Contamination with daylight due to the rising Sun can therefore be neglected as source of RV measurement errors.

A substantial factor influencing the RV data of HD149026 from the night of transit D (2021-04-26) is the lacking environmental stability of MaHPS. The pressure in the tank oscillated with an amplitude of $\sim$0.11 hPa and a highly variable period of 15 to 30 min. The temperature measured at the echelle grating of MaHPS exhibited a steady drift of about 0.07 K during the observation run.

While the temperature and pressure control stability during transit C were still close to the specifications made in Tab. 2.2, the situation worsened somewhat for the pressure control and significantly for the temperature control, owing to higher outside temperatures.

Nevertheless, the same arguments concerning the impact on the RV measurements can be made, since the overall qualitative behavior is similar. The oscillations of the pressure are expected to result in a scattering of the RV values, whereas the temperature drift should cause a RV drift. The overall increasing RV trend of the RV data in Fig. 6.10, where from the model a falling trend is expected, could be caused by the drifting temperature in the spectrograph.

All in all, several effects that heavily influence the RV measurements have been found to play a role in this data set. To the combination of lacking temperature and pressure stability with the unfavorable atmospheric conditions and spectral combination by the Moon makes it impossible to conclusively tell which error source has which impact on the RV measurements of the individual frames.

There is no other possible conclusion than to reject the RV measurements of 2021-04-26 and not consider them for any further use. The RV series presented here can only serve as negative example why environmental control of the spectrograph at the level defined in Tab. 2.2 is required for reliable RV measurements.

In the end, the attempt to combine data from different transit observations of HD149026 was unsuccessful, because each measurement was affected by a unique combination of RV error sources, at a varying extend. Nevertheless, such a combination of data from different nights can be made, if attention is given to avoiding spectral contamination by bright sources, picking favorable atmospheric conditions, and stabilizing the instrument properly before starting an observation run, all of which is harder to achieve when nights are short and outside temperatures are high. Identifying these critical factors was part of this work, therefore observations were carried out intentionally despite the suboptimal conditions outlined here.

6.3.5 Literature data

Measurements of the RM effect for HD149026 have been published by S. Albrecht et al. (2012) and Wolf et al. (2007). The RV data and fit models are given in Fig. 6.11 and Fig. 6.12, respectively.

The first RM effect measurement series for HD149026 by Wolf et al. (2007) was obtained with an average SNR of ∼250 for the individual exposures. The errors from photon noise for each individual exposure were found to be of the order of ∼2 to 3 m/s, but the error bars used for the fit were enlarged by adding another 2.6 m/s in quadrature, obtained from RV data recorded out of transit, to account for stellar effects causing additional RV uncertainties. The residuals of the best fit (Fig. 6.11, bottom) appear to be randomly scattered around zero, with the possible exception of the data points at the end of the transit, which seem to show a slight positive offset. However, since only three data points are available, the concentration may as well be a coincidence.

The RM effect analyses by Wolf et al. (2007) was a relatively early work and better constraints of the planetary system's parameters based on more precise photometric data have become available. Therefore, S. Albrecht et al. (2012) made a re-analysis of the RM effect, using a subset of the RV values and errors of Wolf et al. (2007). While for the original

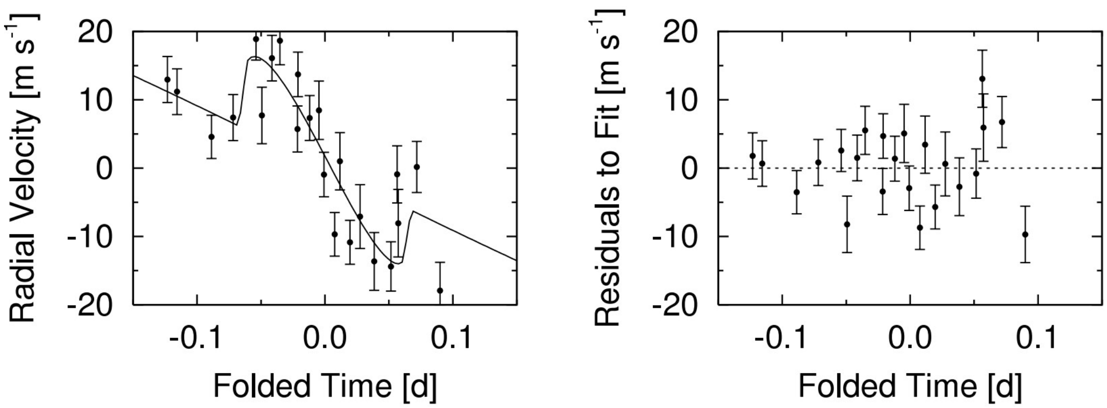

Figure 6.11: RV data of the RM effect for HD149026, obtained during a single transit with HIRES at the Keck I 10 m telescope. Black points: RV measurements; solid line: best fit model. Left panel: RV curve around the transit phase; right panel: residuals between the model and the data. Graphic taken from Wolf et al. (2007).

analysis the residuals between the data and the fit model appeared randomly distributed (Fig. 6.11, right), an indication of a residual structure with positive values in the first half of the transit and negative values in the second half can be observed in Fig. 6.12 (bottom). This demonstrates that the choice of model input parameters has a significant impact on the fit to the data, bringing out potential imperfections that were not noticeable before.

Comparing the RV curves in Fig. 6.11 and Fig. 6.12 with the MaHPS measurements that recovered the RM effect signature given in Fig.6.7 supports the conclusions drawn for the MaHPS observations of HD189733. The main limiting factor when using MaHPS is the size of the telescope, which is fundamentally restricting the SNR that can be reached for an individual exposure at a given exposure times. Nevertheless, even though the data quality may not be good enough to perform an independent fit of the obliquity, it can still serve as inexpensive way to verify whether an observation of the RM effect with increased precision would be fruitful. MaHPS RV measurements could provide a relatively inexpensive way to screen objects for the presence of a RM effect signature, which could then be used as basis for applications for observation time at larger telescopes.

6.4 HAT-P-2

The discovery of the RM effect for HAT-P-2, also known as HD147506, by Winn et al. (2007b) was one of the first ten RM effect measurements for exoplanets. RV measurements from two different telescopes and instruments are available (Winn et al. 2007b; Loeillet et al. 2008) and more recently a re-analysis of the discovery measurement in combination with improved photometric data from Pál et al. (2010) was published (S. Albrecht et al. 2012).

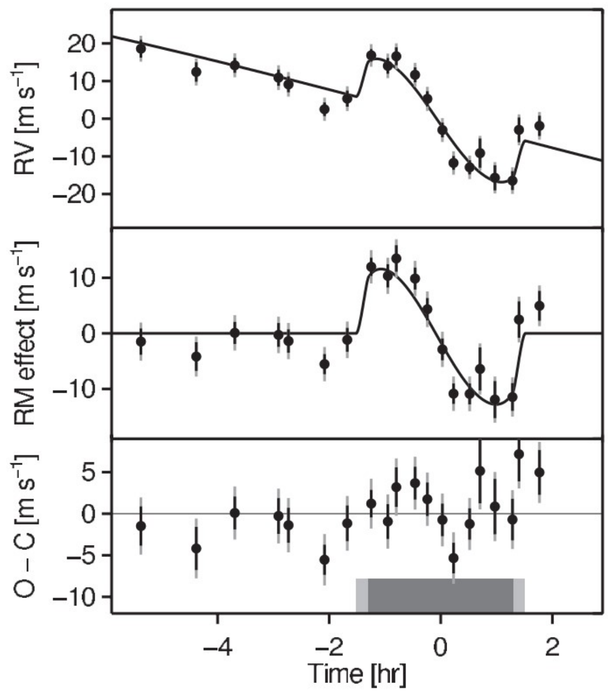

Figure 6.12: Re-analysis of the RV data of the RM effect for HD149026, obtained during a single transit with HIRES at the Keck I 10 m telescope by Wolf et al. (2007), compare Fig. 6.11. Black points: RV measurements; solid line: best fit model. Top panel: RV curve around the transit phase; central panel: RV curve after subtracting of the barycentric motion of the star; bottom panel: residuals between the model and the data, the transit phase is indicated by the gray area. Graphic taken from S. Albrecht et al. (2012).

6.4.1 System characteristics

The parameters characterizing HAT-P-2 and its exoplanet, that were used in the analysis of this work, are given in Tab. 6.7.

HAT-P-2 is a F-type main sequence star (e.g. Loeillet et al. 2008), which has a temperature of $T_{eff} \approx 6250\,\mathrm{K}$ and thus is located right at the Kraft break. Its rotational velocity is fairly high with $v_{rot} \sin i_S = 22900^{+1100}_{-1200}$ m/s, putting it on the edge of the capability of the center-of-mass method to determine RVs. The mass of HAT-P-2, $1.298^{+0.062}_{-0.098}\ M_{Sun}$, is similar to that of HD149026, however the two differ in their evolutionary stage.

The planetary companion of HAT-P-2 is an extremely massive planet with a mass of $8.62^{+0.39}_{-0.55}\ M_{Jup}$, which follows a very eccentric orbit ($e = 0.5172 \pm 0.0019$) with a period of 5.6 d and a rather long transit with a duration of (4.2888 ± 0.0312) h. In addition to the unusually high eccentricity, the planet has a density significantly larger than that of a gas giant, which puts it in a transition zone to very low-mass stars (e.g. Loeillet et al. 2008). Despite the unique properties of the exoplanet orbiting HAT-P-2, measurements of the obliquity show an almost perfectly aligned system with $\lambda = 0.2^{+12.2}_{-12.5}\ ^\circ$.

Owing to the large eccentricity and the high density, HAT-P-2 is an extremely inter-

parameter	value	reference
P	$(5.633\,475\,4 \pm 0.000\,002\,6)$ d	c
T_0 [BJD]	$2\,455\,288.849\,10 \pm 0.000\,37$	c
e	0.5172 ± 0.0019	b
a	$0.068\,14 \pm 0.000\,51$ AU	b
i	$90.0^{+0.85}_{-0.93}$ $^\circ$	a
$v_{rot} \sin i_S$	22900^{+1100}_{-1200} m/s	a
λ	$0.2^{+12.2}_{-12.5}$ $^\circ$	a
i_S	—	—
K	(953.3 ± 3.6) m/s	b
T_P [BJD]	$2\,463\,982.4915 \pm 0.0024$	b
ω	$(188.01 \pm 0.20)^\circ$	b
R_P/R_S	$0.06891^{+0.00090}_{-0.00086}$	a
a/R_S	$10.28^{+0.12}_{-0.19}$	a
T_{eff}	6250 K (fixed)	a
R_P	$0.951^{+0.039}_{-0.053}$ R_{Jup}	a
M_P	$8.62^{+0.39}_{-0.55}$ M_{Jup}	a
R_S	$1.416^{+0.04}_{-0.062}$ R_{Sun}	a
M_S	$1.298^{+0.062}_{-0.098}$ M_{Sun}	a
b	$0.395^{+0.080}_{-0.123}$	d
t_{dur}	(4.2888 ± 0.0312) h	d
RV jitter	$34.9^{+11.0}_{-9.3}$ m/s	c
V-band magnitude	8.69 ± 0.01	e

Table 6.7: Parameters of HAT-P-2 and its exoplanet as used for the analysis in this work. References: a) Loeillet et al. (2008); b) Ment et al. (2018); c) Bonomo et al. (2017); d) Pál et al. (2010); e) Høg et al. (2000).

esting object to study. Both spectroscopic and photometric observations were conducted for further investigation, for instance regarding the planet's atmosphere dynamics and composition (e.g. Lewis et al. 2014).

6.4.2 MaHPS Observations

HAT-P-2 was observed in a total of four nights, where one transit was recorded (2021-02-25) and template spectra were taken in two nights (2021-02-28 and 2021-03-24). In addition, a series of simultaneously calibrated spectra out of transit was recorded too, due to a mix-up of the transit night's date (2021-02-24). A summary of the characteristics of the obtained data sets as well as the observing conditions is given in the following.

Out-of-transit (2021-02-24)

Owing to a miscommunication of the date of the transit night, a full observation run for a transit of HAT-P-2 was executed on 2021-02-24, during which the planet was completely out of transit. Resulting are nine exposures with simultaneous LFC calibration and one, at the end of the series, without simultaneous calibration, all at an exposure time of 1800 s with a median SNR of 92.

The weather conditions during the run were clear, however the atmosphere was contaminated with Sahara dust, which impaired the overall throughput of the atmosphere due to broad-band absorption and scattering effects. This phenomenon was observed to be stronger for shorter wavelengths ($\lesssim 600$ nm) and for exposures with larger airmass. In the course of the observation run, the airmass ranged from 1.5 to 1.0.

The observation was carried out at the end of the night, the last three exposures were taken after astronomical twilight. The very last exposure lasted until about 10 min after sunrise. At the beginning of the series, the Moon had an elevation just below 40° and just before last exposure it set below the horizon. The illumination of the Moon was near completion with 93%, however the angular distance to HAT-P-2 was 92° (measured at 02:00 UT), which could have prevented excessive contamination of the stellar spectrum, as only a small amount of moonlight entered the slit of the dome directly at this configuration.

The spectra obtained from this observation are not suited to be used as templates, because the simultaneous calibration with the LFC holds the possibility that light from the calibration fiber spills over into the spectrum of the science fiber. When constructing the templates, this risk has to be avoided as much as possible, since any additional signal that is not part of the star's own spectrum could lead to systematic errors in the RV determination.

Transit (2021-02-25)

The transit of HAT-P-2b was observed on 2021-02-25 with a total of 10 frames with simultaneous LFC calibration. The exposure time for the first seven frames was 1800 s, while the remaining three exposures were obtained with only 1200 s. The median SNR of all frames is 74.

Similar to the night before, the sky was clear but Sahara dust was in the air. Additionally, there was a light haze that increased in density over the course of the night over time. HAT-P-2 was observed at airmass 1.5 to 1.0.

Also in analogy to the series from the night before, the observation took place at end of night, with four exposures after astronomical twilight and the last one overlapping with sunrise by a few minutes. The Moon was visible at an elevation of 45°, decreasing over time, with an even higher illumination of 98%. The angular distance was slightly smaller with 84°, but the argument of the slit orientation preventing contamination may still be valid in this case.

Templates (2021-02-28)

An observation of template spectra for HAT-P-2 was made on 2021-02-28. Three frames without simultaneous calibration were obtained with exposure time 1800 s and a median SNR of 52.

The night was cloudless, but possibly still contaminated with Sahara dust in upper atmospheric layers, which could explain the low SNR of this night's frames, especially considering that the airmass was very low at 1.03 to 1.01.

The exposure series was taken at the end of the night, starting at astronomical twilight and finishing just before sunrise. The Moon was located at 30° elevation in beginning and 15° at the end, at an illumination of 96% and a distance of 65°, possibly causing some contamination of the spectra.

Templates (2021-03-24)

Another four templates for HAT-P-2 without simultaneous calibration were obtained on 2021-03-24 with an exposure time of 1800 s, yielding a median SNR of 76.

During the exposures, the sky was clear with occasional bits of clouds that were passing through. Furthermore, due to the large distance in time to the other observation runs, it is safe to assume that the frames from this night are not affected by Sahara dust. The airmass for the four frames ranges from 1.04 to 1.01.

This observation run was made at the end of the night and the last two exposures were recorded after astronomical twilight. The Moon showed an elevation of 15° during the first exposure and set before the last exposure was started. The illumination was 82% at a distance of 87°, not completely ruling out spectral contamination.

While the last exposure was running, the telescope stopped and had to be repointed, leading to a small loss of the collected flux and thus the SNR of that frame.

6.4.3 Data analysis

The observations of HAT-P-2 were reduced with the same methods as outlined for the observations of HD189733 (Sec. 6.2.3), using the in-house pipelines GAMSE and MARMOT (description in Sec. 4.1 and Sec. 4.3, respectively).

Reduction with GAMSE

GAMSE was executed automatically after each night of observation with the default parameters as quoted in Sec. 4.1. Table 6.8 lists the frames that were used for the background correction of the exposures with simultaneous calibration, along with the *ThAr* exposures that were chosen as basis for the wavelength calibration.

Similarly to the reduction of HD149026 (Sec. 6.3), the data from nights 2021-02-24 and 2021-02-25 were re-reduced manually with the GAMSE pipeline, because of a missing exposure of the star without simultaneous calibration. The frame with the best SNR from

night	background reference	exposure time [s]	wavelength reference	exposure time [s]	rms [Å]
2021-02-24	20210228_0099	1800	20210224_0045	12	0.00133
2021-02-25	20210228_0099	1800	20210225_0050	22	0.00128
2021-02-28	—	—	20210228_0049	22	0.00133
2021-03-24	—	—	20210324_0078	22	0.00138

Table 6.8: Reference frames used for the background correction and *ThAr* wavelength calibration of GAMSE for the HAT-P-2 data. For nights in which all exposure were taken without simultaneous LFC calibration, no background correction is performed.

the closest possible night in this case was 20210228_0099, all other parameters of GAMSE were left unchanged.

Reduction with MARMOT

The reduction of the HAT-P-2 data with MARMOT to obtain RVs from the wavelength calibrated spectra was made using a script, which contained all necessary MARMOT commands, and an initialization file where the parameters for the reduction were specified.[55] The procedure is identical to that for HD189733, with the set of parameters specific to HAT-P-2 given in Tab. 6.3. Note that in contrast to the other two objects, order 95 had to be excluded from the analysis, as due to the large rotational velocity it contains an additional broad feature, disturbing the RV measurements.

The template for HAT-P-2 was generated from seven individual frames and has a SNR of approximately 176.

Figure 6.13 shows an example of a spectrum of HAT-P-2 (blue line and orange data points), as recorded for physical order 90 during the transit on 2021-02-25 with MaHPS, in direct comparison with the template (green line). The gray-shaded areas correspond to wavelength regions that have been excluded from further analysis in the mask file. The template SNR for order 90 is 177, whereas the SNR of the measured spectrum is 76, a value representative for the complete observation run of 2021-02-25.

In comparison with the other two objects, the width of the spectral lines of HAT-P-2 in Fig. 6.6 is noticeably larger, as expected from the rotational velocity.

In this analysis, both the frames with and without simultaneous calibration were utilized, since no use of the additional wavelength calibration information of the LFC was made.

For the σ-clipping of the order-wise RV results of HAT-P-2, the best coefficient found was 2.0 with a total of 2 iterations. The median error bar for the HAT-P-2 data is 55 m/s, significantly larger than those of HD189733 and HD149026 (12 m/s and 22 m/s). This is due to the fast rotation of HAT-P-2, which causes a considerable broadening of the spectral lines

[55]The script and initialization file, as well as additional files necessary for the MARMOT reduction of HAT-P-2, are provided under `https://github.com/vfahrens/MaHPS_scripts` for download.

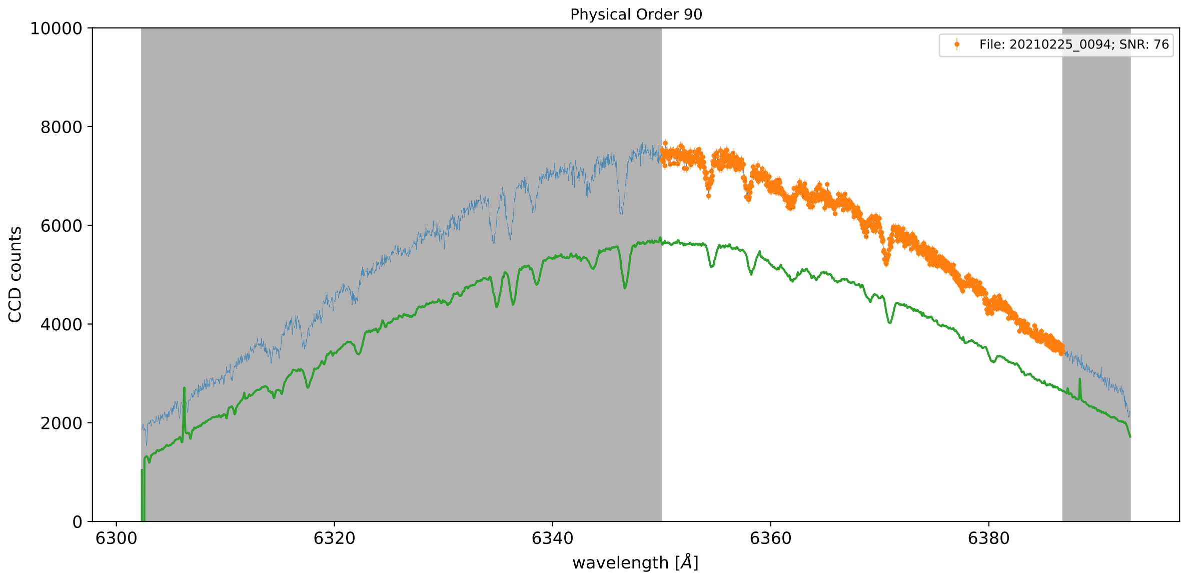

(a) Spectrum of the complete physical order 90.

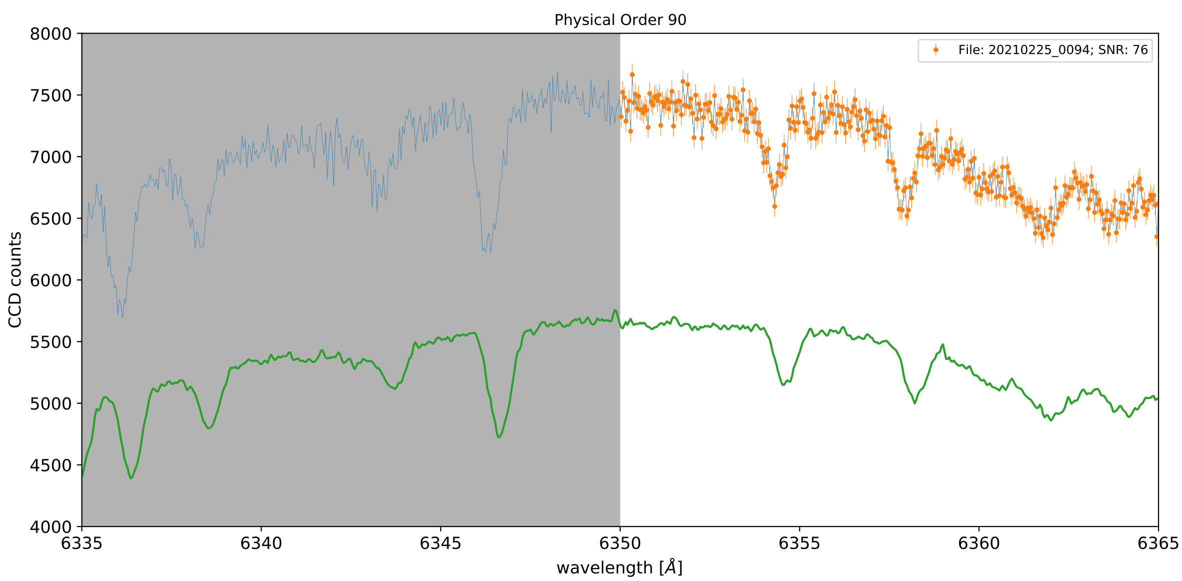

(b) Zoom of physical order 90 to the wavelengths 6335 to 6365 Å.

Figure 6.13: Example of a recorded spectrum of HAT-P-2 for physical order 90, compared with the used template. Blue line: recorded spectrum, extracted with GAMSE; green line: B-spline template from MARMOT pipeline, evaluated at the same wavelengths; orange points: data points of the spectrum contributing to the CCF calculation, error bars are the flux error of each pixel calculated by GAMSE; gray areas: wavelength regions excluded in the mask file. The brightness of the template is scaled down by a factor of 4 for better comparability.

and thus a larger intrinsic uncertainty of the RV determination. Additionally, the transit observations were made in the presence of Sahara dust in the atmosphere, potentially further downgrading the quality of the measured spectra.

Plotting the RV model and data

For the generation of the RV curve models for HAT-P-2, the same strategy as for HD189733, described in Sec. 6.2.3, was employed. A sample of 100 random parameter sets, to be used for the calculation of RV curves with `starry`, was obtained. The measurement values and errors of the input parameters are given in Tab. 6.7. In case a parameter features asymmetric errors, the larger value was adopted to get conservative estimate.

For the additional parameters q_1, q_2 and α, identical distributions as for HD189733 were assumed, with q_1, q_2 being uniformly distributed in $[0, 1]$ and α having a Gaussian distribution with peak and width 0.0 ± 0.5.

The barycentric correction of the template for HAT-P-2 is 11 792 m/s (see Tab. 6.3). The RV offsets are (-911.9 ± 3.0) m/s for 2021-02-25 and (-958.7 ± 3.3) m/s for 2021-02-24 (Tab. 6.4), computed for each night individually. The large amplitude of the offset is almost exclusively due to the different orbital phase the template frames were obtained in and is consistent with the amplitude of the Keplerian RV curve of HAT-P-2.

The fact that the template was generated from exposures of two different nights causes an additional discrepancy, because the mean of the barycentric correction values of the individual frames is not necessarily a good approximation for the overall barycentric correction of the template. However, the observations were made at almost equal orbital phase, so the influence on the RV offset is expected to be small. The offset variation of almost 50 m/s between the two consecutive nights can be ascribed to the overall large uncertainty in the RV determination for HAT-P-2, related to the low SNR values and the broad spectral lines.

For the baseline parameter of the RV model, (0.0 ± 25.6) m/s was adopted for the data set obtained on 2021-02-25 and (0.0 ± 28.9) m/s for the data set from 2021-02-24, as listed in Tab. 6.4.

6.4.4 Results

Transit (2021-02-25)

The MaHPS RV measurements of the RM effect of HAT-P-2 for the observation conducted during the transit on 2021-02-25 are shown in Fig. 6.14 (blue points). The sample of the modeled RV curves (orange lines) and the RVs of the model curves, binned to the exposure time of the observation (red points), are plotted for comparison.

Overall, the RV measurements obtained here follow the modeled RV signal at a better precision than expected from the error bars, with the exception of the last two data points. There are two potential causes for the deviations of the last RV data points: on the one hand the exposure time was shortened and thus the SNR decreased, on the other hand the

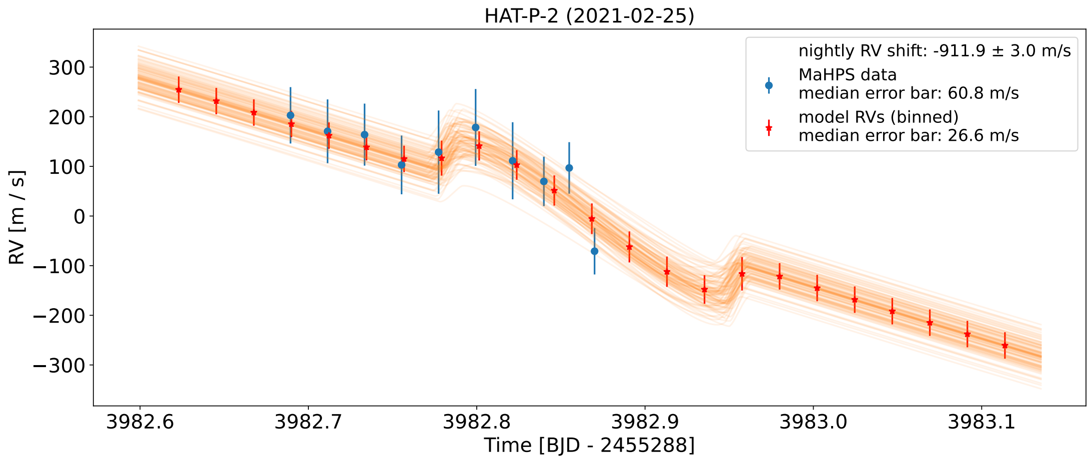

Figure 6.14: RV curve of the HAT-P-2 transit observations with MaHPS (blue points), the sample of RV curve models (orange lines) and the binned RV curve models (red points), which are representing the uncertainty of the literature parameter set for HAT-P-2. Data from 2021-02-25.

observation run was extending until sunrise, leading to a potential contamination by the solar spectrum.

The exposure time of the last three frames was only 2/3 that of the previously recorded frames, causing the SNR to decrease from ∼78 to ∼65. In principle, one would expect larger error bars in such a case, however Fig. 6.14 shows a completely inverse behavior with smaller error bars for the frames with less SNR.

The chance that the last few exposures are contaminated with light from the Sun is high, especially for the very last frame where the exposure time overlapped with sunrise by a few minutes. In fact, there is a steady increase in the SNR for the last three frames, from 62 to 67, which supports the proposal that additional flux from the rising Sun is recorded.

Daylight contamination could be the reason why the error bars for the smaller SNR frames are decreasing. HAT-P-2 has intrinsically heavily broadened line profiles, while the spectrum of the Sun features narrow lines, which contribute much stronger to the CCF. Such a superposition of spectra could cause a virtual gain in precision of the CCF method because the position of the narrow lines is more easily determined, resulting in smaller error bars, however, the determination of the RV for HAT-P-2 is in reality worsened as a significant error is introduced to the RV measurement.

Despite the presence of Sahara dust in the atmosphere, the RV data in Fig. 6.14 do not seem to be subject to any negative effect. The fact that the observation was conducted at airmass <1.5 is for sure beneficial, as the amount of material along the optical path is minimized. In addition, there is also no evidence that the brightness of the Moon, which was close to full Moon phase, posed an issue for the RV measurements. The angular distance of HAT-P-2 and the Moon on the sky is close to 90°, potentially preventing the moonlight from entering the telescope dome or optics directly as the slit is illuminated only from the

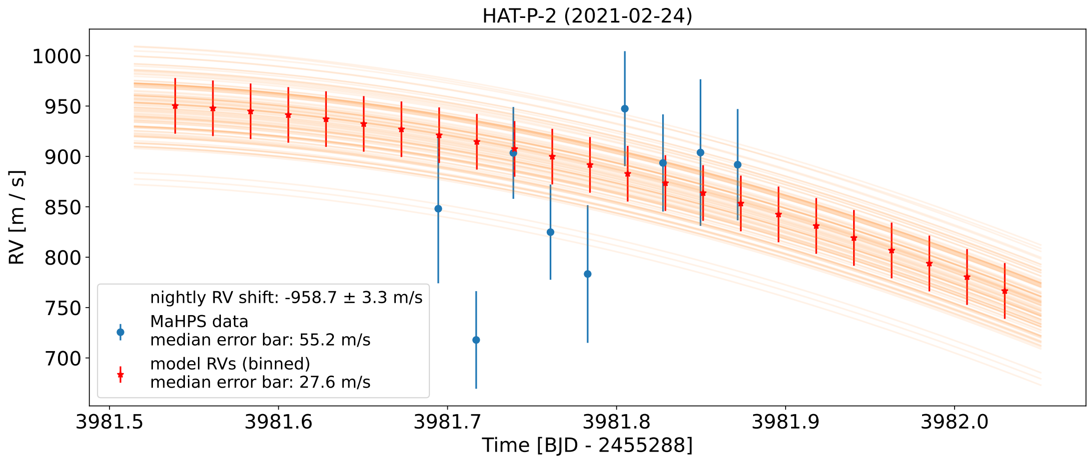

Figure 6.15: RV curve of the HAT-P-2 observations out of transit with MaHPS (blue points), the sample of RV curve models (orange lines) and the binned RV curve models (red points), which are representing the uncertainty of the literature parameter set for HAT-P-2. Data from 2021-02-24.

side.

Finally, considering how well the RV data match the model curves with the exception of the last two frames, the error bars in this measurement are probably overestimated by the order spread method. If there is some RV offset between the individual orders, which is significant but relatively constant, the standard deviation of the RV value distribution will be dominated by that offset, causing the error bars to appear larger than they actually are, if only statistical RV errors were taken into account. Further insight on this topic could be gained by obtaining order-wise RV errors from the MARMOT option that generates a sample of simulated spectra with an equivalent SNR (Sec. 4.3.4) and subsequently calculating the frame-wise RV error with classical error propagation.

Since in the scope of this work it was not possible to observe a complete transit of HAT-P-2, and furthermore at least two out of six data points of the transit phase are suffering from spectral contamination, a fit of λ or other parameters could not be performed. From the data shown in Fig. 6.14, one cannot even make a significant statement about the detection of the RM effect or whether the orbit orientation is prograde or retrograde, however this might change if the error bars can be reduced by applying other methods.

Out-of-transit (2021-02-24)

Figure 6.15 contains the RV measurements for the spectra when HAT-P-2b was out of transit (blue points), recorded one night before the transit shown in Fig. 6.14, together with the sample of model RV curves (orange lines) and the RVs of the model curves, binned to the exposure time of the observation (red points). The two observation runs allow a direct comparison of the RV results from an expected null signal and a RM effect signal.

Of the total of nine exposures, only the second half matches the expected RV curve, while the first half shows a considerable scattering behavior at RV values smaller than predicted. Both observation runs were made in the same part of the night and in comparable conditions, with Sahara dust in the atmosphere and the Moon close to its full phase at a similar distance on the sky. However, the conditions were not identical, potentially explaining the discrepancy of the RV data from 2021-02-24.

The amount of Sahara dust in the atmosphere was larger for the out-of-transit observation shown in Fig. 6.15 than it was for the transit observation, at a level noticeable by bare eye. Unfortunately, a quantification of the difference cannot be made without a dedicated atmospheric particle monitor. An immediate effect of an increased particle density is the decrease of the atmospheric transparency, as light from the star is scattered away from the optical path to the telescope. Given that the observation was started at airmass 1.5 and the last frame was taken close to zenith at airmass 1.0, it could be possible that a large part of the star's signal got lost if the airmass laid above a certain threshold value. This should be visible as decrease of the SNR for frames taken at higher airmass, however that is not the case.

The brightness of the Moon could also affect the RV measurements. Although the Moon's position is similar to the night after (2021-02-25), it nevertheless is slightly different. A possible consequence could be that the moonlight was falling in under just the right angle to be reflected off a surface at the slit entrance, scattering a large amount of the light into the dome, while this exact geometry is not recurring in any other night. The resulting potential contamination of the stellar spectrum could give rise to errors in the RV measurements as seen in Fig. 6.15. The scattering into the dome could have ended abruptly as the Moon's relative position to HAT-P-2 changed over the course of the night, potentially explaining the sudden transition after the first five data points in Fig. 6.15 from widely scattered RVs to RVs that match the expected RV signal rather well.

The combination of a large atmospheric particle density with a bright source like the Moon may also pose a further complication for the RV determination. Before the moonlight reaches the dome, it first gets scattered by the particles, at an amount that is increasing as the elevation of the Moon in the sky decreases. During the observation run on 2021-02-24, the Moon's elevation above the horizon evolved from about 40° in the beginning to 0° as the last exposure was started. It is therefore plausible that the recorded spectra are contaminated with scattered moonlight, either from the dome or from the dust particles, until at one point the airmass of the Moon was too large and the contaminating flux reaching the detector got too low to influence the CCF.

Negative effects of insufficient temperature or pressure stability in spectrograph tank can be quite confidently ruled out, as the control performance does not show any differences between the nights 2021-02-24 and 2021-02-25.

All in all, the RV measurements of HAT-P-2 demonstrate that even small changes in the atmospheric conditions can have a large impact on the accuracy of the RV data. In particular, strategies to avoid contamination of the spectra with the light from other bright sources need to be developed.

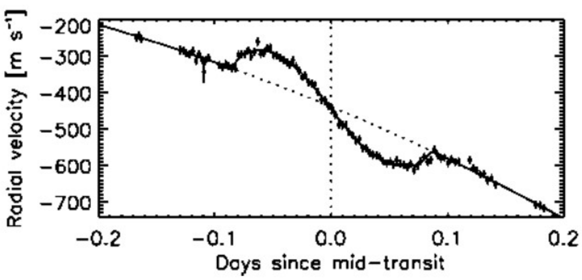

Figure 6.16: RV data of the RM effect for HAT-P-2, obtained during a single transit with HIRES at the Keck I 10 m telescope. Black points: RV measurements; solid line: best fit model. Left panel: RV curve around the transit phase; right panel: residuals between the model and the data. The dotted line indicates the RV signal due to the barycentric motion of the star, note the curvature due to the large eccentricity of the orbit. Graphic taken from Winn et al. (2007b).

6.4.5 Literature data

Measurements of the RM effect for HAT-P-2 have been published by S. Albrecht et al. (2012), Winn et al. (2007b), and Loeillet et al. (2008). The RV data and fit models are given in Fig. 6.16, Fig. 6.17, and Fig. 6.18, respectively.

The first RM effect measurement series for HAT-P-2 by Winn et al. (2007b) was obtained with an exposure time of 200 s and yielded an SNR of ∼200. The errors from photon noise for each individual exposure on average were found to be 7 m/s, but the error bars used for the fit were enlarged by adding another 10 m/s in quadrature, obtained from RV data recorded out of transit, to account for the additional RV uncertainties from stellar effects. The residuals of the best fit (Fig. 6.16, right) do not show any pattern and instead appear to be randomly scattered around zero.

Further observations of the RM effect for HAT-P-2 were conducted by Loeillet et al. (2008) for transits in two different nights. The exposure times for both measurement series were 600 s, resulting in a SNR of ∼70 for the first night (Fig. 6.17, filled circles) and ∼90 for the second night (open circles). The average error bar size due to photon noise is 14 m/s and 10 m/s, but an additional error of 50 m/s due to instrumental uncertainties was added for the fit. The residuals in Fig. 6.17 (bottom) show a significant deviation to positive values just before the mid-time of the transit, which Loeillet et al. (2008) ascribe to a decentering of the star's image during the observation instead of imperfections of the model fit to the data.

The RM effect analyses by Winn et al. (2007b) and Loeillet et al. (2008) were relatively early works and better constraints of the planetary system's parameters based on more precise photometric data have become available. Therefore, S. Albrecht et al. (2012) made a re-analysis of the RM effect, using the RV values and errors of Winn et al. (2007b). While for the original analysis the residuals between the data and the fit model appeared randomly distributed (Fig. 6.16, right), a residual structure with positive values in the

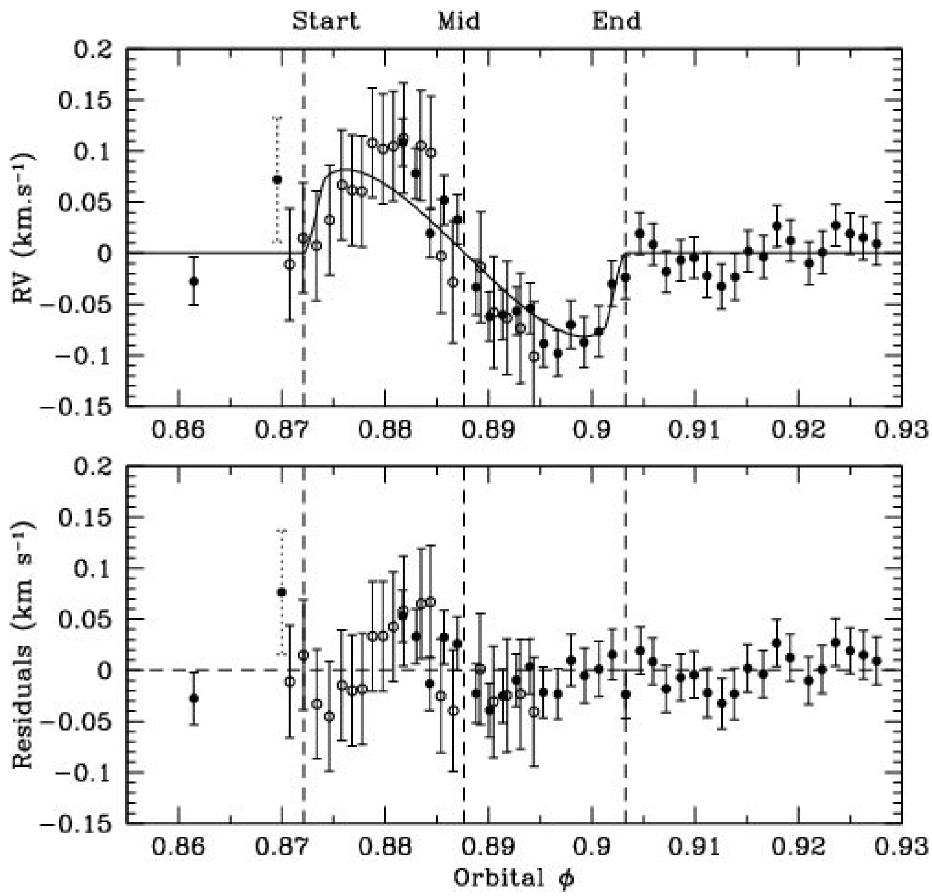

Figure 6.17: RV data of the RM effect for HAT-P-2, obtained during two transits with SOPHIE at the Haute Provence Observatory 1.93 m telescope. Filled circles: RV measurements of the first observation run; open circles: RV measurements of the second observation run; solid line: best fit model. The vertical dashed lines indicate the times of transit start, mid-time and end. Top panel: RV curve around the transit phase; bottom panel: residuals between the model and the data. Graphic taken from Loeillet et al. (2008).

first half of the transit and negative values in the second half can be observed in Fig. 6.18 (bottom). This agrees with the re-analysis of the HD149026 data set and emphasizes that a revision of the input parameters can result in a more precise determination of the system's obliquity angle without the need to record better spectra.

Comparing the RV curves in Fig. 6.16 and Fig. 6.18 with the MaHPS observations that recovered the RM effect signature, given in Fig.6.14, further stresses the importance of the light collection area for constraining the RM effect.

Considering that the SOPHIE data set by Loeillet et al. (2008) was obtained with a telescope that is very comparable in size to the 2.0 m Wendelstein telescope, a direct comparison with the MaHPS observations (Fig.6.14) can be made. In fact, the measurements with the two instruments feature a comparable SNR and the size of the error bars is similar. However, the exposure time of the SOPHIE spectra is shorter by a factor of 3 and thus

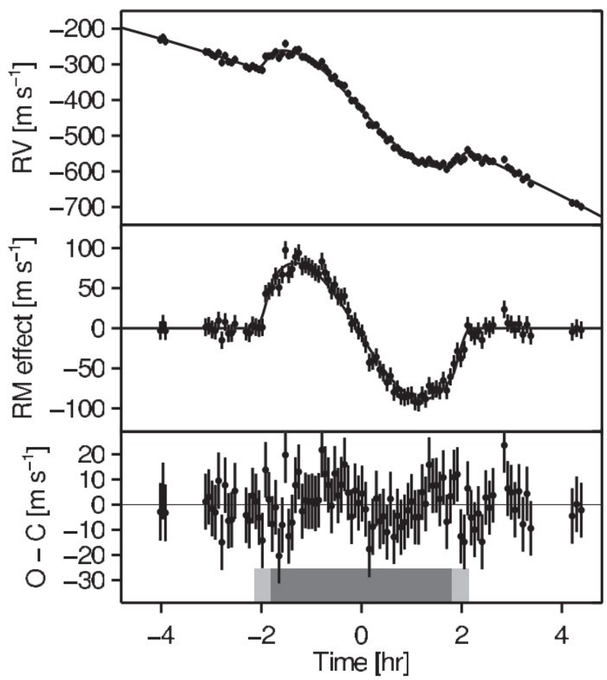

Figure 6.18: Re-analysis of the RV data of the RM effect for HAT-P-2, obtained during a single transit with HIRES at the Keck I 10 m telescope by Winn et al. (2007b), compare Fig. 6.16. Black points: RV measurements; solid line: best fit model. Top panel: RV curve around the transit phase; central panel: RV curve after subtracting of the barycentric motion of the star; bottom panel: residuals between the model and the data, the transit phase is indicated by the gray area. Graphic taken from S. Albrecht et al. (2012).

gives a better time resolution, but it has to be kept in mind that the MAHPS observations suffered from increased atmospheric absorption due to Sahara dust, whereas the SOPHIE measurements were obtained in extremely good conditions. Photometric data of the 2.0 m Wendelstein telescope from the nights with dust contamination showed that the decrease of the atmospheric transparency was significant, easily resulting in a flux reduction by a factor of 2 or 3. Therefore, MaHPS is most likely to perform comparably well to SOPHIE concerning the RV precision and instrument throughput, although a further measurement in better atmospheric conditions would be useful to confirm the instrument performance beyond any doubts.

6.5 Conclusions

The aims of the RM effect measurements presented in this chapter were to make a feasibility study for measurements of the RM effect with MaHPS, to compare the performance of MaHPS to that of other instruments, and to gain experience in conducting time-resolved RV observations.

For all three observed exoplanet host stars, the RM effect signature could be recovered, although at varying degrees of confidence. The comparison of the MaHPS data sets for the three targets with the literature showed that the performance is limited by the relatively small mirror of the Wendelstein telescope, however instruments operated at other small telescopes, like SOPHIE, obtain data with a very similar quality.

The primary challenge for RV measurements with MaHPS that require a time-resolution on the order of an hour or below is to find a suitable trade-off between the exposure time and the obtained SNR. Even if a good compromise between the two parameters is found, there are additional challenges during the observations that can negatively affect the data quality. A summary of such effects encountered in this work is given in the following.

6.5.1 Lessons learned

Various issues have been encountered during the MaHPS observations and their analysis, which unfortunately prevented the determination of an orbital obliquity angle for the observed objects. Nevertheless, the circumstances allow to gain experience with a variety of aspects that influence the RV measurements and to identify points of improvement for the future.

The first finding when reducing the observed spectra was that for data with a relatively low SNR (order-wise SNR values < 100), it can be beneficial to trade the improvement in the wavelength calibration precision from the simultaneous LFC calibration for combining the RV information from a larger number of physical orders, an approach that was followed for the data shown in this work. A potential improvement of that method could be to make use of the information from the simultaneous LFC calibration in the form of determining an overall RV correction from the LFC spectrum for each frame and applying it to the frame-wise RVs, that were obtained from the *ThAr* calibrated data. MARMOT already offers a similar function, however the assessment of the application to the presented data was out of the scope of this work.

Making sure that reference frames of the observed targets without any simultaneous calibration light are recorded in every night is important, a fact that has to be taken into account when planning observations. Especially when data from different nights should be combined, the time evolution of the scattered background light can have negative influences on the RV precision. To rule out such effects, reference frames should be obtained with the same exposure time and in the same observing conditions as the simultaneously calibrated frames.

Regarding the instrument's hardware equipment, it became apparent that an octagonal core fiber is needed as connection from the telescope to the spectrograph, because re-pointings of the telescope to the object occasionally are required. The potential effect of introducing an RV offset in such a situation is drastically reduced for fibers with octagonal instead of round cores.

An interesting finding was that the RV measurements are not as heavily affected by high airmasses as previously expected. As long as the atmospheric conditions are good, meaning the absence of large amounts of particles that are absorbing or scattering the stellar light, and the wavelength regions affected by telluric absorption lines are masked reliably, observations up to airmass 3 have proven to be reliable.

If the atmosphere is contaminated with particles like Sahara dust, observations at low airmasses $\lesssim 1.5$ can still be carried out without a significant loss in RV precision. However, two side effects should to be considered before starting to observe in such conditions: On the one hand, the expected flux from the object is attenuated, resulting in a considerably lower SNR of a single frame. On the other hand, the object's light may be scattered away, but at the same time light from other objects might be scattered into the telescope's light path, increasing the chance of spectral contamination. The latter has been found to be especially strong for bright sources like the Moon or the Sun, if they are located close to the horizon.

In general, contamination of the recorded spectra of an object with moonlight has a significant impact on the RV measurements. The observations in this work demonstrated that strategies to mitigate moonlight contamination as much as possible are absolutely required. Recommendations concluded from this work are to avoid observing a target if the angular distance of the Moon is <120° to avoid light entering the telescope dome either directly or by reflection and scattering from the slit opening. This is valid even if the illumination of the Moon is as low as 20%. However, the angular sky distance cannot serve as the only criterion to determine whether moonlight contamination could be problematic, but the azimuthal distance needs to be taken into account, too. As the dome slit extends in one line from the horizon to the zenith and beyond, a small azimuthal distance will allow the moonlight to directly enter the slit, although the overall angular distance may be large. To make well-founded decisions whether an observation should be carried out or not in a given night, these factors have to be carefully evaluated.

Spectra recorded close to dusk or dawn can be contaminated with daylight, causing errors in the RV measurements. The experience from this work is that such a contamination can safely be ruled out if in decent observation conditions exposures are taken with at least 1 h distance to the time of sunset or sunrise. High ambient humidity or ground-layer fog may raise the need to adopt a more conservative time interval due to the increased amount of scattered light. It has been found that the astronomical twilight time doesn't have to be considered as hard limit for observations and the sunrise and sunset times serve as better references.

As only one observation run was affected with light clouds passing through the field of view, the impact of clouds on the RV measurements could not be studied in detail. Nevertheless, the effect of contamination from bright objects is expected to increase in the presence of clouds due to the high reflectivity.

The impact of the environmental stability on observations with MaHPS was demonstrated with the obtained RV measurements. If the temperature and pressure control show a stable behavior within the specified stability goals, no negative effects can be noted in the measurements. Conversely, if the temperature and pressure inside the spectrograph are not stable enough, then the RV measurements are highly unreliable. Typically, imperfections of the pressure control cause the RV data to show a stronger spread, whereas temperature control deficiencies in the two-layer setup occur as slow drifts of the temperature in the innermost layer, resulting in a drift of the measured RVs. These findings justify the effort that was made in the scope of this work to establish temperature and pressure control systems with reliable performance.

When a combination of RV data from several transits is desired, the required observations should be carefully planned in advance. As can be seen from the example of HD149026, merging data sets from different nights could harm instead of improve the overall results, if the individual data sets are afflicted with systematic errors. In this case, the information about the RM effect signature recovered in only one of four nights would be completely destroyed if the observations were combined.

6.5.2 Future observations

Overall, it can be stated that RM effect measurements with MaHPS are not easy but possible, which is also true for observing the RM effect in objects where the RV anomaly has not been detected before. If the main issue of MaHPS, the low SNR level for a given exposure time, is overcome, e.g. by measuring multiple transits or by conducting simultaneous observations with other telescopes, MaHPS can deliver impactful RV measurements. For that reason, spectroscopic transit observations of further objects are scheduled and some even have started already.

The database of planetary candidates and confirmed planets of the TESS mission is a useful basis to find objects suitable for a RM effect discovery. Not all of the listed objects are observable with MaHPS, due to the position in the sky or being too faint, but for a decent number of candidates MaHPS measurements are feasible. For a selection of promising targets out of this sample, first observations have been obtained in collaboration with the Tautenburg Observatory. The analysis of the spectra unfortunately is still pending, so it is not possible to present any preliminary results or insights as of today.

Even if the data for the TESS candidates do not allow a determination of the obliquity angle, it may well be sufficient to distinguish whether an orbit is prograde or retrograde. Such a discovery would still be valuable, as it could be used to apply for observation time at larger telescopes or to foster further collaborations with other groups.

Chapter 7

Summary and outlook

Scientists have been occupied with describing the processes that enabled the formation of our very own planet Earth and the Solar System since ages. Lacking other sources of information, the planet formation models developed before the end of the 20th century were based solely on the knowledge of the Solar System. The discovery of thousands of exoplanets since the first confirmed detection in 1995 (Mayor and Queloz 1995) has opened up completely new opportunities and challenges for the understanding of the formation and evolution of planetary systems, including the Solar System.

The vast variety of architectures of planetary systems shows that a multitude of effects and parameters are influencing planetary system formation. The aim of this work was to contribute to the understanding of planetary systems and their formation by providing the high-resolution Manfred Hirt Planet Spectrograph (MaHPS), a measurement instrument that allows a more thorough characterization of planetary systems. The required precision of MaHPS was ensured by installing control systems for the environmental stabilization and demonstrated with observations of the Rossiter-McLaughlin (RM) effect.

An introduction to the topic of exoplanets and their detection was given in Chap. 1. The parameters describing a planetary system were defined before presenting an overview of the detection methods, where the strengths and systematic limitations of each method were discussed. The principles of the radial velocity (RV) method were highlighted in more detail, followed by a description of the techniques and instrumentation needed to carry out high-precision RV measurements.

In Chap. 2, the setup of MaHPS is presented. Descriptions of the subsystems for calibration, as well as for thermal and pressure stabilization are given. The chapter is concluded with a discussion of future modifications that would further improve the stability and precision of the instrument. Those include for instance the usage of fibers with octagonal cores, or the installation of a fully automated device for coupling the light from the telescope and the calibration sources into the optical fiber of the spectrograph, both reducing systematic errors of the RV measurements.

A thorough study of the environmental stability of MaHPS is found in Chap. 3. Measurement series with different settings of the temperature and pressure control systems were conducted to evaluate which configuration is best suited to comply with the requirements for a RV measurement stability on the few m/s level. In addition, the performance of the simultaneous calibration method, employing a laser frequency comb (LFC) as calibrator, was demonstrated.

Chapter 4 contains an overview of the data reduction and analysis methods used in this work. The General Astronomical Spectra Extractor (GAMSE) package was used for standard CCD reduction steps and a first wavelength calibration of the spectra. Measurements of wavelength shifts and RVs were conducted with the cross-correlation function (CCF) method, as implemented by the IRAF routine `fxcor` and the Munich Analyzer for Radial Velocity Measurements with B-Spline Optimized Templates (MARMOT).

The orbital obliquity of an exoplanet, which is defined as the angle between the rotation axis of the host star and the normal vector of the exoplanet's orbit, was introduced in Chap. 5. The RM effect was presented as a method to measure the orbital obliquity, since it gives rise to a RV anomaly during the transit of the planet in front of the host star. Different ways of modeling the RM effect to obtain information about the obliquity from the shape of the RV anomaly were addressed and a short overview of alternative obliquity measurement methods was given. The chapter is completed with an extensive discussion of the statistical distribution of orbital obliquities and the arising implications for current planet formation models.

In Chap. 6, observations of the RM effect for the three exoplanet hosts HD189733, HD149026, and HAT-P-2 were shown. For each object, the parameters characterizing the system were given, the observation conditions were summarized, and the resulting RV curves were interpreted. The performance of MaHPS was evaluated by comparison with observations from the literature. The experience gathered from the observations was highlighted and mitigation strategies for potential RV measurement errors were proposed.

The main findings of this work are diverse. On the one hand, it was shown that the technical setup of MaHPS is able to provide RV measurements with a precision of a few m/s, however further improvements can be made for instance by establishing an exposure time monitor or by optimizing the repeatability of coupling light from the telescope into the fiber to the spectrograph. On the other hand, it was found that data with low signal-to-noise ratio (SNR) can profit from customized analysis strategies, such as trading the improved wavelength calibration of simultaneous LFC calibration for the use of more physical orders of the spectrum. Furthermore, observations of the RM effect with MaHPS revealed that RV anomalies during a transit can be successfully recovered at a precision comparable to other spectrographs operated at 2 m class telescopes. Attention has to be given to the observing conditions, as spectral contamination in particular, e.g. with light from the Moon, has proven to heavily impact observations.

With the experience gained from this work, a campaign has been initiated to detect hints of the RM effect signal for planets which up to date lack any information about the obliquity angle. Although MaHPS may not be able to provide a high-quality measurement of the obliquity, this kind of data is nevertheless valuable for identifying promising candidate systems and preparing observations with more precise instruments like ESPRESSO, that allow deeper studies of the planetary systems in question.

Overall, measurements of the RM effect are an important source of information on the dominant mechanisms of planetary system formation and evolution. Combining the measurement results with current theories and simulations allows to refine models and advance the general understanding of planet formation. The RM effect is affected by similar systematic detection limits as the RV method, so that detections of massive, close-in planets are more likely than detections of light-weight planets with larger separations from their host star. Consequently, most of the studied objects belong to the group of hot Jupiters. In order to reach the goal of understanding the formation of small planets like Earth, observations of younger and smaller planets are required. Efforts to relentlessly push the frontiers of instrumentation are paving the way towards the characterization of small planets, enabling studies of the history of Earth analogues.

Bibliography

IAU Resolution B5 (2006). International Astronomical Union. URL: `https://www.iau.org/static/resolutions/Resolution_GA26-5-6.pdf`.

Perryman, M. (2018). *The Exoplanet Handbook*. Cambridge: Cambridge University Press.

Ohta, Y., A. Taruya, and Y. Suto (2005). "The Rossiter-McLaughlin Effect and Analytic Radial Velocity Curves for Transiting Extrasolar Planetary Systems." In: ApJ 622.2, pp. 1118–1135.

Mayor, M. and D. Queloz (1995). "A Jupiter-mass companion to a solar-type star." In: Nature 378.6555, pp. 355–359.

Hatzes, A. P. (2016a). "The Radial Velocity Method for the Detection of Exoplanets." In: *Methods of Detecting Exoplanets: 1st Advanced School on Exoplanetary Science*. Ed. by V. Bozza, L. Mancini, and A. Sozzetti. Vol. 428, p. 3.

González Hernández, J. I. et al. (2018). "ESPRESSO on VLT: An Instrument for Exoplanet Research." In: *Handbook of Exoplanets*. Ed. by H. J. Deeg and J. A. Belmonte, p. 157.

Pepe, F. et al. (2021). "ESPRESSO at VLT. On-sky performance and first results." In: A&A 645, A96, A96.

NASA Exoplanet Archive (2021). California Institute of Technology. URL: `https://exoplanetarchive.ipac.caltech.edu/` (visited on 10/14/2021).

Santos, N. C. et al. (2020). "Detection and Characterization Methods of Exoplanets." In: *Oxford Research Encyclopedia of Planetary Science*. Ed. by P. Read. Oxford University Press, p. 189.

Stassun, K. G. et al. (2018). "The TESS Input Catalog and Candidate Target List." In: AJ 156.3, 102, p. 102.

Obermeier, C. (2016). "Searching for hot Jupiter transits around cool stars." PhD thesis. LMU Munich, Germany.

Quirrenbach, A. (2010). "Astrometric Detection and Characterization of Exoplanets." In: *Exoplanets*. Ed. by S. Seager, pp. 157–174.

Makarov, V. V., N. Zacharias, and C. T. Finch (2021). "Looking for Astrometric Signals below 20 $\mathrm{m\,s^{-1}}$: A Candidate Exo-Jupiter in δ Pav." In: *Research Notes of the American Astronomical Society* 5.5, 108, p. 108.

Beuzit, J.-L. et al. (2019). "SPHERE: the exoplanet imager for the Very Large Telescope." In: A&A 631, A155, A155.

Roques, F., ed. (2021). *exoplanet.eu. The Extrasolar Planets Encyclopaedia*. Observatoire de Paris. URL: `http://exoplanet.eu/` (visited on 10/14/2021).

Gravity Collaboration et al. (2017). "First light for GRAVITY: Phase referencing optical interferometry for the Very Large Telescope Interferometer." In: A&A 602, A94, A94.

Doppler, C. (1846). "Bemerkungen zu meiner Theorie des farbigen Lichtes der Doppelsterne etc. mit vorzüglicher Rücksicht auf die von Herrn Dr. Ballot zu Utrecht dagegen erhobenen Bedenken." In: *Annalen der Physik* 144.5, pp. 1–35.

Lovis, C. and D. Fischer (2010). "Radial Velocity Techniques for Exoplanets." In: *Exoplanets*. Ed. by S. Seager, pp. 27–53.

Einstein, A. (1905). "Zur Elektrodynamik bewegter Körper." In: *Annalen der Physik* 322.10, pp. 891–921.

Lindegren, L. and D. Dravins (2003). "The fundamental definition of "radial velocity"." In: A&A 401, pp. 1185–1201.

Kanodia, S. and J. Wright (2018). "Python Leap Second Management and Implementation of Precise Barycentric Correction (barycorrpy)." In: *Research Notes of the American Astronomical Society* 2.1, 4, p. 4.

Naef, D. et al. (2004). "The ELODIE survey for northern extra-solar planets. III. Three planetary candidates detected with ELODIE." In: A&A 414, pp. 351–359.

Pepe, F. et al. (2002). "The CORALIE survey for southern extra-solar planets VII. Two short-period Saturnian companions to HD 108147 and HD 168746." In: A&A 388, pp. 632–638.

Dumusque, X. et al. (2012). "An Earth-mass planet orbiting α Centauri B." In: Nature 491.7423, pp. 207–211.

Carrier, F. et al. (2005). "Solar-like oscillations in the F9 V β Virginis." In: New A 10.4, pp. 315–323.

Dumusque, X. et al. (2011). "The HARPS search for southern extra-solar planets. XXX. Planetary systems around stars with solar-like magnetic cycles and short-term activity variation." In: A&A 535, A55, A55.

Thorne, A. P. (1988). *Spectrophysics*. 2nd ed. New York: Chapman and Hall.

Eversberg, T. and K. Vollmann (2015). *Spectroscopic Instrumentation: Fundamentals and Guidelines for Astronomers*. Berlin: Springer-Verlag.

de Cuyper, J.-P. et al. (2007). "HERMES, a High-Resolution, Fiber-Fed Spectrograph for the MERCATOR Telescope." In: *Astronomical Data Analysis Software and Systems XVI*. Ed. by R. A. Shaw, F. Hill, and D. J. Bell. Vol. 376. Astronomical Society of the Pacific Conference Series, p. 653.

Chauville, J. et al. (2001). "High and intermediate-resolution spectroscopy of Be stars 4481 lines." In: A&A 378, pp. 861–882.

Abt, H. A., H. Levato, and M. Grosso (2002). "Rotational Velocities of B Stars." In: ApJ 573.1, pp. 359–365.

Caccin, B. et al. (1985). "Terrestrial O2 lines used as wavelength references Experimental profiles and asymmetries vs. model computations." In: A&A 149.2, pp. 357–364.

Campbell, B. and G. A. H. Walker (1979). "Precision radial velocities with an absorption cell." In: PASP 91, pp. 540–545.

Butler, R. P. et al. (1996). "Attaining Doppler Precision of 3 M s^{-1}." In: PASP 108, p. 500.

Cochran, W. D. and A. P. Hatzes (1993). "McDonald Observatory Planetary Search: a high precision stellar radial velocity survey for other planetary systems." In: *Planets Around Pulsars*. Ed. by J. A. Phillips, S. E. Thorsett, and S. R. Kulkarni. Vol. 36. Astronomical Society of the Pacific Conference Series, pp. 267–273.

Lovis, C. and F. Pepe (2007). "A new list of thorium and argon spectral lines in the visible." In: A&A 468.3, pp. 1115–1121.

Bauer, F. F., M. Zechmeister, and A. Reiners (2015). "Calibrating echelle spectrographs with Fabry-Pérot etalons." In: A&A 581, A117, A117.

Ge, J. (2008). "Doppler Exoplanet Surveys: From Single Object to Multiple Objects." In: *Exoplanets*. Ed. by J. W. Mason, p. 21.

Wilken, T. et al. (2012). "A spectrograph for exoplanet observations calibrated at the centimetre-per-second level." In: Nature 485.7400, pp. 611–614.

Milaković, D. et al. (2020). "Precision and consistency of astrocombs." In: MNRAS 493.3, pp. 3997–4011.

Udry, S. et al. (2019). "The HARPS search for southern extra-solar planets. XLIV. Eight HARPS multi-planet systems hosting 20 super-Earth and Neptune-mass companions." In: A&A 622, A37, A37.

Kosyra, R. et al. (2014). "The 64 Mpixel wide field imager for the Wendelstein 2m telescope: design and calibration." In: *Experimental Astronomy* 38.1-2, pp. 213–248.

Lang-Bardl, F. et al. (2016). "The Wendelstein three channel imager (3KK): alignment, commissioning, and first results." In: *Ground-based and Airborne Instrumentation for Astronomy VI*. Ed. by C. J. Evans, L. Simard, and H. Takami. Vol. 9908. Society of Photo-Optical Instrumentation Engineers (SPIE) Conference Series, p. 990844.

Fahrenschon, V. et al. (2020). "Environmental stability achieved for the Manfred Hirt Planet Spectrograph." In: *Society of Photo-Optical Instrumentation Engineers (SPIE) Conference Series*. Vol. 11447. Society of Photo-Optical Instrumentation Engineers (SPIE) Conference Series, 114473H.

Kellermann, H. (2021). "Commissioning of the high-resolution comb-calibrated spectrograph at the Wendelstein-Observatory and development of calibration and fitting software packages for the hunt of exoplanets." Unpublished Ph.D. dissertation. Ludwig-Maximilians-Universität München.

Pfeiffer, M. J., C. Frank, and D. Baumüller (1992). "The fibre optic-coupled Cassegrain Echelle Spectrograph FOCES." In: *Astronomische Gesellschaft Abstract Series*. Vol. 7. Astronomische Gesellschaft Abstract Series, p. 191.

Grupp, F. et al. (2010). "Pressure and temperature stabilization of an existing Échelle spectrograph." In: *Ground-based and Airborne Instrumentation for Astronomy III*. Ed. by I. S. McLean, S. K. Ramsay, and H. Takami. Vol. 7735. Society of Photo-Optical Instrumentation Engineers (SPIE) Conference Series, p. 773573.

Grupp, F., S. M. Hu, and L. Wang (2009). "Modeling the image distortion of echelle spectrographs with T&P changes." In: *Techniques and Instrumentation for Detection of Exoplanets IV*. Ed. by S. B. Shaklan. Vol. 7440. Society of Photo-Optical Instrumentation Engineers (SPIE) Conference Series, 74401G.

Grupp, F. et al. (2011). "Pressure and temperature stabilization of an existing Échelle spectrograph II." In: *Techniques and Instrumentation for Detection of Exoplanets V*. Ed. by S. Shaklan. Vol. 8151. Society of Photo-Optical Instrumentation Engineers (SPIE) Conference Series, p. 815119.

Brucalassi, A. et al. (2012). "Pressure and temperature stabilization of an existing Échelle spectrograph III." In: *Ground-based and Airborne Instrumentation for Astronomy IV*. Ed. by I. S. McLean, S. K. Ramsay, and H. Takami. Vol. 8446. Society of Photo-Optical Instrumentation Engineers (SPIE) Conference Series, 84462F.

Brucalassi, A. et al. (2013). "Pressure and temperature stabilization of an existing Échelle spectrograph IV." In: *Techniques and Instrumentation for Detection of Exoplanets VI*. Ed. by S. Shaklan. Vol. 8864. Society of Photo-Optical Instrumentation Engineers (SPIE) Conference Series, 88641H.

Brucalassi, A. et al. (2016). "Stability of the FOCES spectrograph using an astro-frequency comb as calibrator." In: *Ground-based and Airborne Instrumentation for Astronomy VI*. Ed. by C. J. Evans, L. Simard, and H. Takami. Vol. 9908. Society of Photo-Optical Instrumentation Engineers (SPIE) Conference Series, 99085W.

Pfeiffer, M. J. et al. (1998). "FOCES - a fibre optics Cassegrain Echelle spectrograph." In: A&AS 130, pp. 381–393.

Kellermann, H. et al. (2020). "Verification observations of the Manfred Hirt Planet Spectrograph." In: *Society of Photo-Optical Instrumentation Engineers (SPIE) Conference Series*. Vol. 11447. Society of Photo-Optical Instrumentation Engineers (SPIE) Conference Series, 114474K.

Kellermann, H. et al. (2015). "A new fiber slit assembly for the FOCES spectrograph." In: *Techniques and Instrumentation for Detection of Exoplanets VII*. Ed. by S. Shaklan. Vol. 9605. Society of Photo-Optical Instrumentation Engineers (SPIE) Conference Series, 96051R.

Kellermann, H. et al. (2016). "Multi-fiber coupling through a miniature lens system into the FOCES spectrograph." In: *Ground-based and Airborne Instrumentation for Astronomy VI*. Ed. by C. J. Evans, L. Simard, and H. Takami. Vol. 9908. Society of Photo-Optical Instrumentation Engineers (SPIE) Conference Series, p. 990863.

Kellermann, H. et al. (2019). "First results of the 4-fiber upgrade of the high-resolution comb calibrated spectrograph FOCES." In: *Society of Photo-Optical Instrumentation Engineers (SPIE) Conference Series*. Vol. 11117. Society of Photo-Optical Instrumentation Engineers (SPIE) Conference Series, 111171O.

iKon-L Series - datasheet (2020). Oxford Instruments.

Strassmeier, K. G. et al. (2008). "PEPSI: the Potsdam Echelle Polarimetric and Spectroscopic Instrument for the LBT." In: *Ground-based and Airborne Instrumentation for Astronomy II*. Ed. by I. S. McLean and M. M. Casali. Vol. 7014. Society of Photo-Optical Instrumentation Engineers (SPIE) Conference Series, 70140N.

PTC10 - Programmable Temperature Controller - manual (2019). Stanford Research Systems.

Bansal, H., R. Sharma, and S. Ponpathirkoottam (2012). "PID Controller Tuning Techniques: A Review." In: 2, pp. 168–176.

George, T. and V. Ganesan (2020). "Optimal tuning of PID controller in time delay system: a review on various optimization techniques." In: *Chemical Product and Process Modeling*, p. 20202001.

Gebläsekonvektoren Flex-Geko: Technische Daten (2018). Fläkt Group.

KIT-Z50-TKEA - technical data (2021). Panasonic. URL: `https://www.aircon.panasonic.eu/DE_de/model/kit-z50-tkea-cs-z50tkea-cu-z50tkea/` (visited on 09/01/2021).

Temperature Control - Tuning a PID (Three Mode) Controller - manual (2021). Omega Engineering.

Krecker, K. et al. (2020). "Multifocal station for the Wendelstein 2m Fraunhofer Telescope." In: *Society of Photo-Optical Instrumentation Engineers (SPIE) Conference Series*. Vol. 11447. Society of Photo-Optical Instrumentation Engineers (SPIE) Conference Series, p. 1144763.

Wang, L. et al. (2016). "A new generation of spectral extraction and analysis package for Fiber Optics Cassegrain Echelle Spectrograph (FOCES)." In: *Software and Cyberinfrastructure for Astronomy IV*. Ed. by G. Chiozzi and J. C. Guzman. Vol. 9913. Society of Photo-Optical Instrumentation Engineers (SPIE) Conference Series, 99133O.

Wang, L. et al. (2017). "Line profile analysis of the laser frequency comb in FOCES." In: vol. 10400. Society of Photo-Optical Instrumentation Engineers (SPIE) Conference Series, p. 104001V.

Wang, L. et al. (in prep.). "GAMSE: A Data Reduction Software for Echelle Spectrographs." In: *TBD*.

Howell, S. B. (2006). *Handbook of CCD Astronomy*. Vol. 5.

Horne, K. (1986). "An optimal extraction algorithm for CCD spectroscopy." In: PASP 98, pp. 609–617.

Tody, D. (1986). "The IRAF Data Reduction and Analysis System." In: *Instrumentation in astronomy VI*. Ed. by D. L. Crawford. Vol. 627. Society of Photo-Optical Instrumentation Engineers (SPIE) Conference Series, p. 733.

Tody, D. (1993). "IRAF in the Nineties." In: *Astronomical Data Analysis Software and Systems II*. Ed. by R. J. Hanisch, R. J. V. Brissenden, and J. Barnes. Vol. 52. Astronomical Society of the Pacific Conference Series, p. 173.

Fitzpatrick, M. J. (1993). "The IRAF Radial Velocity Analysis Package." In: *Astronomical Data Analysis Software and Systems II*. Ed. by R. J. Hanisch, R. J. V. Brissenden, and J. Barnes. Vol. 52. Astronomical Society of the Pacific Conference Series, p. 472.

Creative Commons license CC-BY-SA-3.0 (2021). Creative Commons Corporation. URL: `https://creativecommons.org/licenses/by-sa/3.0/legalcode` (visited on 10/08/2021).

Tonry, J. and M. Davis (1979). "A survey of galaxy redshifts. I. Data reduction techniques." In: AJ 84, pp. 1511–1525.

Alpaslan, M. (2009). "A quick guide to FXCOR." In: *arXiv e-prints*, arXiv:0912.4755, arXiv:0912.4755.

Wenger, M. et al. (2000). "The SIMBAD astronomical database. The CDS reference database for astronomical objects." In: A&AS 143, pp. 9–22.

Zechmeister, M. et al. (2018). “Spectrum radial velocity analyser (SERVAL). High-precision radial velocities and two alternative spectral indicators.” In: A&A 609, A12, A12.

Bouchy, F., F. Pepe, and D. Queloz (2001). “Fundamental photon noise limit to radial velocity measurements.” In: A&A 374, pp. 733–739.

Artigau, É. et al. (2018). “Optical and Near-infrared Radial Velocity Content of M Dwarfs: Testing Models with Barnard’s Star.” In: AJ 155.5, 198, p. 198.

Murphy, M. T. et al. (2007). “High-precision wavelength calibration of astronomical spectrographs with laser frequency combs.” In: MNRAS 380.2, pp. 839–847.

Holt, J. R. (1893). “Spectroscopic Determination of Stellar Rotation.” In: *Astronomy and Astro-Physics (formerly The Sidereal Messenger)* 12, p. 646.

Schlesinger, F. (1910). “The Algol-variable δ Librae.” In: *Publications of the Allegheny Observatory of the University of Pittsburgh* 1.20, pp. 123–134.

Rossiter, R. A. (1924). “On the detection of an effect of rotation during eclipse in the velocity of the brighter component of beta Lyrae, and on the constancy of velocity of this system.” In: ApJ 60, pp. 15–21.

McLaughlin, D. B. (1924). “Some results of a spectrographic study of the Algol system.” In: ApJ 60, pp. 22–31.

Queloz, D. et al. (2000). “Detection of a spectroscopic transit by the planet orbiting the star HD209458.” In: A&A 359, pp. L13–L17.

Hatzes, A. P. (2016b). “The Architecture of Exoplanets.” In: Space Sci. Rev. 205.1-4, pp. 267–283.

Narita, N. et al. (2009). “First Evidence of a Retrograde Orbit of a Transiting Exoplanet HAT-P-7b.” In: PASJ 61, pp. L35–L40.

Winn, J. N. et al. (2009). “HAT-P-7: A Retrograde or Polar Orbit, and a Third Body.” In: ApJ 703.2, pp. L99–L103.

Sasaki, S. and Y. Suto (2021, in press). “Disentangling the stellar inclination of transiting planetary systems: Fully analytic approach to the Rossiter-McLaughlin effect incorporating the stellar differential rotation.” In: PASJ.

Albrecht, S. et al. (2021). “A Preponderance of Perpendicular Planets.” In: ApJ 916.1, L1, p. L1.

Fabrycky, D. C. and J. N. Winn (2009). “Exoplanetary Spin-Orbit Alignment: Results from the Ensemble of Rossiter-McLaughlin Observations.” In: ApJ 696.2, pp. 1230–1240.

Gaudi, B. S. and J. N. Winn (2007). “Prospects for the Characterization and Confirmation of Transiting Exoplanets via the Rossiter-McLaughlin Effect.” In: ApJ 655.1, pp. 550–563.

Winn, J. N. (2011). “The Rossiter-McLaughlin effect for exoplanets.” In: *The Astrophysics of Planetary Systems: Formation, Structure, and Dynamical Evolution.* Ed. by A. Sozzetti, M. G. Lattanzi, and A. P. Boss. Vol. 276, pp. 230–237.

Winn, J. N. (2010). “Exoplanet Transits and Occultations.” In: *Exoplanets.* Ed. by S. Seager, pp. 55–77.

Bieryla, A. et al. (2021). “Stellar Parameter Classification of TESS recon spectra from TRES and FIES.” In: *Posters from the TESS Science Conference II (TSC2)*, p. 124.

Montet, B. T. et al. (2020). "The Young Planet DS Tuc Ab Has a Low Obliquity." In: AJ 159.3, 112, p. 112.

Giménez, A. (2006). "Equations for the Analysis of the Rossiter-MCLaughlin Effect in Extrasolar Planetary Transits." In: ApJ 650.1, pp. 408–413.

Hirano, T. et al. (2010). "Analytic Description of the Rossiter-Mclaughlin Effect for Transiting Exoplanets: Cross-Correlation Method and Comparison with Simulated Data." In: ApJ 709.1, pp. 458–469.

Boué, G. et al. (2013). "New analytical expressions of the Rossiter-McLaughlin effect adapted to different observation techniques." In: A&A 550, A53, A53.

Luger, R. et al. (2019). "starry: Analytic Occultation Light Curves." In: AJ 157.2, 64, p. 64.

Bedell, M. et al. (2019). "WOBBLE: A Data-driven Analysis Technique for Time-series Stellar Spectra." In: AJ 158.4, 164, p. 164.

Johnson, M. C. et al. (2021, subm.). "An Aligned Orbit for the Young Planet V1298 Tau b." In: *arXiv e-prints*, arXiv:2110.10707, arXiv:2110.10707.

Gray, D. F. (2005). *The Observation and Analysis of Stellar Photospheres*. Cambridge: Cambridge University Press, p. 462.

Albrecht, S. et al. (2012). "Obliquities of Hot Jupiter Host Stars: Evidence for Tidal Interactions and Primordial Misalignments." In: ApJ 757.1, 18, p. 18.

Short, D. R. et al. (2018). "Accurate Computation of Light Curves and the Rossiter-McLaughlin Effect in Multibody Eclipsing Systems." In: AJ 156.6, 297, p. 297.

Cegla, H. M. et al. (2016). "The Rossiter-McLaughlin effect reloaded: Probing the 3D spin-orbit geometry, differential stellar rotation, and the spatially-resolved stellar spectrum of star-planet systems." In: A&A 588, A127, A127.

Hirano, T. et al. (2011). "Improved Modeling of the Rossiter-McLaughlin Effect for Transiting Exoplanets." In: ApJ 742.2, 69, p. 69.

Shporer, A. and T. Brown (2011). "The Impact of the Convective Blueshift Effect on Spectroscopic Planetary Transits." In: ApJ 733.1, 30, p. 30.

Kipping, D. M. (2013). "Efficient, uninformative sampling of limb darkening coefficients for two-parameter laws." In: MNRAS 435.3, pp. 2152–2160.

Oshagh, M. et al. (2016). "Can stellar activity make a planet seem misaligned?" In: A&A 593, A25, A25.

Oshagh, M. et al. (2018). "Activity induced variation in spin-orbit angles as derived from Rossiter-McLaughlin measurements." In: A&A 619, A150, A150.

Addison, B. C. et al. (2021). "The Youngest Planet to Have a Spin-Orbit Alignment Measurement AU Mic b." In: AJ 162.4, 137, p. 137.

Di Gloria, E., I. A. G. Snellen, and S. Albrecht (2015). "Using the chromatic Rossiter-McLaughlin effect to probe the broadband signature in the optical transmission spectrum of HD 189733b." In: A&A 580, A84, A84.

Borsa, F. et al. (2021). "Atmospheric Rossiter-McLaughlin effect and transmission spectroscopy of WASP-121b with ESPRESSO." In: A&A 645, A24, A24.

Gandolfi, D. et al. (2012). "Doppler tomography of transiting exoplanets: a prograde, low-inclined orbit for the hot Jupiter CoRoT-11b." In: A&A 543, L5, p. L5.

Dai, F. et al. (2017). “The Stellar Obliquity, Planet Mass, and Very Low Albedo of Qatar-2 from K2 Photometry.” In: AJ 153.1, 40, p. 40.
Ahlers, J. P. et al. (2020). “KELT-9 b’s Asymmetric TESS Transit Caused by Rapid Stellar Rotation and Spin-Orbit Misalignment.” In: AJ 160.1, 4, p. 4.
Sanchis-Ojeda, R. et al. (2013). “Kepler-63b: A Giant Planet in a Polar Orbit around a Young Sun-like Star.” In: ApJ 775.1, 54, p. 54.
Sanchis-Ojeda, R. et al. (2011). “Starspots and Spin-orbit Alignment in the WASP-4 Exoplanetary System.” In: ApJ 733.2, 127, p. 127.
Lai, D., F. Foucart, and D. N. C. Lin (2011). “Evolution of spin direction of accreting magnetic protostars and spin-orbit misalignment in exoplanetary systems.” In: MNRAS 412.4, pp. 2790–2798.
Chatterjee, S. et al. (2008). “Dynamical Outcomes of Planet-Planet Scattering.” In: ApJ 686.1, pp. 580–602.
Fabrycky, D. C. and S. Tremaine (2007). “Shrinking Binary and Planetary Orbits by Kozai Cycles with Tidal Friction.” In: ApJ 669.2, pp. 1298–1315.
Petrovich, C. et al. (2020). “A Disk-driven Resonance as the Origin of High Inclinations of Close-in Planets.” In: ApJ 902.1, L5, p. L5.
Wang, S. et al. (2021). “The Aligned Orbit of the Eccentric Warm Jupiter K2-232b.” In: AJ 162.2, 50, p. 50.
Kley, W. and R. P. Nelson (2012). “Planet-Disk Interaction and Orbital Evolution.” In: ARA&A 50, pp. 211–249.
Lai, D. (2012). “Tidal dissipation in planet-hosting stars: damping of spin-orbit misalignment and survival of hot Jupiters.” In: MNRAS 423.1, pp. 486–492.
Boley, A. C., A. P. Granados Contreras, and B. Gladman (2016). “The In Situ Formation of Giant Planets at Short Orbital Periods.” In: ApJ 817.2, L17, p. L17.
Addison, B. C. et al. (2018). “Stellar Obliquities and Planetary Alignments (SOPA). I. Spin-Orbit Measurements of Three Transiting Hot Jupiters: WASP-72b, WASP-100b, and WASP-109b.” In: AJ 156.5, 197, p. 197.
Winn, J. N. et al. (2010). “Hot Stars with Hot Jupiters Have High Obliquities.” In: ApJ 718.2, pp. L145–L149.
Maeder, A. (2009). *Physics, Formation and Evolution of Rotating Stars.*
Winn, J. N. et al. (2007a). “The Transit Light Curve Project. V. System Parameters and Stellar Rotation Period of HD 189733.” In: AJ 133.4, pp. 1828–1835.
Gizon, L. and S. K. Solanki (2003). “Determining the Inclination of the Rotation Axis of a Sun-like Star.” In: ApJ 589.2, pp. 1009–1019.
Wang, X.-Y. et al. (2021, subm.). “SOLES II: The Aligned Orbit of WASP-148b, the Only Known Hot Jupiter with a Nearby Warm Jupiter Companion, from NEID and HIRES.” In: *arXiv e-prints*, arXiv:2110.08832, arXiv:2110.08832.
Triaud, A. H. M. J. (2018). “The Rossiter-McLaughlin Effect in Exoplanet Research.” In: *Handbook of Exoplanets*. Ed. by H. J. Deeg and J. A. Belmonte, p. 2.
Hébrard, G. et al. (2011). “The retrograde orbit of the HAT-P-6b exoplanet.” In: A&A 527, L11, p. L11.

Dawson, R. I. (2014). "On the Tidal Origin of Hot Jupiter Stellar Obliquity Trends." In: ApJ 790.2, L31, p. L31.

Anderson, D. R. et al. (2015). "The Well-aligned Orbit of Wasp-84b: Evidence for Disk Migration of a Hot Jupiter." In: ApJ 800.1, L9, p. L9.

Marigo, P. et al. (2008). "Evolution of asymptotic giant branch stars. II. Optical to far-infrared isochrones with improved TP-AGB models." In: A&A 482.3, pp. 883–905.

Brown, D. J. A. et al. (2017). "Rossiter-McLaughlin models and their effect on estimates of stellar rotation, illustrated using six WASP systems." In: MNRAS 464.1, pp. 810–839.

Stefansson, G. et al. (2021, subm.). "The Warm Neptune GJ 3470b has a Polar Orbit." In: *arXiv e-prints*, arXiv:2111.01295, arXiv:2111.01295.

Dawson, R. I. and S. H. Albrecht (2021, in prep.). "From Warm Planets to Perpendicular Hot Planets." In: *arXiv e-prints*, arXiv:2108.09325, arXiv:2108.09325.

Hessman, F. V. et al. (2010). "On the naming convention used for multiple star systems and extrasolar planets." In: *arXiv e-prints*, arXiv:1012.0707, arXiv:1012.0707.

Southworth, J. (2011). "Homogeneous studies of transiting extrasolar planets - IV. Thirty systems with space-based light curves." In: MNRAS 417.3, pp. 2166–2196.

Pogson, N. (1856). "Magnitudes of Thirty-six of the Minor Planets for the first day of each month of the year 1857." In: MNRAS 17, pp. 12–15.

Jensen, E. (2013). *Tapir: A web interface for transit/eclipse observability*.

Winn, J. N. et al. (2006). "Measurement of the Spin-Orbit Alignment in the Exoplanetary System HD 189733." In: ApJ 653.1, pp. L69–L72.

Triaud, A. H. M. J. et al. (2009). "The Rossiter-McLaughlin effect of CoRoT-3b and HD 189733b." In: A&A 506.1, pp. 377–384.

Collier Cameron, A. et al. (2010). "Line-profile tomography of exoplanet transits - I. The Doppler shadow of HD 189733b." In: MNRAS 403.1, pp. 151–158.

Casasayas-Barris, N. et al. (2017). "Detection of sodium in the atmosphere of WASP-69b." In: A&A 608, A135, A135.

Addison, B. C. et al. (2019). "Minerva-Australis. I. Design, Commissioning, and First Photometric Results." In: PASP 131.1005, p. 115003.

Koen, C. et al. (2010). "UBV$(\mathrm{RI})_C$ JHK observations of Hipparcos-selected nearby stars." In: MNRAS 403.4, pp. 1949–1968.

Dumusque, X. (2014). "Deriving Stellar Inclination of Slow Rotators Using Stellar Activity." In: ApJ 796.2, 133, p. 133.

Heng, K. et al. (2015). "A Non-isothermal Theory for Interpreting Sodium Lines in Transmission Spectra of Exoplanets." In: ApJ 803.1, L9, p. L9.

Louden, T. and P. J. Wheatley (2015). "Spatially Resolved Eastward Winds and Rotation of HD 189733b." In: ApJ 814.2, L24, p. L24.

Wolf, A. S. et al. (2007). "A Determination of the Spin-Orbit Alignment of the Anomalously Dense Planet Orbiting HD 149026." In: ApJ 667.1, pp. 549–556.

Carter, J. A. et al. (2009). "Near-Infrared Transit Photometry of the Exoplanet HD 149026b." In: ApJ 696.1, pp. 241–253.

Ment, K. et al. (2018). "Radial Velocities from the N2K Project: Six New Cold Gas Giant Planets Orbiting HD 55696, HD 98736, HD 148164, HD 203473, and HD 211810." In: AJ 156.5, 213, p. 213.

Zhang, M. et al. (2018). "Phase Curves of WASP-33b and HD 149026b and a New Correlation between Phase Curve Offset and Irradiation Temperature." In: AJ 155.2, 83, p. 83.

Høg, E. et al. (2000). "The Tycho-2 catalogue of the 2.5 million brightest stars." In: A&A 355, pp. L27–L30.

Stevenson, K. B. et al. (2012). "Transit and Eclipse Analyses of the Exoplanet HD 149026b Using BLISS Mapping." In: ApJ 754.2, 136, p. 136.

Winn, J. N. et al. (2007b). "Spin-Orbit Alignment for the Eccentric Exoplanet HD 147506b." In: ApJ 665.2, pp. L167–L170.

Loeillet, B. et al. (2008). "Refined parameters and spectroscopic transit of the supermassive planet HD 147506b." In: A&A 481.2, pp. 529–533.

Pál, A. et al. (2010). "Refined stellar, orbital and planetary parameters of the eccentric HAT-P-2 planetary system." In: MNRAS 401.4, pp. 2665–2674.

Bonomo, A. S. et al. (2017). "The GAPS Programme with HARPS-N at TNG . XIV. Investigating giant planet migration history via improved eccentricity and mass determination for 231 transiting planets." In: A&A 602, A107, A107.

Lewis, N. K. et al. (2014). "Atmospheric Circulation of Eccentric Hot Jupiter HAT-P-2b." In: ApJ 795.2, 150, p. 150.

Virtanen, P. et al. (2020). "SciPy 1.0: Fundamental Algorithms for Scientific Computing in Python." In: *Nature Methods* 17, pp. 261–272.

van der Walt, S., S. C. Colbert, and G. Varoquaux (2011). "The NumPy Array: A Structure for Efficient Numerical Computation." In: *Computing in Science Engineering* 13.2, pp. 22–30.

Acknowledgments

First and foremost, I would like to thank Ben for going through all the highs and lows with me. Thanks for sacrificing so much to give me the chance to achieve what I always aspired. You were the one that had to bear with me, every time I was nervous, stressing myself out and losing my mind again, but you managed to give me a feeling of security and sanity no matter what. You were always open for discussions when I didn't have any clue and you were listening to my countless lamentations. Thank you so much for caring about me and for teaching me not to care about my work in my spare time. And thanks for proofreading my thesis although the times are rough for you also. Although I am rarely voicing it directly, my gratitude for your support is endless.

A lot of people were involved in one or the other way during my time as PhD student. Not all will be explicitly mentioned here (sorry!), but please be assured that I am grateful for getting to know each single one of you and I appreciate every little bit of support brought my way.

I want to express my deep thanks to my family, for letting me go my own way and always believing that I could achieve what I wanted, even though they don't understand what it is all about. Thanks for your support in any form, for teaching me to be independent and for setting the stage so I can reach my goals. Another thank you goes to Alex for brightening my days with cats, for spending time to proofread everything, and for providing a couch that withstands any spilled wine. I need to thank Andreas for offering his service as proofreader and consequently fighting through numerous pages of awfully uninspiring technical details of the experimental setup.

My many colleagues of course also deserve lots of gratitude, for patiently listening to all kinds of questions or problems and for their unlimited willingness to help at any time.

Thanks to Roberto for allowing me to carry out this work, thanks for giving me numerous opportunities to learn and for the encouraging words when I was close to desperation. I appreciate that you gave me free hand in my work and trusted me to complete my tasks without close supervision. Nevertheless, you always reacted quickly when issues showed up, sometimes even before I noticed problems myself. A further thank you goes to Ralf Bender for providing the framework of the project.

Huge thanks go to Hanna for sharing the love and hate to the spectrograph, condensed in the countless hours of aligning optics at the mountain. The two of us have always been a great balance of optimism and frustration and I have enjoyed our collaboration through the years. I want to thank Frank for believing that MaHPS is worth the effort, for his endless enthusiasm for small and big problems, and for the mindset that any task can be an easy task. And a thank you also goes to Liang, for all the time spent to optimize GAMSE and for letting me get in touch with Chinese culture first hand.

Thanks to Christian for extensive discussions, no matter the topic, for a memorable trip to the McDonald Observatory, and for all the positivity and chances to let out the frustration, either at the USM or in spare time. Thanks also to Arno for not being afraid of thinking on unconventional ways and patiently working towards solutions, even though being fully booked all the time. Thanks to Jana and Markus for all the opportunities to chat about things that are going on and for not being afraid of the big changes.

Thanks to Florian for always being open for questions and providing solutions, for taking care despite all other responsibilities and for having a reliable documentation at hand when it matters. Thanks to Claus for listening, talking, knowing the pain and providing a very welcome distraction with his mobile zoo. Thanks for Ulrich for the support, also concerning any career development opportunities, and for being honest when honesty was due. And thanks to Jan, in combination with Claus, for all the effort invested in El Señor, which was a workhorse for many of my tasks.

I also want to thank Wolfgang, Michael and Christoph for bearing the countless calls when some part of MaHPS was going wrong again. Thanks for all your effort and patience, for introducing me to the little knacks of the observatory, and for welcoming me at that special place. Thanks also to the mechanical and electronical staff of the USM, for instance Ady, Peter, Herbert, Marco, Achim or Helmut, for providing your expertise when my knowledge was at an end.

Special words of appreciation go to the spectroscopy team at Tautenburg, for sharing their love for exoplanet science and years of experience in spectroscopy. Many thanks go to Eike in particular, for patiently answering numerous questions and willingly sharing his vast knowledge. Thanks for being such a positive role model and for never tiring to promote the fascination and importance of high-resolution spectroscopy.

MaHPS was named in honor of Professor Manfred Hirt, president of the association of friends of the Munich University Observatory, who played a key role in upgrading the Wendelstein Observatory with its 2m Fraunhofer telescope.

This research has made use of the NASA Exoplanet Archive, which is operated by the California Institute of Technology, under contract with the National Aeronautics and Space Administration under the Exoplanet Exploration Program.

This research has made use of NASA's Astrophysics Data System.

This research has made use of the SIMBAD database, operated at CDS, Strasbourg, France (Wenger et al. 2000).

The `staralt` tool, developed by Peter Sorensen, Marco Azzaro, and Javier Méndez of the Isaac Newton Group of Telescopes, was utilized in this work. The Isaac Newton Group of Telescopes (ING) is owned by the Science and Technology Facilities Council (STFC-UKRI) of the United Kingdom, and it is operated jointly with the Nederlandse Organisatie voor Wetenschappelijk Onderzoek (NWO) of the Netherlands and the Instituto de Astrofísica de Canarias (IAC) of Spain. IAC's contribution to ING is funded by the

Spanish Ministry of Science, Innovation and Universities. The telescopes are located in the Spanish Observatorio del Roque de los Muchachos on La Palma, Canary Islands, which is operated by the IAC.

The analysis within this paper made extensive use of scipy (Virtanen et al. 2020) and numpy (van der Walt et al. 2011).

Curriculum Vitae

Vanessa Fahrenschon

8th April 1992	born in Göppingen (Germany) nationality: German

---

Sept. 2002 – June 2011	Werner-Heisenberg-Gymnasium Göppingen *high school education*
31st May 2011	**A-level ("Abitur")**, grade 1.2

Sept. 2011 – Sept. 2014	Ludwig-Maximilians-Universität München *undergraduate studies*
16th Sept. 2014	**Bachelor of Science Physics**, grade 2.06

Oct. 2014 – April 2017	Ludwig-Maximilians-Universität München *graduate studies*
Aug. 2015 – Feb. 2016	Universidad de La Laguna *ERASMUS exchange semester*
27th April 2017	**Master of Science Astrophysics**, grade 1.49

June 2017 – Oct. 2021	Max-Planck-Institut für extraterrestrische Physik Garching *employment as PhD student*

____

Vanessa Fahrenschon